ADVANCING UNDERGROUND DRILLING WITH PARTICLE RHEOLOGY

by

Benjamin A. Appleby

© Copyright by Benjamin A. Appleby, 2023

All Rights Reserved

A thesis submitted to the Faculty and the Board of Trustees of the Colorado School of Mines in partial fulfillment of the requirements for the degree of Doctor of Philosophy (Chemical Engineering).

Golden, Colorado

Date _____

Signed: _____
Benjamin A. Appleby

Signed: _____
Dr. Joseph R. Samaniuk
Thesis Advisor

Signed: _____
Dr. Michael A. Mooney
Thesis Co-advisor

Golden, Colorado

Date _____

Signed: _____
Dr. Daniel Knauss
Professor and Interim Department Head
Department of Chemical & Biological Engineering

ABSTRACT

This thesis addresses material processing and technological challenges in underground drilling. Material processing includes the breakdown and fluidization of soil materials primarily composed of clay and granular particles at low ($\geq 16.7wt\%\ Solids$) and high ($\leq 3wt\%\ Solids$) water content. In chapter 3, for low water content soils, a viscometer was developed with a calibration procedure used for complex fluid samples with granular particles. This procedure was modified with the Bingham Plastic constitutive relationship to include shear-thinning/shear-thickening and yield stress behavior. This work expands viscometer capabilities to measure samples with particles surpassing 4cm in size and captures additional viscometric material properties. In chapter 4, for high water content soils, a flow loop was built to measure the viscometric power-law parameters of bentonite drilling fluid slurry with soil cuttings, cuttings returns. Learned from this work, classifying soil cuttings and drilling fluids by clay type, clay to sand ratio, and water content was not enough to capture viscometric differences between cuttings returns samples from a drill site compared to a model sample made in the lab.

Fluid circulation loss, one of the largest problems in underground drilling, was addressed with technological work. In chapter 5, a contra-rotating propeller pump system was built to evaluate the efficacy of installing pumps along a drill string to reduce drilling fluid pressures and prevent a fluid circulation loss event. Learned from this work, the design principles of single propeller pumps could not be applied to contra-rotating propellers and the separation distance between propellers play a major role in their performance. In chapter 6, fluid circulation loss to porous media was addressed. A porous media cylinder was built to model this scenario and used to learn that adding sand to either water or a bentonite slurry would clog a gravel bed and allow drilling fluid pressure to rebuild, preventing fluid circulation loss.

In summary, this thesis provides methods and tools to measure and quantify viscometric material properties of soil materials to understand its processing and engineering suggestions to manage drilling fluid pressure and avoid fluid circulation loss events.

TABLE OF CONTENTS

ABSTRACT ii
LIST OF FIGURES viii
LIST OF TABLES xvi
ACKNOWLEDGMENTS xvii
CHAPTER 1 INTRODUCTION 19
1.1 Underground drilling: Molding the Earth to Suit your Needs 19
1.2 Soil Materials 20
1.3 Thesis Organization 22
1.4 Major Findings and Conclusions 22
CHAPTER 2 BACKGROUND 25
2.1 Fast Horizontal Directional Drilling 25
2.1.1 Drilling Fluid Pressure Management 27
2.2 Soil Materials 29
2.2.1 Distinction amongst soils 29
2.2.2 Clays 30
2.2.3 Granular solids 31
2.2.4 Variations in soil underground 32
2.3 Fluidizing Soil Materials 33
2.3.1 Effects of particles on viscosity 33
2.3.2 Colloidal Suspensions 33
2.3.3 Granular Dispersion 36
2.3.4 Quantifying their Rheology 44
2.4 Turbomachinery Fundamentals for Pumps 45
2.4.1 Centrifugal Pump fundamentals 45
2.5 Thesis Statement 48
CHAPTER 3 CALIBRATING AN INDEX-TYPE MIXER TO MEASURE VISCOMETRIC PROPERTIES OF HIGH-SOLIDS, HETERGOGENEOUS SOIL 49

3.1 Abstract 51
3.2 Introduction 51
3.3 Materials and Methods 56
3.3.1 Setup 57
3.3.2 Calibration procedure 58
3.4 Results and Discussion 60
3.4.1 Calibration results 60
3.4.2 Soil viscometer evaluation 61
3.5 Discussion 63
3.5.1 Soil material exploration 63
3.5.2 Soil material viscometric summary 64
3.6 Conclusions 65
3.7 Major Findings and Conclusions 66
CHAPTER 4 CHARACTERIZING THE NON-NEWTONIAN VISCOSITY OF HIGH-SOLIDS DRILLING-FLUID DISPERSIONS BY FLOW LOOP 67
4.1 Abstract 69
4.2 Introduction 69
4.3 Materials and Methods 72
4.3.1 Material preparation & characterization 72
4.3.2 Methods 74
4.3.3 Viscometric characterization 79
4.4 Results and Discussion 80
4.4.1 Comparison between model and field-test cuttings returns samples 80
4.4.2 Flow and Pressure Drop Results 82
4.4.3 Power law indices analysis 85
4.5 Conclusions 89
4.6 Major Findings and Conclusions 90

CHAPTER 5 CONTRA-ROTATING PROPELLERS IN SERIES AS AN AXIAL PUMP TO INCREASE SPEED AND BOREHOLE LENGTH IN UNDERGROUND DRILLING 91

5.1 Abstract 92
5.2 Introduction 93
5.3 Materials and Methods 96

5.3.1 Materials/Design 96
5.3.2 Method 98

5.4 Results and Discussion 101
5.5 Conclusions 108
5.6 Major Findings and Conclusions 109

CHAPTER 6 FLUID-DRIVEN CLOGGING TO PREVENT FLUID CIRCULATION LOSS IN UNDERGROUND DRILLING 110

6.1 Abstract 111
6.2 Introduction 112
6.3 Materials and Methods 112

6.3.1 Materials 113
6.3.2 Method 115

6.4 Results and Discussion 118

6.4.1 Flow through porous media 119
6.4.2 Clogging 121
6.4.3 Exploring clogging 125
6.4.4 Dynamics of clogging 126

6.5 Conclusions 128
6.6 Major Findings and Conclusions 128

CHAPTER 7 FUTURE WORK 129

7.1 Soil Viscometer 129

7.1.1 How to include a Herschel-Bulkley constitutive expression instead of a Bingham Plastic expression so that the thin-gap approximation is satisfied? 129

7.1.2 How to characterize the viscometry of clay materials that have history? 130
7.1.3 Do granular particles influence viscometry similar to colloids with hard-sphere interaction potentials? 131
7.1.4 What micromechanical modifications are additives making to soil materials to "improve" their viscometric properties? 132
7.2 Flow Loop 132
7.2.1 How does the formation and dynamics of a particle bed alter the hydrodynamic and viscometric properties of the cuttings returns? 132
7.2.2 How do clay cuttings affect drilling fluid rheology over time? 133
7.3 Series Distributed Pump 133
7.3.1 Is separation distance important when the rear propeller is operating at a lower rotational speed in contra-rotating propellers? 133
7.3.2 Does propeller design play a larger role in pressure boost when the two propellers are not operating at the same rotational rate? 134
7.3.3 How well do any of these empirical design principles hold up with non-Newtonian fluids, like a bentonite slurry? 134
7.3.4 What would need to be done so that this work could lead to building empirical models? 134
7.4 Permeation Cell 135
7.4.1 Simulation proposal 135
7.4.2 How would hydrodynamic contributions affect clogging? 137
7.4.3 What are the effects of non-Newtonian fluids on flow through porous media at larger pore sizes? 138
7.4.4 Can the particle bed formation that results in clogging be shown with a model experimental system? If so, then can those dynamics be captured in a time-dependent model? 138
CHAPTER 8 CONCLUSIONS 140
REFERENCES 142
APPENDIX A SOIL VISCOMETER 160

A.1 Raw torque and rotation rate data from the soil viscometer 160

APPENDIX B FLOW LOOP 163

B.1 Bentonite dispersion viscosity and yield stress characterization 163

B.2 XRD analysis of bentonite samples 167

B.3 Particle size distribution analysis of model and field test formation samples 169

B.4 Non-linear regression code..... 171

APPENDIX C PERMEATION CELL 181

C.1 Hydraulic fracturing in soil mixtures report..... 181

Abstract 181

Introduction..... 181

Soil fracture..... 183

Fracture Analysis 191

Conclusion 195

C.2 Flow regimes 196

C.3 Flow sweep of drilling fluid 199

C.4 Small Angle Oscillatory Shear (SAOS) rheology of drilling fluid 201

C.5 Shear-thinning characterization..... 202

C.6 Dynamic clogging model – Relating pressure and flow rate 204

APPENDIX D USE OF COPYRIGHTED MATERIAL AGREEMENTS..... 207

LIST OF FIGURES

Figure 2.1 Schematic of fast horizontal directional drilling (HDD). From left to right, drilling fluid is pumped into an inner pipe that is fed underground by a pipe-pusher with a second outer pipe. The front of the inner pipe is connected to a cutterhead where drilling fluid exits and recirculates into the annular space between the pipes, cleaning the borehole by carrying away soil cuttings. With fast HDD, drilling fluid pressure is influenced by the length of borehole, speed of drilling, and soil cuttings content, and needs to be maintained below the strength of the surround soil formation to avoid failure and frac-out of the formation. 25

Figure 2.2 Illustration of a frac-out event. When drilling fluid pressure exceeds the strength of the soil formation then fissures form in the surrounding soil, releasing drilling fluid pressure in these fractures and reducing the drilling fluid pressure and flow re-circulating in the annular space between pipes. 27

Figure 2.3 a). For the viscosity range of bentonite spanning 1-100 1/s in steady-shear, bentonite samples at variable water content were measured. Bentonite concentrations greater than 80 wt% can be commonly expected under realistic geological conditions b). Instead of viscosity, torque is compared in a cup and bob geometry for bentonite concentrations lower than 20 wt%, and the sample at bentonite content greater than 20 wt% was measured in a 20mm hatched plate with sandpaper adhered to the peltier plate. The red line is the upper torque limits of the TA instruments DHR-3 rheometer. 30

Figure 2.4 Diagram depicting elastic contact using the Hertz law for two hard spheres in contact, to retrieve the normal contact force between two particles. The particles on the left are in contact with no deformation made and the particles on the right are in contact with a deformation δ applied to each sphere from equally applied normal forces. The grey zone is describing the zone of deformation. This is based on a figure from Granular Media[8]. 38

Figure 2.5 Force and reaction force diagram detailing the tangential and normal forces acting on a stationary block. 39

Figure 2.6. Diagram of a centrifugal pump based on the work of Wilkes 3rd edition[94]. 46

Figure 2.7. Velocity breakdown of the fluid moving out of a centrifugal pump. 46

Figure 2.8. Characteristic curve the non-dimension flow rate and pressure drop performance for a centrifugal pump..... 47

Figure 3.1 Schematic of the cutterhead breaking down soil into cuttings that will then flow through the annular space between the pipes..... 49

Figure 3.2. Decision tree from learned experiences and existing literature for the calibration route to take depending on measurement geometry. If there is global z or r directional circulation due to the measurement geometry then a power number calibration approach is needed, if not an effective inner radius approach can be used to determine the effective viscometric properties of a material. 55

Figure 3.3. Soil viscometer setup, where an industrial drill press was modified into a rheometer by changing out the drill bit with a lid that the central shift sits inside of and exchangeable measurement geometries can be attached to, coupled with a sample chamber that sits on a low friction plate while two force transducers hold the chamber in place and measure the torque acting on the chamber from the sample of interest. The right hand images is the

measurement geometry used with angled flights designed to measure samples with high solids content, yield stress, and viscosity. 57

Figure 3.4. Calibration results for the angled-flight measurement geometry using a 16.7 wt% bentonite sample. a) includes the averaged data, in orange triangles, tracking torque at increments of rotations per minute (RPM). b) takes those torque values and calculates what the effective inner radius (R_i) would be at those operating conditions. From this dataset, an R_i value that minimizes the total average error is selected. This R_i value is then used to calculate how torque values should be varying with RPM and plotted as the black line in the left-hand panel and compared to the collected torque data. 60

Figure 3.5. Using the calculated Ri value from Figure 3.4, the (a) averaged torque and RPM data can be converted into effective viscosity and effective shear-rate values and can be compared to the steady-shear flow curve collected of the same 16.7wt% bentonite sample on the DHR-3 rheometer. b) is the same flow curves as a) but on a linear plot. c) is the absolute difference normalized by the TA DHR-3 values between the Soil Viscometer and the TA DHR-3 data extended from an extrapolation of the collected data. 61

Figure 3.6. Realistic soil materials explored by the Soil Viscometer and the bench-top DHR-3 rheometer. Materials include the 16.7 wt% bentonite, 33.3 wt% bentonite, and the 33.3 wt% bentonite mixed with Encapsul, an industry material of biomass derived oil that improves the workability of clay materials. The data follows the same representation as Figure 3.5, open dark blue symbols are DHR-3 data, shaded blue symbols are DHR-3 data extended to greater shear-rate by fitting them with the Bingham Plastic constitutive equation, and orange data is from the Soil Viscometer. Each symbol shape represents the material characterized. 63

Figure 4.1 Illustration of soil cuttings being removed from a borehole and the potential effects they may have on drilling fluid pressures. 67

Figure 4.2. Schematic illustration and image of the flow loop. Sensor port locations indicated in blue are labeled 1 through 10 from right to left. Circled numbers indicate components: (1) Pump, (2) Electromagnetic Flow Meter, (3) Paddlewheel Flow Meter, (4) Absolute Pressure Transducer, (5) Differential Pressure Transducer, (6) Absolute Pressure Transducer, (7) Doppler Flow Sensor, (8) 187 Liter Reservoir. The flow loop is about 20 feet in width and uses a clear 4-inch schedule 40 PVC and capable of flow beyond 600 gallons per minute. 76

Figure 4.3. Differential pressure transducer position placement. The distance, L, away from the elbow were tested while maintaining constant length between the pressure transducer were tested at a range of flow rates to determine a pressure transducer position that would be minimally affected by turbulence from the elbow. 78

Figure 4.4. Comparison of pressure drop vs velocity for model and field-test cuttings returns samples. The trendline is based on tap water without any cuttings. 82

Figure 4.5. Experimental values of pressure drop and flow rate for model cuttings returns samples. The red highlighted region illustrates regimes where observable solids settling occurred. 83

Figure 4.6. Experimental pressure drop and flow rate data for each cuttings returns sample from field-test solids concentrate. The red highlighted region illustrates regimes where observable solids settling occurred. 83

Figure 4.7. Image of flowing fluid (light grey, upper part) over settled solids (dark grey, lower part) during flow loop testing. The fluid contained 35 wt% solids, and was at an average velocity of 1.73 m/s. 84

Figure 4.8. Shields Parameter Analysis. The pressure drop data collected from the flow loop is converted to Shields parameter using Equation 4.7 and Equation 4.8. 85

Figure 4.9. Projected pressure drop – velocity curve with the BNS and Dodge & Metzner model based on the experimental data for the model fluid, samples 1-7. Data points are the experimental data, dashed lines are the BNS model, and dotted lines are the Dodge & Metzner model. 88

Figure 4.10. Projected pressure drop – velocity curve with the BNS and Dodge & Metzner model based on the experimental data for the field-test concentrate, samples 8-12. Data points are the experimental data, dashed lines are the BNS model, and dotted lines are the Dodge & Metzner model. 88

Figure 5.1 Illustration of the contributions distributed pumping can have on underground drilling to redistribute drilling fluid pressure from a point-source to along the drill string to mitigate frac-out and fluid circulation loss. 93

Figure 5.2**.** a) Comparison between propellers designed for low and high pressure to determine whether design principles for single propellers can be applied to contra-rotating propellers in series. The left propeller is designed for half the pressure head as the right propeller. b) Illustration of two propellers along the same axis operating in counter-rotation to impart axial flow but mitigating rotational flow caused by the rotation of the propellers. 97

Figure 5.3**.** A schematic of the contra-rotating propellers in series. External motors operate the rotation of propellers inside the setup while the absolute pressure, differential pressure, and flow rate are measuring the fluid pumped by the propellers. A throttle valve is used to expand the operable range of flow rates within the setup. The data is collected with a laptop and NI Instruments data acquisition device. The external motors are controlled by a motor control box and are sealed from the internal fluid by a set of ball bearings. The internal series propellers, blown up on the top-right, arrangement is defined by their center-to-center separation distance, L, and the propeller blade diameters, D. 99

Figure 5.4. Response of single propeller and series contra-rotating propellers to varying rotation rate and then spacing between series propellers. Each figure plots the differential pressure drop across the propeller(s) and flow rate as a function of the same rotation rate for both propellers. Dark blue is the differential pressure data graphed onto the primary y-axis and orange is flow rate graphed onto the secondary y-axis. The top left of each figure has a L/D ratio which is the center-to-center separation distance between propeller blades normalized by the diameter of the propellers. S is when a single propeller is used. The gradation of fill for each data point is indicated on the right side of the figure and represents the extent the ball valve is open to throttle flow in the loop. At 100% the ball valve is fully open and at 0% the ball valve is closed. 102

Figure 5.5. Pump curves developed for each propeller set and configuration (spacing). Each figure graphs the differential pressure drop across both contra-rotating propeller(s) as a function of flow rate. a) is the set of contra-rotating propellers designed for a pressure head of 3.5 meters. b) is the set of contra-rotating propellers designed for a pressure head of 7 meters. Each figure is the data collected at a rotation rate both propellers are operating at, the symbol for each data set represents the L/D separation distance, and the color is to

distinguish between data sets. The flow rate of each data set is controlled by throttle valve opening – the throttle valve is opened more to increase the flow rate while the separation distance and rotation rate of the propellers remain the same. 104

Figure 5.6. Effects of separation distance on pump performance. Each figure graphs the differential pressure drop across both contra-rotating propeller(s) as a function of flow rate. The symbol of each data point is associated with their respective L/D separation distance values indicated in the top right of each figure. The color of each data set represents the rotation rate both propellers are operating at. The flow rate of each data set is controlled by throttle valve opening – the throttle valve is opened more to increase the flow rate while the separation distance and rotation rate of the propellers remain the same. 106

Figure 5.7 Efficiency evaluation for the three L/D separation distances measured with the contra-rotating propellers as a function of rotation rate. Efficiency is the ratio between the output hydrodynamic energy and the input electrical energy. Hydrodynamic energy is the product of the flow rate and differential pressure drop. The symbols of each data set is consistent with the L/D separation distance indicated in the top right of each figure and the gradation of shading is a function of throttle valve opening. At 100% the valve is completely open and at 25% the valve is 25% open to flow. 108

Figure 6.1 Illustration of porous media encountered underground that would lead to drilling fluid loss, reducing drilling fluid pressure and stopping the removal of soil cuttings from the borehole. 110

Figure 6.2. Permeation cell set-up. From left to right, an in-house air source is used to control flow through the system with a pressure regulator(1, PC). Air pressure is fed into a tank (4, V-Mud) that can be changed out with water, drilling mud, and drilling mud with solids content. Fluid entering and exiting the porous media cylinder (11a-c) will be measured with inlet flow velocity (7, doppler flow meter) and pressure sensors (8) on the upstream and downstream ends. Two cells were used for experiments, a 25.4 mm (1 inch) diameter cylinder that's 607 mm (2 feet) long and a 203 mm (8 inch) inner diameter cylinder that's 911 mm (3 feet) long. The cell is sealed with mesh (10) on both ends to only allow fluid in and out of the system. One end of the cell has a removeable mesh so that the desired coarse soil can be replaced as needed. A pressure-regulator will be used downstream to maintain a constant minimum pressure in the system as needed or will be used to hold water in the system in the case of saturated soil formations. Outflow from the cylinder is collected in a bucket (13, V-Outlet, Scale) connected to a force transducer to measure the outlet flow velocity. 113

Figure 6.3. Permeation cell build. From the left, a holding tank(1) is connected to an air regulator(2) that controls the fluid pressure moving out the bottom of the vessel and through the ¾" hose to the permeation cell(3) (3" and 1" inner diameter cylinders at the top picture and 8" ID cylinder at the bottom picture). A force transducer(4) holding a bucket to capture the effluent from the porous media cylinder measures the outlet flow velocity (bottom left) from the 203 mm (8 inch) cylinder. The differential pressure transducer(5) hose connects to both ends of the permeation cell and sits behind the cell. The absolute pressure sensor(6) sits just downstream of the vessel. The doppler sensor(7) measures inlet flow velocity into the cell. The LabJack data acquisition device(8) sits above the setup. 116

Figure 6.4. Darcy's law evaluation of pressure drop versus flow velocity for water flow through sand and gravel. a) is the 25 mm (1-inch) ID cell filled with sand, b) is the 203 mm (8-inch) ID cell filled with gravel. The green data points are data values collected for flow

velocity over a range of pressure drop values corresponding to the left green axis. The trendline is Darcy's law estimation of pressure drop versus flow velocity using the low flow velocity values to calculate bed permeability for each cell material. The black dashes are the pore Reynolds numbers at each flow velocity and correspond to the right black axis. 119

Figure 6.5. Pressure drop versus flow velocity data of water data collected in the 8-inch porous media cylinder filled with gravel, and flow through porous media models were fit to the experimental parameters to determine the effects unaccounted for in Darcy flow. Darcy's law expression is from calculating discharge velocity from the measured differential pressure of the system. Forchheimer's Equation and Ergun's Equation are from fitting to the experimental data. 120

Figure 6.6. Real-time data of permeation cell tests comparing colloidal deposition to clogging. The left-hand side panels were tests performed in the 1-inch cylinder and the right-hand side panels were tests performed in the 8-inch cylinder. a) is water flowing through sand, b) water flowing through gravel, c) 1.5wt% bentonite slurry flowing through sand, d) 1.5wt% bentonite slurry flowing through gravel, and e) water and 17vol% (7wt%) sand flowing through gravel. 122

Figure 6.7. Real-time data comparisons of clogging before and after particles are introduced into the system. All panels are using the 8-inch cylinder filled with gravel. The left-hand side panels are flow of fluid without granular particles and the right-hand side is with sand in the fluid. a) water flowing through gravel starting at 8 psi of static pressure, b) water and 17vol% (7wt%) sand flowing through gravel starting at 8 psi of static pressure, c) water flowing through gravel starting at 4 psi of static pressure, d) 17vol% (7wt%) sand in water flowing through gravel starting at 4 psi of static pressure, e) 1.5wt% bentonite in water flowing in gravel starting at 8 psi of static pressure, f) and 17vol% (7wt%) sand in 1.5wt% bentonite in water flowing in gravel starting at 8 psi of static pressure. 125

Figure 6.8. Clogging evaluation of the 203 mm (8 inch) cylinder between the 3 scenarios with sand laden fluids; water and sand at 8 psi, water and sand at 4 psi, and bentonite slurry and sand at 8 psi., a) is comparing the temporal clogging dynamics between the 3 scenarios, b) is comparing the 3 scenarios as a function of solids entering the cylinder relative to the total pore volume of the cell. 126

Figure 7.1. LAMMPS system setup 136

Figure A.1 Raw torque data collected from the soil viscometer across a range of rotation rates over 150 seconds. The torque data points used in Chapter 3 are average values of these data points. This data is for 33.3 wt% bentonite samples. 160

Figure A.2 Raw torque data collected from the soil viscometer across a range of rotation rates over 150 seconds. The torque data points used in Chapter 3 are average values of these data points. This data is for 33.3 wt% bentonite samples + Encapsul. 161

Figure A.3 Raw torque data collected from the soil viscometer across a range of rotation rates over 150 seconds. The torque data points used in Chapter 3 are average values of these data points. This data is for 16.7 wt% bentonite samples. 162

Figure B.1 Flow sweep data of 3wt% bentonite, performed from 1 – 200 1/s, with increasing shear-rate. 163

Figure B.2 Flow ramp loop with shear stress as the independent variable, measured from high to low stress. The yield stress was determined by the peak in viscosity to be 0.00126 Pa. 163

Figure B.3 Flow ramp loop using shear stress as the independent variable but plotting in terms of shear-rate and shear stress. 164

Figure B.4 Flow sweep data of 3wt% Michels bentonite, performed from 1 – 200 1/s, with increasing shear-rate. 164

Figure B.5 Flow ramp loop with shear stress as the independent variable, measured from high to low stress. The yield stress was determined by the peak in viscosity to be 0.942 Pa. 165

Figure B.6 Flow ramp loop using shear stress as the independent variable but plotting in terms of shear-rate and shear stress. 165

Figure B.7 Powder X-ray diffraction data collected over a 2θ from 10-80 with a step size of 0.02 and 120 seconds per step. The setup was operated with a divergence slit of 1/8", beam attenuator (mask) of 10mm, and anti-scatter slit of 1/2" and set at conditions of 45 kV tension and 40 mA of current. Bragg-Brenato geometry was used for the incident beam optics and Xcelerator optics were used for the diffracted beam optics. Only SiO_2-polymorphs were investigated for the data analysis to focus on the mineralogical differences between the bentonite used in the field-test and model cuttings samples..... 167

Figure B.8 Powder X-ray diffraction data collected over a 2θ from 10-80 with a step size of 0.02 and 120 seconds per step. The setup was operated with a divergence slit of 1/8", beam attenuator (mask) of 10mm, and anti-scatter slit of 1/2" and set at conditions of 45 kV tension and 40 mA of current. Bragg-Brenato geometry was used for the incident beam optics and Xcelerator optics were used for the diffracted beam optics. Only SiO_2-polymorphs were investigated for the data analysis to focus on the mineralogical differences between the bentonite used in the field-test and model cuttings samples..... 168

Figure B.9 Sieve test particle size distribution curve for model cuttings sand (Mason sand). The data is from three trials by three separate experimentalists and each data point is an average value with error bars representing the standard deviation between each trial. 169

Figure B.10 Sieve test particle size distribution curve for field-test cuttings, represented by core samples collected at representative depths along the drill path. Depths B1-3, B1-4, B1-5, and B1-6 represents 15'-17', 20'-22', 25'-27', 30'-32', respectively. The first three data points fall on top of one another at the 100% percent finer mark. 170

Figure C.1 a) Conceptual design of the fracture tank (Frac-Tank), a plexiglass box houses a wooden insert that confines a soil sample to the front face of the box. Ports in the wooden insert introduce fluid through pilot holes drilled into the soil sample to fracture the soil while observing the front face. b) Top down view of the Frac-Tank, the wooden two-by-fours apply confinement pressure to the soil below them. The black piece is the wooden insert confining the soil sample and introducing fluid into the soil. The white attachment connected to the black insert is a standpipe filled with fluid and air pressure is modulated at the top to measure and control fluid pressure. 184

Figure C.2 Post-fracture images of soil fractured in the Frac-Tank. Top row: 30% Kaolinite – 70% Sand central port fluid introduction, a) No confinement pressure, 6, 1 inch tall layers, water, b) 8, 1 inch tall layers, water, 2 psi confinement pressure c) 8, 1 inch tall layers, 2.4wt% Bentonite drilling mud, 2 psi confinement pressure. Bottom row: d) 30% Kaolinite – 70% Sand, 8, 1 inch tall layers, side port 2.4wt% Bentonite fluid introduction,

2 psi confinement pressure, e) 16% Cement – 84% Kaolinite, 8 inch tall, 7 day cure, center port 2.4 wt% Bentonite fluid introduction, 2 psi confinement pressure. 185

Figure C.3 (Left) Comparison of fracture pressure of 30% Kaolonite-70% White sand with and without confinement pressure of 2 psi fractured through the center port with water. The data follow experiments in Figure C.2a and C.2b. Most similar to the data of Decker and Clemence (1981) using low plasticity clays at liquidity indices of 0 and 0.5, while the kaolinite used was at 2.23. The red dots are following Elasticity theory outlined in Mitchell and Soga (2005). *Fundamentals of Soil behavior*. (Right) Review of clay fracture data as a response to confining pressure (Marchi *et al*. (2014). Fracturing Pressure in Clay). The red dots represent the data shown in the bar graph (Left). Appendix B shows the liquidity index calculation and comparison to literature. 186

Figure C.4 Comparison of fracture pressure of 30% Kaolinite-70% White Sand fractured through the center port with water and 2.4wt% Bentonite slurry under 2 psi confinement pressure. The data is from experiments in Figure C.2b and C.2c. 187

Figure C.5. Comparison of fracture pressure of 30% Kaolinite-70% White Sand fractured through the center port and side port with 2.4wt% Bentonite slurry under 2 psi confinement pressure. The data is from experiments in Figure C.2c and C.2d. 189

Figure C.6. Comparison of fracture pressure of 30% Kaolinite-70% White Sand and 16% Cement-84% Kaolinite fractured through the center port with 2.4wt% Bentonite slurry under 2 psi confinement pressure. The data is from experiments in Figure C.2c and C.2e. 190

Figure C.7. After fracture of the side port experiment in Figure C.2d, the fracture was manually closed, and fluid pressure was applied to fracture again. 194

Figure C.8 Schematic of flow regimes dependent on values of pore Reynolds numbers, Re_P. 197

Figure C.9 Predicted pressure drop behavior across the permeation cell dependent on the flow regime experienced as defined by pore Reynolds number. 198

Figure C.10 Viscosity curves of a) 1.5wt% Black Hills Bond Bentonite slurry (BHB), b) 3wt% Michels Maxgel bentonite slurry, and c) 3wt% BHB. The blue triangles are the viscosity curves of the bentonite slurries and the orange line at the bottom of a) and c) are the viscosity curves of water to reference the viscosity of water and its Newtonian behavior, independent of shear-rate. 200

Figure C.11 Elastic moduli data collected for drilling fluids to date. Data obtained from using SAOS to quantify electrostatic interactions between clay platelets of drilling fluids. 202

Figure C.12 Steady-shear measurement of 2.8wt% bentonite in a DHR-3 rheometer. 203

Figure C.13 Schematic representation of the permeation cell filled with gravel. Drilling fluid is flowing through the system (left), followed by the introduction of solids to the drilling fluid leading to plugging of pores in the cell (right)..... 204

Figure C.14 Expected flow rate and pressure drop behavior of the permeation cell with respect to the evolution of plugging. 205

Figure D.1 Copyright permission for re-use of paper published in Physics of Fluids in Chapter 4. Characterizing the Non-Newtonian Viscosity of High-Solids Drilling Fluid Dispersions by Flow Loop, *Physics of Fluids* 34, no. 5 (May 2022): 053313. Copyright 2022 American Institute of Physics..... 207

Figure D.2 Co-author permission for re-use of paper published in Physics of Fluids in Chapter 4. Characterizing the Non-Newtonian Viscosity of High-Solids Drilling Fluid Dispersions by Flow Loop, *Physics of Fluids* 34, no. 5 (May 2022): 053313. Copyright 2022 American Institute of Physics..... 208

LIST OF TABLES

Table 3.1. A summary of the Bingham Plastic parameters for each soil same and compared between the Soil Viscometer (SV) and the TA Instruments DHR-3 (DHR) rheometer. These include η_{PL}, the viscous component; τ_0, the yield stress of the samples; and R^2, the coefficient od determination for fitting a Bingham Plastic model to the measured shear-stress-shear-rate data. 65

Table 4.1. Composition breakdown for the model cuttings returns samples. 72

Table 4.2. Composition breakdown for the field-test cuttings returns samples prepared from the field-test concentrate. 73

Table 4.3. Density of each cuttings returns sample. 74

Table 4.4. Sensor specifications include all pressure and flow rate sensors. 77

Table 4.5. Power law indices of each cuttings returns sample obtained from non-linear regression and using constraints from conventional rheometer data. 87

Table 5.1 Sensor and motor specifications. 100

Table 6.1. Summary of relevant material properties of bentonite slurries, gravel, and sand. The fluid properties M and n represent the power-law parameters to quantify the viscous and shear-thinning behavior. BHB is Black Hills Bond Bentonite. 114

Table 6.2. Summary of clogging experiments performed using sand and gravel as the porous media material. All experiments performed with sand as the bed material are completed in the 25.4 mm (1-inch) cylinder and all gravel experiments are performed in the 203 mm (8-inch) cylinder. 118

Table 6.3. Summary of clogging criteria presented in the background in comparison to the actual filter and particle sized used in experiment that led to clogging. 124

Table B.1 Tabulated data collected from the sieve test particle size distribution characterization for Mason sand. 169

Table B.2 Tabulated data collected from the sieve test particle size distribution characterization for field-test cuttings, represented by core samples collected at representative depths along the drill path. 170

Table C.1. Summary of fracture experiments displayed in Figure C.2. 185

Table C.2 Comparing the influence of soil compressive and tensile strength with fracture initiation pressure of 30%Kaolinite-Sand and 16%Cement-Kaolinite fractured through the center port with drilling mud (2.4wt% Bentonite) under 2 psi of vertical confining pressure. 192

Table C.3 Pre-factor and exponent to quantify shear-thinning behavior of drilling muds using the power-law model as a convenient exponential expression, $\eta = K \cdot \dot{\gamma}^{n-1}$. 204

ACKNOWLEDGMENTS

I am appreciative of the opportunity to have worked with Dr. Joe Samaniuk and learn from him over the past five years as we have navigated through the muddy world of particle rheology in underground drilling.

To my co-advisor Dr. Michael Mooney, thank you for your persistent curiosity and high standards that have challenged me and captured my imagination in every brainstorming session.

To my committee members, Dr. Nanette Boyle, Dr. Xiaolong Yin, and Dr. David Marr, thank you all for the thoughtful feedback and questions that have made my work the best that it could be, and encouraging me to be a better communicator, critical-thinker, and researcher.

To my current and former Soft Matter and Interfaces lab mates, David Goggin, Shalaka Kale, Jess Troxler, Jianger Yu, Amy Chacon, Matteo Liserre. David, while I only knew you for a short time, I always look back on our scientific discussion with fondness and appreciate the rigor with which you engaged with science, becoming a role-model that I hoped to emulate. Shalaka, thank you for your friendship. Through our conversations and experiments together, you taught me what the life of a researcher should look like – not every day was easy, but your tenacity in the lab and care in cultivating relationships provided a great example that I too wanted to follow. Jess, thank you for your encouragement and camaraderie as we navigated our journeys learning about rheology. Amy and Matteo, thank you for your questions and support in the lab that have made me a better researcher.

To the undergraduate researchers I have had the pleasure of mentoring over the years: Courtney Stanton, Samuel Einspahr, and Arpit Mishra, and the high school researcher Megan Wilkins, thank you for challenging me to better understand and communicate our research projects.

To Rakshith Shetty, thank you for your wisdom in designing experiments, persistent curiosity, and authenticity in talking about your journey as a researcher.

To Bryant Robbins, your critical thinking and our discussions were invaluable in designing fruitful projects and rigorously evaluating their success.

To Jon Peters, your expertise and efforts in building experiments were invaluable.

To my friends, who have all contributed in making my graduate school experience a cherished time and have supported me in your own unique ways that I will always be forever grateful for.

To Michaela, thank you for your continual belief in me that inspired my final push to finish this thesis and continuing to strive after my potential.

To my family, your love, support, and reassurance provided a stability that I could depend on whenever I felt uncertain while doing this work.

CHAPTER 1 INTRODUCTION

1.1 Underground drilling: Molding the Earth to Suit your Needs

The application of this work is for the military to provide supplies to troops. To achieve this objective the speed of existing drilling technology needed to be increased by an order of magnitude while retaining precise control of its trajectory at shallow depths (<100 ft) for boreholes 4 inches in diameter. Two main technologies on the market that best fit these metrics are horizontal directional drilling (HDD) and directional drilling (DD). HDD is a technology for precisely controlled shallow (< 30m) drilling but they operate at slow operational speeds of 0.0025 - 0.01 m/s[1–5]. Current slow drilling speeds result in additional costs and labor, making them more expensive than open-cut methods of excavating trenches[6]. HDD can be made more cost-effective at faster operational speeds that cut down on labor and on-site expenses. DD is a high-powered technology with an emphasis on speed rather than maneuverability, reaching speeds up to 0.08 - 0.19 m/s. To increase the drilling speed of HDD while maintaining its nimble movement, DD technology must be integrated with HDD. Drilling at higher speeds means that soil cuttings from the underground formation need to be evacuated more quickly and high solids content ($> 20wt\%\ Solids$) drilling fluid viscosity will need to be better quantified to predict drilling fluid pressures. In underground drilling, drilling fluids are pumped into boreholes through the drill string to remove sand, clay, sediment, rock, etc. broken down by the drill bit[7]. This complex mixture of solids and drilling fluids is termed “cuttings returns”. To capture drilling and operational speed, the term rate of penetration (ROP) is used to represent the linear speed the equipment advances forward during drilling, dependent on formation excavation and cuttings removal. In this work, the ROP of HDD is increased by an order of magnitude by incorporating DD technology to develop fast HDD, and the engineering challenges of fast HDD are addressed with tool and methodology development.

Research areas actively working with soil materials and developing methods to process them with existing knowledge are the mining and drilling communities. In mining and geotechnical engineering many kinds of tools and machinery have been built to fluidize ground materials for removal, this includes but is not limited to tunnel boring machines (TBM), HDD, and auger mining. The tools developed for these different modes of underground material excavation have predominately been developed empirically because theoretical understanding of

these materials is lacking. Materials of interest for this thesis will include the size of gravel and smaller because the challenges associated with rock drilling is breaking down the material and is a technological challenge, while soil materials also include the transport of material after breakdown as well and is an engineering challenge[7]. The major toolset of soil mechanics is focused on static stress states and failure of material dependent on stress states, skillsets not as well-equipped to handle dynamic movement of soils. While rheology is a skillset focused on the flow of materials that include but not limited to polymer solutions, hydrogels, and colloidal suspensions. Because of these backgrounds, rheology is well-suited to address the flow challenges and characterization of soil materials in flow but is currently limited by existing instrumentation. Materials commonly characterized by the rheological community include polymer solutions, hydrogels, and colloidal suspensions that have low elasticity and viscosity compared to soils. Soil materials are commonly clay materials that can have viscosities surpassing 10^6 Pa·s and granular particles like silica sands can have elastic moduli surpassing 10^3 Pa. These quantities far surpass the torque capabilities of most commercially available rheometers that measure softer materials with viscosities in the 10^{-3}-10^2 Pa·s and elastic moduli in the 10^{-1}-10^2 Pa ranges. Rheological knowledge exists to characterize the flow properties of soil material slurries, but their viscous and granular nature presents challenges not traditionally encountered.

1.2 Soil Materials

Soil materials are made of particles that span in size from colloidal to granular length-scales and are present as mixtures of a colloidal material, clay and a granular material, often sand. Granular materials can also include granules, pebbles, gravel, cobble, and even larger particles. These materials in terms of complex fluids are extreme in their deviation from materials typically measured in this field, which presents many instrumentation challenges because they were not designed to characterize such large particle sizes and viscosities. The materials of interest in this thesis will cover depths less than 100 ft.

Granular matter is a subset of soft matter where many of the colloidal interactions are no longer present and are modified at these larger length-scales (>100μm)[8,9]. At these larger length-scales gravity and frictional interactions dominate rather than electrostatic interactions and Brownian motion. Because of this, there are additional challenges, especially related to history, because without Brownian motion continually inputting energy into the system, in the form of

perturbations, particles are less likely to reach an energy minimum but remain trapped in local minima, resulting in a greater diversity of particle configurations. This means that the history of processing granular materials will determine their configuration and how they respond to the stresses acting upon them. Granular matter is ubiquitous in nature and industrial processes, they are the second most commonly processed material, behind water[8]. The transportation and separation of granular matter are present in almost all industrial processes including catalysis (catalyst material), distillation (flow through a packed bed), pharmaceuticals (separating solid products from a fluid feed), and many more application areas. Even with all these applications, as a material they are rarely studied in isolation, but usually in the context of a system.

Clay materials are a challenging material to process in underground drilling, and there are currently very few solutions when they are encountered. Practically speaking, they are avoided as much as possible because of the variability in their material properties with water content, exchangeable cation content, and minerology. These factors will significantly affect their viscometric properties that include viscosity, yield stress, and their transition from fluid-like to plastic-like behavior. Looking at water content alone in Wyoming Na-bentonite, a commonly used drilling fluid constituent, the transition from dilute, to semi-dilute, to concentrated will mean orders of magnitude increase in viscosity ($\sim 10 - 10^4\ Pa \cdot s$) and yield stress ($10 - 10^3\ Pa$), these are values measured in a benchtop rheometer at bentonite concentration from 3 to 33 wt% but values expected in the field can exceed 80 wt%. At concentrations above 33 wt%, clays exhibit plastic-like behavior and no longer deform uniformly which requires empirical testing that mimic in the field conditions because those same modes of deformations cannot be replicated with lab rheometers. These deformation modes include clays that ball up, create clods, roll, compress, cohere, and detach from one another and with the machinery as its being processed. Large variations in rheological properties can lead to redirection of the drilling string due to expansion from exposure to drilling fluid, balling up and adhesion to the cutterhead, and unwanted accumulation along the drill string resulting in operational challenges for fluid pressure management and mobility of the drill string. Current mitigation strategies to reduce viscosity and yield stress are foam or polymer additives, combined with soils in a process called "conditioning", but they are currently used based on trial-and-error. If the role of additives could be better understood, then more effective strategies could be employed during drilling to mitigate the challenges associated with processing of clay materials.

The role of additives is to reduce the attraction between clay at either granular or colloidal length-scales. Polymer additives function by disrupting the clay structures formed, by breaking down those electrostatic interactions then the corresponding viscometric properties will be reduced. That is the intended goal of additives, but a fundamental study of this functionality has not yet been well-explored. The soil viscometer setup (Chapter 3) is well-suited for this study to capture the effects of additives on fluid-like or plastic-like soils. Foam additives reduce attraction at a granular scale, creating voids between clay clods, and reducing the overall density of the transported material slurry. In practice, foam additives work well with sands, reducing frictional interactions to significantly reduce the bulk viscosity and yield stress during transportation out of the borehole. But with clays underground, their water content is so low that any available water is readily absorbed into the clay, collapsing foam interfaces, and preventing its functionality.

The work covered in this thesis will be focused on soil materials, but the implications of the experimental tools and techniques developed for this work are broadly applicable to the transport of granular matter, and across all underground drilling technologies.

1.3 Thesis Organization

This thesis is made up of eight chapters; Chapter 1 gives an overview on the application and material focus of this work (underground drilling and soil materials) followed by an organization of the thesis, and summaries of the major findings in each body of work, (Chapters 3 through 6). Chapter 2 gives a review of the literature and touches on important background material which will inform and motivate the following chapters. Chapters 3 through 6 give the independent work performed in this thesis and are arranged based on the order complex material processing challenges appear, in the context of underground drilling. Each chapter can be read independently and come together to provide an overview of identified soft matter processing challenges in underground drilling. Chapter 7 gives future research questions that developed from the findings in this thesis. Chapter 8 gives conclusions on how this thesis has contributed to the field of underground drilling, and more broadly to the field of granular matter and solids processing.

1.4 Major Findings and Conclusions

Chapter 3 is an extension to an existing calibration procedure used for viscometers with complex measurement geometries previously applied to polymer solutions and biomass. When

applied to clay materials, a Bingham Plastic constitutive equation needs to be used to account for a material's yield stress and to fulfill the theoretical assumptions to use a non-Newtonian fluid as a calibration material. For bentonite clays, there reaches a transition point between 33 and 16.7 wt% bentonite in water that the material becomes plastic-like and begins deforming as a solid at which point the history of deformation influences the viscometric properties that are measured. Calibration needs to be done before the plastic-like transition to obtain uniform deformation of the material. The wide applicability of this calibration procedure for many complex measurement geometries allowed us to fabricate an impeller that could be used with granular particles gravel and larger. The broader implications of this work are that the upper limit of measurable viscometric properties of complex materials with large viscosities ($> 10^4\ Pa \cdot s$) and particle sizes ($> 10^1\ mm$) has been extended, and the viscometric characterization needs to be tailored to its application for clay materials that behave plastic-like.

Chapter 4 uses existing theory and empirical correlations to characterize the effects of soil cuttings on the viscometric properties of drilling fluids to predict the expected pressure drop needed for operation of a drill string. The results of this work suggest that the unique variations in mineralogy and other geological variables on soil materials determine the viscometric properties that broad classifications of sand and clay type (bentonite, kaolinite) do not capture. Soil cuttings from the drill site gave notably different viscometric properties compared to recreating soil cuttings knowing the clay type, water content, and ratio of sand to clay content. Depending on flow regimes, the Shields parameter can also distinguish when settling will and will not play a role in influencing measured viscometric properties. The broader implications of this work are that increasing solids content will result in greater viscosities and shear-thinning behavior but to predict expected pressure drop effects of soil cuttings on drilling fluids depends on the extent of solids settling and viscometrically characterizing soil material specific to the drill site.

Chapter 5 studies the use of contra-rotating propellers as axial flow pumps to address the event that drilling fluid pressure will exceed the strength of the surrounding soil formation and frac-out will occur even knowing the expected drilling fluid and cuttings returns pressures due to operation at high speeds, shallow depths, or over long distances. The results of this work suggest that contra-rotating propellers would provide an added benefit compared to singular propeller systems and that the separation distance between the propellers play a major influence in their performance as a pump. Overall, contra-rotating propellers give a greater pressure drop boost and

flow rate contributions with rotation rate compared to singular propellers. The broader implication of this work is that separation distance between contra-rotating propellers play a significant role in their performance as a pump, more so that the design of the propeller blades.

Chapter 6 studies fluid-driven clogging of porous media to mitigate fluid circulation loss if soil materials with large voids ($> 10^1\ mm$) are encountered and cannot be mitigated by drilling fluid pressure management. The results of this work suggest that gravel as a porous media bed can be clogged with sand to reduce drilling fluid circulation loss and rebuild drilling fluid pressure. Fluid-driven clogging are hypothesized to be controlled by particle to pore size ratio and fluid shear stress to gravitational stress ratio constrained by the system geometry. The broader implication of this work is that fluid-driven clogging has many similarities to gravity-driven clogging but can be done with smaller particle sizes than expected and the fundamental physics behind why needs to be further explored before fluid-driven clogging can be utilized to addressing drilling fluid circulation loss to porous media beds.

CHAPTER 2 BACKGROUND

2.1 Fast Horizontal Directional Drilling

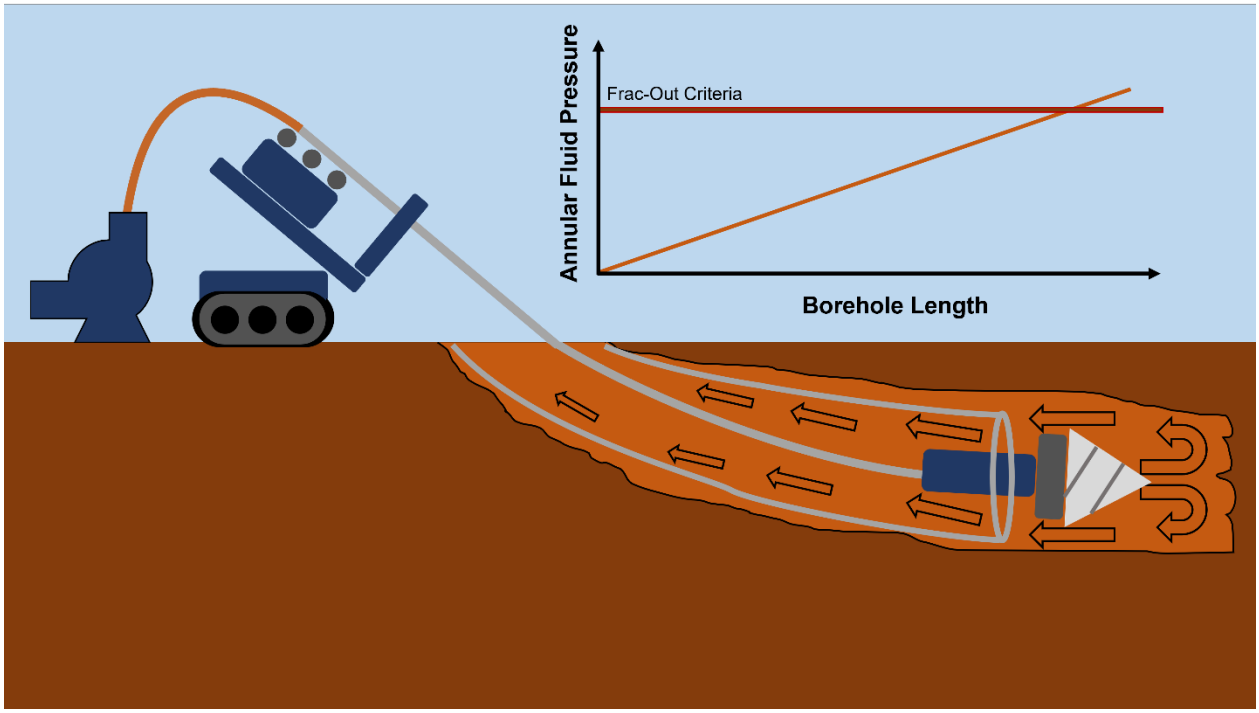

Figure 2.1 Schematic of fast horizontal directional drilling (HDD). From left to right, drilling fluid is pumped into an inner pipe that is fed underground by a pipe-pusher with a second outer pipe. The front of the inner pipe is connected to a cutterhead where drilling fluid exits and recirculates into the annular space between the pipes, cleaning the borehole by carrying away soil cuttings. With fast HDD, drilling fluid pressure is influenced by the length of borehole, speed of drilling, and soil cuttings content, and needs to be maintained below the strength of the surround soil formation to avoid failure and frac-out of the formation.

In horizontal directional drilling (HDD), a pilot hole is initially drilled along the desired borehole path where once it reaches the target at the surface a reamer is attached and ran back to the entrance of the pilot hole, sometimes requiring multiple passes, to incrementally enlarge the borehole[4,10–12]. Pipeline installation is then followed once the reaming step has enlarged the pilot hole to fit the product pipeline. This technology is predominately used by utility companies because of its versatility in sensing and nimble movement to avoid underground objects[4]. Often to carefully install lines in crowded underground spaces, avoid existing lines and minimize restoration needed after drilling. HDD drill string maneuverability comes from their small pipe diameters giving flexibility as the drill bit is pushed down hole. Commonly the cutterhead has a bias from the drill bit or by jets cutting preferentially cutting into the formation to create a slight angle of attack that when the drill string is pushed it will follow that bias, and rotating the drill

string will allow the setup to position the bias in a different direction[13,14]. Directional drilling (DD) uses pipes with larger diameters ($\geq 4\ inches$) that are less flexible and require rotating the drill bit to breakdown soil materials along with pushing to advance the drill string. A bottom hole assembly (BHA) is often used and includes one or multiple attachments behind the cutterhead to control the trajectory of the drill string and provide force to break down soil materials[15]. The technology developed for this project is fast HDD, marrying HDD and DD technologies by incorporating the power and additional maneuverability of DD and its BHA with the flexibility of smaller HDD pipes along with a double pipe system and continuous feeding of coiled pipe to achieve fast drilling metrics.

In fast HDD the main components of focus include the cutterhead that breaks down soil material, a double pipe connected to the back of the cutterhead, and a pipe pusher that pushes the whole assembly continuously underground (Figure 2.1). The cutterhead has sensors and controls, taken from HDD and DD technology, just behind the cutterhead to determine position and alter the trajectory of the borehole being drilled. The pipe trailing the cutterhead supplies drilling fluids that hydraulically power the cutterhead, picking up soil cuttings, and conveying them back to the surface at the entry point of the drill string. Rather than a single pipe system used in traditional HDD it is a double pipe, the inner pipe supplies clean drilling fluid to the cutterhead and disperses soil cuttings into the drilling fluid to then flow into the annular space between the two pipes driven by drilling fluid pressure. The annular space between pipes returns soil cuttings to the entrance of the hole. The double pipe design reduces the time that high drilling fluid pressure is in contact with the soil formation to reduce damage that can weaken the integrity of the borehole. This will allow the drill string to operate at higher drilling fluid pressures and reduce the potential for fluid loss circulation from damaging the soil formation and void spaces along the borehole. The greatest fluid pressure experienced by the borehole is at the front of the cutterhead, and then decreases as it exits the borehole through the annular pipe space that is open to atmosphere at the entrance of the borehole. The cuttings returns are retained to prevent environmental contamination and the soil solids are removed so that the drilling fluid can be recycled. Maintaining drilling fluid pressure to clean the borehole of soil cuttings is critical to the advancement of drilling so that the cutterhead can continue breaking down new soil and lengthening the borehole.

2.1.1 Drilling Fluid Pressure Management

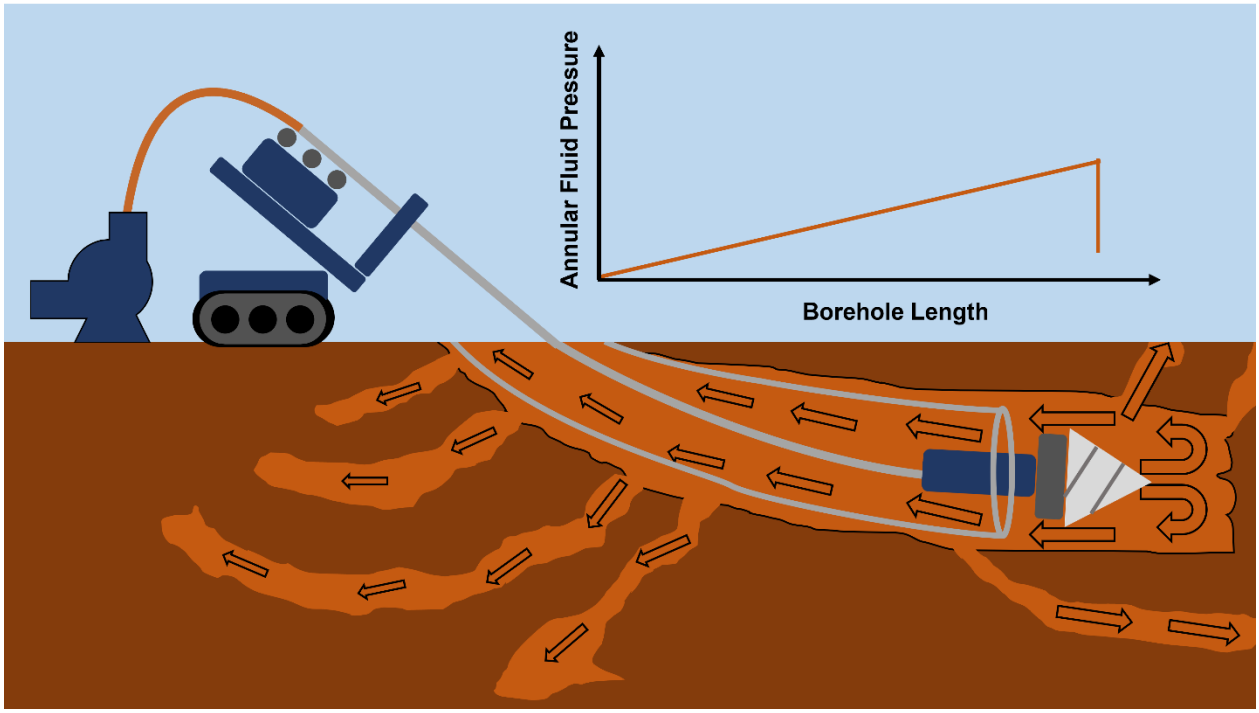

Figure 2.2 Illustration of a frac-out event. When drilling fluid pressure exceeds the strength of the soil formation then fissures form in the surrounding soil, releasing drilling fluid pressure in these fractures and reducing the drilling fluid pressure and flow re-circulating in the annular space between pipes.

Drilling at higher speeds also means removing soil cuttings at a faster rate, requiring higher drilling fluid pressures and typically, the pressure near the drill bit will be the largest pressure the borehole wall experiences, and if the pressure near the drill bit exceeds the strength of the surrounding formation, the hole walls fracture and cuttings are no longer removed from the borehole (Figure 2.2). Once a fracture is initiated it becomes a path of least resistance for the cuttings returns, and the flow of cuttings returns to the hole entrance reduces or ceases entirely. The loss of cuttings returns has as least two important consequences: a significant increase in the risk of the entire drill string becoming stuck, and an inability to recover and reuse the drilling fluid after it returns to the surface in the cuttings returns[10]. Continuous loss of drilling fluid at large volumes is prohibitive from both a cost and logistics standpoint when considering borehole lengths at the kilometer scale. In the fast HDD setup, drilling fluid flow rates operated at 600 GPM over 500 meters for a 0.1 meter diameter borehole at a drilling speed of 20ft/min means that the time of drilling will be 82 minutes and the total amount of drilling fluid needed without

recycling is greater than 49,000 gallons of drilling fluid. These drilling fluid challenges are specific to shallow drilling in soft ground, whereas in Petroleum and Geothermal applications are typically in hard ground dealing with rock formations that will present their own unique challenges, falling outside the scope of this work.

Pressure management is achieved by understanding the viscometric properties of cuttings returns, the combination of drilling fluid and the effects of cut solids on the fluid. Drilling fluid is bentonite clay suspended in an aqueous medium, typically water. These fluids are shear-thinning due to the presence of the platelet-shaped clay particles[16], a desirable characteristic for underground drilling. Shear-thinning fluids slow the settling of solids due to a higher viscosity when at rest, while reducing fluid pressure with a lower viscosity at high flow rates compared with an equivalent Newtonian fluid[17]. Solids concentration and the solids material is dependent on the surrounding soil formation and the connection between soil cuttings and their viscometric effects on cuttings returns viscosity is generally unknown. In practice, solids concentration is maintained between 5 and 15 vol%. If the viscometric properties of cuttings returns is known, then the drilling fluid pressure can be predicted downhole at any operating condition.

Even knowing the expected drilling fluid pressure does not guarantee the prevention of fluid circulation loss. In underground drilling one of the greatest means of failure is loss of circulation. Loss of circulation means that drilling fluid is no longer flowing through the drill string and cleaning the cutter face from soil cuttings buildup. This can be catastrophic for many reasons, unable to remove soil cuttings the drill string can no longer advance because the force required to push the rig further along becomes unfeasible if the soil isn't first broken down, if the drill string cannot advance then it may be lost underground because the borehole is too long and the frictional stress of pulling it out of the borehole is too great. Drilling fluid no longer circulating could also mean drilling fluid is building up elsewhere which oversaturates the ground resulting in degradation of soil formation integrity making it difficult to prevent the collapse of the borehole. Loss of circulation can happen because of multiple reasons but most commonly it is cause by drilling fluid pressures that are too high and exceeds the strength of the surrounding formation, creating fractures underground which drilling fluid will readily flow through, also called frac-out. The challenge with pressure management of drilling fluids is with boreholes that continue growing in length require greater and greater fluid pressure to pump the fluid down and out of the borehole.

2.2 Soil Materials

Soil materials are formed by the breakdown of rock through a mechanical or chemical method. Rocks are large masses of either a singular mineral or many minerals. The breakdown of rocks can occur mechanically by water, wind, ice, or temperature changes that yield smaller particle sizes. Rock breakdown can also occur chemically, by changing the chemical makeup and altering the strength of the material. Over time rocks become small enough in size that they become soil and are gathered into deposits typically by water, wind, ice, or gravity.

2.2.1 Distinction amongst soils

Soil materials are traditionally categorized based on particle size with the criteria for soil classifications established by organizations including Massachusetts Institute of Technology, U.S. Department of Agriculture, American Association of State Highway and Transportation Officials, and unified Soil Classification System. This work will follow the Unified System because it is used by the U.S. Army Corps of Engineers and the American Society for Testing and Materials (ASTM). Based on this standard, soil material with particles sizes between 76.2-4.75 mm are classified as gravel, 4.75-0.075 mm are sand, and below 0.075 mm are fines. Fines is the biggest distinction between the other standards, fines sizes encompass both silt and clay, which are delineated by the other standards, but merged as one in the Unified System.

2.2.2 Clays

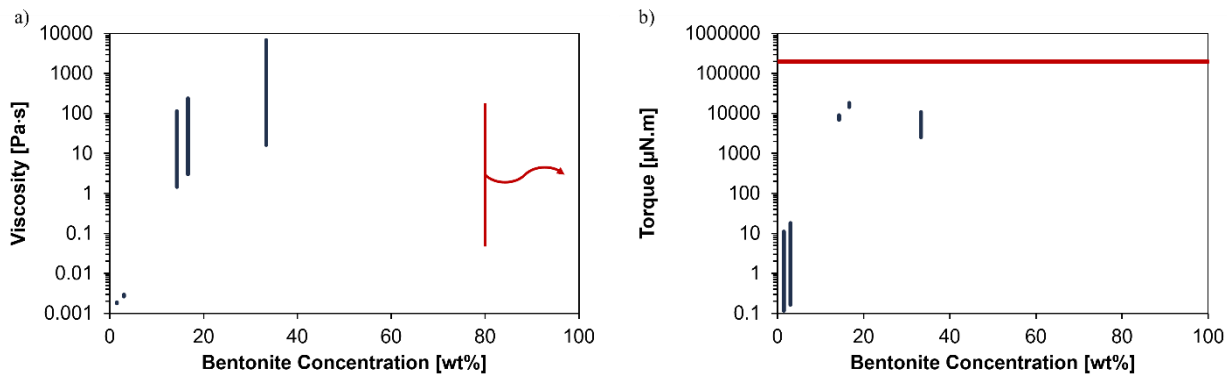

Figure 2.3 a). For the viscosity range of bentonite spanning 1-100 1/s in steady-shear, bentonite samples at variable water content were measured. Bentonite concentrations greater than 80 wt% can be commonly expected under realistic geological conditions b). Instead of viscosity, torque is compared in a cup and bob geometry for bentonite concentrations lower than 20 wt%, and the sample at bentonite content greater than 20 wt% was measured in a 20mm hatched plate with sandpaper adhered to the peltier plate. The red line is the upper torque limits of the TA instruments DHR-3 rheometer.

Clay materials have been extensively studied because of how prevalent they are around the world and their complexity[18]. Any geology that is currently near or has been in the past around a body of water has a strong likelihood to have clay. Clays are made up by the erosion of rocks over time to yield basic mineral constituents, some of which are clay minerals likely to bond to one another and form colloidal structures which are what is typically considered clay when digging up soil from a yard[19]. Common clay minerals include smectite, kaolinite, and illite but this work will primarily focus on bentonite an uncommon clay mineral derived from volcanic ash rather than rocks. Bentonite will be the focus because of its superior properties that make it useful for drilling operations, and because they present the greatest challenge during drilling. The signature property that sets bentonite apart is its ability to absorb water. Bentonite is composed of clay platelets of montmorillonite with an exchangeable cation between the platelets, commonly sodium or calcium. These cations give bentonite its water absorbing qualities because of their strong tendency to bond to water. Colloidal structures are made by reaching a high enough clay platelet density that electrostatic interactions between the negatively charged faces and edges of the clay platelets will induce a dipole moment with surrounding water, providing the positive charge needed for platelets to assemble into higher-ordered structures that can densify. The mineralogy differences between types of clays will alter the assembly of clay platelets and alter their bulk viscometric properties. The water content of clays typically found underground are at

bentonite concentrations of 80wt% or greater. As seen in Figure 2.3, these make for challenging materials to drill through with high viscosities ($> 10^4\ Pa \cdot s$) that easily surpass traditional benchtop shear rheometers and their high yield stresses ($> 10^3\ Pa$) would eject the material from capillary rheometers once the fluid yields and begins flowing. The absorption of water can cause them to expand and alter the stress state of soil underground and bias the trajectory of drill strings. Other clay materials have similar viscometric properties, but their ability to absorb water is less dramatic making them less of a worst-case scenario. As a drilling fluid, bentonite easily disperses in water, giving the fluid a yield stress and shear-thinning characteristics that improve the efficiency of removing soil materials cut by the drill string, making them ideal as a drilling fluid.

2.2.3 Granular solids

Granular matter is uniquely distinct from soft matter because of its size, where Brownian motion becomes negligible and history becomes important[20,21]. Brownian motion for colloidal particles act as a constant perturbation that nudges these particles along the energy landscape to a minimum and not to become trapped in a local energy minimum. These perturbations also reset the particles to a low minimum orientation, and without this perturbation the history of granular particles then becomes paramount in its current orientation and corresponding physical behavior, including physical contacts, shear history, gradation, breakdown into smaller particles, and particle-particle interactions. Since history becomes important in the physics of granular matter, its quantification becomes a more important matter in describing these materials. To simplify this, physicists and engineers have used effective spheres, aspect ratio, surface roughness or surface area, and density to quantify these materials. In this work, many of these parameters will not be necessary or can be averaged into a bulk material property because the calculus necessary to relate particle characteristics to the material properties becomes untenable where rheology and viscometry treat these materials as an effective continuum. There will be work discussed in this thesis where these characteristics will be a driver of the physics, but a more fundamental understanding is needed before these additional complexities can be included.

2.2.4 Variations in soil underground

2.2.4.1 Geological

As rocks breakdown over time they collect where they are broken down, residual; or collected by an external force, transported. The transportation of soils results in many unique deposits with distributions of particle size and mineralogy dependent on the rock formation they are derived from the means of transportation. Common soil deposits and their transportation include colluvium, by landslide; lacustrine, accumulation at a lake; alluvial/fluvial, deposited by running water; glacial, from the advancement or melting of glaciers; aeolian, carried by the wind; and organic soil, from the decomposition of organic matter. Each of these methods for soil deposit formation and the origin of the rock will yield wide variations and determine the concentration of fines and larger particle size materials and their distribution underground.

2.2.4.2 Water

The presence of water will affect the mechanical properties of soil materials encountered underground. The depth of the water table relative to a soil deposit will alter the water content of the soil because cohesive clay soils will readily uptake water into and onto their platelet-like structures, impacting the assembly of the platelets. Water also provides a means of transporting ions into and away from clays, also impacting the assembly of clay platelets. Depending on the uptake or drainage of water from clays, this will affect the stress state of the soil material and the surrounding formation. The time for equilibrium to be reached will also determine the stress and clay consolidation state that will affect the compression and extensional strength of the soil material[19]. In granular materials, water fills the interstitial space and provides a pore water pressure that affects the interactions between particles, and the total strength of the granular material.

2.2.4.3 Depth

Depth will also affect the strength of soil with the general rule that as the depth increases the strength of the soil formation increases vertically. At greater depths, soil will be under greater stress from the additional soil above it, causing it to consolidate along the axis of gravity and increasing the particle density along that same axis. This is why when frac-out occurs, it initiates horizontally and moves to the surface, following the path of least resistance[22–24].

2.3 Fluidizing Soil Materials

2.3.1 Effects of particles on viscosity

Soil materials are broken down into classifications by particle size and the general addition of particles to a fluid will increase its viscosity. Adding particles to a fluid sample of finite volume will effectively displace a volume of fluid and replacing that volume with a solid. This heterogenous mixture will then fall between that of a homogenous fluid and a discrete solid and the corresponding rheological properties will include those of a pure fluid and that of a solid, with greater viscosities, yield stress, and elasticity. All particle concentrations discussed in this work will remain in the concentrated regime with high enough particle densities that multiple particles are interacting with one another.

2.3.1.1 Krieger-Doherty

For concentrated non-colloidal particles added to a fluid their displacement of a fluid volume is the most common way to describe particle contributions to a system, volume fraction. For general applications in suspension rheology, the Krieger-Doherty relationship is commonly used to capture the increase in viscosity with volume fraction, Equation 2.1[25].

$$\eta_r = \left(1 - \frac{\phi}{\phi_{max}}\right)^{-[\eta]\rho\phi_{max}} \tag{2.1}$$

Where the relative viscosity, η_r, is a function of the volume fraction, ϕ, maximum packing fraction, ϕ_{max}, and for hard spheres the dimensionless intrinsic viscosity is $[\eta]\rho$ = 2.5, where ρ is the particle density. This relationship fails with additional complexities but the expression has been modified to accommodate them, including particles size distribution[26–30] and aspect ratio[31–33]. Realistically, Krieger-Doherty cannot be applied to complex systems of cuttings returns of granular particles with settling, variations in aspect ratio and particle size distribution, and frictional interactions that are also dispersed in a colloidal dispersion of bentonite clay platelets. Because of these complexities, empirical correlations will be necessary to quantify the viscosity for such a heterogenous mixture of particles in a fluid.

2.3.2 Colloidal Suspensions

Platelets of bentonite clay will be the predominate colloidal particles in handling soil materials for underground drilling. Bentonite clay is the preeminent clay used as a drilling fluid

because it readily absorbs water, making it an easy additive to combine on-the-fly during drilling and because of that absorption and interplatelet interactions readily forms structures to develop shear-thinning and yield stress properties that can disperse soil cuttings and convey them out of the borehole. It should be noted that classification systems that include clay are defined by particle size, but to make a particle truly clay it needs a cohesive nature. That means that clay soil material also includes particles that are not clay because they are not cohesive.

2.3.2.1 Bentonite slurries

In the context of DD and HDD, bentonite slurries are one of the most common fluids used to transport soil cuttings out of the borehole. Bentonite slurries consist of mined bentonite clay and water at concentrations from 3-5wt% (wt% = $\frac{m_B}{m_B+m_w}$) depending on the desired application. This concentration can be beyond the transition from a sol to a gel, signifying a colloidal network has developed across a sample depending on the mineralogy of bentonite used[34]. Bentonite is primarily composed of sodium montmorillonite clay and functions well as a drilling fluid slurry because they are a shear-thinning yield stress fluid that can be purchased cheaply. Shear-thinning properties mean that with increasing flow rates (~ shear-rates) the viscosity will decrease and make the material easier to pump, and at lower flow rates (~ shear-rates) a higher viscosity will develop – slowing down the rate of settling in the soil material being transported. Shear-rate is the normalized rate of deformation a material experiences so that a universal quantity could be applied to any system. The typical mental image of shear-rate is a static system with fluid between two parallel plates, and once one plate moves at steady velocity then the fluid experiences a shear-rate, the gradient of velocity between the two plates. This is commonly simplified as the velocity of the moving plate divide by the distance between the two plates. The yield stress of the slurry also contributes to the prevention of settling by keeping soil materials dispersed when a minimum stress is not being applied to the fluid. This is ideal in solids transport because soil materials remain entrained in the drilling fluid when flow is slow but is easy to pump when flow rates are high. The conveying of soil cuttings is often termed carrying capacity, which describes the effects of yield stress and shear-thinning properties to disperse soil cuttings and subsequently remove them from the borehole. In practice settling occurs because many of the soil materials are granular particles that would require a high yield stress to keep them suspended, which would require an untenable concentration of bentonite that would result in viscosities that would quickly burnout the pumps. But by increasing the viscosity of the drilling

fluid with Bentonite the shear stress applied to the particles increase and disperse the granular particles so that they can be convected out of the borehole.

Bentonite slurries have shear-thinning and yield stress behaviors because of the colloidal structure. Bentonite clay is made of colloidal size platelets composed of silicon oxide with exchangeable cations between the platelets. The surfaces and edges are negatively charged. This structure is what gives bentonite slurries and clays their unique properties. At low bentonite platelet concentrations in water the mixture behaves as a colloidal suspension. The micromechanical concept that gives bentonite slurry their rheological properties is the breakdown and alignment of platelets during flow. Platelet structures are built up when no stress is applied to the slurry because of the charged faces and edges with water bonding the two, and this structure gives the material a yield stress, needing a critical stress threshold to be reached to breakdown the structure and commence flow. The buildup of structure is induced by Brownian motion of the colloidal platelets. Once flowing, the platelet structures further breakdown from the shear and align with the direction of flow, reducing the resistance to flow at greater shear-rates (flow rates). There are many more nuances and complexities not covered in this rheological description of colloidal suspension because the main concern of this thesis is on the viscometric properties of the bentonite slurry and the macroscopic effects on underground drilling that operate at high-shear rates well above instances where system stability, non-spherical particles, electrostatic interactions, and many more contribute to the fluid's rheology. These subjects are thoroughly covered elsewhere[9].

2.3.2.2 Colloidal Networks

The soil transported by the bentonite slurry will typically be clay and sand. Bentonite clays encountered underground have low water content and behave as a dense colloidal structure, that have been called either glasses or gels which depends on whether an ordered or disordered colloidal structure exists, but their bulk effects remain the same[35]. As clay platelet concentrations increase they begin interacting electrostatically to form tactoids, higher order platelet structures, and these tactoids assemble into larger structure that are commonly described as card house like, creating a structure that span the sample[36]. With higher bentonite content (> 40wt%), the structures become more interconnected meaning greater elasticity, larger viscosities ($> 10^4\ Pa \cdot s$), and larger yield stresses ($> 10^3\ Pa$) that surpass the measuring capabilities of benchtop

steady-shear rheometers. In clay soils encountered underground, bentonite content can easily surpass 80wt%.

2.3.3 Granular Dispersion

Other soil materials encountered underground at depths of ~ 100ft can include sand, pebbles, granules, gravel, and cobble. These macroscale granular materials will also need to be transported out of the borehole, luckily these granular materials will either be avoided or broken down into gravel, pebbles, granules, and sand. These materials are much denser that the drilling fluid slurry and will settle, but because of the drilling fluid slurry rheology and the high operating flow rates ($600\ GPM$) the granular solids will be dispersed and evacuated out of the tunnel. With these granular solids and soft-solid clays the main interactions will be frictional interactions between solids and hydrodynamics.

2.3.3.1 Settling and Shields Parameter

With granular soil materials is a common challenge to avoid because of the disruptions settling causes to the drill string from interrupting flow from the drill bit back to the surface and preventing the removal of soil cuttings. Many mitigation strategies have been developed to address this that include mechanical, rotating pipes, double pipe systems to reduce cuttings and borehole wall adhesion; and rheological, using bentonite slurries, polymer solutions, and various synthesized suspensions with yield stress and viscous properties that will reduce settling. Even with these strategies, it is unclear which is the most effective due and treated as a black box because of the variability in underground soil conditions and the anecdotal approach used in practice to modify drilling fluid depending on the appearance of cuttings returns. With drilling fluids, novel additives are constantly being published because improvement to a drilling operation is dependent on the soil geology and the rheological modifications made to the drilling fluid, but neither are quantified with high accuracy. Improvement in drilling operations could be due to variations in the formation geology rather than modifications made to the drilling fluid and how drilling fluids are rheologically modified are unknown.

Settling during flow is best described by the Shields parameter, a nondimensional number comparing wall shear stress and buoyancy stress, the magnitude indicating the tendency for solids to settle – values greater than 1 less likely to settle and values less than 1 more likely to settle. In Equation 2.2, Shields parameter (θ) is expressed as the ratio between the wall shear

stress and the stress caused by settling. Pressure drop is converted to wall shear stress by Equation 2.3.

$$\theta = \frac{\tau_w}{gd(\rho_s - \rho_f)} \tag{2.2}$$

$$\tau_w = \frac{\Delta P \cdot d_p}{4L} \tag{2.3}$$

Seen in Equation 2.3, if the pressure drop of the system increases then the wall shear stress will increase, and increasing viscosity with bentonite content increase pressure drop of the system.

2.3.3.2 Particle Interactions

The interactions between particles are broken down into normal and tangential contact forces. Where the normal contact force is modelled as an elastic contact, commonly using a variation of the Hertz law and is summarized in Figure 2.4 where two particles in contact will deform each particle, designated by the grey area and the deformation is a function of particle geometry and mechanical properties[37–40].

Normal contact force

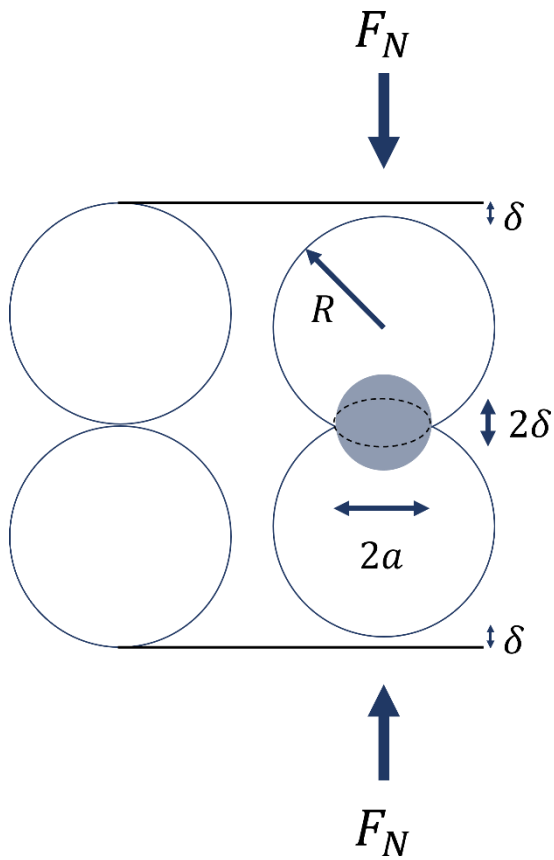

Figure 2.4 Diagram depicting elastic contact using the Hertz law for two hard spheres in contact, to retrieve the normal contact force between two particles. The particles on the left are in contact with no deformation made and the particles on the right are in contact with a deformation δ applied to each sphere from equally applied normal forces. The grey zone is describing the zone of deformation. This is based on a figure from Granular Media[8].

$$F_N = \frac{4E\sqrt{R}}{3(1-v_P^2)}\delta^{\frac{3}{2}} \tag{2.4}$$

$$a = \sqrt{\delta R} \tag{2.5}$$

Equation 2.4 forms the basic expression used for normal contact force between particles, and additional complexities have been added since its inception to include cohesion[37,41–46] and dampening[47–50]. The normal force is a function of the material elastic modulus, E, particle radius, R, particle Poisson's ratio, v_p, and particle deformation, δ. This expression also translates to the kinetic energy of particles as collisions transform into their movement away[40]. In Equation 2.6 the energy of collision, E_c, is a function of particle mass, m, and velocity, v, which can be converted to elastic energy, E_{el}, in Equation 2.7 and can be defined by the normal force

multiplied by the deformation and is a function of the elastic modulus, particle radius, particle deformation, particle speed, v, and time of collision, t_c.

$$E_c = 2 \cdot (1/2)m\mathrm{v}^2 \tag{2.6}$$

$$E_c \sim E_{el} \sim F\delta = (E\sqrt{R}\delta^{3/2})(\mathrm{v}t_c) \tag{2.7}$$

$$t_c \sim \left(\frac{m^2}{RE^2\mathrm{v}}\right)^{1/5} \tag{2.8}$$

Tangential contact force

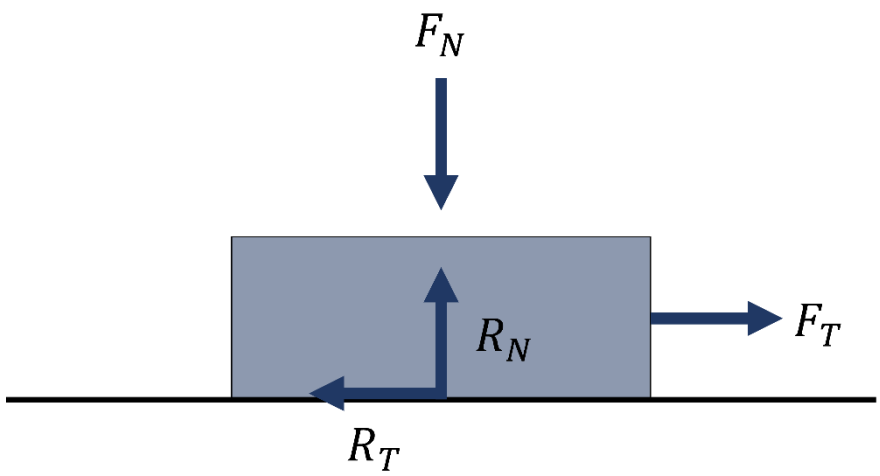

Figure 2.5 Force and reaction force diagram detailing the tangential and normal forces acting on a stationary block.

$$|R_T| = \mu_s|R_N| \tag{2.9}$$

Tangential contact force comprises the basic concept of friction, where the tangential force needed to move a block from a stationary position to sliding is equivalent to the product of the friction coefficient and the normal force acting on the block, Figure 2.5 Force and reaction force diagram detailing the tangential and normal forces acting on a stationary block.[8,51] and expressed in equation 2.9. Equation 2.9 is an expression for tangential contact force between particles, where the tangential reactionary force is a product of the frictional coefficient and the normal reactionary force action on the stationary block. The frictional coefficient has also been explored in microscopic detail and derived based on the asperities and contacts of the rough surfaces[52]. Additional complexities can also be included in the model to include additional modes

of motion for the tangential contact[53] and no-slip conditions between the two particles[54–57]. The additional modes of motion include rolling[40,49,51,53,58–63] and twisting friction[49].

Hydrodynamics

The hydrodynamics of fluid particle interactions are complex at time and length-scales of drilling operations with astronomical numbers of particles that include particle-particle interactions and fluid-particle interacts of the fluid acting on the particle and the particle movement through fluid acting on the surrounding fluid. Because of all of these interactions, bulk-scale theoretical or first-principle relationships have yet to be derived and are predominately explored at the particle level due to the computational expense and difficulty to observe experimentally[8].

The basics of fluid-particle interactions goes back to creeping flow of a particle sedimenting or falling through a fluid under laminar flow. This simple example can be described by a simple expression, seen in Equation 2.10[64,65], and can be generalized with a pressure gradient to turbulent flow, see Equation 2.11[8]. And a falling particle is described with Equation 2.12.

For laminar flow around a particle,

$$F_d \sim -\eta d u^p, generally \tag{2.10}$$

$$F_d = -3\pi\eta d u^p, for\ a\ sphere$$

For turbulent flow around a particle,

$$F_d = -\frac{\pi}{8} C_\infty \rho_f d^2 u^p \mathbf{u}^p \tag{2.11}$$

$$C_\infty = 0.47, smooth\ sphere;\ 1, natural\ grains$$

$$u_{fall} = \sqrt{\frac{\rho_p - \rho_f}{\rho_f} \frac{4gd}{3C_\infty}} \tag{2.12}$$

Beyond these expression, there are multitudes of hydrodynamic complexities[66] that can be included like unsteady flows - accelerating fluid, relative velocity difference, magnus forces, lubrication forces[67,68], and the effects of those hydrodynamics on the collision between particles[69,70]. The connection of these interactions to bulk viscometric properties have yet to be made beyond simulation work and requires empirical expressions to capture all of these effects at the bulk scale with viscometric properties of fluid-particle mixtures under varying flow conditions.

2.3.3.3 Flow through porous media

There has been a long interest in predicting the relationship between flow rate and pressure drop, especially driven by industrial process with packed beds commonly used for separations or catalysis[71]. Darcy's law was one of the earlier attempts at identifying this relationship, born from empirical testing of flowing water through porous media under laminar flow conditions, relating flow rate to pressure drop by a ratio between the permeability of the porous media and the viscosity of the fluid (See Equation 2.14)[72]. But at greater flow rates where inertia becomes non-negligible Darcy's law begins to fail.

$$q = -\frac{k}{\mu}\nabla p \tag{2.13}$$

Darcy's law is the flow rate, q, equals the soil permeability, k, divided by the fluid viscosity, μ, and multiplied by the pressure drop across the cell, ∇p.

To distinguish between flow regimes where Darcy's law fails, the pore Reynolds number is used to describe flow through porous media. The pore Reynold's number is the ratio between inertial and viscous forces where the inertial term is the product of fluid density, ρ, fluid velocity, v, and pore size assumed to be bed particle diameter, d, and the viscous term is fluid viscosity, μ, Equation 2.15.

$$Re_{pore} = \frac{\rho v d}{\mu} \tag{2.14}$$

There are also expressions developed to account for inertial contributions in porous media flow. Ergun's equation is a semi-theoretical model that spans a wide range of flow regimes from Darcy/viscous to turbulent flow. Equation 2.16 is Ergun's equation, the pressure drop, ΔP, normalized by the length traveled by the fluid, L, is related to the porous material's porosity, ϵ; density, ρ; and packed particle diameter, d_s. A and B are the empirical fittings parameters specific to the bed. The meaning of the empirical parameters are still up for debate and their significance have not been determined[73].

$$\frac{\Delta P}{L} = A\frac{(1-\epsilon)^2\mu}{\epsilon^3 d_s^2}u + B\frac{(1-\epsilon)\rho}{\epsilon^3 d_s}u^2 \tag{2.15}$$

Ergun's equation is derived from treating porous media void spaces as a collection of capillary tubes. Researchers have subsequently tested a range of porous media flows, primarily in packed beds, to determine the range of empirical constants, making it possible to predict flow in Darcy/viscous to turbulent flow regimes[73–75].

$$\frac{\Delta P}{L} = \frac{\mu}{K}u + \rho\frac{F}{\sqrt{K}}u^2 \tag{2.16}$$

$$K = \frac{\epsilon^3 d_s^2}{36\kappa(1-\epsilon)^2}$$

Forchheimer's equation is another expression that includes inertial contributions. The pressure drop across the cell is a parabolic function of the fluid velocity and includes parameters of viscosity, μ, Forchheimer constant, F, fluid density, ρ, Kozeny-Carman constant, κ, and intrinsic permeability, K, Equation 2.17.

Most drilling fluids are also non-Newtonian, commonly either including polymers, colloids, surfactants, or particles as well. Recently there have been investigations in expanding models for flow through porous media to begin incorporating non-Newtonian fluids, but there is much to be explored yet[74,76,77]. For the most part, research on porous media flow models for non-Newtonian fluids is still growing.

2.3.3.4 Clogging

Gravity-driven clogging

Jamming of orifices by granular material have long been studied and empirical relationships have been developed to determine the geometric dimensions, rate of flow, and the effect of gravity[78,79]. Probabilistic models have also developed from these empirical studies to determine the likelihood of clogging depending on geometry of the particulate and the orifice size[80–82]. There is little literature on fluid-driven clogging of orifices with particles[83] and no literature or model development to describe fluid-driven particles clogging in porous media. In fluid-driven clogging, there are clear connections between diameters of the orifice and particle, fluid velocity, and restriction volume fraction (ratio between volume of particles filling up an orifice volume), but no relationships developed collapses the data onto a trend independent of granular length-scales[84]. Gravity-driven clogging literature has determined that in 2-dimensional systems of circular disks, clogging occurs when the orifice diameter is twice the diameter of the disk and no clogging when the orifice is 5 times the disk diameter or greater[82], Equation 2.18.

$$D_{filter} \leq 2D_{particle} \tag{2.17}$$

Fluid-driven clogging

While Ergun's equation is a good point of reference, solids content in the fluid is a crucial factor unaccounted for in existing models of flow through porous media. Sands and silts are common materials encountered during drilling and the extent of their dispersion depends on flow regime and fluid properties[85–87]. At low flow regimes, particle dispersion will be dominated by settling which can naturally lead to clogging of the porous medium. Clogging behavior is the dynamic to static transition of jamming, deposition, or plugging of pore space in granular soils. It ties together subjects from many well studied research areas including jamming of particles through orifices, deposition of colloids in porous media, and clogging of orifices with particle-laden fluids[80,88,89]. The specific situation of clogging of gravel with sand carried by a fluid has been studied empirically and with many analogous systems to compare against, but it is lacking its own theoretical approach[79,80,89,90].

Earthen dam filter criteria are the closest empirical evaluation of granular clogging of porous media with fluid laden with solids. The purpose of dam filters is to create a porous bed downstream of a water filled earthen dam that traps solids but allows fluid to flow through[89]. Erosion of earthen dams is one of the major causes for failure and it occurs when solids carried by water are allowed to flow away from the dam. To remedy this, empirical evaluation of soil sizes have been carried out to create a porous bed downstream of the dam to capture solids and prevent erosion that would weaken the structural integrity[89]. The result of this are criteria that determine the threshold particulate size and pore size that will lead to clogging and prevent erosion.

$$D_{filter} < 10 \cdot D_{particle} \tag{2.18}$$

$$D_{filter} < 4 \cdot D_{particle} \tag{2.19}$$

There are two empirical criteria recommended by Terzaghi to prevent dam erosion, equation 2.19 and 2.20. Terzaghi's early consulting work, he recommended equation 2.19 for effective dam filters and equation 2.20 is based on the classic text of Terzaghi and Peck (1948)[91] and the experiments performed by Bertram (1940) that also accounts for soil retention[92]. Both equations are expressed in weight percentage of fines content above or below a particle diameter,

but since our system has a narrow size distribution the equations have been simplified to bed and particle diameters.

$$D_{filter} < 6 \cdot D_{particle} \tag{2.20}$$

Equation 2.21 is from Casagrande, who conducted a thorough series of permeameter tests that also accounted for the influence of air and ions in water that could alter clogging[92]. They determined that the criteria should be 6 rather than 4 or 10 to retain soil.

Foster and Fell determined that the ratio between DF15 and DB85, filter diameter where 15 wt% particles are finer and base diameter where 85 wt% is finer, is the only driver of significance to determine filter criteria[89]. DF15 is simplified to D_{filter} and DB85 is $D_{particle}$ since our system does not have size distributions. Their proposed criteria is for no erosion and derived from analyzing coarse sandy gravels compared between lab results and in-service dams[89], equation 2.22.

$$D_{filter} \leq 11.2 \cdot D_{particle} - 0.84 \tag{2.21}$$
$$DF15 \leq 11.2 \cdot DB85 - 0.84$$

2.3.4 Quantifying their Rheology

The addition of granular soil materials will result in an unclear relationship with the corresponding viscometric properties because granular materials do not exhibit Brownian motion, no equilibrium structure will develop, and many meta-stable states can be achieved without this perturbation. However, some general observations from colloidal rheology can still be applied to granular dispersion system. One is that the viscosity will increase with greater solids content, because effectively the dispersions are not being deformed by the flow and exclude fluid volume. This means that within the same borehole space comparing the flow of a pure fluid versus a fluid with particle dispersions, less fluid is being deformed when dispersions are present – reducing the effective shear-rate of the system while maintaining the same shear stress and hence increasing the viscosity (stress/shear-rate). In addition, the shear stress should increase with dispersions as well because there will be more energy dissipation from wakes following the granular particles and frictional dissipation from particles interacting with one another, increasing the effective viscosity. Overall, granular soil materials as dispersion are complex in water alone due to their hydrodynamic and frictional interactions without Brownian

motion. The addition of non-Newtonian medium of bentonite drilling fluid increases the system complexity. Because of these challenges, much of the experimental work with realistic granular systems are characterized with empirical relationships, often branching off from polymer solutions and polymer melts that measure bulk viscometric properties[93].

2.4 Turbomachinery Fundamentals for Pumps

Pumping is vital in underground drilling, to mix and convey drilling fluid down the borehole and remove soil cuttings. The mixing of water with bentonite clay to form a bentonite slurry is typically done above ground and done with centrifugal pumps to quickly mix and hydrate the clay powder[4]. The bentonite slurry is then pumped underground with positive displacement pumps so that the drilling fluid flow rate can be precisely controlled during operation when greater flow rates may be needed to operate a mud motor that rotates the drill bit or to decrease flow rate to reduce fluid loss during a fluid circulation loss event[4]. Pumps are critical machinery in controlling drilling fluid pressures underground and especially with fast HDD to remove cuttings at a fast rate and providing a greater pressure head for longer boreholes.

2.4.1 Centrifugal Pump fundamentals

To understand the effects of pump operation on drilling fluid pressures a simple example breaking down the semi-theoretical relationships for a centrifugal pump will be discussed. In centrifugal pumps, they operate as a rotating wheel with vanes and water flows into the center of the wheel and as the wheel rotations with guide vanes a centrifugal force is applied to the water driving it to the edge and out of the pump, as seen in Figure 2.6. From this simple diagram, the velocity component of the fluid moving out of the pump can be broken down into vectors and

used to describe the expected pressure head and flow rate performance of the pump and a characteristic curve can be built.

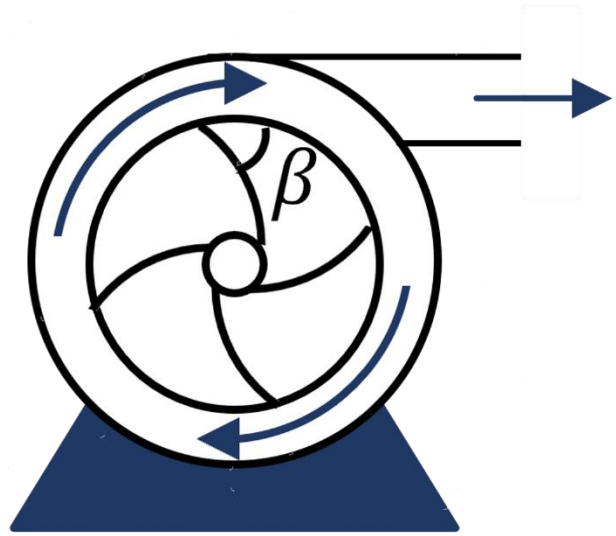

Figure 2.6. Diagram of a centrifugal pump based on the work of Wilkes 3rd edition[94].

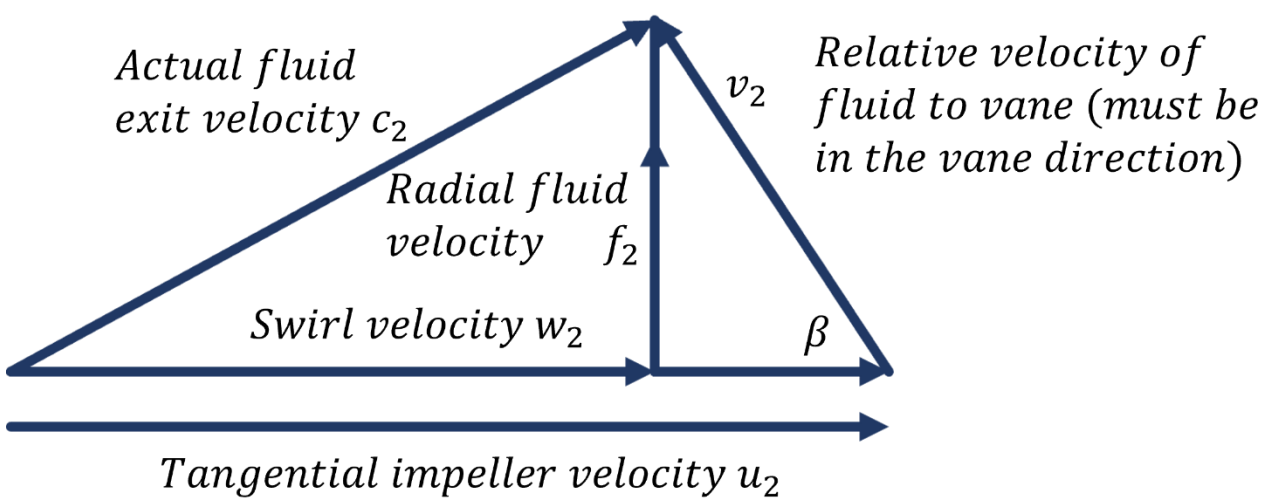

Figure 2.7. Velocity breakdown of the fluid moving out of a centrifugal pump.

Following Figure 2.7, the fluid moving out of a centrifugal pump can be broken up into velocity vectors that can be used to calculate the pressure head and flow rate of the pump. Equation 2.23 expresses how the tangential impeller velocity can be used to calculate the expected pressure head of the pump[94]. The pressure head, Δp, is a function of the fluid density, ρ, and tangential impeller velocity, u_2.

$$\Delta p = \rho u_2^2 \tag{2.22}$$

The flow rate from the pump is described in Equation 2.24, where the flow rate, Q, is the product of the volume of fluid moving out of impeller ($2\pi r_2 d$) and the radial fluid velocity (f_2)[94].

$$Q = 2\pi r_2 d f_2 \tag{2.23}$$

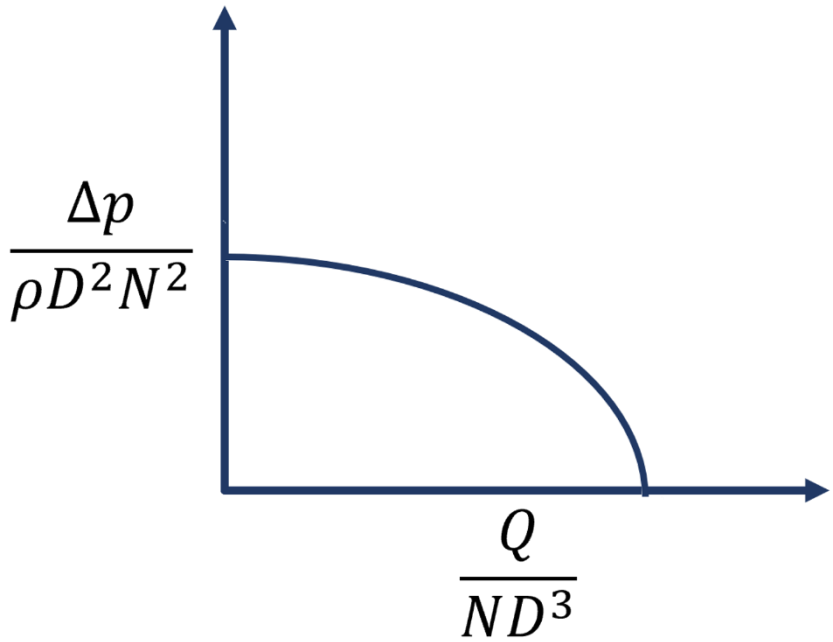

Figure 2.8. Characteristic curve the non-dimension flow rate and pressure drop performance for a centrifugal pump.

The pressure drop and flow rate expression can also be non-dimensionalized following Figure 2.8, to create a characteristic curve for centrifugal pumps. This general trend can also be expressed as Equation 2.25, that describes the reflected exponential trend, and the system constants, a & b, can empirically capture the differences between pumps.

$$\Delta h = a - bQ^n \tag{2.24}$$

2.5 Thesis Statement

From an assessment of the literature and discussions with industry professionals, it is clear there is a lack of understanding of the viscometric material properties of fluidized soil materials and their corresponding application in underground drilling, limiting the field's advancement. It is also well-known that maintaining drilling fluid pressure is one of the biggest challenges in underground drilling and is far from being resolved. ***Thus, the central hypothesis of this thesis is: The advancement of underground drilling can be enabled with particle rheology and tool development to probe the fluid mechanics of soil material within a drill string and address the origin of fluid circulation loss.***

CHAPTER 3 CALIBRATING AN INDEX-TYPE MIXER TO MEASURE VISCOMETRIC PROPERTIES OF HIGH-SOLIDS, HETERGOGENEOUS SOIL

Modified from a paper to be submitted to *Journal of Rheology*

Benjamin A. Appleby[1,2] , Muhammad Ishaq[3], Ali Vossoughian[3], Jamal Rostami[3], and Joseph R. Samaniuk[l,4]

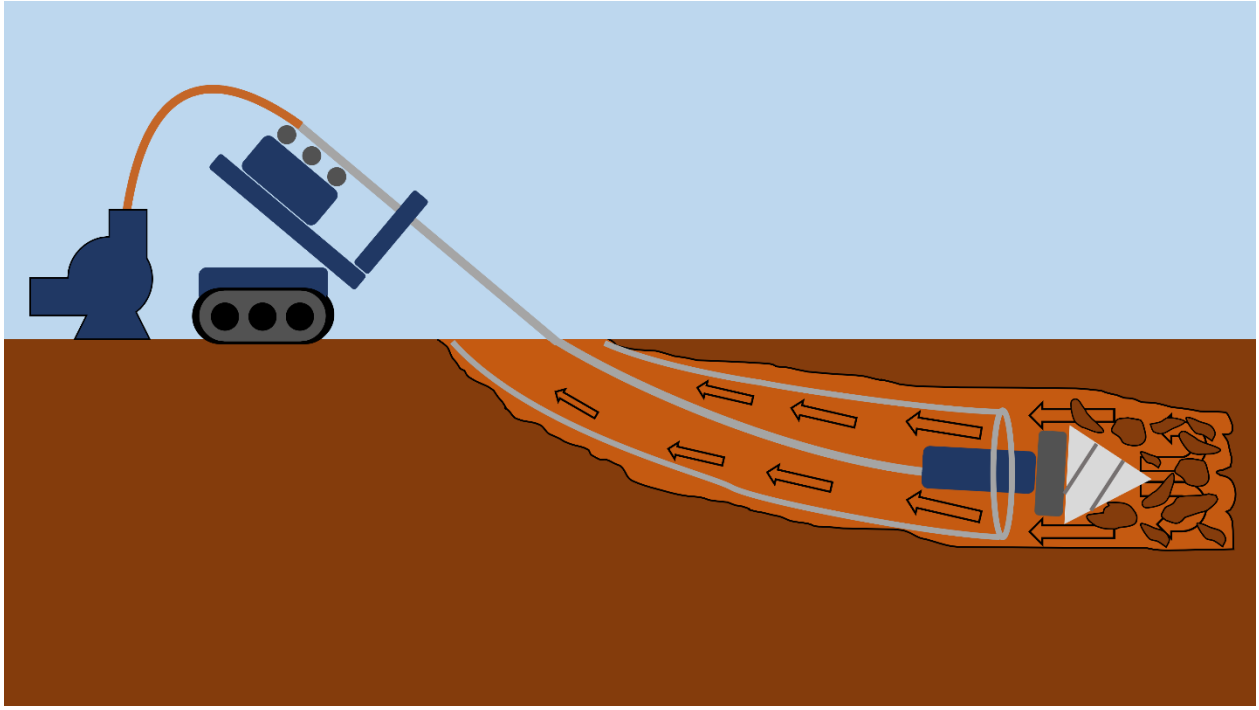

Figure 3.1 Schematic of the cutterhead breaking down soil into cuttings that will then flow through the annular space between the pipes.

Tools used to breakdown soil materials come in many shapes and sizes because their designs are often empirical in nature but many of them have common features, often with teeth to cut soil material down into small enough parts that they can be conveyed out of the borehole and with a rotating action to self-clean the teeth so that soil material does not build up on the tooling (Figure 3.1). The challenge of designing tooling from theoretical principles is the lack of

[1] Graduate Student and Associate Professor, respectively, Department of Chemical and Biological Engineering, Colorado School of Mines.
[2] Primary researcher and author.
[3] Graduate Student, Graduate Student, and Professor, respectively, Department of Mining Engineering, Colorado School of Mines.
[4] Graduate advisor, Author for correspondence.

information on the true viscometric properties of soil materials. Properties that are necessary in simulating a material's stress-strain relationship, and how they will behave when interacting with a cutterhead. These material properties are desirable because of their universality. In this context they are used to model material processing by a cutterhead, but they can also be used for pumping soil cuttings, flow through a pipe, and other scenarios where the material can be treated as a continuum. Since soil materials have multiple constituents ranging in colloidal and granular particle sizes and are under a wide range of environmental conditions, traditional bench-scale instruments cannot characterize them because of their large particle sizes ($> 1\ mm$), viscosities ($10^4\ Pa \cdot s$), and memory. At the time of this work, viscometric characterization of soil materials larger than a millimeter in size was limited, but there were many examples of comparable systems and calibration approaches in the biomass literature, material that also has granular sized particles.

In this work we have applied the calibration procedure developed by Bousmina *et al*[95] used for polymer melts and extended to biomass slurries[96–99], and applied it to clay slurries up to the limit where the slurry transitions from fluid-like to plastic-like behavior. The novel contributions of this work are in measuring the true viscometric material properties for a low water content bentonite slurry ($\geq 16.7wt\%$) with a range of gravel content approaching its packing fraction and incorporating a Bingham Plastic constitutive equation into this calibration procedure rather than a power-law empiricism. Prior to this work soil materials were measured with index-type devices that outputted values that could not be applied in simulations because the data was specific to the measurement device. The calibration method we employ gives measured material properties independent of the device, allowing them to be applied to any simulation or numerical analysis. While this work has extended the range of measurable materials, after a higher enough bentonite concentration the material transitions from fluid-like to plastic-like behavior where it retains memory and how it is deformed will impact the measured stress-strain relationship obtained for it. The work presented in this chapter is most relevant in clay soils at their liquid limit or greater water content and with granular particles up to the size of gravel. This is relevant in HDD and DD where the underground formation is below the water table and in slurry TBMs rather than Earth Pressure Balance TBMs, where the soil remains fluid-like. However, with plastic-like materials their deformation history is retained, meaning the measured viscometric properties will be dependent on the method of deformation. This system can be used to measure viscometric properties of a material if the same method of deformation in the field

can be replicated with the device. This work provides a path forward to quantify how the constituents of soil materials impact the ability of cutterheads to break down the material, particularly with soil materials that have granular particles.

3.1 Abstract

Rheological properties of soil material are a challenge to characterize because of their large length-scale ($> 1\ mm$) and torque requirements that exceed the capabilities of most commercially available rheometers. The aim of this study is to apply the calibration procedure from Bousmina (1999) to convert a mixer into a viscometer capable of handling large particle sizes ($19.05\ mm$) and torque requirements to measure the effective material properties of realistic soil materials[95]. State-of-the-art soil viscometers utilize assumptions from constitutive equations or computational fluid dynamics (CFD) to calculate measured shear stress and shear rate without verifying the accuracy of measured values[100]. Calibrations performed in this work provide measured values to calibrate the soil viscometer without depending on unrealistic assumption. This work will provide a calibration pathway for measurement geometries with and without global flows beyond the traditional theta direction. The challenges of determining the yielded region of yield stress fluids relative to the geometry of the system will also be addressed. This work presents a pathway for calibrating viscometers to measure high viscosity ($> 10^4\ Pa \cdot s$), particle-laden material, with a minimum particle dimension of 19.05 mm, material commonly encountered in shallow underground drilling.

3.2 Introduction

Characterizing the viscometric properties of granular materials and slurries with granular solids are challenging and often qualitative comparisons are the best that can be achieved. But this provides very little information that can be applied to other systems, only relative differences between samples can be determined.

Mixers have been used to measure complex fluids with high elasticity particles, but they have not been calibrated to measure viscometric properties of real soil materials of clay and granular particles[101–115]. There have been many devices built to characterize viscometric properties but they are limited to index-type devices that do not provide universally applicable material properties because of an oversimplification of the calibration procedure[100,116–119]. Two common calibration procedures include derived relationships and back calculation using

computational fluid dynamics (CFD) models with an assumed constitutive equation[106,120]. Derived relationships commonly use a couette analogy, where no matter the geometry an approximate couette based on the same cup radius and rotation speed, the same torque will be measured[121]. Back calculations are inherently flawed because an assumed constitutive equation is needed to determine stress-strain behavior of the material. And these procedures are only used to determine shear stress and shear rate so a constitutive equation can be fitted to the data without accounting for the physics behind the significance of each model. Since the physics of plastic-like clays and bulk granular matter has not been well understood at a continuum level, CFD will be assuming that all soil materials will be interacting with the measurement geometry in the same way, but a large part of experimental rheology is in the interpretation of torque values from a rheometer and observing the measured material to determine the limitations of a measurement.

In the biomass community, there has been a history of developing and calibrating viscometers to measure the viscosity and yield stress of biomass slurries. The slurries of interest balance high solids content ($> 20wt\%$ Solids) to maximize yield in a chemical process while low enough to reduce processing challenges, including non-Brownian particles, wall slip, settling, and ejection[122–129]. From all of these rheological challenges there has become well established procedures to calibrate a rotational device capable of measuring viscosity and yield stress. Fibrous particles found in biomass are flexible and can be broken down by mixer-type devices, while gravel would more likely jam and harm many of these devices. There has been measurement geometries developed to measure complex fluids with high elasticity particles, but they have yet characterized these samples[124,130,131]. The challenges experienced with biomass measurements include non-Brownian particles, settling of samples, and high viscosities which overlaps with soil materials and can be referenced in making viscometric measurements of soil materials.

Traditional shear rheometers require a few key assumptions to calculate material properties – laminar flow, uniform shear profile, and uni-directional flow. Using cylindrical coordinates and a cup and bob geometry as an example, the flow will be independent of the “z” and θ – direction and only a function of the radial direction, “r”. These assumptions become challenged depending on the measurement geometry and the material of interest. An extension of the couette geometry is the 4-bladed vane, where re-circulation of flow occurs between the vanes, but recirculation does not affect the material beyond the vanes and an assumed geometry radius can be made with great accuracy. This geometry is advantageous for measuring materials

with large particle sizes ($> 1\ mm$) that would jam a cup and bob geometry and high viscosities that would require high normal stress to insert the geometry into the material[123]. A fractal vane has also been developed by the McKinley group as a geometry between a vane and a bob, which is easier to insert into materials and not jam when particles are present, but also reduce the recirculation between vanes[132]. The vane geometry set the precedent for the couette analogy that has now been used in a variety of mixers and rotating geometries[95,133]. This analogy falls short when the original rheometer assumptions are invalidated, like in the case of z-directional flow or the effective couette cannot be easily determined[124,134]. These cases have been addressed with additional calibration procedure extensions that account for complex flows[124] and an effective inner radius[95]. The development of any new rheometer will need to address the effects of its own unique geometry and the expected behavior of the materials that will be characterized.

This work is specifically addressing soil materials which require unique measurement geometries and will have material properties outside the norm, including predominately clays, sands, and gravel. An easy conceptual understanding of this is granular materials like sand and gravel have particles where frictional contacts dominate their interactions. Dilation is a common behavior of sand, when sheared the sand will tumble and create force chains that apply a stress on its surroundings. This stress will either result in a net total increase in stress applied to the sample or the total volume containing the same will increase. Because of these force chains, sand is also hard to measure in a traditional rheometer – often leading to shear-thickening and jamming that will stop the deformation and could potentially damage the instrument[103,135–137]. Alternative attempts at measuring sand has also shown the common transitions from inertial to transition to stationary flow within a short length-scale[134], making it challenging to determine the effective couette created by a measurement geometry. It has also been shown that particle size distribution, volume fraction, and stress-state have major effects on the strength of the material. Clays, like sands exhibit many of the same parameter dependence, but since they are colloidal in size they also have time-dependent material properties dependent on the water content, pH, exchangeable cations, and mineralogy[93,138,139]. This work will provide a guide to calibrate true viscometric properties so that these parameters can be explored in detail and be used to compare viscometers rather than independent index-type devices that are can only be compared with itself.

This work will follow the calibration procedure of Bousmina (1999)[95] and is an extension of the procedure developed by Goodrich and Porter[140] for determining the effective inner radius produced by any measurement geometry that does not generate an axial flow, and this value will

remain as a constant value and can be used like effective concentric cylinders to determine the viscometric properties of soft materials. G&P use a brabender torque-rheometer on polymer melts to convert rpm and torque values into rheological units of shear-rate and viscosity. The calibration procedure requires that the rotation rate and torque of the instrument is known and a calibration fluid that can be both ran in the new measurement geometry and a trusted rheometer to characterize the viscometric properties. With the rotation rate and torque data and steady-shear flow sweep of a calibration fluid, the effective inner radius can be determined and then used in the derived Navier-Stokes expression for an effective concentric cylinder setup to determine the shear-rate and viscosity relationship based on the rotation rate and torque of index-type mixer, converting it to a viscometer. Bousmina (1999) extended this work by showing that both a Newtonian and non-Newtonian calibration fluid can be used for this procedure because there is a geometric point between these effective concentric cylinders that when derived for will produce rotation rate – shear-rate and torque – viscosity relationships in independent of the measured fluid's rheology. They provided theoretical proof of this geometric point and verified it experimentally with dilute polymer solutions.

If there was z-directional flow then Pimenova & Hanley[124] can be used but would require both a Newtonian and non-Newtonian calibration fluid whereas Bousmina *et al*. only requires a non-Newtonian calibration fluid. For our system, a high minimum torque ($> 15\ N \cdot m$) is needed, and the corresponding Newtonian calibration fluid would be too expensive. The basics of the Bousmina's procedure require a geometry with no z-directional flow, and the calibration fluid needs to be measurable in a traditional shear-rheometer. The Bingham Plastic model is used because a bentonite slurry will be used for calibration and is known to have a yield stress. Any constitutive relationship can be chosen for calibration, but beyond simple models the math becomes more complicated without any added value because the relevant characteristics of bentonite slurry are well captured by the Bingham Plastic model – yield stress. The calibration method covered in Bousmina *et al*. will be detailed in the methods section, but the main premise of it is to assume an effective radius – dependent on the flow profiles generated by any geometry where the flow direction is only in the θ – direction, Figure 3.2. Decision tree from learned experiences and existing literature for the calibration route to take depending on measurement geometry. If there is global z or r directional circulation due to the measurement geometry then a power number calibration approach is needed, if not an effective inner radius approach can be used to determine the effective viscometric properties of a material.. The effective inner radius is

a system dependent value that represents an inner diameter, as if the geometry were assumed to be a couette. In their work, the effective inner radius has been proven to be independent of the fluid rheology and rotation speed, remaining as a calibration constant.

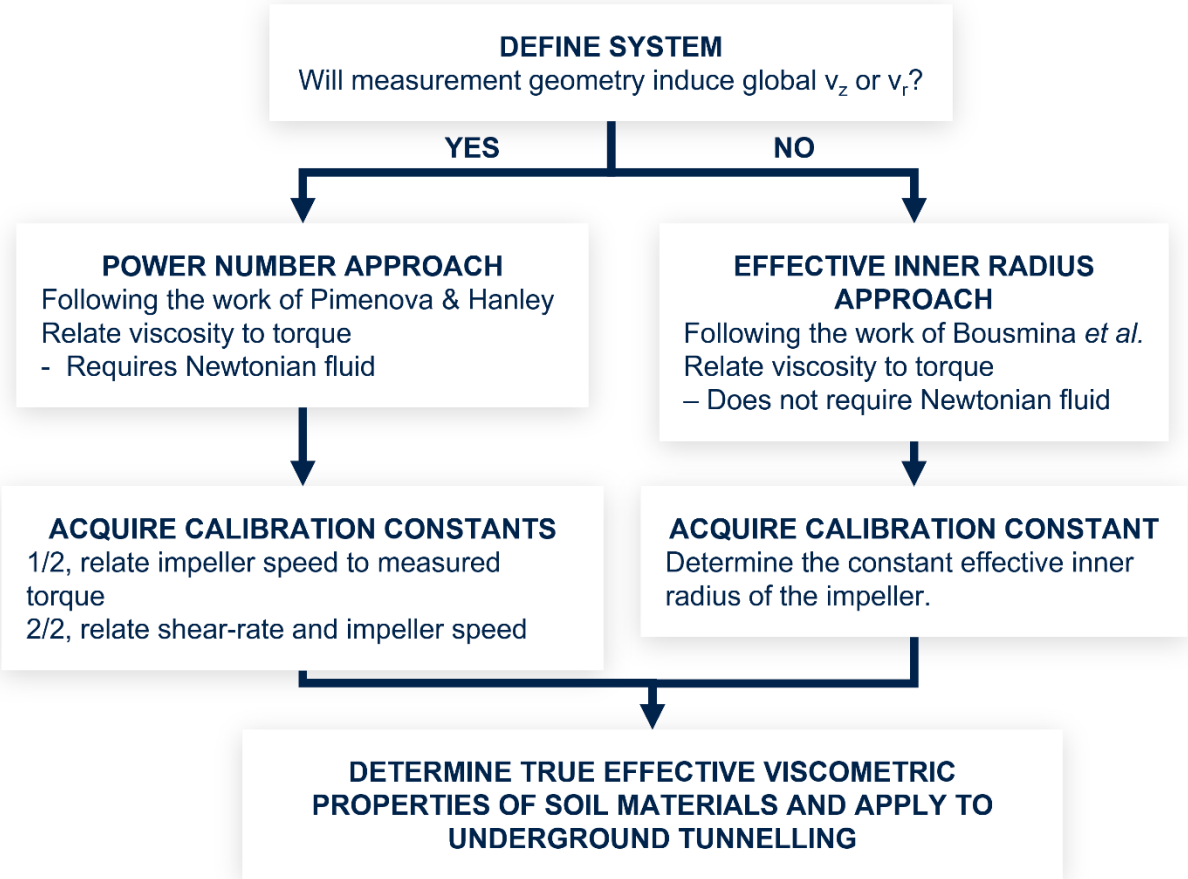

Figure 3.2. Decision tree from learned experiences and existing literature for the calibration route to take depending on measurement geometry. If there is global z or r directional circulation due to the measurement geometry then a power number calibration approach is needed, if not an effective inner radius approach can be used to determine the effective viscometric properties of a material.

Figure 3.2 summarizes the distinction between the two calibration procedures Effective Inner Radius and Power Number, developed by Bousmina *et al.*[95] and Pimenova & Hanley[124], respectively. Determine whether there is global axial flow in the system which will then determine the appropriate calibration approach, if axial flow then Pimenova & Hanley needs to be used and requires a Newtonian and non-Newtonian calibration fluid, if there is no axial flow then Bousmina can be used and requires only a non-Newtonian calibration fluid. P&H account for axial flow in their derivation whereas Bousmina does not. An additional caveat of the

Bousmina, effective inner radius procedure is that a thin-gap approximation needs to be reached. The thin-gap approximation states that the ratio of effective inner radius to the inner radius of the sample volume is greater than 0.85. This criterion is necessary to simplify the calculations and treat the non-Newtonian calibration fluid as a Newtonian fluid, otherwise a non-Newtonian fluid cannot be used to calibrate the setup. This often requires an iterative process in designing a measurement geometry and selecting a calibration fluid that will achieve the thin-gap approximation while sensing torque values appropriate for the transducers.

The effective inner radius calibration procedure requires determining the effective inner radius using a calibration fluid, either Newtonian or non-Newtonian, which will be characterized in a standard rheometer and compared against the torque and rotation rate data of the setup to be calibrated to calculate the effective inner radius calibration constant. Ri, the effective inner radius, will be used to relate torque to effective viscosity and rotation rate to effective shear rate. The calibration approach is independent of the rheology of the calibration fluid because with the thin-gap approximation, there lies a geometric point that has been theoretically shown to be independent of the fluid rheology[95]. This calibration procedure is the culmination of three different works. The basis of the procedure was developed by Goodrich & Porter[140] for polymer melts in a Brabender torque-rheometer. Bousmina *et al.* extended their work in a twin rotor batch mixer by using a non-Newtonian calibration fluid and justifying its accuracy[95]. And our work couples their procedure with a new measurement geometry without axial flow inspired by an impeller with angled flights developed for biomass by Klingenberg *et al*.[133].

3.3 Materials and Methods

The calibration procedure used is an effective inner radius approach, following the work of Bousmina *et al.* (1999)[95]. This work assumes that no matter the configuration of the measurement geometry, as long as there are no global flows, and the material is only deformed in the rotating direction of the measurement geometry then an effective inner radius is produced. An effective inner radius is assuming that whatever complex flow profile developed in the sample can be simplified to a cup and bob geometry where a bob at a constant radial size can be mathematically used to replace any complex measurement geometry to calculate the effective viscometric properties of complex fluids.

3.3.1 Setup

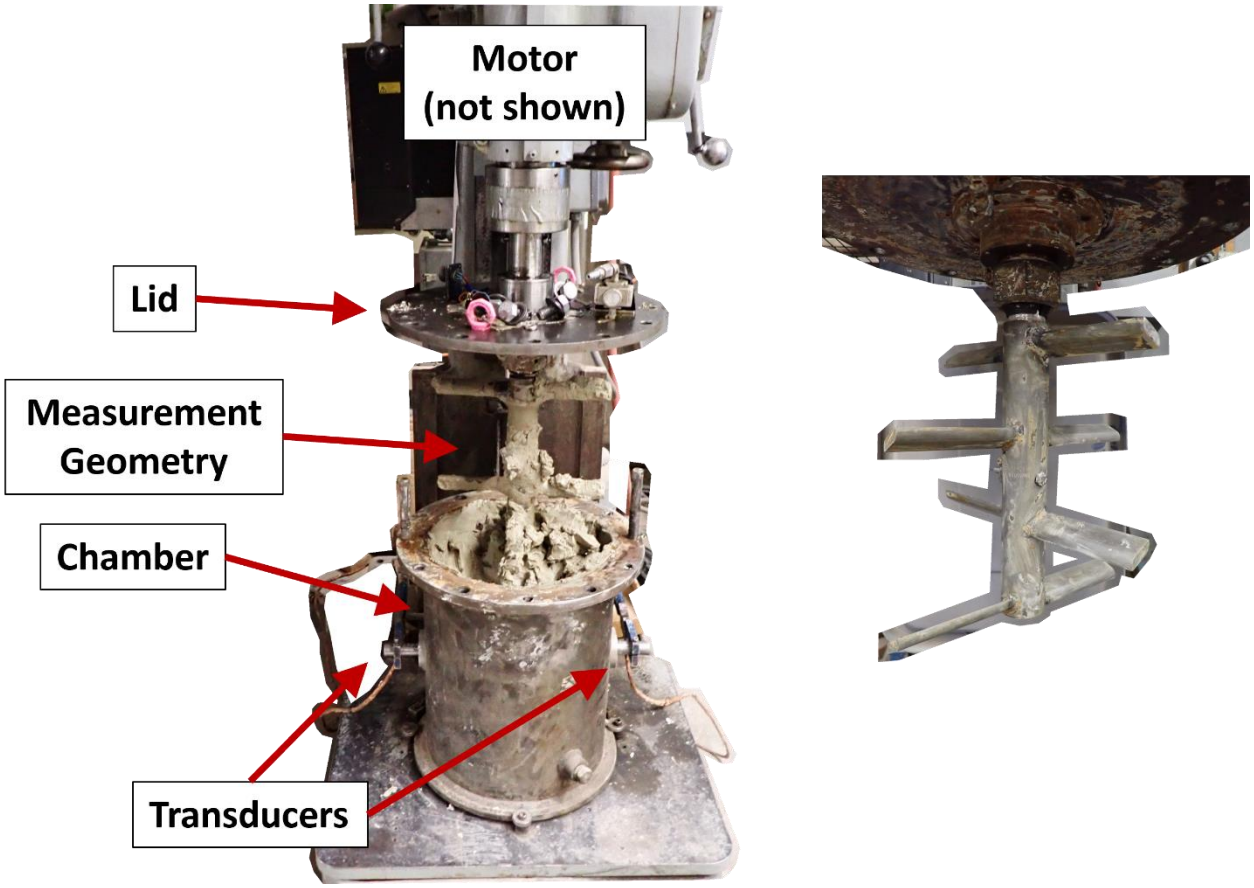

Figure 3.3. Soil viscometer setup, where an industrial drill press was modified into a rheometer by changing out the drill bit with a lid that the central shift sits inside of and exchangeable measurement geometries can be attached to, coupled with a sample chamber that sits on a low friction plate while two force transducers hold the chamber in place and measure the torque acting on the chamber from the sample of interest. The right hand images is the measurement geometry used with angled flights designed to measure samples with high solids content, yield stress, and viscosity.

The experimental setup is shown in Figure 3.3 where an industrial drill press has been modified into a viscometer for soil materials. In the left-side image, the shaft of the drill press has been converted to solely a shaft attached to a lid that can move up and down, rotate at a specified rotations per minute (RPM), and with pin holes to attach any desired measurement geometry of choice. The torque is measured by two force transducers attached to opposite sides of a sample chamber. The sample chamber sits on a low-friction plate, allowed to freely rotate but held stationary by the force transducers. The right-side images is the angled-flight geometry that was calibrated and used to measure the viscometric properties of soil materials. The design of the geometry is based on the work of Klingenberg *et al*. (2017)[133], where they were measuring high

solids content biomass ($15 - 20wt\%$) and wanted a geometry that would not jam from granular fibers and would also suspend the granular fibers. This design uses a 1 foot long, 1.5 inch schedule 80 pipe as the central shaft, and the angled flights are spaced 0.0973 meters apart across the length of the shaft. Each flight consists of two arms on opposite sides of the central shaft, and each flight is 45 degrees offset from one another so that they are equally spaced apart when viewed from above. The diameter from the tip of one arm to another is 0.2964 meters. Each arm is pitched at a 30 degree angle and made from 1 inch by 0.5 inch rectangular bar stock where the top corner of the lower side and the bottom edge of the higher side are rounded off. The bottom three flights of the geometry have the blades angled to push sample up and prevent settling, while the top flight pushes material down to prevent global fluid movement up and down. This geometry was also chosen to handle granular particle sizes and reduce jamming that could occur between the inner chamber walls and the outer geometry arms.

3.3.2 Calibration procedure

The effective inner radius approach is the calibration procedure of focus for this manuscript, as determined by the expected flow profiles of the measurement geometry. Our work then uses these developed procedures to apply to soil materials assuming a Bingham Plastic constitutive relationship[141].

The calibration procedure is taking the Bingham Plastic constitutive equation, Equation 3.1, and plugging it into the momentum balance using Navier-Stokes in the θ-direction, Equation 3.2.

$$\tau_{r\theta} = \tau_0 + \eta_{PL}\dot{\gamma}(r) \tag{3.1}$$
$$\tau_{r\theta} = \tau_0 + \eta_{PL}\left[\left|r\frac{\partial}{\partial r}\left(\frac{u_\theta}{r}\right)\right|\right]$$

$$\frac{\partial\left(\mathrm{r}^2(\tau_{\mathrm{r}\theta})\right)}{\partial \mathrm{r}} = 0 \tag{3.2}$$

From these two expressions, the velocity profile is solved for using Mathematica, yielding Equation 3.3.

$$u_\theta(r) = \left[\frac{2\eta_{PL}\omega + 2\tau_0 \ln\left[\frac{R_e}{R_i}\right]}{2\eta_{PL}\left[\frac{1}{R_e^2} - \frac{1}{R_i^2}\right]}\right] \cdot \left[\frac{r}{R_e^2} - \frac{1}{r}\right] + \frac{\tau_0 r}{\eta_{PL}} \ln\left[\frac{R_e}{r}\right] \tag{3.3}$$

The expression for torque is shown with Equation 3.4 and will be used to determine the effective inner radius calibration constant, R_i.

$$\Gamma = 2\pi R_i h \cdot R_i \cdot \tau_{r\theta}|_{r=R_i} = 2\pi R_i^2 h \cdot [\tau_0 + \eta_{PL}\dot{\gamma}] \tag{3.4}$$

Using torque and rotation rate from the mixer to be calibrated and experimental data of the Bingham Plastic parameters found on a TA Instruments DHR-3 rheometer, the calibration constant can be solved for. The Bingham Plastic model generates a geometric series when the velocity profile is solved for, and Matlab's geometric series function is used to determine the Ri value. Ri will be used as the measurement geometry's calibration constant and be used to solve for the effective shear-rate and viscosity measured in the soil viscometer, using Equations 3.5 and 3.6.

$$\eta_a(\dot{\gamma}) = \frac{\Gamma}{N} \frac{\left(\frac{R_e}{R_i}\right)^2 - 1}{8\pi^2 L R_e^2} \tag{3.5}$$

$$\dot{\gamma}_a(N) = \frac{2\pi N}{\ln\left(\frac{R_e}{R_i}\right)} \tag{3.6}$$

The viscosity and shear-rate both have a subscript "a" because these are both apparent values. Within the soil viscometer there is a complex flow field of radial and local axial flow that will result in multiple shear-rates locally, but this will average out into a bulk value because rotation rate is applied, and torque is measured across the whole sample. The particle size that can be measured by the system is constrained to granular material that does not approach the gap size, <0.1*(Re-Ri) . The calibration fluid of choice was bentonite clay because of its high viscosity and low cost.

In the power number calibration, a Newtonian calibration fluid is needed while the effective inner radius approach can be done with either a Newtonian or non-Newtonian fluid. And for our system chamber 10 gallons of fluid is necessary which would lead to prohibitive costs to obtain a fluid at a high enough viscosity and quantity. It was much more cost-effective to use bentonite clay as a calibration fluid for its high viscosities, and low cost.

3.4 Results and Discussion

3.4.1 Calibration results

Based on the effective inner radius calibration, torque data across a range of RPMs were collected in the Soil Viscometer and used to find the effective inner radius calibration constant. Using water the lower torque limit sensitivity of the Soil Viscometer was determined to be 5 N-m and based on the upper force transducer limits that measure torque the upper limit is 60 N-m.

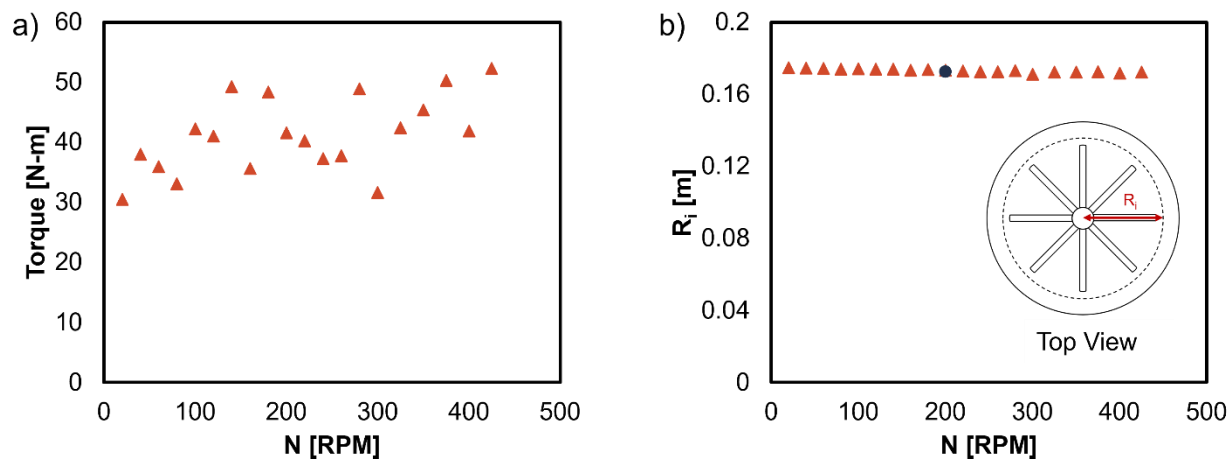

Figure 3.4. Calibration results for the angled-flight measurement geometry using a 16.7 wt% bentonite sample. a) includes the averaged data, in orange triangles, tracking torque at increments of rotations per minute (RPM). b) takes those torque values and calculates what the effective inner radius (R_i) would be at those operating conditions. From this dataset, an R_i value that minimizes the total average error is selected. This R_i value is then used to calculate how torque values should be varying with RPM and plotted as the black line in the left-hand panel and compared to the collected torque data.

Figure 3.4a is the torque data averaged over each 60 seconds for each RPM from the Soil Viscometer and the Bingham Plastic parameters from a TA Instruments DHR-3 rheometer are determined to evaluate the effective inner radius calibration constant that is then used to calculate torque and back compare against the collected torque data from the Soil Viscometer, based on Equations 3.1 and 3.4 using a 16.7 wt% bentonite sample. In Figure 3.4b, the effective inner radius is depicted, a geometric point beyond the radius of the measurement geometry. Each torque data point is collected by averaging the raw data at each RPM (50-400 RPM) once torque has reached steady-state over a minimum of 2 minute (Appendix A). This shows that R_i remains a steady value, which is desired for a calibration constant, but the corresponding torque values

are sensitive to small changes in R_i. The viscosity calculations match up nicely between the data collected on the DHR-3 and will be discussed next.

3.4.2 Soil viscometer evaluation

To check the efficacy of the calibration procedure, torque and RPM from the averaged Soil Viscometer measurements are converted to effective shear-rate and viscosity to compare against the steady-shear flow sweep in the DHR-3 of the same bentonite clay material.

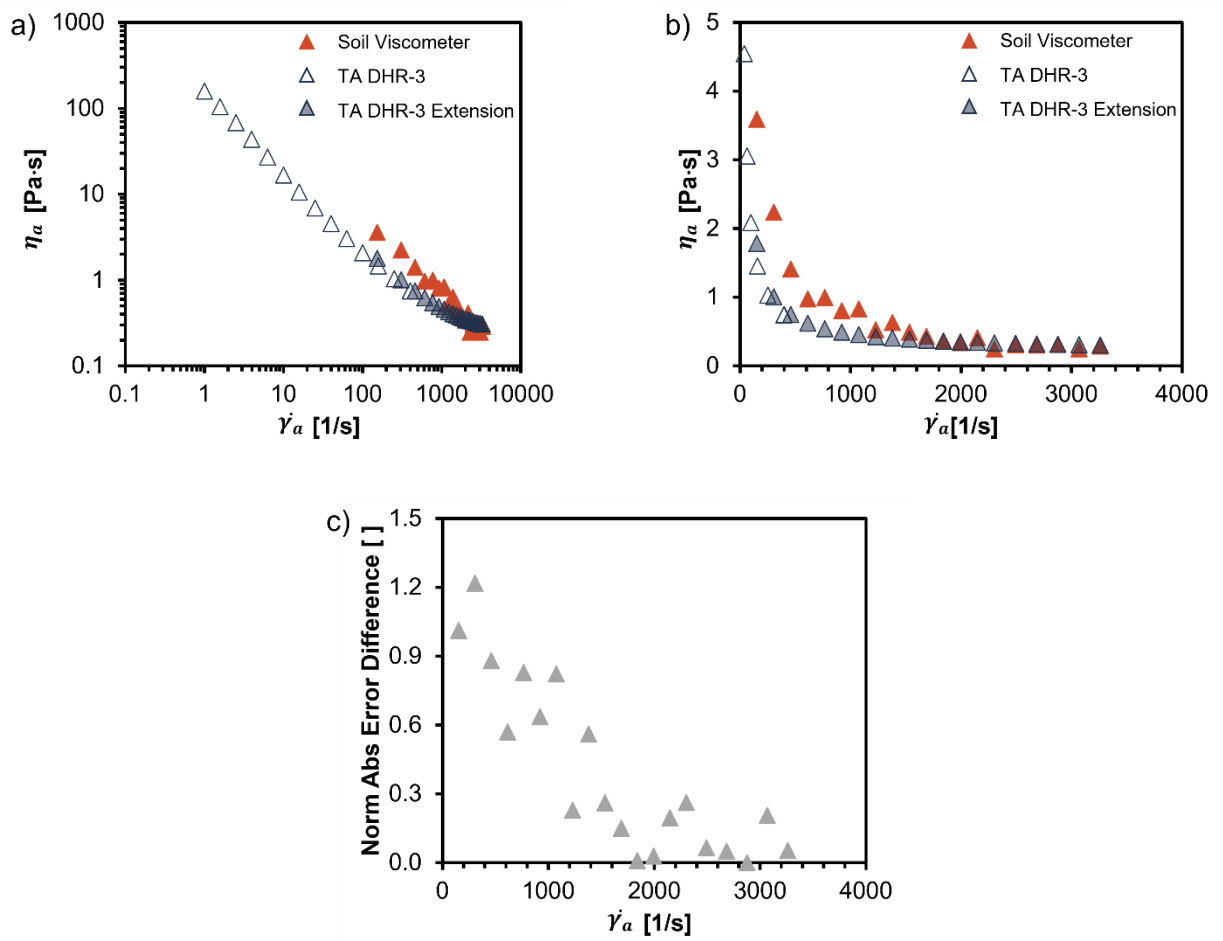

Figure 3.5. Using the calculated Ri value from Figure 3.4, the (a) averaged torque and RPM data can be converted into effective viscosity and effective shear-rate values and can be compared to the steady-shear flow curve collected of the same 16.7wt% bentonite sample on the DHR-3 rheometer. b) is the same flow curves as a) but on a linear plot. c) is the absolute difference normalized by the TA DHR-3 values between the Soil Viscometer and the TA DHR-3 data extended from an extrapolation of the collected data.

In Figure 3.5a, the dark blue triangles are the dataset collected by the DHR-3, with the open symbols directly collected data and the shaded in symbols fitting a Bingham Plastic model

to them and extending the data to cover the same shear-rate values measured in the Soil Viscometer. The orange triangles are data from the Soil Viscometer. At overlapping shear-rates the Soil Viscometer gives greater values than the DHR-3 but then more closely line up at higher shear-rates ($> 100\frac{1}{s}$). The difference in viscosity values between the Soil Viscometer and the DHR-3 is due to the logarithmic axis. Figure 3.5b, changes the figure to linear axis so that the differences between datasets can be more easily observed. These differences could be addressed in the future with more sensitive force transducers in the Soil Viscometer or higher viscosity materials to increase the data signal strength of the Soil Viscometer. Figure 3.5c looks more closely into the differences in viscosity values by evaluating the absolute difference normalized by the viscosity prediction from the DHR-3 data where at greater viscosities the viscosity values become more reliable. At shear-rates below 1400 1/s, the soil viscometer data difference is greater than double the value but at greater shear-rates the differences hover around 20% or below. With the size of the Soil Viscometer ($10\ gallons$) and moving parts, friction is expected to give more erroneous results at lower shear-rates due to lower sensitivities from smaller torque values and rotation rates less than a revolution a second which can increase internal friction from smaller lubrication forces within the motor. The main conclusion from Figure 3.5 is that measurements in the Soil Viscometer will skew towards higher viscosities than what's measured in more accurate instruments and measurements are more reliable at shear-rates greater than 1400 1/s.

3.5 Discussion

3.5.1 Soil material exploration

The value of the Soil Viscometer is its ability to characterize realistic soil materials with large particle sizes ($> 15.08\ mm$) and higher viscosities ($> 10^4\ Pa \cdot s$). Samples with greater bentonite content and suspensions of gravel in bentonite will be explored in this section to address the effects of low water content and particle volume fraction of particles ¾" in size at the smallest dimension, a first of its kind viscometric comparison.

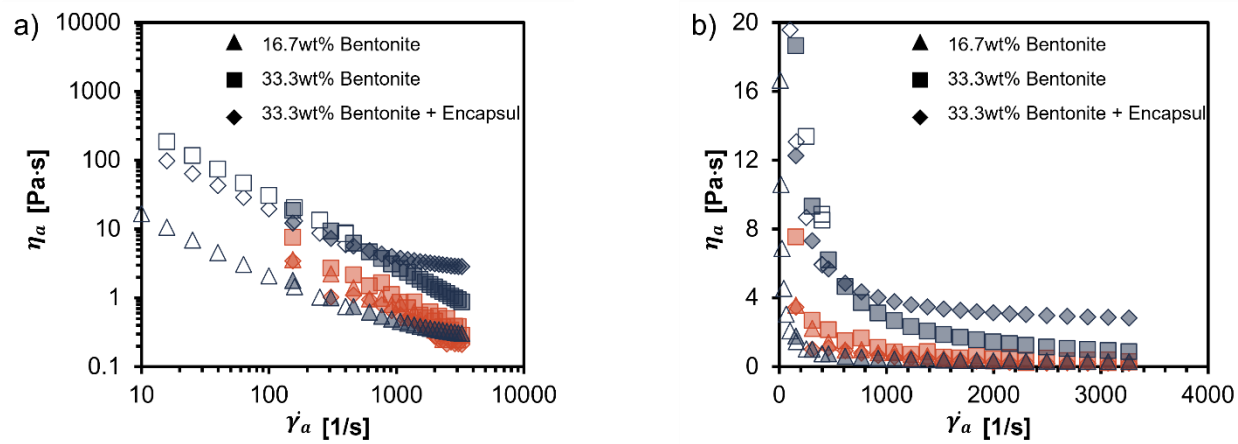

Figure 3.6. Realistic soil materials explored by the Soil Viscometer and the bench-top DHR-3 rheometer. Materials include the 16.7 wt% bentonite, 33.3 wt% bentonite, and the 33.3 wt% bentonite mixed with Encapsul, an industry material of biomass derived oil that improves the workability of clay materials. The data follows the same representation as Figure 3.5, open dark blue symbols are DHR-3 data, shaded blue symbols are DHR-3 data extended to greater shear-rate by fitting them with the Bingham Plastic constitutive equation, and orange data is from the Soil Viscometer. Each symbol shape represents the material characterized.

In Figure 3.6, two high viscosity samples were characterized by the Soil Viscometer, a 33.3 wt% bentonite sample and a 33.3 wt% bentonite with Encapsul as an additive. Encapsul is a well-known industrial additive that improves the workability of clay materials, it is an oil derived from biomass. In Figure 3.6, the coloring of the data symbols follows that of Figure 3.6 where open blue symbols is data collected by a TA Instruments DHR-3 rheometer, the shaded blue symbols are an extension of the rheometer data based on Bingham Plastic modelling of the available data, and the orange data is that collected from the Soil Viscometer. Each symbol represents the sample characterized, triangles are 16.7 wt% bentonite, squares are 33.3 wt% bentonite, and diamonds are 33.3 wt% bentonite with Encapsul. The data shows that the Soil Viscometer is measuring a lower viscosity for the two low water content bentonite samples, 33.3

wt%. A lower viscosity than that measured by the DHR-3 is because of the water content of that sample. At 33.3wt% water content, bentonite has transitioned to more of a plastic -like material that breaks and reforms rather than flow homogenously. The bentonite appears to transition from liquid to plastic behavior between 16.7 and 33.3 wt%, and the liquid limit lies between those two concentrations. Due to this behavior, rather than deforming uniformly, the material is pulled along in the open-space between the flights of the measurement geometry (Figure 3.3). Rather than measuring the viscosity of the sample, the frictional drag of the material is instead measured which will give a lower viscosity because only a small amount of material is being deformed and transferring the momentum between the measurement geometry to the sample and to the chamber wall.

The rheological properties of clay incorporated with Encapsul, a biomass based oil to reduce word needed to mix, has not been quantitatively characterized as a viscometric property until now. Purely looking at the DHR-3 data collected in Figure 3.6a, Figure 3.6b, and

Table 3.1 for the 33.3wt% bentonite with and without Encapsul, the additive results in a lower yield stress and higher plastic viscosity. This difference is best characterized by the difference in viscosity with shear-rate. Based on the Bingham Plastic equation, at low shear-rates yield stress will play a larger role in the material's viscosity, the 33.3wt% sample has a greater viscosity. But as the shear-rate increases the trends flip and the 33.3wt% bentonite with Encapsul has a greater viscosity after a shear-rate of 600 1/s. This subtlety is not captured by the Soil Viscometer which measures the 33.3wt% bentonite without additive as having a higher viscosity at all measured shear-rates. It appears that Encapsul is lowering viscosity at low shear-rates and affects the shear-thinning nature of the clay at high shear-rates, indicating that the clay interactions may have changed. But more thorough characterizations needs to be performed before that claim can be supported.

3.5.2 Soil material viscometric summary

To summarize the rheograms of the three soil samples, their respective Bingham parameters are presented in

Table 3.1 to quantitatively compare the differences in the steady-shear trends between the samples. Due to the poor fitting of the 33.3wt% Bentonite data, the Bingham Plastic parameters are not reliable to compare against the other data sets.

Table 3.1. A summary of the Bingham Plastic parameters for each soil same and compared between the Soil Viscometer (SV) and the TA Instruments DHR-3 (DHR) rheometer. These include η_{PL}, the viscous component; τ_0, the yield stress of the samples; and R^2, the coefficient od determination for fitting a Bingham Plastic model to the measured shear-stress-shear-rate data.

Method	η_{PL} [Pa·s]	τ_0 [Pa]	R^2
SV			
33.3 wt% Bentonite	0.02	992	0.01
33.3 wt% Bentonite + Encapsul	2.37	1518	1
16.7 wt% Bentonite	0.06	639	0.28
DHR			
33.3 wt% Bentonite	1.64	2860	0.94
33.3 wt% Bentonite + Encapsul	2.37	1518	0.89
16.7 wt% Bentonite	0.23	238	0.97

3.6 Conclusions

Breaking down soil material and removing the cuttings will be an ever present challenge in the underground drilling community. Soil materials have inherent challenges that state-of-the-art instrumentation cannot handle, high viscosities ($> 10^4\ Pa \cdot s$) and large particle sizes ($> 1\ mm$). Many instruments built to characterize soil materials have not been calibrated to measure true viscometric properties and instead act as index-type devices. We modified an existing calibration procedure and applied it to an industrial drill press turned viscometer to quantify low water content bentonite slurries with gravel, a model soil material with high viscosity and granular particles. The calibration procedure uses an Effective inner radius approach and a non-Newtonian calibration fluid of 16.7% bentonite slurry to obtain a calibration constant that produced similar results as a TA Instruments DHR-3 rheometer at high-shear rates ($> 100\frac{1}{s}$). While 16.7% bentonite slurry is low water content, in-situ clays can have lower still, and the material will behave plastic-like where it no longer deforms uniformly and retains a deformation history. This is seen as a lower viscosity compared to the predictions provided by data collected by the DHR-3 rheometer. The frictional

drag of the material is being measured rather than the material property. A soil viscometer has been calibrated, capable of measuring soil materials with viscosities and particle sizes unable to be measured in traditional shear rheometers.

3.7 Major Findings and Conclusions

The calibration of a new viscometer is a simple but detail oriented process that requires knowledge of the measurement geometry and material of interest to achieve a calibration capable of characterizing viscometric properties of future materials.

The upper limit of measurable viscometric properties of complex materials with large viscosities and particle sizes has been extended, and the viscometric characterization of clay materials need to be tailored to its application below a water content that results in plastic-like behavior.

CHAPTER 4 CHARACTERIZING THE NON-NEWTONIAN VISCOSITY OF HIGH-SOLIDS DRILLING-FLUID DISPERSIONS BY FLOW LOOP

Modified from a paper published in Physics of Fluids[5].

Jianger Yu (俞江迩)[6,7], Benjamin A. Appleby[6,7], Michael A. Mooney[8], and Joseph R. Samaniuk[6,9]

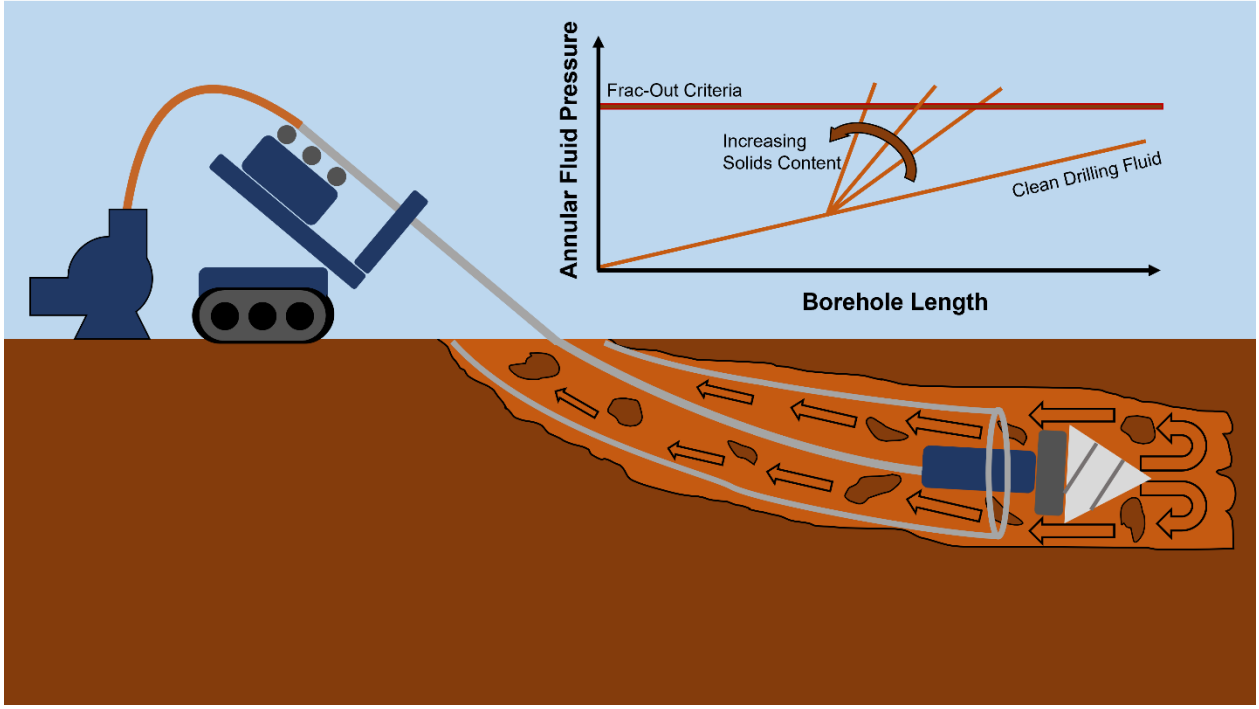

Figure 4.1 Illustration of soil cuttings being removed from a borehole and the potential effects they may have on drilling fluid pressures.

Pressure management of fluid in underground drilling is a critical piece of any drilling operation. Typically, mud engineers, trained specialists in identifying the effects of return drilling fluid cuttings on drilling progress. By evaluating the system operational parameters and drilling performance, they can determine how the drilling fluid needs to be modified to continue

---

[5] Reprinted with permission from Phys. Fluids. Yu, Jianger, Benjamin A. Appleby, Michael A. Mooney, and Joseph R. Samaniuk. "Characterizing the Non-Newtonian Viscosity of High-Solids Drilling Fluid Dispersions by Flow Loop." *Physics of Fluids* 34, no. 5 (May 2022): 053313. https://doi.org/10.1063/5.0083982.

[6] Post-Doctoral Researcher, Graduate Student and Associate Professor, respectively, Department of Chemical and Biological Engineering, Colorado School of Mines.

[7] Primary researcher and author.

[8] Professor, Department of Civil and Environmental Engineering, Colorado School of Mines.

[9] Graduate advisor, Author for correspondence.

progressing and hitting project metrics. They determine the composition of the drilling fluid, which can include mud content, polymer content, and other additives dependent on the expected geological conditions compared to what is observed. Ultimately, their job is a black box in terms of a fundamental physics understanding, built on passing information from one generation of engineer to another. To begin understanding that black box, rheological concepts can be applied to quantify the effects of solids content on the viscometric properties of drilling fluid slurries, which can include amount, type, and many more. Because knowing the relationship between solids content and viscometric properties will give operational engineers the theoretical tools to predict fluid pressures throughout the drill string (Figure 4.1).

At the time of this work there was limited rheological data on drilling fluid – soil cuttings slurries. Within the context of Fast HDD, these slurries will include mm-size particles operating at high flow rates where turbulence will be present, and the soil cuttings will be dispersed throughout the fluid. There is expansive literature on empirical correlations for polymer solutions under turbulent flow, relating flow speed and pressure drop in pipes to their power law parameters[142–145] but limited work applying these correlations to drilling fluid slurries[146–148]. Within the context of slurry pipe flows, two research areas have developed; hole cleaning of particles[149–152] and correlations relating non-Newtonian turbulent flow conditions to measured viscometric properties[142–145], but these two areas have not been combined into one. To the best of my knowledge there have not been studies that have focused on determining power-law parameters for particles dispersed in drilling mud.

In this work, we provide a methodology to determine the power-law parameters for sand dispersed in drilling mud and experimental data of those parameters across a wide range of solids content (30-49wt% from field test material, and 3-35wt% from lab synthesized material). Comparing these two data sets revealed that lab synthesized materials would yield drastically different pressure drop values across the same flow rates, showing that sand and clay fraction information alone cannot be used to model the soil cutting experienced during real drilling operations. We also learned that the fit quality of our power-law parameters depended on the dispersity of the sand particles in the slurry. The Shields parameter was useful in evaluating the transition from bifurcated flow with settled solids to fully suspended flow and determining the regime where the pressure drop and flow rate data would provide the best fits for the empirical correlations. This work provided an approach and experimental data to predict the downhole pressure drop of cuttings return to manage fluid pressures and reduce ground fracturing. The field

test drilling revealed that even knowing approximate fluid pressure is not enough to prevent ground fracturing when there is no recourse in lowering downhole fluid pressures.

4.1 Abstract

Increasing the speed of drilling operations is of commercial and military interest for transportation infrastructure as well as rapid installation of underground utilities in urban settings and over long distances. A significant challenge to increasing speed in horizontal directional drilling is pressure and flow rate management of drilling fluids circulating into and out of the borehole, removing solids cut free by the drill bit. The mixture of solids and drilling fluid results in a highly complex fluid suspension, typically with a shear-thinning continuum. It is challenging to characterize the viscometric behavior of these suspensions, and such data is limited in the literature. It is increasingly important to understand and accurately model the viscosity of these suspensions since high drilling speeds increase drilling fluid flow rate, approaching the pressure limits that borehole walls can withstand before failure. In this work we characterize the viscometric properties of a drill test and model drilling fluid suspension in a custom-built flow loop with solids concentrations up to 45 wt%. The fluid viscosity is reported in terms of power-law parameters, which can be used to predict pressure drop during real drilling conditions. We found a significant difference in viscometric response between the drill test and model drilling fluid suspensions. And Shields parameter can capture the influence of solids settling on the measurable pressure losses. An important conclusion is that even model drilling fluid suspensions prepared with geotechnical data from a drill site may have significantly different viscometric characteristics than those relevant during a drilling operation.

4.2 Introduction

This work focuses on the viscosity of cuttings returns required to make high-speed HDD possible. One major constraint to high-speed HDD is removing cuttings and excavating the formation at high speeds. Increasing ROP requires knowledge of drilling fluid viscosity before and after cuttings loading to predict the expected pressure drop of the system and ultimately fluid pumping speeds that can be utilized and preventing frac-out. Viscometric properties of the cuttings returns are a major factor influencing the pressures near the drill bit. To drill at higher speeds requires greater fluid pressure to match the drilling fluid flow rate with the removal rate of cuttings. Cuttings returns pressure will decrease as they flow back to the hole entrance due to

friction losses[153,154]. Pressure management and predicting fluid pressure from the viscometric properties of cuttings becomes vital in preventing fracture and fluid loss.

Solids concentration in cuttings returns will vary with the formation and the relationship between it and the effects of solids on cuttings returns viscosity is generally unknown. In practice, the concentration of solids is typically maintained within a window between 5 and 15 vol%, but fluctuates with changes in ROP, drilling resistances, and drilling fluid pressures[86,155]. At low solids concentrations the cuttings returns viscosity will be lower with higher drilling fluid flow rates and high pressures. At high solids concentrations the cuttings returns viscosity will be higher with lower drilling fluid flow rates and high pressures. A minimum in the pressure is obtained at a particular solids concentration for any given combination of drilling variables. Since cuttings returns pressure is a limiting factor in high-speed drilling applications, it is critical to understand what conditions will lead to this minimum pressure. A formidable challenge to identifying these conditions is in understanding the relationship between the cuttings returns viscosity and the solids concentration. Modeling the pressure vs flow rate relationship requires this understanding, but identifying flow properties of suspensions of clay, sand, silt, and rock under turbulent conditions has multiple challenges. First, conventional rheometers are generally inadequate for these measurements, where rapid settling of highly heterogeneous solids at high concentrations demands non-viscometric flows, and torque transducers with high limits[122]. Second, the complexity of particle size, shape, density, along with the inclusion of clay dispersions generally forbids application of theory derived from first principles for colloidal suspensions to date. Empirical measurements of cuttings returns viscosity to obtain these relationships is warranted in these instances, but there is extensive variability in formation composition in even a single drilling site that makes it difficult to know the applicability of any one measurement of cuttings returns viscosity on any given ground conditions.

A flow loop is a valuable tool to understand how high concentrations of solids influence the viscosity of cuttings returns and to extract apparent viscometric material functions under flow conditions similar to drilling operations. In underground drilling the complex fluid flows in an annular space, but material properties are independent of geometry so a flow loop with simple pipe flow is acceptable and simple to use, removing additional geometric influences that could add noise to the complex fluid characterization. A flow loop can also be used to identify

conditions of solids settling, and to understand the problems caused by settling on the experimental measurements. In general, turbulent flow of non-Newtonian fluids has been shown in the literature to be challenging to produce accurate and consistent results[144,145,156–158]. There have been multiple attempts to derive analytical, semi-theoretical, and empirical correlations for pressure and flow rate relationships, but wide variations exist when comparing between the many developed correlations[159], and the source of the variation is not well understood[143,158,160]. Various explanations for these variations have been suggested, including pipe roughness by Szilas[144]; assuming steady-state conditions rather than unsteady-state by Trinh[161]; and the effects of elasticity in emulsions by Werner[162]. The experimental approach described here can be used with any correlation relating pressure drop and flow rate developed for non-Newtonian fluids, although the focus is characterization of the shear thinning nature of cuttings returns.

In this work we describe the construction of a custom flow loop for measuring viscometric properties of high-solids concentration cuttings in a bentonite-based drilling fluid and use it to characterize viscometric properties. The validity of using measurements of viscometric properties of a "model cuttings returns sample" based on approximate formation composition of an actual drilling site are also investigated by comparing a model cuttings returns sample with actual cuttings returns obtained from a drill site. A power-law model[163,164] with solids-concentration dependent parameters is sufficient to characterize the viscometric properties. Clay suspensions have orders of magnitude smaller yield stress than the stresses originating from a plastic viscosity and shear rate term (Appendix B, Figure B.4 and Equation. B.1). Contributions of yield stress to the measured pressure loss at the flow rates used are small, making a power-law model sufficient rather than a more complicated model including a yield stress. Observations of solids settling in the flow loop agree well with theoretical analysis based on the dimensionless Shields parameter. Critical findings include that the viscosity of model cuttings returns samples cannot be trusted to represent real cuttings returns samples based on simple sand-to-kaolinite clay ratio approximations, and that fluidized solids regimes must be identified in flow loop measurement of these systems to properly report representative viscometric properties.

4.3 Materials and Methods

4.3.1 Material preparation & characterization

Two types of formation cuttings returns samples were prepared, one a lab-made model fluid and the other a field-test concentrate. Each sample required their own preparation procedures. The model fluid is made by mixing (1) C144 mason *sand* from Jones Fine Sand in Denver, CO (70% of sand greater than 0.4 mm, particle size distribution in Appendix B, Figures B.9 and B.10); (2) PONDSEAL-200 natural unaltered high swelling sodium *bentonite* from Redmond Minerals, Inc. in Grand Junction, CO; (3) ASP 600 hydrous aluminum silicate (*kaolinite*) from BASF Corporation in Charlotte, NC; and (4) tap *water*. These components will be referred to as sand, bentonite, kaolinite, and water. The model fluid was mixed based on expected formation cuttings returns with solid concentrations from 3 – 35 wt% composed of 3:1 sand to kaolinite clay based on geotechnical data from the expected drill site, and 3 wt% bentonite in water was the drilling fluid. 3 wt% bentonite will now be referred to as bentonite slurry. Clay is present as kaolinite and bentonite, kaolinite is found in the formation and bentonite is used as the drilling fluid. Table 4.1 details the composition of the model fluid for the various samples tested.

Table 4.1. Composition breakdown for the model cuttings returns samples.

Sample #	Water Mass (kg)	Bentonite Mass (kg)	Kaolinite Mass (kg)	Sand Mass (kg)	Total Mass (kg)	Solid Fraction (wt/wt)
1	211	6.53	0	0	218	0.03
2	211	6.53	3.38	13.5	234	0.10
3	211	6.53	6.30	25.2	250	0.15
4	211	6.53	9.45	37.8	265	0.20
5	211	6.53	13.1	52.2	283	0.25
6	211	6.53	16.7	66.6	301	0.30
7	211	6.53	21.6	86.4	326	0.35

The field-test concentrate was collected from horizontal directional drilling in Central Louisiana. The concentrate was collected with a 76 wt% solids content (solids weight, both

dispersed and settled, as a percent of the total sample weight) that includes sand, kaolinite, and bentonite. A notable difference between the model and field-test concentrate cuttings returns is that the drilling fluid used for the field test was an industry provided bentonite. Bentonite slurry was used to dilute the field-test concentrate, which is PONDSEAL-200, not the industry bentonite. Table 4.2 includes composition data for the cuttings returns samples prepared and tested from the field-test concentrate.

Table 4.2. Composition breakdown for the field-test cuttings returns samples prepared from the field-test concentrate.

Sample #	Water Mass (kg)	Bentonite Mass (kg)	Sand and Kaolinite Mass (kg)	total mass (kg)	Solid fraction (wt%/wt%)
8	106.62	2.40	100.38	209.40	0.49
9	129.32	3.10	100.38	232.80	0.44
10	159.52	4.05	100.38	263.95	0.40
11	197.32	5.25	100.38	302.95	0.35
12	250.22	6.90	100.38	357.50	0.30

Solids contents were measured by drying samples. Samples were mixed for 30 seconds and dispensed into 100 ml open-top containers in approximately 50 ml volumes. The mass of the samples was weighed before and after drying to obtain the measured solids concentrations. Drying was performed in a Thermo Scientific Gravity Convection Oven at 80°C over 48 h.

Density is a critical input in the correlations to determine the viscometric properties of our cuttings returns samples. Density was obtained by measuring the mass of known volumes using a 250 ml volumetric flask, and drying samples in an oven at 80°C overnight. The densities are highly correlated to the solids type and concentration.

Table 4.3 includes the densities of each cuttings returns sample tested.

Table 4.3. Density of each cuttings returns sample.

Sample #	Sample Type	Solids Fraction	Density (g/ml)
1	Model	0.03	1.018
2	Model	0.10	1.033
3	Model	0.15	1.042
4	Model	0.20	1.076
5	Model	0.25	1.114
6	Model	0.30	1.216
7	Model	0.35	1.343
8	Field-test Concentrate	0.49	1.445
9	Field-test Concentrate	0.44	1.387
10	Field-test Concentrate	0.40	1.330
11	Field-test Concentrate	0.35	1.279
12	Field-test Concentrate	0.30	1.230

4.3.2 Methods

Correlations are used to determine power-law parameters from the measured data of pressure drop and flow rate from the flow loop, and from density measurements. A flow loop was selected rather than a conventional rheometer because: (1) the cuttings returns samples contain large particles (e.g, sand, gravel) that exceed the measurement gap of conventional rheometers, (2) the flow loop mimics the actual drilling process with similar flow rates, pipe dimensions, and flow regimes (turbulent flow), while conventional rheometers are best suited for measurements under laminar flow.

The flow loop was designed and built to reach flow rates above 600 gallons-per-minute (0.038 m^3/s) in 4-inch schedule 40 PVC piping. The average shear-rates assuming a Newtonian parabolic profile spanned 98-367 s^{-1} for flow rates from 160-600 GPM. An illustration of the flow loop is shown in Figure 4.2. From left to right, the flow loop consists of a holding tank (8), open to atmosphere, which feeds a pump (1), controlled by a variable frequency drive dictating

the flow rate. The pump is a self-priming centrifugal pump from Gormon-Rupp, model T4A60S-B, with 4-inch suction and discharge, designed to handle up to 3-inch diameter solids. The electric motor is 3-phase, from Baldor, model ECP4110T, that can supply 40 HP and 1775 RPM. The variable frequency drive is from DURAPULSE, model GS3-2040. The pump circulates cuttings returns through the flow loop where pressure and flow rate are measured at the top (4, 5, 6, 7) by absolute and differential pressure transducers, and a doppler flow meter. The cuttings returns can be cycled in an open or closed loop configuration by either directing cuttings returns back to the holding tank (close valve 4, open valve 6), or bypassing the holding tank (close valve 6, open valve 4 & 5). A National Instruments data acquisition system takes in the flow rate and pressure data to catalog in unison. The schematic illustration is shown in Figure 4.2.

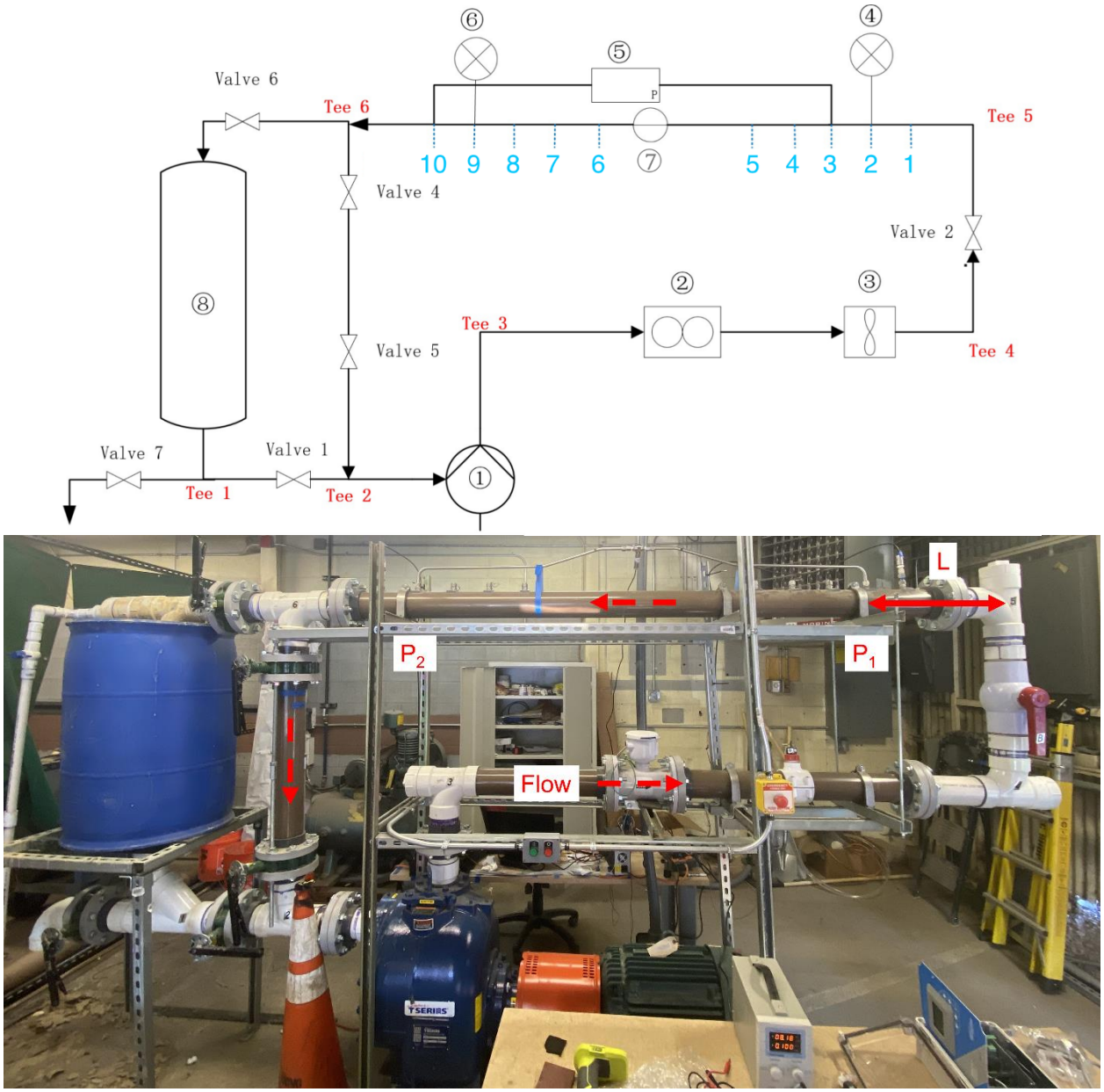

Figure 4.2. Schematic illustration and image of the flow loop. Sensor port locations indicated in blue are labeled 1 through 10 from right to left. Circled numbers indicate components: (1) Pump, (2) Electromagnetic Flow Meter, (3) Paddlewheel Flow Meter, (4) Absolute Pressure Transducer, (5) Differential Pressure Transducer, (6) Absolute Pressure Transducer, (7) Doppler Flow Sensor, (8) 187 Liter Reservoir. The flow loop is about 20 feet in width and uses a clear 4-inch schedule 40 PVC and capable of flow beyond 600 gallons per minute.

Detailed information of each sensor is included in Table 4.4. Due to the high solid concentration of the cuttings returns samples, neither the paddlewheel flow meter nor the electromagnetic flow meter provided reliable measurements, thus all flow rate data was obtained from the doppler flow meter and paddle wheel sensor was far upstream (~ 30 pipe diameters)

from the measurement section of the flow loop, as shown in Figure 4.3. Pressure loss data used in calculating fluid properties came from the differential pressure transducer rather than the absolute pressure transducers because of the superior resolution of the differential sensor.

Table 4.4. Sensor specifications include all pressure and flow rate sensors.

Sensor Type	**Sensor**	**Supplier**	**Range**	**Accuracy (Full Scale Range)**	**Output Signal**
Pressure	Absolute Pressure Transducer, Model PX409-050GV	Omega Engineering Inc.	0–344 kPa	±0.25% ±.86 kPa	Voltage 0–5 VDC
Pressure	Differential Pressure Transducer, Model PX409-001DWUV	Omega Engineering Inc.	0–6.9 kPa	±0.08% ±5.5E-3 kPa	Digital
Volumetric Flow	Doppler Flow Meter, DFM 6.1	Greyline	0–12 m/s (0–0.099 m^3/s)	±2% ±2.0E-3 m^3/s	Voltage 0–5 VDC

Measurements of flow rate and pressure were performed along the highest horizontal section of the flow loop. The upstream 90°-bend leading into this section, labeled "Tee 5" in Figure 4.2, introduces eddies in the flow that propagate downstream and potentially influence pressure measurements[165–169]. Such flow disturbances, or "pipe swirl", decay with distance, and it is important to understand the effect on measured pressure as a function of distance from Tee 5. Multiple sensor ports were installed downstream of Tee 5 where pressure sensor connections can be made to measure the influence of pipe swirl. Pressure loss measurements with the differential pressure sensor ($\Delta P = P_1 - P_2$) were made at 5 different upstream sensor port locations (the downstream port location, Port#10, was held constant) for six different flow rates of water at approximately 25°C measured with an infrared temperature sensor. Results of those measurements are shown in Figure 4.3. The pressure differential measured is normalized by the distance between the upstream and downstream ports and is plotted as a function of the normalized distance of the upstream port from Tee 5. The distance is normalized by the pipe

inner diameter, and the zero position is taken as the center of the vertical section of pipe between Tee 4 and Tee 5. Error bars show a single standard deviation on triplicate measurements. Port #1 and #2 correspond to L/D distances from Tee 5 of 3.9 and 5.3, respectively, and results from those ports differ considerably from results obtained from the three ports further downstream, suggesting the influence of pipe swirl on the measurements. Port #3, with an L/D of 7, provides pressure loss values similar to those from Ports #4 and #5 within the error, suggesting that this is sufficiently far enough downstream to avoid measurable interference from upstream eddies through at least a flow rate of 0.034 m^3/s (540 GPM). Port #3 was chosen for experiments based on these results and the need to maximize the distance between upstream and downstream pressure measurement locations to maximize measurement resolution. The distance between Port #3 and Port #10, the two connections of the differential transducer, was 1.89 meters.

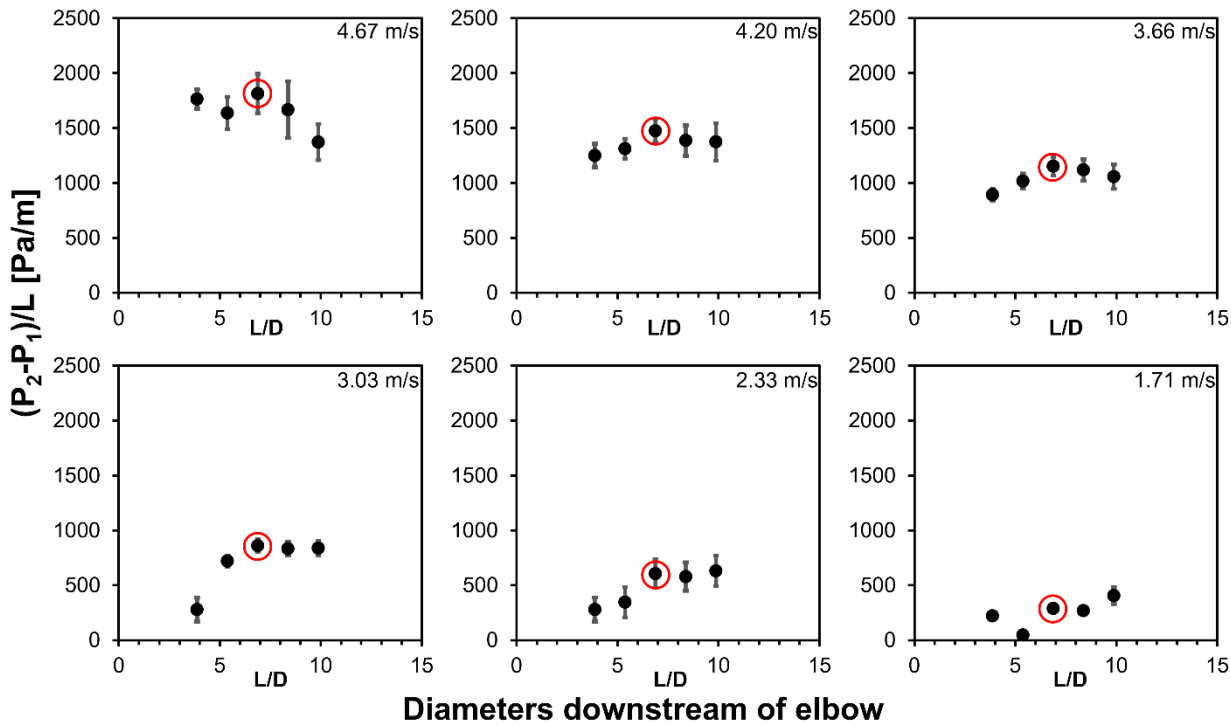

Figure 4.3. Differential pressure transducer position placement. The distance, L, away from the elbow were tested while maintaining constant length between the pressure transducer were tested at a range of flow rates to determine a pressure transducer position that would be minimally affected by turbulence from the elbow.

4.3.3 Viscometric characterization

The cuttings returns samples are generally considered as non-Newtonian fluids, so the power law model was selected to describe their viscometric behavior. The power law model can be written as:

$$\eta = m(\dot{\gamma})^{n-1} \tag{4.1}$$

where $\dot{\gamma}$ is shear rate, η is viscosity, and n and m are power law indices that depend on the viscometric properties of the fluid. n is the dimensionless flow behavior index that equals 1 for Newtonian fluid, $n<1$ for shear-thinning fluid, and $n>1$ for shear thickening fluid. m is the flow consistency index that can range from 0.001 for water and beyond 10^6 for malleable bentonite clays with water content beyond their liquid limit (the unit of m depends on the value of n).

Determining these power law indices, and how they vary with increasing solids concentration in drilling fluid samples, is the primary objective of these flow loop measurements. To achieve this objective, three parameters need to be measured: (1) the density of drilling fluids with various cuttings returns concentrations, (2) the average velocity (or flow rate) of the flow, and (3) the pressure drop when the drilling fluids flow through a section of straight pipe.

The flow rate and the pressure drop can be used to obtain the friction factor, f, using[170,171]:

$$f = \frac{1}{4}\left(\frac{D}{L}\right)\left(\frac{\Delta P}{\frac{1}{2}\rho <v>^2}\right) \tag{4.2}$$

D is the pipe diameter and dP is the pressure drop, ΔP, over the length of the pipe section, L, that drilling fluids flow through (in the flow loop system, it is the distance between the pressure transducers). ρ is the density of fluid, and v is the average velocity, which can be calculated from the flow rate.

Another important parameter is the Reynolds number (Re) of the flow. Since the fluids are non-Newtonian, the expression for Re is[143]:

$$Re = \frac{D^n v^{2-n}\rho}{8^{n-1}m}\left(\frac{4n}{1+3n}\right)^n \tag{4.3}$$

where ρ is the density of fluid, v is the average fluid velocity, and n and m are the power law indices in Equation 4.3.

Based on Equations 4.2 and 4.3, a relation between the friction factor and Reynolds number is required to determine *n* and *m* from the flow loop tests. For laminar flow, the relation is[159]:

$$f = \frac{16}{Re} \tag{4.4}$$

There are many models that describe the relationship between the friction factor and power law indices for turbulent flow of a power law fluid. Many of these models can be found in reference[159]. In this study, two classic models were used: the Dodge & Metzner model, and the Bobok, Navratil, and Szilas (BNS) model[144]. Of the many empirical correlations relating pressure drop and flow rate to fluid power-law parameters, the Dodge & Metzner model is the first, and the most classical model used for describing a power-law fluid in turbulent flow, and the BNS model has been shown to be one of the most accurate[142]. Despite the highly non-linear nature of both, they are a readily fit to data with non-linear regression algorithms. The Dodge & Metzner model can be written as:

$$\frac{1}{\sqrt{f}} = \frac{4}{n^{0.75}} \log_{10}\left[Re \cdot (4f)^{1-\frac{n}{2}}\right] - \frac{0.4}{n^{1.2}} \tag{4.5}$$

The BNS model is analytically-deduced for non-Newtonian fluids[144], and can be written as:

$$\frac{1}{\sqrt{f}} = \frac{4}{n} \log_{10}\left[Re \cdot (4f)^{1-n/2}\right] + 1.51^{n/2}\left(4.24 + \frac{1.414}{n}\right) - \frac{8.03}{n} - 2.114 \tag{4.6}$$

In this work all flow was turbulent during testing, thus Equations 4.2, 4.3, 4.5 and 4.6 were applicable. Once the flow rate and pressure drop data were obtained, the power-law indices (*n*) and (*m*) were calculated from the non-linear equation system above. The non-linear regression was performed with a custom Python script. The code is included in Appendix B.4.

4.4 Results and Discussion

4.4.1 Comparison between model and field-test cuttings returns samples

There are notable viscometric differences between the model and field-test cuttings returns. In Figure 4.4 the model cuttings returns and the field-test cuttings returns data are plotted as normalized pressure drop vs flow velocity for direct comparison. Field-test cuttings returns yield a significantly higher pressure drop compared to the model cuttings returns at the same flow speed and solids concentration. Although the density for both types of cuttings returns

samples are similar at each concentration, the components (kaolinite clay, bentonite clay, sand, silt, etc.) originated from different sources and will have subtle, but significant differences in particle size, chemistry, and composition that can yield measurable differences in viscometric properties. This is captured in the data in Table 4.5 where the consistency index, *m*, of the field-test cuttings returns are significantly higher than the model cuttings returns samples. It has been well established in the literature that subtle differences in electrolyte content, pH, exchangeable cations, and clay composition can account for this offset in pressure drop values related to a difference in the consistency index[18,139]. Even though these variations are well known, the characterization of these differences are seldom reported along with their respective power-law parameters. Since clay platelet interactions are known to exhibit wide variations in viscometric properties, we suspect that the bentonite clay variation in our model and field-test cuttings returns and the differences in sand particle size distribution are responsible for the differences between the two trends in Figure 4.4. The particle size distribution of the sand between samples indicates that the field-test cuttings are finer than the model cuttings (Appendix B, Figures B.9 and B.10). It is also known in literature that particle size distribution can affect the pressure drop in pipe flow[149]. The two cuttings returns samples are also both heterogeneous mixtures of sand and dispersed clay, so individually or together mineralogy and particle size distribution is the root cause rather than clay agglomeration. Powder X-ray diffraction (XRD) confirms the mineralogy differences between the two bentonite clays, indicating that silica oxide is the major compound in the two cuttings returns bentonite clay fluid, but it exists as different SiO_2-polymorphs between the two fluids (SI 7 & SI 8). The field-test cuttings contains an abundant amount of cristobalite in addition to quartz which is the dominant SiO_2-polymorph in the model cuttings sample. Cristobalite is known to form crystals < 2μm that has the potential to affect gel formation and alter the viscosity of the bentonite dispersions[138]. The field-test cuttings returns bentonite clay fluid also contains additional silicate minerals not found in the model cuttings returns (Appendix B, Figures B.7 and B.8). The difference in bentonite originates from the industry bentonite used during the field test drilling compared to the bentonite used for model cuttings returns.

The trendline seen in Figure 4.4 is for turbulent pipe flow of water, using a Newtonian expression[171]. The model cuttings returns align closely with the trendline. The steady-shear flow sweep data of the continuum bentonite clay fluid between each sample further supports the assertion that mineralogy between the two samples could be one cause for this offset in pressure drop values across the same flow rate. The industry bentonite clay fluid of the field-test sample had multiple orders of magnitude greater viscosity than the model bentonite clay fluid across the same flow sweep from 1 – 200 1/s characterized in a cup and bob geometry on a TA Instruments DHR-3 rheometer (Appendix B, Figure B.1 and B.4).

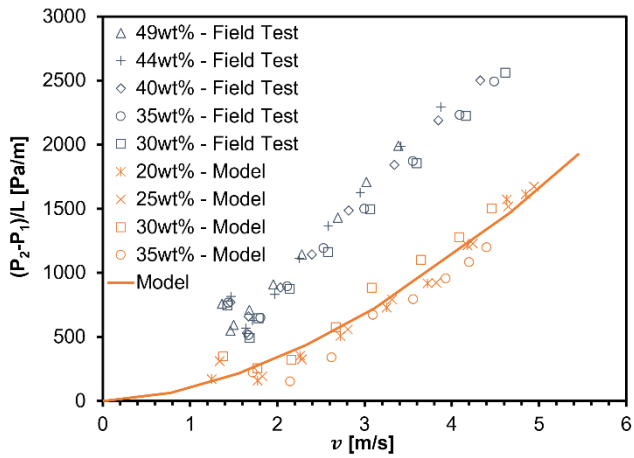

Figure 4.4. Comparison of pressure drop vs velocity for model and field-test cuttings returns samples. The trendline is based on tap water without any cuttings.

The model cuttings returns samples were prepared with geotechnical data from the drilling site suggesting a composition of sand and kaolinite of approximately 70:30 mass ratio, so the conclusion of Figure 4.4 is that only knowledge of sand and kaolinite ratios is insufficient to model viscometric behavior of cuttings returns in practice.

4.4.2 Flow and Pressure Drop Results

Flow rate and pressure drop are needed in the empirical correlations, and were measured in the cuttings returns samples at flow rates from 3.97 m/s to 4.53 m/s. Figure 4.6 presents the results of the flow loop experiments for the model cuttings returns samples, and Figure 4.6 presents the results of the flow loop experiments for the cuttings returns samples obtained from field-test drilling.

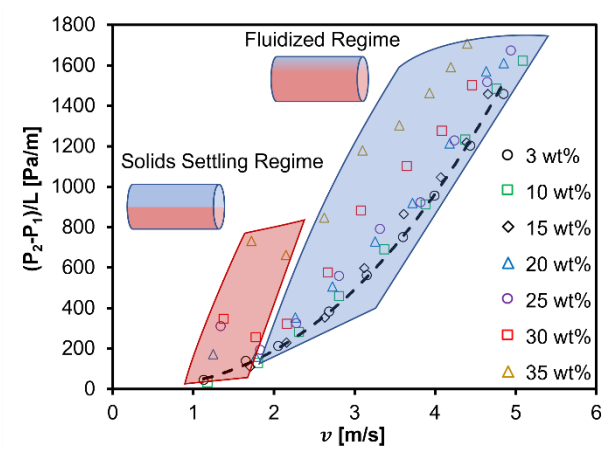

Figure 4.5. Experimental values of pressure drop and flow rate for model cuttings returns samples. The red highlighted region illustrates regimes where observable solids settling occurred.

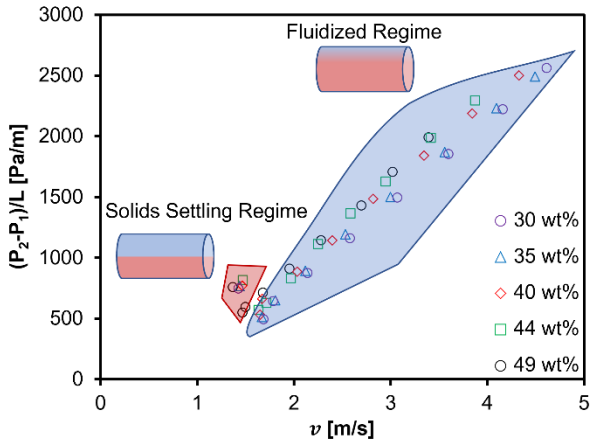

Figure 4.6. Experimental pressure drop and flow rate data for each cuttings returns sample from field-test solids concentrate. The red highlighted region illustrates regimes where observable solids settling occurred.

Higher flow rate and larger solids fractions result in larger pressure drops in the fluidized regime where flow rates are greater than 1.7 m/s and 2.6 m/s for the field-test cuttings returns and the model cuttings returns, respectively. In Figure 4.6 and Figure 4.6 there is a minimum in the pressure drop data for solids fractions above 20 wt% that occurs at approximately 1.7 m/s. In this region of flow, extensive settling of solids within the pipe occurred and significantly reduced the cross-sectional area available to flow. With increasing flow rate above 1.7 m/s, settled solids were increasingly entrained in the flow and the cross-sectional area of flow increased. This minimum in the data is evident for all solids fractions, but with greater solids fraction the minimum shifts to the right, to higher flow velocities, where greater flow rate is needed to suspend cuttings returns with more solids content. No minimum is seen in Figure 4.6 in samples

1-3 where solids content was less than 15 wt%. Figure 4.7 contains an image showing visible solids settling in the 35 wt% model fluid sample (#7) during flow loop operation at a flow velocity of 1.73 m/s. The light gray is the flowing fluid in the upper part of the horizontal pipe, while the darker bottom part of the pipe contains settled solids.

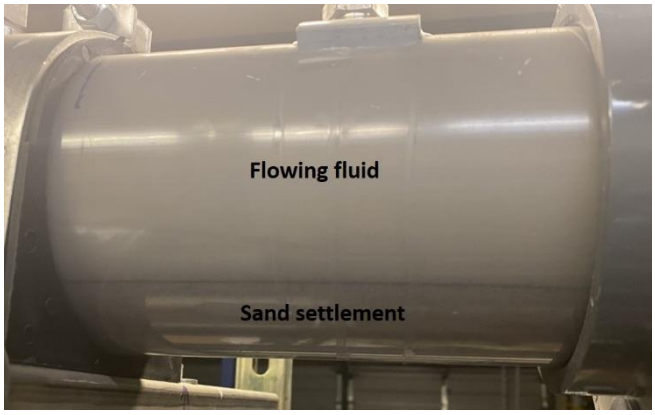

Figure 4.7. Image of flowing fluid (light grey, upper part) over settled solids (dark grey, lower part) during flow loop testing. The fluid contained 35 wt% solids, and was at an average velocity of 1.73 m/s.

In Figure 4.8 all data for the model and field-test concentrate cuttings returns is included and plotted as the dimensionless Shields parameter as a function of flow velocity[172,173]. Shields parameter is a ratio between wall shear stress and buoyancy forces, the magnitude indicating the tendency for solids to suspend in a flow or settle. In Equation 4.7, Shields parameter (θ) is expressed as the ratio between the wall shear stress and the stress caused by settling. Pressure drop is converted to wall shear stress by Equation 4.8.

$$\theta = \frac{\tau_w}{gd(\rho_s - \rho_f)} \tag{4.7}$$

$$\tau_w = \frac{\Delta P \cdot d_p}{4L} \tag{4.8}$$

When the Shields parameter is below 1 the driving stresses from gravitational settling dominate, and above 1 the flow stresses leading to solid suspension are dominant. At low flow rates the effects of settling are seen in the local minimum in pressure drop and can also be visually observed. Based on this analysis, all power-law parameter estimations were be done with data above a flow rate of 1.7 m/s for the field-test concentrate and 2.6 m/s for the model cuttings returns to minimize the influence of solids settling on the correlation fits to the data.

Two important conclusions result from this analysis of Shields parameter and settling observations during flow loop measurements. The first is that a delineating line represented by a Shields parameter of 1 can be used to identify regimes of flow where viscometric modeling of fully suspended flow can be relied on to provide pressure drop calculations, and where solids settling and flow partitioning prohibits the use of those models. The second conclusion is that observations of settling in flow loops can be reliably connected to settling dynamics through the Shields parameter in such a way that flow regimes that lead to solids-settling (and thus plugging concerns during drilling) can be empirically identified.

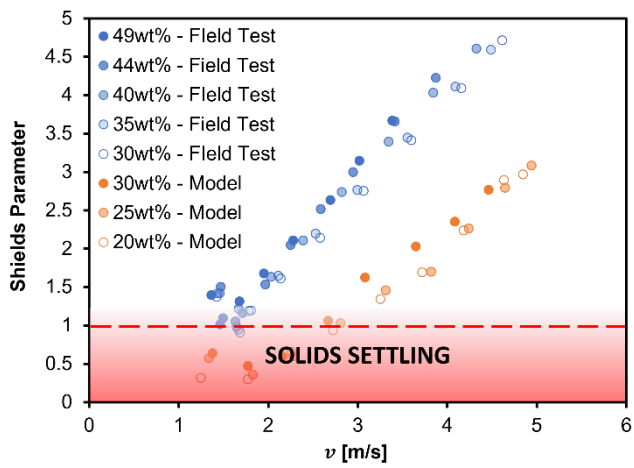

Figure 4.8. Shields Parameter Analysis. The pressure drop data collected from the flow loop is converted to Shields parameter using Equation 4.7 and Equation 4.8.

4.4.3 Power law indices analysis

By first determining cuttings returns sample densities and the applicable pressure drop and flow rate data, power-law indices can now be determined with empirical correlations. The applicable pressure drop – flow rate data was determined by the Shields parameter analysis to identify a regime where solids settling is no longer dominate, at flow rates greater than 1.7 m/s and 2.6 m/s for the field-test cuttings returns and the model cuttings returns, respectively. If we were interested in the settled/partially settled regime, the extent of settling could be used to semi-quantitatively characterize the weight percent of solids suspended under each flow condition. By employing Equations 4.2, 4.3, 4.5, and 4.6, a nonlinear equation system with “n” and “m” as the unknown parameters, can be developed. An in-house nonlinear equation solver programmed in Python is used to determine power-law and consistency indices that are shear-thinning and increase in viscosity with solids content.

Using the nonlinear solver, “n” and “m” values for each cuttings returns sample are presented in Table 4.5. In the model cuttings returns sample, *n* decreases with increasing solids fraction indicating greater shear-thinning behavior with greater solids content. The 3 wt% model fluid sample (#1), which is pure bentonite in water at a concentration of 3 wt% has a *n* value of 0.99, indicating near Newtonian behavior. With increasing solids fraction the value of *n* decreased incrementally to a value of 0.41 for the 35 wt% model fluid sample (#7), indicating increasingly shear-thinning behavior as would be expected for a particulate suspension. In the field-test cuttings returns samples there was no obvious trend in power-law index with solids fraction. Shear-thinning is still present in these samples, with *n* values in the range of 0.55 to 0.75. The model cuttings returns samples tended to have a smaller value of *n* at a given solids concentration, potentially because of differences in particle size, clay concentration, and type of clay between the field-test concentrate and the model cuttings returns, although the exact reason for this is unknown.

The *n* values obtained by the Dodge & Metzner and BNS models match closely, but values of *m* differed more. The *m* values from the BNS correlation are larger than from the Dodge & Metzner correlation. The expectation is that the value of *m* increases as the solid concentration increases, but this was not always the case for the field-test concentrate cuttings returns samples. The reason for this is still unclear, although the highly non-linear nature of both correlations means that fitting the correlation to the data can yield multiple solution values for *n* and *m*.

Table 4.5. Power law indices of each cuttings returns sample obtained from non-linear regression and using constraints from conventional rheometer data.

Sample #	D & M n	D & M m	BNS n	BNS m
1	0.99	0.0006	0.97	0.0008
2	0.78	0.0132	0.74	0.0272
3	0.98	0.0009	0.96	0.0011
4	0.91	0.0029	0.84	0.0080
5	0.84	0.0100	0.81	0.0180
6	0.51	0.4355	0.47	1.8470
7	0.41	2.1342	0.44	2.4496
8	0.65	0.7704	0.65	1.0311
9	0.74	0.3402	0.74	0.4026
10	0.54	2.3015	0.54	4.0956
11	0.57	1.5926	0.57	2.5542
12	0.56	1.7236	0.56	2.8533

To assess the validity of the calculated *n* and *m* indices they are then used to recreate the pressure drop and flow rate curves seen in Figure 4.6 and Figure 4.6. Figure 4.10 and Figure 4.10 include the predictions by the Dodge & Metzner and BNS models overlaid on the experimental data. The pressure drop vs flow velocity curves match the experimental data well, especially at high flow velocities. The power law indices estimated from the data can be used to calculate the expected pressure drop for the drill string at data points with Shields parameter values greater than one.

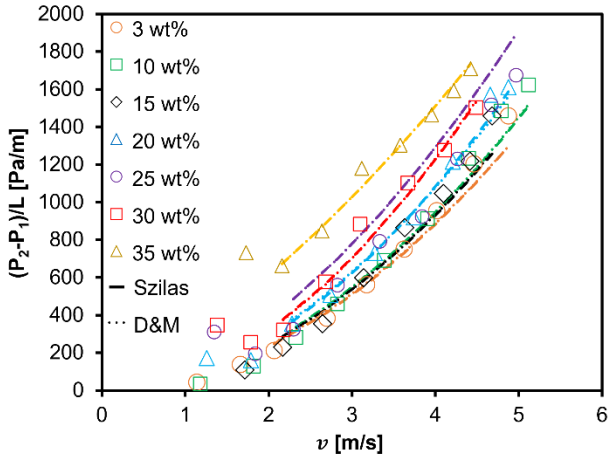

Figure 4.9. Projected pressure drop – velocity curve with the BNS and Dodge & Metzner model based on the experimental data for the model fluid, samples 1-7. Data points are the experimental data, dashed lines are the BNS model, and dotted lines are the Dodge & Metzner model.

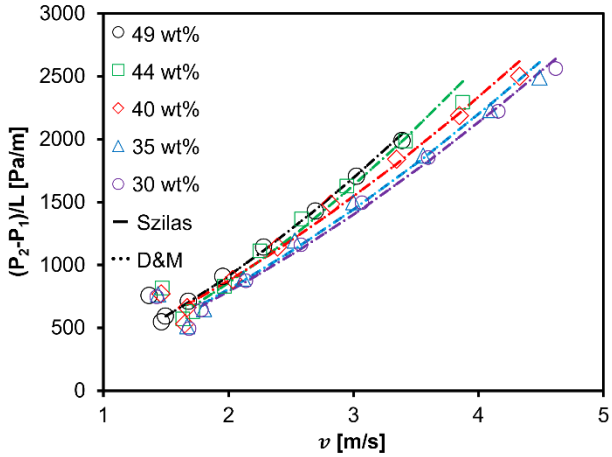

Figure 4.10. Projected pressure drop – velocity curve with the BNS and Dodge & Metzner model based on the experimental data for the field-test concentrate, samples 8-12. Data points are the experimental data, dashed lines are the BNS model, and dotted lines are the Dodge & Metzner model.

Pressure drop data from drilling pipes have been used for over a decade to parameterize hole cleaning and quantify drilling fluid viscosity under in-situ temperature and pressure conditions[146,148,174]. Flow loops have also been used to explore the major parameters driving hole-cleaning[149–152] but both hole-cleaning and characterizing cuttings returns viscosity has not been done together. Hole cleaning studies are typically fundamental and attempt to understand the drivers behind dispersion and movement of granular material[175–177]. It is also well known that granular materials affect the overall viscosity of the complex fluid as seen in variations of pressure drop when they are included in flow[149], but the viscometric characterization of these

complex fluids with dispersion is either left out or smeared by the addition of concentric or eccentric pipes that contribute to the pressure drop[174,178,179]. This paper provides an experimental approach to characterize the fluid properties of drilling fluids with solids. This work is focused on particles fully dispersed in the drilling fluid but can be extended to determine the power-law parameters of complex fluids with partially suspended particles or bed formation. Power-law parameters are sufficient to describe the viscometric properties of the fluid because the effects of yield stress to pressure drop of the bentonite clay fluid was found to be negligible (Appendix B.1). Mixer-type rheometers have also been used to characterize dispersion viscosity[178], but they often ignore the extent of solids settling and would need to introduce additional flow streams to suspend solids that would require a calibration procedure not currently done[124].

4.5 Conclusions

Viscometric characterization of drilling fluids containing solids in concentrations ranging from 3 wt% to 45 wt% was performed in a custom flow loop apparatus. Measurements of pressure loss as a function of flow rate were performed on two different materials: a model cuttings returns material prepared from sand, kaolinite, bentonite, and water, in ratios intended to approximate the formation conditions at a drill site, and a material comprised of drilling fluid and solids collected from drill tests at the drill site. Two different correlations relating friction factors to flow rate for power-law fluids in turbulent flow were fit to the flow loop data to obtain estimates of power law parameters. The results indicate that a power law constitutive model is suitable for the materials. Increasing solids content led to a decrease in the power-law index n, and an increase in the consistency index, m, indicating an increase in both viscosity and shear thinning behavior. The data provides a relationship between power-law parameters and solids concentration that is not present in the literature, but which is critical for use in computational modeling of pressure losses during drilling. A surprising result was the significant difference in pressure loss values between the model material and the material collected at the drill site, approximately a factor of two difference. Considering the limited data available on such materials, an important finding is that a model cuttings returns material prepared with a simple sand-to-kaolinite clay ratio from geotechnical data from a particular drill site cannot be trusted in experiments to provide representative viscometric parameters of materials encountered in field testing. A second important finding was the observation that the Shields parameter, a ratio of viscous stresses to gravitational stresses, was consistent with pressure loss measurements that

indicated a transition at particular flow rates from fully suspended, homogeneous flow, to a bifurcated flow with settled solids. The significance is that Shields parameter can be a valuable quantitative tool in predicting flow rates where the onset of flow problems associated with solids settling can be expected.

4.6 Major Findings and Conclusions

Newly collected viscometric data on cuttings returns covering a wide range of solids content have been obtained from a drill site, and the unique mineralogy of a drill site will significantly affect their measured viscometric properties.

CHAPTER 5 CONTRA-ROTATING PROPELLERS IN SERIES AS AN AXIAL PUMP TO INCREASE SPEED AND BOREHOLE LENGTH IN UNDERGROUND DRILLING

Modified from a paper to be submitted to *Underground Space Construction & Tunnelling*

Benjamin A. Appleby,[10,11] Rakshith Shetty,[12] Michael A. Mooney[12], and Joseph R. Samaniuk[10,13]

Extending the work from Chapter 4, this chapter focuses on using fluid pressure predictions and developing a mitigation plan when fluid pressures will be too high and lead to frac-out. There are multiple means of reducing fluid pressure with existing technology, drill for short distances, operate at slower speeds and flow rates, or drilling deeper underground. However, all these approaches would counter-act the goals of this research, drilling underground at high-speeds, over a long distance, and at shallow depths. New technology was needed to address this challenge, and axial flow pumps were the simplest first option, but their use begged the question of how much pressure boost they would provide and how many would need to be installed for a project to be beneficial. The work of Williams *et al.*[180], Samora *et al.* [181], and Alexander *et al.*[181] provides the groundwork for designing simple turbines to generate energy at high flow rates. Guided by this work, Shetty *et al.* designed propellers to act as pumps, providing a pressure boost during high flow rates[182]. Notable pressure boosts have been shown from propeller/turbine designs to operate as axial flow pumps, but they were limited by their pressure boosts and would require many of them to be installed to maintain fluid pressure below that of frac-out conditions. Their work inspired this chapter to address the question of whether an axial flow pump design could be made more compact and provide a greater pressure boost to minimize the number of pumps needed. We address this challenge by investigating a contra-rotating propeller design that incorporates two propellers in series that have mirror-image blade designs so that the flow profiles of one fed into the other, reducing the rotational motion of the fluid

[10] Graduate Student and Associate Professor, respectively, Department of Chemical and Biological Engineering, Colorado School of Mines.
[11] Primary researcher and author.
[12] Postdoctoral Researcher and Professor, respectively, Department of Civil and Environmental Engineering, Colorado School of Mines.
[13] Graduate advisor, Author for correspondence.

while maintaining the axial motion to minimize energy loss from turbulence to improve pressure boost.

In this work, we determine that separation distance between propellers is a major factor in their performance as axial flow pumps, more important than the design of propeller blades. This setup gives an efficient option to control fluid pressures, theoretically extending the length of drilling at high-speeds and shallow depths indefinitely. This work also provides another connection between propellers used in air and propellers used for water, to generate new fundamental knowledge on designing contra-rotating propellers to function as axial flow pumps.

5.1 Abstract

A new axial flow pump design has been proposed and tested implementing contra-rotating propellers in series to provide a notable pressure boost and mitigate fluid circulation loss challenges experienced in underground drilling. One of the biggest modes of failure in underground drilling is loss of fluid circulation caused by over-pressurizing drilling fluid which leads to soil fracture, creating void spaces that drilling fluid readily escapes to. The over-pressurization of the drilling fluid is caused by drilling at shallow depths, for long distances, or high flow rates that result in fluid pressure exceeding the strength of the surrounding geological formation. To mitigate this point source of pressure, a series of pumps placed along the drill string could instead be employed to provide pressure boosts to convey the drilling fluid and cuttings to reduce high fluid pressures locally. By providing pressure boosts along the drill string, over-pressurizing the fluid becomes more difficult, and the length of the drilling job can be theoretically extended indefinitely. This method of fluid pressure management will be termed distributed pumping. In this work, we design and built a set of contra-rotating propellers to act as an axial distributed pump and explore the parameters that control its efficacy as a pump. The effects of propeller rotation rate, separation between propellers, and flow rate on provided pressure boost from the pump are systematically characterized. In comparison to a singular propeller, contra-rotating propellers provide an added pressure boost benefit, but the reason why remains unclear and design principles from singular propeller design do not apply to contra-rotating propellers.

5.2 Introduction

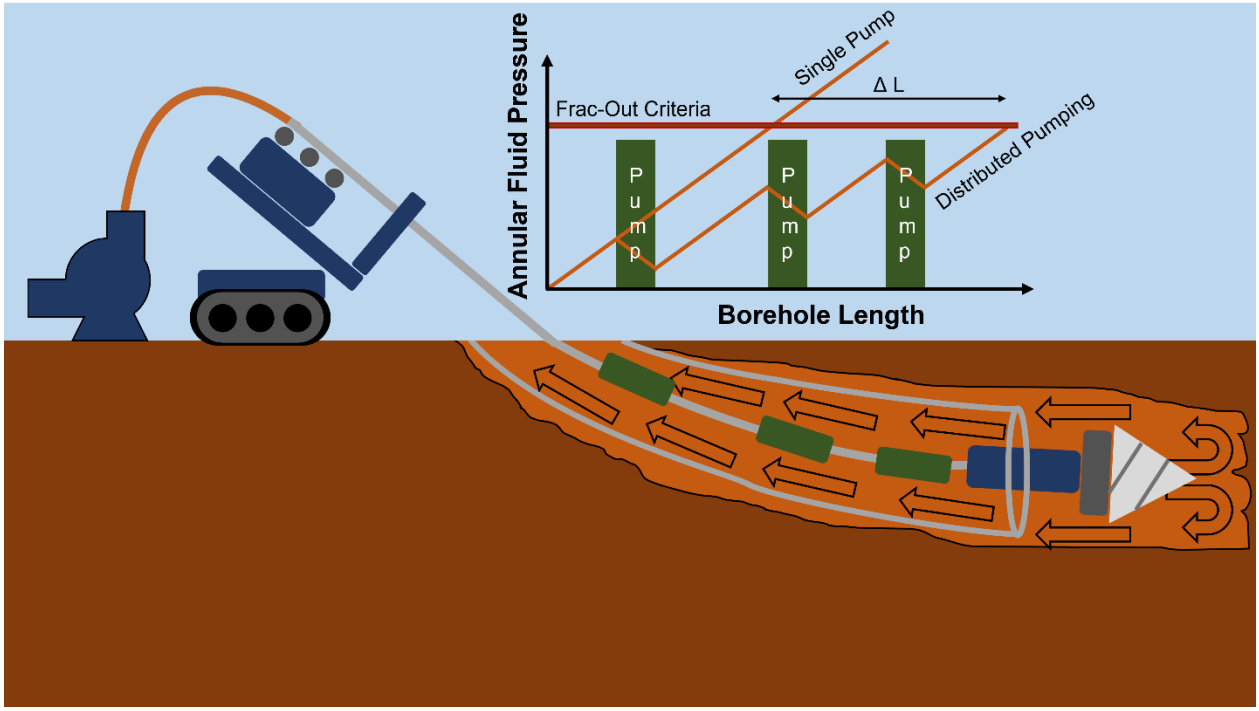

Figure 5.1 Illustration of the contributions distributed pumping can have on underground drilling to redistribute drilling fluid pressure from a point-source to along the drill string to mitigate frac-out and fluid circulation loss.

Axial pumps are a potential solution to addressing high point pressure sources at the cutterhead that can lead to frac-out by distributing pressure boosts throughout the borehole, allowing drill strings to reach greater lengths without fracturing the ground and losing drilling fluid[182]. Figure 5.1 illustrates this concept. The light grey lines are the piping of the drill string, with a cutterhead at the far right end, and distributed pumps in green along the inner pipe. In Figure 5.1, with increasing borehole length the drilling fluid pressure of the single pump line in orange will eventually surpass the strength of the surrounding soil and result in frac-out. If instead, pumps are installed along the drill string, then the fluid pressure can be distributed along the length of the borehole rather than as a point source, theoretically increasing the length of drilling indefinitely. Shetty *et al.* tested out multiple propeller designs to operate as axial flow pumps that were able to provide a notable pressure boost under expected HDD operating conditions, providing a proof-of-concept that distributed pumping could be a feasible solution[182]. The challenge with their work is that the pressure boosts provided by their propellers would require customized piping and many pumps installed at short distances apart because of the low

pressure boost provided. Our work explores this concept further by presenting a new distributed pump design that would provide greater pressure boosts, reducing the cost of a distributed pumping system by lowering the amount of pumps needed to reach the desired fluid pressures and lowering both capital and operational costs for their use.

Within turbomachines, propellers are the main component of focus in axial pumps – and propellers have been well-studied in aviation and underwater space in open systems and in series. Series propeller designs came about with a contra-rotating configuration so that they can more efficiently provide thrust. This is done by reducing the turbulence caused by the rotational motion imparted to a fluid from a propeller. A single propeller spinning will impart rotational and axial motion in one direction. A second propeller is incorporated with a contra rotation to impart rotational motion in the opposite direction and additional motion in the axial direction. This serves to cancel out rotational motion rather than adding to it, reducing energy loss caused by turbulence from excessive rotational motion. The design of each contra-rotating series propeller is also dependent on the system of application. For example, underwater propellers in series have been designed with a trailing propeller that is smaller than the leading propeller because water is so viscous it reduces the radial size of the flow streams. In contrast, contra-rotating propellers in air can maintain the same radial size because the flow streams do not change much in size moving from the front to the tailing propeller. For axial pumps, since they are not part of an open system but rather a confined pipeline, the propellers designed in this work will maintain the same radial size and will be evaluated for its added pressure boost in comparison to a singular propeller.

Predictive theory does not exist that can describe the physics behind the design and performance of contra-rotation propellers used as axial flow pumps, whether in propeller theory or pump theory. For centrifugal pumps, there exists semi-theoretical expressions relating flow rate to pressure drop derived from breaking down the velocity components of fluid moving off of a centrifugal pump blade but these relationships have their limitations[94]. The characteristic curve between centrifugal pumps will have the same qualitative trends but cannot be quantitatively related to one another and require a characteristic curve to be made at each operating rotation rate. Centrifugal pumps exhibit a flipped exponential curve, shown by Eqn. 2. In comparison, the flow rate and pressure drop curve for axial flow pumps using contra-rotating propeller do not share the same qualitative description and have a flipped logarithmic curve. With the differences in characteristic curves, the theory used for centrifugal pumps do not adequately describe contra-rotating propeller systems.

The semi-empiricism used for centrifugal pumps is in Equation 5.1[94].

$$\Delta P = a - bQ^n \tag{5.1}$$

Like the centrifugal pump, contra-rotating propellers have a sustained pressure boost over a wide-range of flow rates. This is beneficial compared to single propeller systems that have characteristic curves in the shape of a steep parabola, with a higher pressure boost, but greater variability in that boost across flow rates[183]. Breaking down the velocity components of propellers is more challenging than centrifugal pump blades, because blades used in aerospace propellers have both a camber and twist angle component to them. When looking axially down the blade of a propeller, there is a variation in its thickness, the camber, and along that same perspective the blade will rotate as a function of its axial position. These concepts are adapted from aeronautics where camber improve the lift and twist angle improves the distribution of lift across the blade. These additional complexities mean that propeller blade theory is dependent on numerical analysis and computational fluid dynamics simulations near the blade to evaluate its performance, that have resulted in guidelines in blade design but without a unifying theory[184]. The addition of contra-rotation propellers also adds complexity, where the flow profile of the front propeller is feeding into the rear propeller and their performance and interrelated. Then their operation as an axial flow pump means that the fluid is confined to a pipe, and additional

feedback from that confinement will further impact their performance. These complexities means that no clear theory based on first-principles exist, but their development is based on physical and simulation evaluations.

Semi-empirical theory can be derived for axial flow pumps by breaking down the velocity vectors experienced by the fluid when in contact with a propeller blade and then mathematically massaged in terms of flow rate and pressure drop. These expressions for flow rate and pressure drop are connected to the rotational operation of axial flow pump propellers and can predict expected trends in pump curve behavior. This general theory will then be extended to contra-rotating pumps in series and the applicability will be evaluated.

5.3 Materials and Methods

5.3.1 Materials/Design

The propellers are designed following the work of Williams *et al.* who have provided an excel sheet and guide to capture the challenges of designed curved propellers for applications in micro-hydraulic turbines[180], and configured as pumps by Shetty *et al*.[182]. Using the same propeller design framework presented by them and exploring whether those same design principles could be applied to contra-rotating propellers[180,181]. Shetty *et al.* used design principles summarized by Williams *et al.* to design turbines for axial flow pumps[180,182]. Propeller design is challenging and often done using computational fluid dynamics software to evaluate their efficacy, but the set of empirical relationships aggregated by Williams *et al.* has guided our propeller designs to optimize for the desired pressure boost through modifications to the hub and blade size as well as the camber and twist angle of the blades[180]. This is best shown in Figure 5.2, where the left most propellers are designed for a lower pressure head and the right most propellers designed with a higher pressure head.

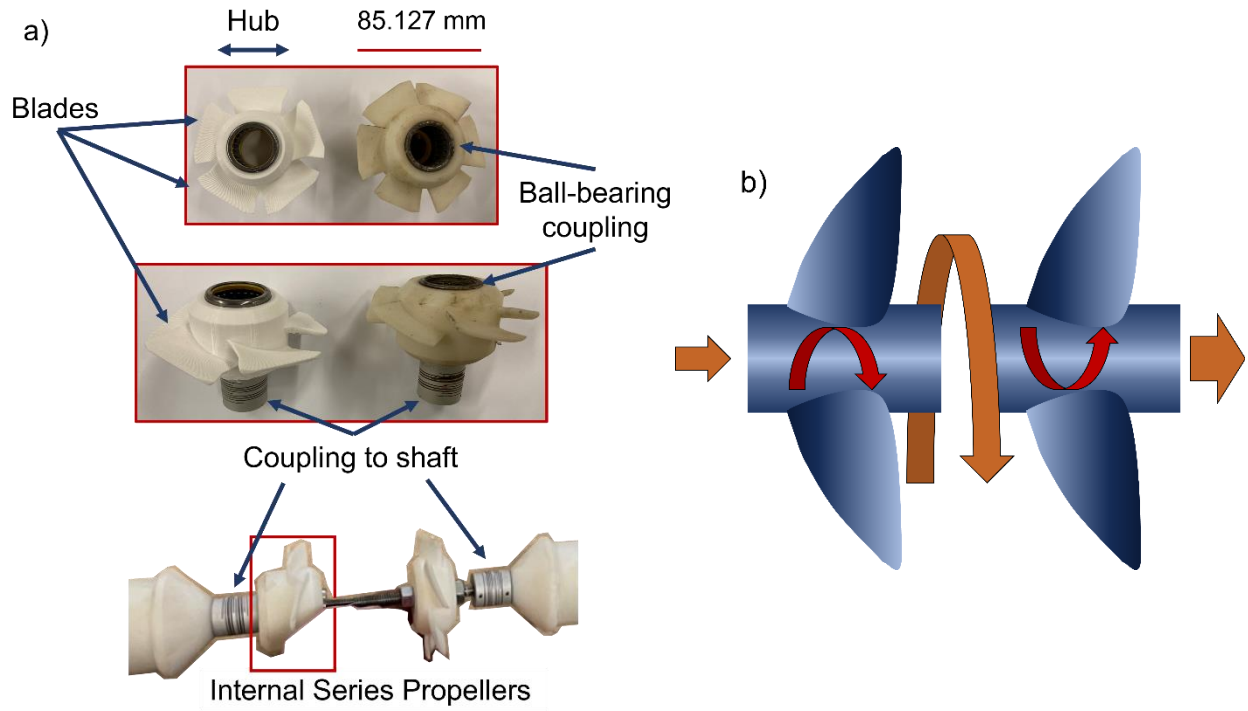

Figure 5.2**.** a) Comparison between propellers designed for low and high pressure to determine whether design principles for single propellers can be applied to contra-rotating propellers in series. The left propeller is designed for half the pressure head as the right propeller. b) Illustration of two propellers along the same axis operating in counter-rotation to impart axial flow but mitigating rotational flow caused by the rotation of the propellers.

In Figure 5.2, two propeller designs came about from constraining each to have the same hub to blade diameter ratio but to maximize or minimize fluid pressure. In Figure 5.2a the left propeller was designed for a pressure head of 3.5 meters and the right propeller designed for a pressure head of 7 meters, and both at the same flow rate. The low pressure propeller has a greater reduction in blade width moving from the outer edge blade to the hub of the blade. The low pressure propeller also has a greater curvature than the high pressure propeller, looking along the height of the blade, there is a greater rotation from the outer edge of the blade to the hub. The difference in color is due to material availability when printing the material out of plastic. Both propellers are made of ABS plastic, but they used different coloring agents because the low-pressure propeller was printed using additive manufacturing with filament while the high pressure propeller used resin The low pressure propeller is made of ABS while the high pressure propeller is made of ABS resin using stereolithography. Inset within each one is a roller bearing that allows a bob connected to the mirrored propeller pair to fit inside, allowing them to rotate in opposite directions. The mirrored pair of each propeller is curved in the same direction, but the

angle that it attached to the hub of the propeller is mirrored. This means that the fluid in contact with the propellers will feel momentum in the same axial direction but opposite rotational directions. This is illustrated in Figure 5.2b, where the contra-rotating propellers are setup along the same axis while drilling fluid flows into the first propeller, leaving with rotational and axial motion while the second propeller rotating in the opposite direction reduces the rotational motion and further enhancing the axial flow.

5.3.2 Method

The functionality of the test setup is to explore contra-rotating series propellers as axial flow pumps, specifically the efficacy of contra-rotation and exploring how the flow profiles generated by the two propellers would interact with one another to create a meaningful pressure boost to mitigate high fluid pressures that could lead to frac-out scenarios during underground drilling.

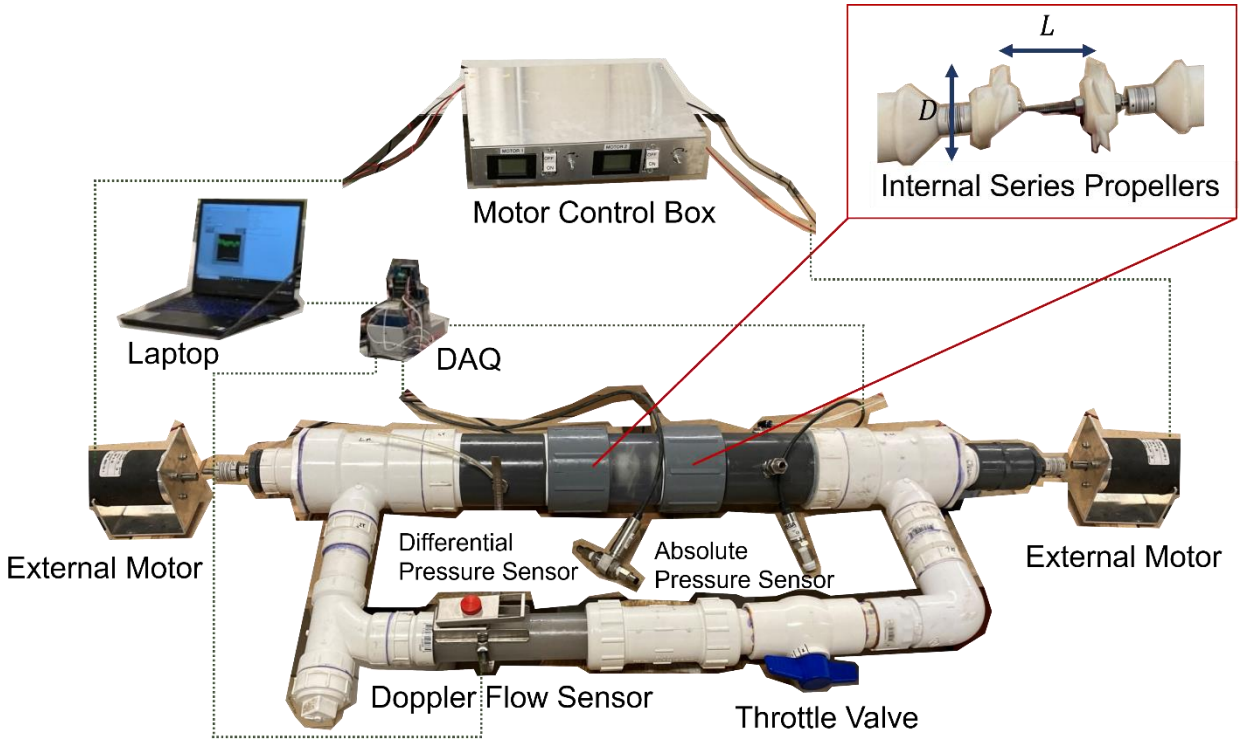

Figure 5.3**.** A schematic of the contra-rotating propellers in series. External motors operate the rotation of propellers inside the setup while the absolute pressure, differential pressure, and flow rate are measuring the fluid pumped by the propellers. A throttle valve is used to expand the operable range of flow rates within the setup. The data is collected with a laptop and NI Instruments data acquisition device. The external motors are controlled by a motor control box and are sealed from the internal fluid by a set of ball bearings. The internal series propellers, blown up on the top-right, arrangement is defined by their center-to-center separation distance, L, and the propeller blade diameters, D.

The experimental setup is shown in Figure 5.3. A 4 inch PVC pipe assembly makes up the body of the setup with a 2 inch PVC section that connects the ends to form a loop. The contra-rotating propellers are inside the 4 inch section of the assembly mounted along two separate axles, one for each propeller and connected by bearing that allow for contra-rotation while in the same axial plane. Additional bearings are used to connect the outer ends of the axles to external motors that will separately control the rotation rate of each propeller while keeping fluid within the loop. Each external motor is operated by its own controller housed in the motor control box, with each controller adjusting the voltage applied to each motor to reach the desired rotation rate. An Omega differential pressure sensor is mounted on both sides of the propellers, and an Omega absolute pressure sensor is mounted upstream of the propellers. A doppler flow sensor is mounted on the clear 2 inch section of the PVC pipe to measure flow rate within the system. The doppler sensor depends on the delay between radar signals that are reflected from

particles in the fluid to measure the velocity of the particles that is used to calculate flow rate in the setup from user inputted pipe diameter dimensions. To provide particles for the doppler sensor, the fluid used includes 0.036wt% bentonite to include particles in the fluid without modifying the rheology of the fluid. 0.036wt% is at a small enough concentration that the viscosity and rheology of the fluid does not impact the fluid flow within the system. More information on the sensors and motor are provided in Table 5.1.

Table 5.1 Sensor and motor specifications.

Equipment	Type	Measurement	Range
Pressure	Gauge	ΔP	0-103 kPa (15 psi) [0-5V]
Flow	Doppler	Q	0-500 L/m (132 GPM) [0-5V]
Motor	Brush	RPM	0-5,000 RPM [24V, 15A]

A ball valve is used in the 2 inch pipe section to throttle flow within the system and explore a wider range of flow rates. The arrangement of the internal series propellers are defined by an L/D ratio, where "L" is the center-to-center separation distance between propellers, and "D" is the blade diameter of the propellers. For every L/D separation distance tested, the amount of throttling is also adjusted, at positions of 100, 75, 25, and 0% open to cover a breadth of flow rates the contra-rotating propellers could experience. During testing a National Instruments data acquisition system collects data from the two pressure sensors and the doppler flow sensor, while a simple LabView program plots and records the data in real-time.

The experimental setup used in this work is an updated version based on the original design of Shetty *et al.*, where there is a 4 inch PVC pipe assembly that allows for visualization of the propellers rotating under varying rotation speeds while flow rate and pressure changes are measured[182]. The modifications made to the setup from Shetty *et al.* include replacing the inner fluid loop with external motors instead[182]. Rather than having a system using a flow loop to provide flow to an inner loop to power the propellers and circulate flow in an outer loop, motors replace the flow loop and provide control on both rotational speed and contra-rotation. External motors also allow for finer control of each propeller to further explore the effects of contra-rotation that would be difficult to capture if they were instead controlled by fluid flow rate. The motors are permanent magnet direct current brush motors operating at 24VDC and 15A from ElectroCraft (Model#: DPP685-185V24). These modifications result in a more simplistic setup

that requires less operational time, total fluid volume, and control over each propeller individually.

Each experiment is run by filling the system with a dilute bentonite fluid and priming the pressure sensors and attaching the doppler sensor while removing trapped air bubbles in the system by rocking it back and forth before sealing the loop. Once the system is primed, the test assembly is secured to the table and the external motors are connected to the axles by frictional couplings. A baseline value of pressures and flow rate are taken before the motors are turned on, followed by turning on the motors and running through a range of rotation rates (500, 1000, 1500, 2000, 2500 RPM) for every propeller separation and throttle valve position while measuring the absolute pressure, differential pressure, and flow rate of the system. The rotation rates of the system were determined by what was physically feasible. At 500 RPM the data collected is consistent but has more volatility compared to the higher rotation rates, and 2500 RPM was the upper limit because at higher rotation rates mechanical issues occurred more often from couplings coming undone, leaks developing, and wear in the system along with variability in the data from vibrations caused by the motors. The separation distance between the propellers spans L/D = 0.5, 0.75, and 1. These values are distances normalized by the diameter of the propellers. A L/D = 1 separation distance means that the center to center distance between propellers is one propeller diameter apart.

5.4 Results and Discussion

The operation of the axial pump test assembly is filling the system with water and securing the system to a table and controlling the external motors of the system to spin in opposite directions while the angle of the propeller blades will push fluid in the same direction. The following set of experiments is performed in this manner by increasing the rotation rate of each propeller and matching the two propellers as best as possible and recording the flow rate and differential pressure change across the two propellers. Figure 5.4 illustrates the operation of the axial pump test assembly, where the system is setup with a designated separation distance between the propellers and then the rotation rate of each setup is applied, and the corresponding pressure drop and flow rate are measured. This was intentionally designed to explore the relationships between flow profiles developed by the contra-rotating propellers rather than focusing on pump performance, which traditionally controls flow rate to evaluate performance.

To adjust the flow rate, a ball valve is used to throttle the flow between 0%, 25%, 75%, and 100% closed where 0% is fully closed and 100% is all the way open.

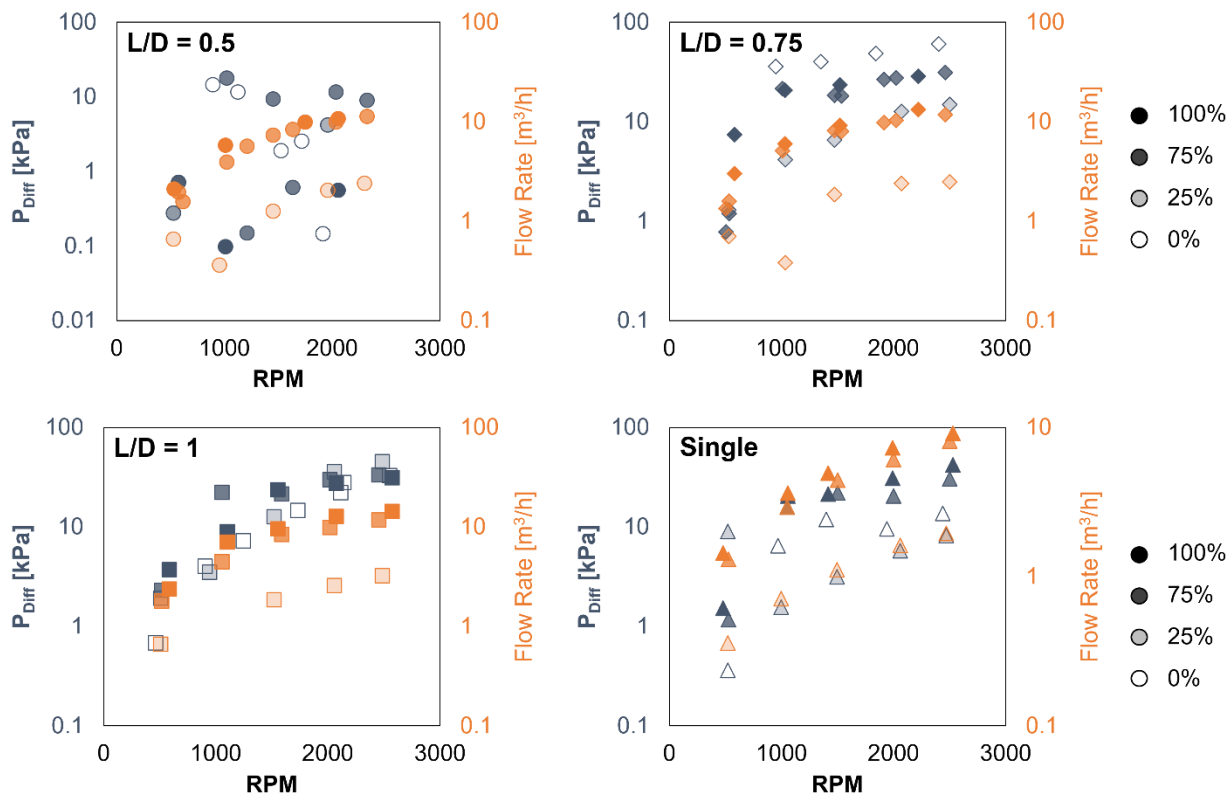

Figure 5.4. Response of single propeller and series contra-rotating propellers to varying rotation rate and then spacing between series propellers. Each figure plots the differential pressure drop across the propeller(s) and flow rate as a function of the same rotation rate for both propellers. Dark blue is the differential pressure data graphed onto the primary y-axis and orange is flow rate graphed onto the secondary y-axis. The top left of each figure has a L/D ratio which is the center-to-center separation distance between propeller blades normalized by the diameter of the propellers. S is when a single propeller is used. The gradation of fill for each data point is indicated on the right side of the figure and represents the extent the ball valve is open to throttle flow in the loop. At 100% the ball valve is fully open and at 0% the ball valve is closed.

Figure 5.4 gives the general trend of propeller operation as an axial pump. With increasing rotation rate, the pressure and flow rate increase in a logarithmic manner and the values level off. This is not the case at the L/D = 0.5 separation which has different trends at each throttle valve opening. For the L/D = 0.5 separation distance when the throttle valve fully closed the differential pressure decreases almost linearly with increasing rotation rate, but for 25% open throttle valve the pressure trend increases then levels out, and for 100% open throttle valve there is a dip then increase in pressure. Besides the singular propeller, it is seen that flow rate and pressure have a negative relationship – when one increases then the other decreases. At the same

operating rotation rates the amount of energy the propellers imparted to the fluid should be the same but the distribution of that energy between pressure and flow rate is controlled by the throttling ball valve.

In trying to understand the factors most influencing pump performance for contra-rotating propellers, the design principles behind propellers was first investigated. As seen in Figure 5.5 and following the work of Williams *et al.* Samora *et al.*, and Alexander *et al.*, singular propellers can be designed by iteratively applying empirical relationships between desired operation and blade shape[180,181,184]. Propeller blades can be designed for greater or lesser pressure head, and Figure 5.5, showcases those two designs. Figure 5.5a is the propeller designed for lower pressure and Figure 5.5b is the propeller designed for greater pressure. It should be noted that 500 rpm is a poor indicator of performance across all figures due to a large variability in the measured pressure compared to the other rotation rates.

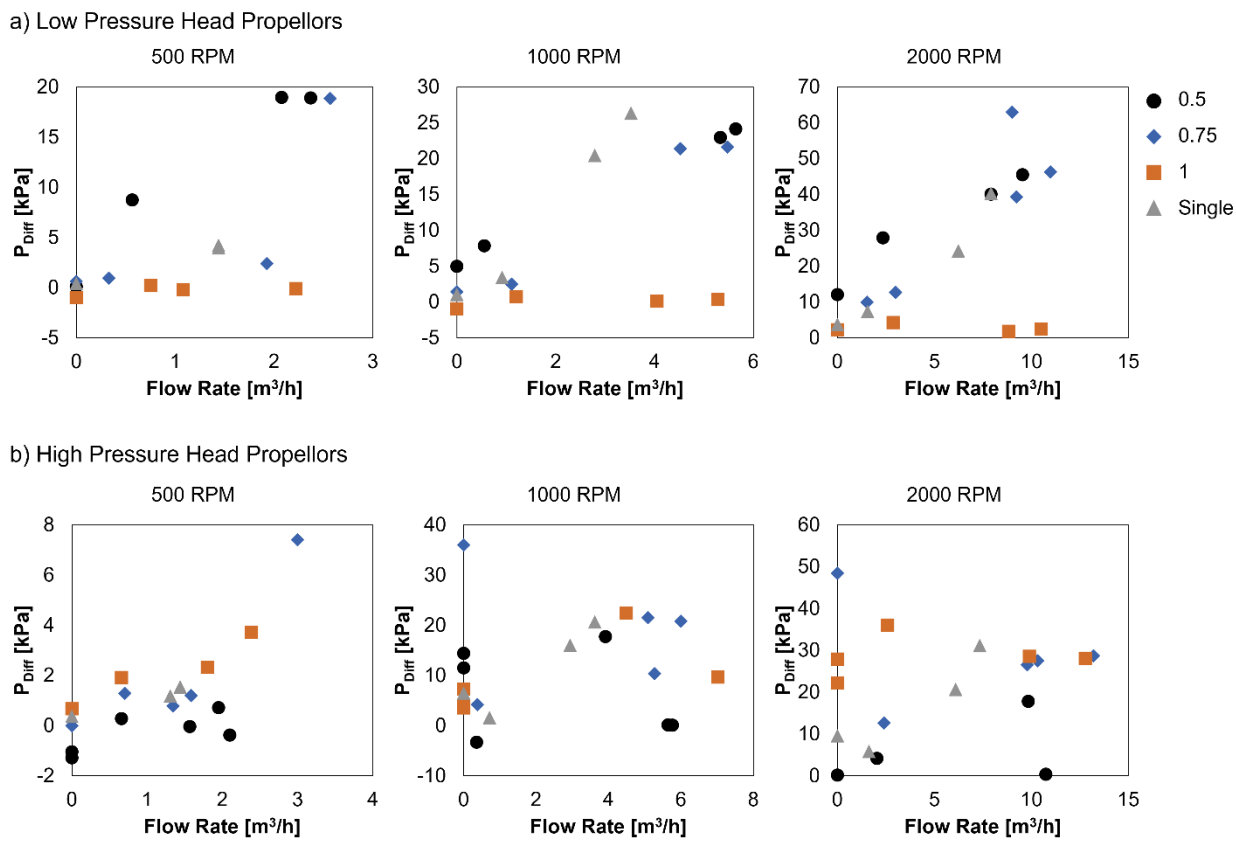

Figure 5.5. Pump curves developed for each propeller set and configuration (spacing). Each figure graphs the differential pressure drop across both contra-rotating propeller(s) as a function of flow rate. a) is the set of contra-rotating propellers designed for a pressure head of 3.5 meters. b) is the set of contra-rotating propellers designed for a pressure head of 7 meters. Each figure is the data collected at a rotation rate both propellers are operating at, the symbol for each data set represents the L/D separation distance, and the color is to distinguish between data sets. The flow rate of each data set is controlled by throttle valve opening – the throttle valve is opened more to increase the flow rate while the separation distance and rotation rate of the propellers remain the same.

Pump curves are used to evaluate the performance of pumps by comparing the operating flow rate of a pump to the corresponding pressure head the pump will provide. This is a common presentation of pump performance when evaluating a pump for an application. While this is a convenient means of showing pump performance it does not fully capture these pump systems, because depending on operating rotation rate each pump configuration is providing both a pressure and flow rate boost to the fluid.

Figure 5.5, explores the connection between singular propeller design and then their performance as contra-rotating propellers in series. Figure 5.5 presents the flow rate and pressure

curves developed for each series propeller configuration with each separation indicated by a different data symbol and each figure is a different operating rotation rate. Figure 5.5a is the low-pressure head propeller and Figure 5.5b is the high-pressure head propeller. Besides the ability to reach a greater pressure at no flow, the high-pressure head propeller achieves similar pressures as the low-pressure head propeller along the same flow rates and rotation rates. Even with their obvious variations in curvature and dimensions of the blade design they exhibit nearly the same performance when there is flow. The design changes employed for single propellers does not result in a notable difference for contra-rotating propellers in series.

Even if singular propeller design principles do not apply to contra-rotating propellers in series, the presentation of data in Figure 5.5 does give a glimpse at the complex interplay between system variables. Seen in Figure 5.5, the L/D = 1 separation distance amongst both propeller designs reaches a low pressure value gradually with increasing flow rate. Whereas a L/D = 0.75 separation distance has the pressure falling more quickly and the 0.5 separation has pressures that hover around a similar value across all flow rates. These flow rates are controlled by both the rotation rate of the propellers and the extent of throttling employed by the system's ball valve. The pressures produced by these contra-rotating propellers depends on the separation between the two and the flow imposed on them, a convolution of many variables.

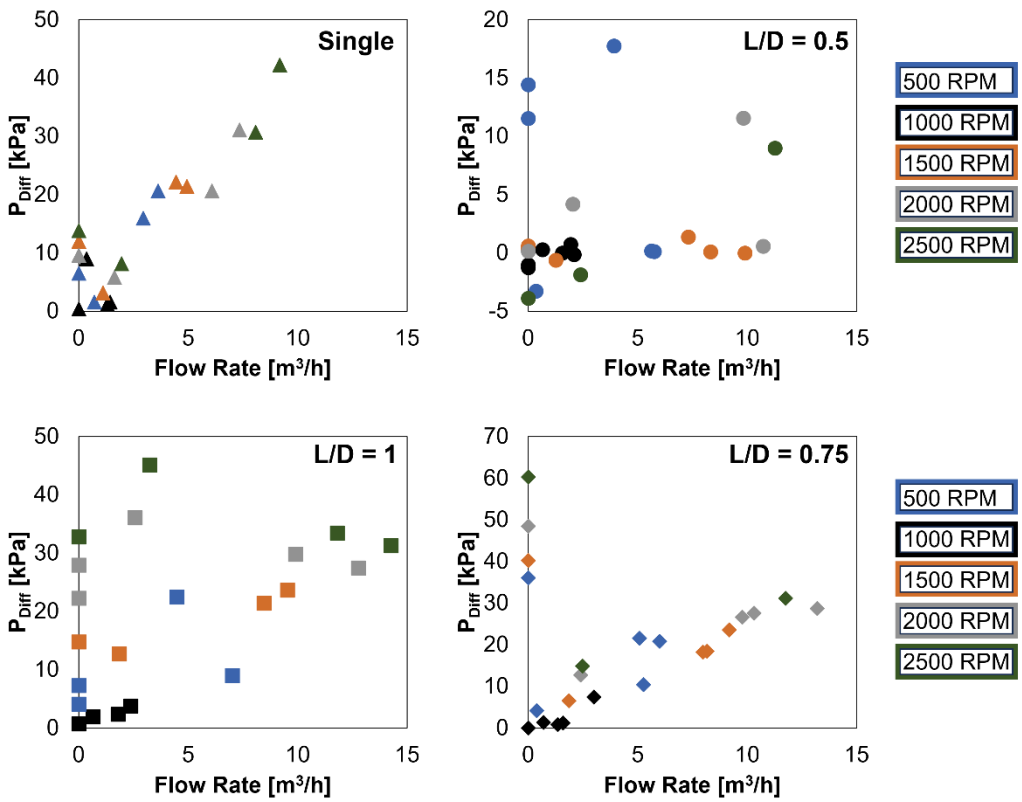

Figure 5.6. Effects of separation distance on pump performance. Each figure graphs the differential pressure drop across both contra-rotating propeller(s) as a function of flow rate. The symbol of each data point is associated with their respective L/D separation distance values indicated in the top right of each figure. The color of each data set represents the rotation rate both propellers are operating at. The flow rate of each data set is controlled by throttle valve opening – the throttle valve is opened more to increase the flow rate while the separation distance and rotation rate of the propellers remain the same.

The mechanical understanding of why contra-rotating propellers have an added benefit compared to singular propellers is that the contra-rotation reduces the system's energy loss from contributions to rotational flow[183,185]. As one propeller rotates it imparts an axial and rotation trajectory to a fluid and the added rotational trajectory adds to the system's turbulence and thus energy loss from energy dissipation. A second propeller reduces the system's turbulence by contributing a rotational trajectory to the fluid in the opposite direction, cancelling out the trajectory of the first propeller while applying greater energy to fluid flow in the axial direction. The system's independent variables: separation distance, flow rate throttling, and rotation rate will all be different means of affecting these flow profiles and the efficacy of these rotational flow profiles cancelling out and encouraging greater axial flow while reducing energy loss to turbulence. Figure 5.6 explores this further by allowing a range of flow rates but systematically

evaluating input energy into the system, propeller rotation rate. The energy of the fluid system is dictated by the rotation rate of the propellers and transfer of energy from the propellers to the fluid can be improved or hampered by the flow profiles generated by the system configuration and operation. For the contra-rotating propellers, it can be seen in Figure 5.6, that in general the pressure increases with rotation rate, and so does the flow rate. The trends in pressure reduction at greater flow rate is also specific to the separation distance between propellers but remains qualitatively similar between rotation rates. The L/D = 0.5 separation distance shows that the pressure increases and then levels out, while the 0.75 and 1 separations have pressures that steadily decrease with increasing flow rate, with 0.75 decreases more rapidly. The single propeller can be quickly seen that rotation rate does not play a role in its pressure output and the pressure values remains around the same values, that are much lower than those of the contra-rotating propellers.

While the contra-rotating propellers have been systematically studied in terms of operating rotation rates, corresponding flow rates, and resulting system pressures the understanding connecting these system variables and their predicted performance has not yet been explored. For the data to be fitted to the empiricism, Equation 5.1, the pressure value needs to grow increasingly smaller with flow rate, because of this only the L/D = 1 and 0.75 separation distance for the contra-rotating propellers can be used for the fitting analysis. For these two separations the fittings represent the data well with R^2 values of 0.97 or greater but each trendline needs to be fitted for ever rotation rate. This is useful when data is known at the desired operating rotation rate but remains limited when data has not been collected for a specific rotation rate.

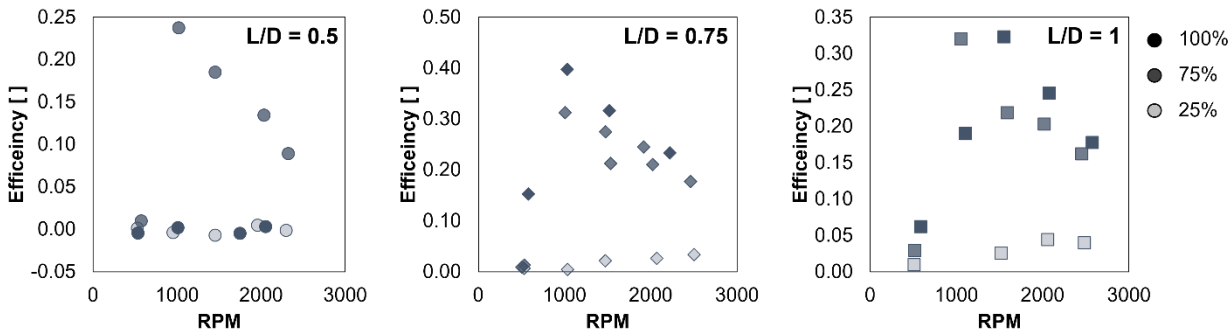

Figure 5.7 Efficiency evaluation for the three L/D separation distances measured with the contra-rotating propellers as a function of rotation rate. Efficiency is the ratio between the output hydrodynamic energy and the input electrical energy. Hydrodynamic energy is the product of the flow rate and differential pressure drop. The symbols of each data set is consistent with the L/D separation distance indicated in the top right of each figure and the gradation of shading is a function of throttle valve opening. At 100% the valve is completely open and at 25% the valve is 25% open to flow.

To normalize the performance of each separation distance, rotation rate, and flow throttling variation, their respective efficiencies are evaluated in Figure 5.7. Efficiency is defined as the ratio between the output hydrodynamic energy and the input electrical energy. Hydrodynamic energy is the product of the flow rate and differential pressure. The general trends seen across all separation distances is that the efficiency decreases with increasing rotation rates, with the greater flow rates more significantly affected by rotation rates. However at the L/D = 0.5 separation distance, only one set of data, which is neither the greatest flow nor no flow, impacted by rotation rate. The L/D = 0.75 separation distance operates at the highest efficiency at a rotation rate of 1,000 RPM and the highest flow rate with no throttling of the flow. Across Figure 5.4, Figure 5.5, and Figure 5.6 the L/D = 0.5 separation distance performance is the most unpredictable. Excluding L/D = 0.5 separation distance, efficiency increases with greater flow rates, seen at separation distances of 0.75 and 1 in Figure 5.7.

5.5 Conclusions

In this work we have provided insights into applying the design concepts of contra-rotating propellers to axial flow pumps. This system will provide a needed pressure boost in underground drilling to prevent over-pressurizing the drilling fluid and overcoming the surrounding ground strength that would lead to ground fracture and create a frac-out scenario. We have fabricated an experimental setup representative of fast horizontal directional drilling specifications that include two propellers operating in contra-rotation to drive water in a closed

loop to assess its performance under varying rotation rates, separation distances, and flow rate conditions. The data collected supports the claim that contra-rotating propellers will provide a greater pressure boost to the drilling fluid than a singular propeller system. Separation distance between propellers were shown to be an important factor for performance, where the trend between pressure drop and flow rate persists across rotation rates and throttling of the flow. The empirical design principles from singular propellers were also found to not apply to contra-rotating propellers, where propellers designed for different pressure boosts achieved similar performances at the same operating conditions. Semi-theoretical modelling from centrifugal pump theory was also shown to not capture the physics of contra-rotating propellers, not fitting well to the additional variations in the datasets when the data diverged from flipped logarithmic behavior. Contra-rotating propellers are different from centrifugal pumps in their blade complexity, interactions between flow profiles of the front and rear propellers and constraining the flow around propellers to a pipe, all of which is not accounted for in centrifugal pump theory. Greater understanding of the effects of flow profiles between propellers is needed before their performance as axial flow pumps can be predicted. In this work, a L/D = 0.75 separation distance was shown to produce the greatest pressure boost and be the most efficient because of the fluid interplay between the contra-rotating propellers, more important than the blade design of the individual propellers.

5.6 Major Findings and Conclusions

The L/D = 0.75 separation distance between contra-rotating propellers used as axial flow pumps has been shown to play a major role in producing the highest pressure boost and greatest efficacy, more important than the blade design of the individual propellers.

CHAPTER 6 FLUID-DRIVEN CLOGGING TO PREVENT FLUID CIRCULATION LOSS IN UNDERGROUND DRILLING

Modified from a paper to be submitted to *Granular Matter*

Benjamin A. Appleby[14,15], Michael A. Mooney[16], Alexander J. Pak[14], and Joseph R. Samaniuk[14,17]

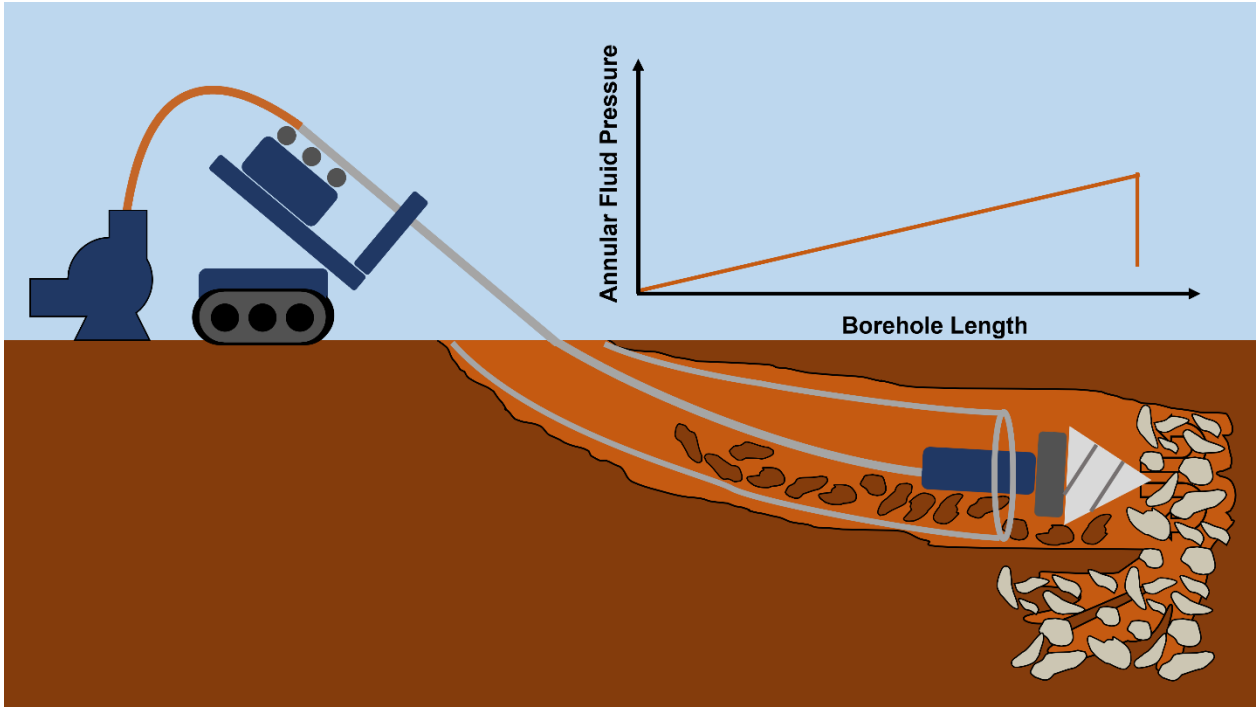

Figure 6.1 Illustration of porous media encountered underground that would lead to drilling fluid loss, reducing drilling fluid pressure and stopping the removal of soil cuttings from the borehole.

This work looks at the problem of fluid circulation loss from porous media rather than from frac-out. Geological conditions underground can have a wide range of variability, and one of them is a concentration of porous material, which are commonly found near bodies of water similar to clay. This chapter came about to address the event that porous media like a gravel deposit is encountered and fluid pressure management alone was not enough to prevent fluid circulation loss (Figure 6.1). Initially, this work was going to focus on non-Newtonian flow

---

[14] Graduate Student, Assistant Professor, and Associate Professor, respectively, Department of Chemical and Biological Engineering, Colorado School of Mines.
[15] Primary researcher and author.
[16] Professor, Department of Civil and Environmental Engineering, Colorado School of Mines.
[17] Graduate advisor, Author for correspondence.

through porous media, thinking that the fluid rheology could be controlled to plug up porous media, but based on experiments it was quickly determined that porous media of sand or larger particles ($> 1\ mm$) would require more than a bentonite slurry to stop flow. Preliminary experiments showed that once drilling fluid pressure exceeded the strength of the soil fractures would form horizontally and the soil above the fracture would be heaved up (Appendix C.1). Sand was instead used to clog a gravel bed because it is a commonly used material and can be incorporated into the drilling fluid of a drill string without much issue. After the first experiment, it became apparent that sand would readily clog gravel even under moderate flow conditions – opening the door for additional questions on how fluid-driven clogging could be achieved intentionally. In this work we show that sand could be used to clog a gravel bed in the event of fluid circulation loss to rebuild fluid pressure and recover fluid circulation. This was shown through experimental work to further explore the drivers of this phenomenon. The stress contributions of the system from a fluid driving force and gravity determined whether particles would settle, and the system geometry determined the dynamics for particle bed formation that was needed to reach a great enough particle density that particles could bridge a pore opening and clog. This work highlights the need for fluid circulation loss strategies that account for the variability of the geology underground and fluid rheology modifications beyond bentonite concentration or the addition of polymers. Computational efforts could be used in the future to further interrogate the influence of particle settling and its connection to clogging.

6.1 Abstract

An exploratory study has been performed investigating fluid-driven clogging of porous media to address fluid circulation loss that could be experienced in underground drilling. Fluid circulation loss can be a major mode of failure in underground drilling because of the potential for the drill string to become stuck when soil cuttings can no longer be removed, and drilling cannot progress. Porous media encountered underground contain void spaces that will be readily filled by pressurized drilling fluid, but granular particles can readily fill those voids to allow drilling fluid pressure to rebuild and recirculate. In this work experiments have been performed to evaluate the major parameters controlling fluid-driven clogging in porous media so that knowledge of this phenomenon could be used in underground drilling. An experimental setup termed a permeation cell was constructed to hold model porous media of gravel and sand while drilling fluid and drilling fluid laden with sand could be introduced into the system while fluid pressure and flow rate are

controlled and measured to quantify clogging events. Experiments showed that a 1.5wt% bentonite slurry alone could not clog either porous media beds of sand or gravel, but a fluid whether water or a 1.5wt% bentonite slurry laded with sand could clog a porous bed of gravel – indicated by a recovery of fluid pressure. Applications for this work includes underground drilling and broadly solid processing where granular particles in fluids encounter an orifice whether to promote or mitigate separation of the two phases.

6.2 Introduction

Clogging porous media with particles is a potential solution to fluid circulation loss when porous media is encountered underground, but this system is highly complex and interconnected with porous media flow and fluid-driven clogging. As theoretical and empirical efforts continue there still lacks a model able to predict results or control fluid-driven clogging in porous media[78,186]. To investigate this phenomenon a new experimental setup termed the permeation cell was designed and fabricated to address fluid loss to porous media. The design consists of a model porous media bed that can be either gravel or sand with fluid with or without sand flowing into the permeation cell while fluid pressure drop and flow rate are measured with time to quantitatively describe clogging.

6.3 Materials and Methods

A permeation cell was designed and constructed to investigate fluid loss in coarse soils and to develop mitigating strategies to reduce such losses during drilling. The system is like a packed bed, where coarse soils including sands and gravel are packed into a clear PVC tube, represented by part 11 in Figure 6.2, termed the porous media cylinder. Each end of the pipe is sealed with a strainer that holds the porous media in place without removing particles in the fluid, and drilling fluid is introduced to the pipe by a pressure vessel, represented by part 4 in Figure 6.2, while pressure drop and flow rate is measured across the porous media cylinder. More details are covered in section 6.3.2.

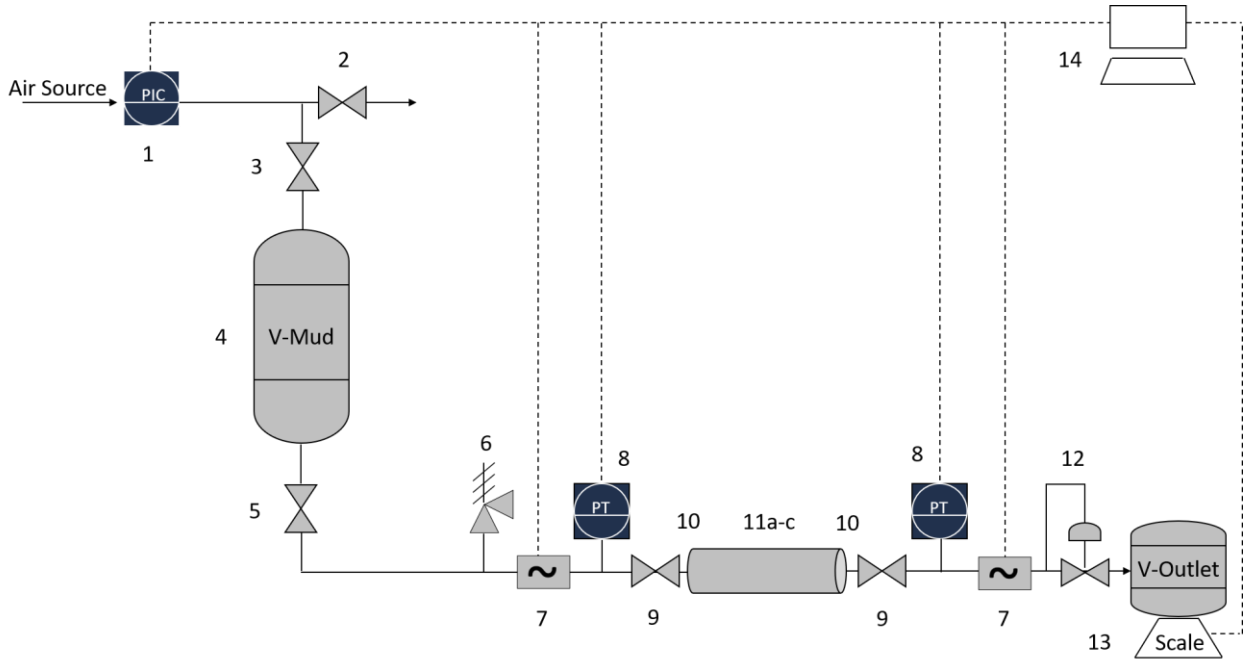

Figure 6.2. Permeation cell set-up. From left to right, an in-house air source is used to control flow through the system with a pressure regulator(1, PC). Air pressure is fed into a tank (4, V-Mud) that can be changed out with water, drilling mud, and drilling mud with solids content. Fluid entering and exiting the porous media cylinder (11a-c) will be measured with inlet flow velocity (7, doppler flow meter) and pressure sensors (8) on the upstream and downstream ends. Two cells were used for experiments, a 25.4 mm (1 inch) diameter cylinder that's 607 mm (2 feet) long and a 203 mm (8 inch) inner diameter cylinder that's 911 mm (3 feet) long. The cell is sealed with mesh (10) on both ends to only allow fluid in and out of the system. One end of the cell has a removeable mesh so that the desired coarse soil can be replaced as needed. A pressure-regulator will be used downstream to maintain a constant minimum pressure in the system as needed or will be used to hold water in the system in the case of saturated soil formations. Outflow from the cylinder is collected in a bucket (13, V-Outlet, Scale) connected to a force transducer to measure the outlet flow velocity.

6.3.1 Materials

Two types of granular materials were used for the porous media bed, gravel and sand, and the two fluids representing drilling fluid were water and 1.5wt% Wyoming Bentonite slurry. Wyoming bentonite is a well-used industry term to specify sodium montmorillonite mined from Wyoming and used as a drilling fluid in underground drilling because of its ability to remove soil cuttings, pump easily, and lubricate the cutterhead[10]. Since Wyoming bentonite is mined it has variations in chemical makeup and composition that result in a wide range of fluid properties when added to water. Table 6.1 is a comparison of Wyoming bentonite slurries, Black Hills Bond LLC (BHB) at 1.5wt% and 3wt%. Each of these slurries features slight shear-thinning behavior

where viscosity decreases with increasing shear-rate, characterized by a TA Instruments DHR-3 Rheometer (Appendix C, Figure C.10).

Table 6.1. Summary of relevant material properties of bentonite slurries, gravel, and sand. The fluid properties M and n represent the power-law parameters to quantify the viscous and shear-thinning behavior. BHB is Black Hills Bond Bentonite.

		Fluid Properties	
Material	Particle Size [mm]	M	n
Water	N/A	0.001	1
1.5 wt% BHB	~ l,000 and less	0.0026	0.1033
3 wt% BHB	~ l,000 and less	0.0026	0.11
Gravel	9.5	N/A	N/A
Sand	1.19-0.590	N/A	N/A

The sand size is 16/30 mesh size (0.0469-0.0232 inch, 0.59-1.19 mm), obtained from Sierra Sands. This size was the finest particle size distribution that could be found and the largest sand size that would encourage clogging and determine whether sand could clog gravel. Particle density for the sand was 2.58 g/mL obtained over an average of three samples with standard deviation below 2% of the density value. The porosity was determined from the particle and bulk density to be 0.36.

The gravel size is 3/8 inch, with the smallest dimension being 3/8 inch and a wide distribution of aspect ratios. Larger porous media material could not be obtained because of the size of container needed, because following ASTM standard D2434.32844[187], to prevent preferential flows along a cylinder's walls the cylinder holding the particle material should have an inner diameter 8-12 times larger than the particle size. The goal of the design was to model the worst-case scenario for fluid circulation loss, so the goal was to have the largest gravel size possible. An 8-inch inner diameter permeation cell was the largest size that could be obtained before becoming exorbitantly expensive to obtain the cylinder and appropriate fittings. Following the ASTM standard, the largest available gravel size was 3/8 inch. Particle density for the gravel was 2.73 g/mL obtained over an average of three samples with standard deviation below 3% of the density value. The porosity was determined from the particle and bulk density to be 0.38.

6.3.2 Method

The goal of the experimental setup is to investigate the reduction of fluid loss when highly permeable soils ($> 10^0\ mD$) like coarse sands, gravel, cobble, and boulders are encountered during drilling, which requires a system to house and investigate flow through porous media with drilling fluids with and without particles flowing through it. In the literature, soil cuttings in drilling fluid are dominated by sand, silt, and other millimeter-length particles[85–87,188]. Clay cuttings are assumed to dissolve into the drilling fluid and modifying the drilling fluid's rheology[189]. Based on experimental literature, the permeation cell was designed to process sands, silt, and bentonite slurries. The system was designed with the assumptions that the fluid is incompressible, inaccessible voids do not influence flow, and solids transport from erosion does not occur.

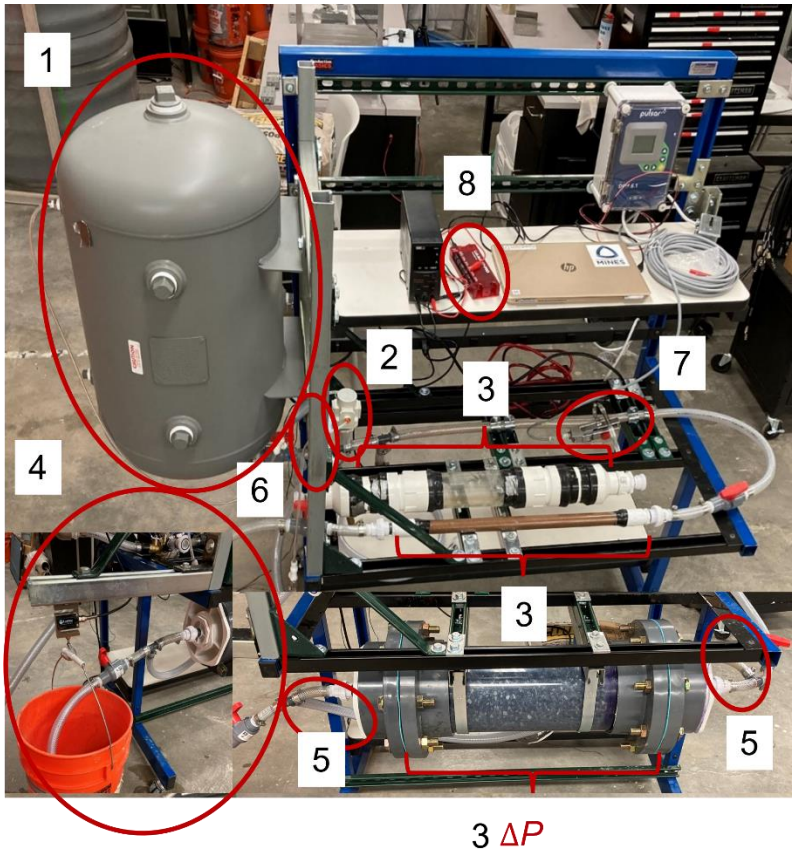

Figure 6.3. Permeation cell build. From the left, a holding tank(1) is connected to an air regulator(2) that controls the fluid pressure moving out the bottom of the vessel and through the ¾" hose to the permeation cell(3) (3" and 1" inner diameter cylinders at the top picture and 8" ID cylinder at the bottom picture). A force transducer(4) holding a bucket to capture the effluent from the porous media cylinder measures the outlet flow velocity (bottom left) from the 203 mm (8 inch) cylinder. The differential pressure transducer(5) hose connects to both ends of the permeation cell and sits behind the cell. The absolute pressure sensor(6) sits just downstream of the vessel. The doppler sensor(7) measures inlet flow velocity into the cell. The LabJack data acquisition device(8) sits above the setup.

As seen in Figure 6.3, the permeation cell consists of a clear PVC pipe that is the porous media cylinder(Figure 6.3(1)), with mesh covered ends to hold porous material in place during flow. There are three options for the size of the pipe, 1.5-inch, 4-inch, or 8-inch O.D., which can be used to accommodate different flow regimes by balancing flow rate with pressure drop. Smaller tubes have significantly greater pressure drops and flow rates while larger tubes have lower pressure drops and flow rates. The size of the porous media cylinder is limited to an inner diameter 8–12 times larger than the particle size diameter to reduce the effects of preferential flow along the side walls[187]. This limits the size of the permeation cell used to an 8-inch or smaller O.D. due to the increasing cost of clear PVC pipe at greater sizes and the large demand

on the equipment to maintain pressure drops and flow rates across a large diameter permeation cell. Based on the cylinder specifications, the coarse soil testing will be limited to gravels and smaller-sized soils that fall within the specified size range of 1 in. or smaller. Gravel will be used in the 8-inch cylinder while sand can be used in any of the three sizes of cylinders but is kept to the 1-inch and 3-inch inner diameter cylinders due to limited material. Larger cylinders will require more sensitive measurements and larger volumes of fluid but will be able to house both large and small coarse soil sizes, extending the range of testable gravels. Smaller cylinders will yield more sensitive measurements but are limited to sand and small gravel sizes. The doppler sensor(Figure 6.3(7)) can be seen mounted on the hose leading into the porous media cylinder to measure the inlet flow velocity, with a red knob. To measure the outlet flow velocity a force transducer(Figure 6.3(4)) holding a bucket has been installed to catch the effluent stream coming out of the porous media cylinder and converted to volumetric flow rate by density and scale to velocity by the hose diameter. An absolute pressure transducer(Figure 6.3(6)) is upstream of the porous media cylinder and a differential pressure transducer spans the porous media cylinder. The holding tank(Figure 6.3(1)) housing the drilling fluid with or without particles is equipped with a voltage controlled mixer to modulate mixing speed in the tank and disperse particles as well as possible before flowing through the system and into the porous media cylinder. The mixer is not pictured in the figure but sits at the top of the tank where the plug is. A LabJack data acquisition (DAQ) system(Figure 6.3(8)) is used along with a LabJack graphic user interface (GUI) made on LabView to record the flow velocity and pressure data in real-time during the experiment.

The system is run by first priming with water to remove air trapped in the system. Once primed the permeation cell is sealed off with a ball valve and the holding tank(Figure 6.3(1)) is charged with the desired drilling fluid (and solids as necessary). The pressure head of the holding tank is modulated with air to provide the driving force introducing the drilling fluid and solids into the porous media cylinder. A tank size of 30 gal was selected based on price point, flow regimes obtainable, and ability to hold sand. Vessels greater than 30 gal become twice or more expensive, and larger tank sizes become cumbersome to operate and transport. Vessels smaller than 30 gal will have openings that become easier to clog with sand. Drilling fluid is allowed to flow by releasing the holding tank into the system and allowed to reach steady-state. Drilling fluid of 1.5wt% bentonite slurry was selected because it exhibits non-Newtonian behavior similar to that of 3wt% bentonite slurry, but requires less material, and they are both at representative

concentrations that would be used in practice. The system independent variables are particle size, drilling fluid rheology, and drilling fluid inlet pressure. The dependent variables will be fluid flow velocity and fluid pressure across the porous media cylinder. Solids content can be introduced into the system by filling the pressure vessel with solids before the flow experiments. The line leading from the tank has a 1-inch O.D.; therefore, solids sizes should be less than 0.1 in. to prevent blockages[92]. Preferential flow along the smooth interior of the tubes should not be an issue because the particle to tube inner diameter ratio is small enough to reduce such effects, following ASTM standard D2434-19[187].

6.4 Results and Discussion

The data collected for this system encompass four rheological different fluids, water, 1.5wt% bentonite slurry, and both fluids with sand; two flow regimes, Darcy and inertial; and two porous media materials, gravel and sand. These parameters will be used to explore the effects of fluid rheology, fluid pressure, and particle to orifice ratio on clogging.

Table 6.2 summarizes the experiments performed with the permeation cell setup. All tests that used sand as the bed material were performed using a 25.4 mm (1-inch) inner diameter porous media cylinder. The tests with gravel as the bed material used the 203 mm (8-inch) inner diameter cylinder. Water and bentonite slurry are used with both bed materials and the addition of particles in the form of sand were also performed with the Gravel bed experiments with each fluid. bentonite slurry alone did not clog the sand or gravel. When sand was present, clogging occurred rapidly in the gravel bed - reducing fluid flow rates by an order of magnitude.

Table 6.2. Summary of clogging experiments performed using sand and gravel as the porous media material. All experiments performed with sand as the bed material are completed in the 25.4 mm (1-inch) cylinder and all gravel experiments are performed in the 203 mm (8-inch) cylinder.

Test #	Bed Material	Fluid Material
1	Sand	Water
2		1.5wt% bentonite Slurry
3	Gravel	Water
4		1.5wt% bentonite Slurry
5		Water - Sand (17 vol%)
6		Bentonite Slurry - Sand (17 vol%)

6.4.1 Flow through porous media

The fluid flow regimes were identified for these systems and appropriate pressure drop-flow rate models were applied. The flow regimes of this system spanned from 1 to 400 pore Reynolds numbers, where the lower range was captured by the sand bed while the gravel bed captured higher pore Reynolds numbers. This range of pore Reynolds numbers span Darcy and inertial[190].

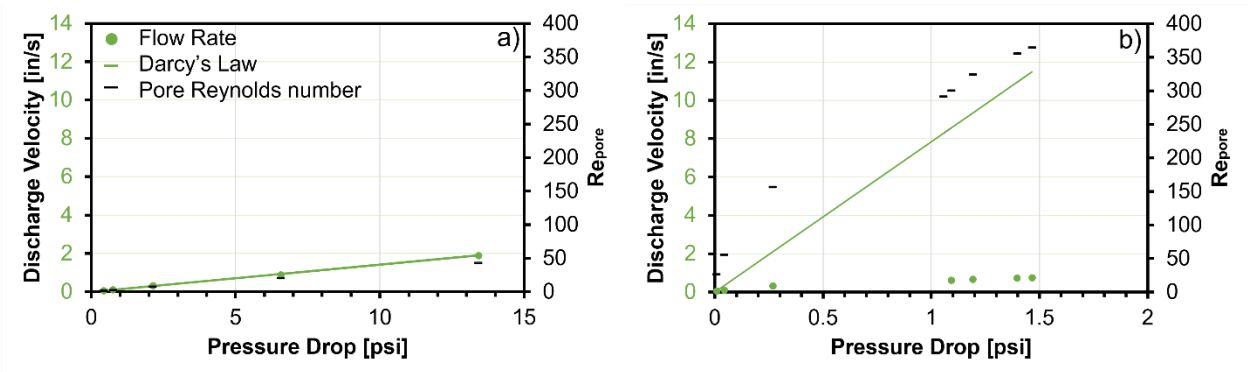

Figure 6.4. Darcy's law evaluation of pressure drop versus flow velocity for water flow through sand and gravel. a) is the 25 mm (1-inch) ID cell filled with sand, b) is the 203 mm (8-inch) ID cell filled with gravel. The green data points are data values collected for flow velocity over a range of pressure drop values corresponding to the left green axis. The trendline is Darcy's law estimation of pressure drop versus flow velocity using the low flow velocity values to calculate bed permeability for each cell material. The black dashes are the pore Reynolds numbers at each flow velocity and correspond to the right black axis.

In Figure 6.4a, pressure drop across the 1-inch cylinder filled with sand is graphed as a function of discharge velocity with the green dots as the data collected, the trend-line is Darcy's law, Equation 2.14, using the low discharge velocity data to calculate sand permeability, and the black dashes are the pore Reynolds number which are graphed on the secondary y-axis. Figure 6.4b is the same plot as Figure 6.4a but using data collected from water flow through the 8-inch cylinder filled with gravel. The data in 3a closely matches up with the theoretical curve predicted by Darcy's law even though the pore Reynolds number exceeds 25, the upper limit of the laminar regime[190]. However, in Figure 6.4b the data in the green dots have a much lower pressure drop than predicted by Darcy's law. In flow through gravel, the pore Reynolds number spans from 50 and up to 400 which is well beyond laminar flow and inertial contributions will play a larger role in the flow. The inertial contributions will lead to additional instabilities and turbulence leading to energy loss and will result in a lower flow velocity than predicted by Darcy's law as a function of pressure drop. Both bed materials also have similar porosities 0.36 for sand and 0.38 for

gravel, indicating the pore space volume between the two is similar, but tortuosity between the two can still vary widely. Since the gravel pore spaces are larger, there is a larger length-scale meaning a greater tendency for turbulence to develop, as seen in the pore Reynolds number, Equation 2.15 and Figure 6.4.

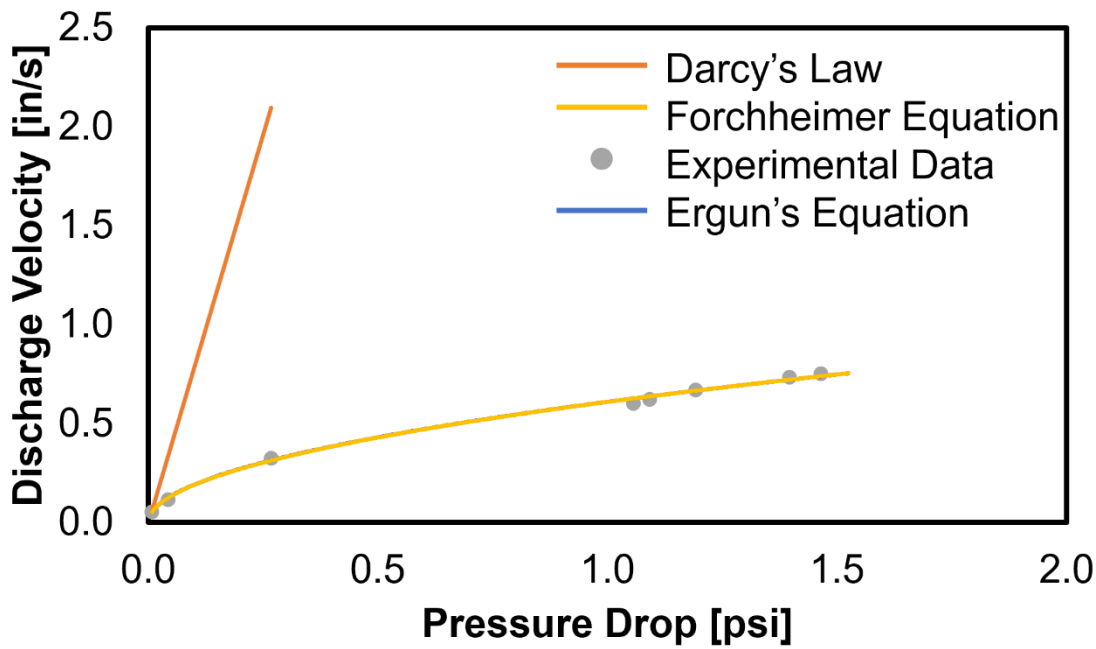

Figure 6.5. Pressure drop versus flow velocity data of water data collected in the 8-inch porous media cylinder filled with gravel, and flow through porous media models were fit to the experimental parameters to determine the effects unaccounted for in Darcy flow. Darcy's law expression is from calculating discharge velocity from the measured differential pressure of the system. Forchheimer's Equation and Ergun's Equation are from fitting to the experimental data.

Figure 6.5 presents pressure drop versus flow velocity data of water data collected in the 8-inch cylinder. The experimental data are the grey dots and the colored trendlines used Darcy's law, Ergun's equation, and Forchheimer's equation, equations; 2.14, 2.16, and 2.17 respectively. Darcy's law overpredicts the expected flow velocity for each corresponding pressure-drop because laminar flow, where energy loss is minimized is the major assumption. Darcy's law is determined from calculating the discharge velocity from an input of measured differential pressure drop of the system. In Ergun's equation, A and B were fitted to be 100 and 78.5, respectively, based on minimizing the average difference in pressure drop between the model prediction and the experimental data. Forchheimer's equation fits the experimental data well because its fittings parameters can adjust for both pressure drop and fluid discharge velocity. The fitting parameters were κ and F, they are the Kozeny-Carman (or Kozeny) constant and the

Forchheimer constant[73,191]. The Kozeny-Carman constant used was 5 for a packed bed and the Forchheimer constant was fit to be 25 by minimizing the average difference in pressure drop between the model and experimental data. The Forchheimer constant accounts for the internal structure of the porous media, which is caused by the packing resulting from the surface roughness of the gravel and aspect ratio[73]. The takeaways from this model fitting is that the flow regime in gravel is beyond laminar flow and contain inertial contributions caused by the flow rates and internal structure of the porous media, which is well captured in the Ergun and Forchheimer porous media flow models.

6.4.2 Clogging

Clogging occurs in gravel when sand fills the pore spaces of the gravel and severely constricts flow. In the porous media cylinders filled with gravel, clogging happens within 2-3 gravel diameters in depth and happens in less than 6 minutes depending on the flow conditions. The sand concentration was selected to be 17 vol% because soil cuttings can range from 5-25 vol% and the field test application for this work has cuttings dominated by sand so an extreme scenario would be 70% of the 25vol% soil cuttings were all sand.

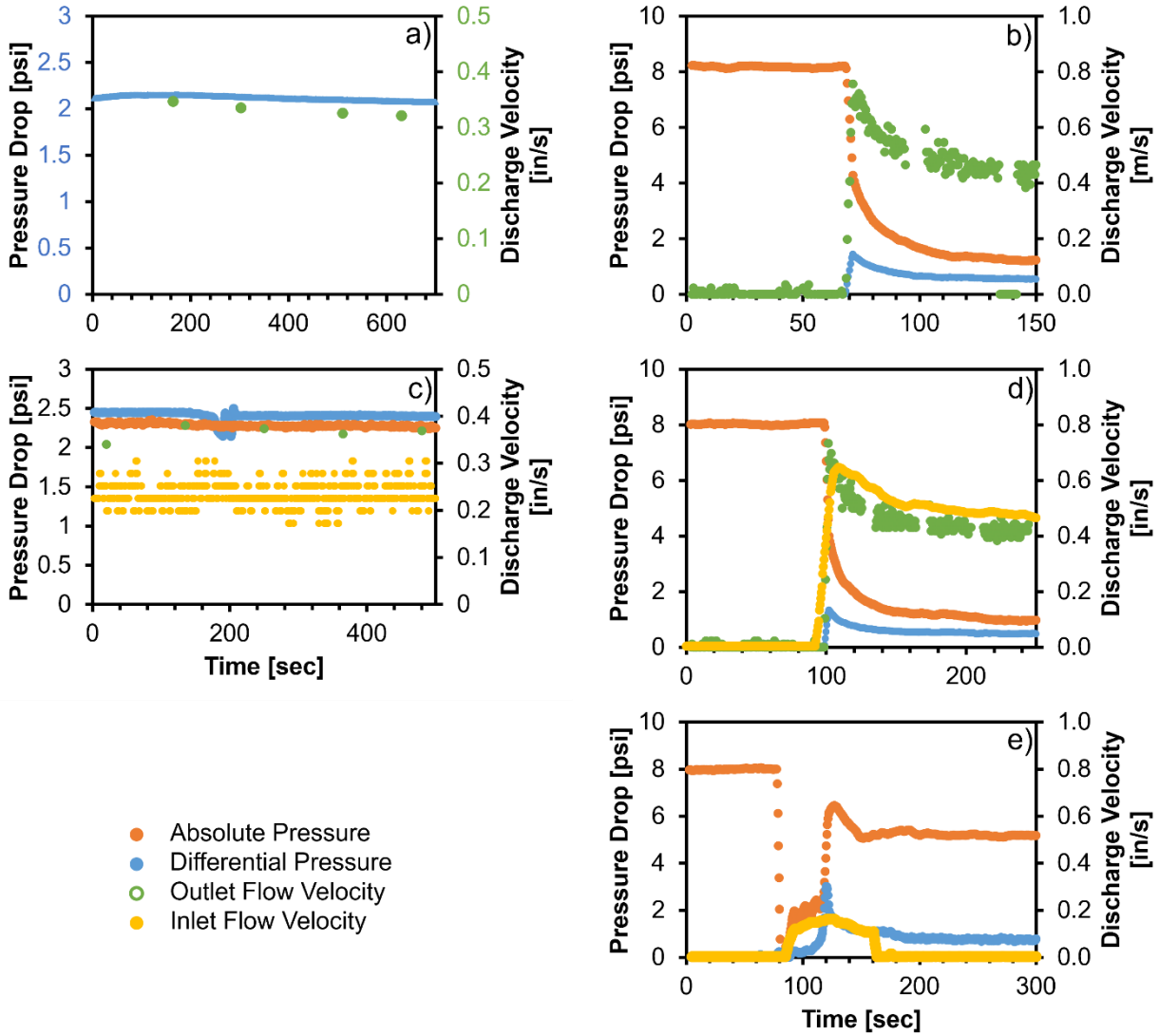

Figure 6.6. Real-time data of permeation cell tests comparing colloidal deposition to clogging. The left-hand side panels were tests performed in the 1-inch cylinder and the right-hand side panels were tests performed in the 8-inch cylinder. a) is water flowing through sand, b) water flowing through gravel, c) 1.5wt% bentonite slurry flowing through sand, d) 1.5wt% bentonite slurry flowing through gravel, and e) water and 17vol% (7wt%) sand flowing through gravel.

The data collected in Figure 6.6 is the real-time progression of pressure and discharge velocity change in situations with and without clogging. The absolute pressure upstream of the cylinder is in orange, the differential pressure across the cylinder is in blue, the flow into the cylinder is in yellow, and the flow out of the cylinder is in green. With each experiment the cylinder is filled with fluid and pressurized and isolated while sand particles and bentonite clay are added to the holding tank and mixed while pressurizing then introduced into the system through a ball valve. In Figure 6.6a and Figure 6.6c, water and bentonite clay respectively are

flowed through a sand bed, and each data set remains at a constant steady-state value because no clogging occurs. In Figure 6.6b and Figure 6.6d water and bentonite clay are respectively flowed through a gravel bed where at time 70 and 100 seconds the pressurized fluid flows into the porous media cylinders. The pressure drop decreases as the system reaches a steady-state because of the competition between inlet air pressure regulation and outlet fluid flow. Figure 6.6c and Figure 6.6d show that bentonite slurry alone cannot reduce fluid loss compared to their water equivalent experiments in Figure 6.6a and Figure 6.6b, which exhibit nearly identical pressure profiles.

In Figure 6.6e, pressurized water with sand at a concentration of 17vol% (7wt%) flows in at 80 seconds and the pressure drops to reach a steady-state value with flow but increases at 120 second as clogging occurs, providing a resistance to flow, allowing pressure to build and stabilize, after 180 seconds the system reaches a steady-state pressure because of clogging and at a lower pressure because some flow is still allowed to occur and confirmed visually. Clogging is indicated by the peak in flow when the sand is sensed by the doppler sensor then precipitously drops off as flow becomes restricted. The differential and absolute pressure values also follow this trend and reach a steady-state higher than without clogging. In all experiments of clogging, no sand flows out of the permeation cell and depositions occur within the first 2-3 gravel diameters. A drastic reduction of flow velocity and a rebuild of the fluid pressure happens in less than 2 minutes. This means that even in the event of fluid circulation loss, the porous media bed encountered can be filled with particles to regain fluid pressure and reduce fluid loss.

The sand size is between 0.59-1.19 millimeters and the gravel size and assumed pore size is 9.5 millimeters. An early seminal study of orifice jamming driven by gravity stated that blocking occurs when the particle diameter is ¼ the size of the orifice, while in our study the particle size is an order of magnitude smaller than the orifice[192]. As seen in Table 6.3, the real material sizes used that led to clogging has a ratio of 10.67 which closely matches the clogging criterion presented in the early work of Terzaghi and the thorough evaluation of soil material done by Foster and Fell[89,92].

Table 6.3. Summary of clogging criteria presented in the background in comparison to the actual filter and particle sized used in experiment that led to clogging.

Criteria	$D_{filter}/D_{particle}$	Actual $D_{filter}/D_{particle}$
Early Terzaghi	<10	10.67
Late Terzaghi	<4	
Casagrande	<6	
Foster & Fell	≤ 10.45	
To	≤2	

6.4.3 Exploring clogging

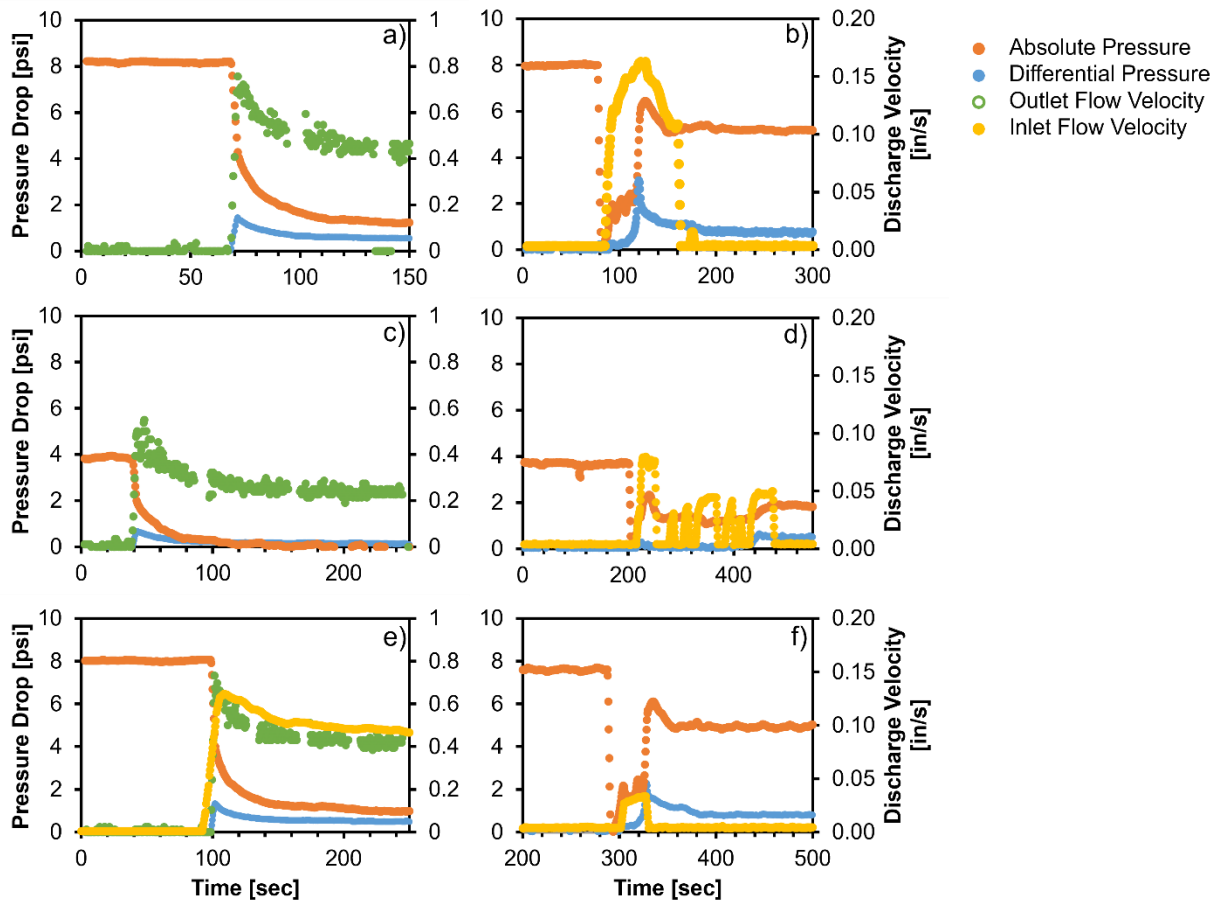

Figure 6.7. Real-time data comparisons of clogging before and after particles are introduced into the system. All panels are using the 8-inch cylinder filled with gravel. The left-hand side panels are flow of fluid without granular particles and the right-hand side is with sand in the fluid. a) water flowing through gravel starting at 8 psi of static pressure, b) water and 17vol% (7wt%) sand flowing through gravel starting at 8 psi of static pressure, c) water flowing through gravel starting at 4 psi of static pressure, d) 17vol% (7wt%) sand in water flowing through gravel starting at 4 psi of static pressure, e) 1.5wt% bentonite in water flowing in gravel starting at 8 psi of static pressure, f) and 17vol% (7wt%) sand in 1.5wt% bentonite in water flowing in gravel starting at 8 psi of static pressure.

Knowing that water-laden with sand will result in clogging, additional variables were investigated – including fluid pressure and rheology. In Figure 6.7, three scenarios of clogging were investigated. The left-side panels are experiments of only fluid flowing through gravel and the right-side panel are the same experiments but with 17vol% (7wt%) sand added to the fluid. The first scenario, Figure 6.7a and Figure 6.7b, is the base case of 8 psi static starting pressure using water where clogging occurs in less than 2 minutes. Scenario 2, Figure 6.7c and Figure 6.7d, is 4 psi static starting pressure using water where clogging occurs in under 5 minutes – a

longer time and with a stick-slip appearance of clogging and unclogging until clogs stabilize. While an interesting phenomenon, it is unclear whether this is an artifact of the permeation cell or the transitions between suspension settling and flow within the system before reaching the porous media cylinder. Scenario 3, Figure 6.7e and Figure 6.7f, is 8 psi static starting pressure using 1.5wt% bentonite slurry where clogging occurs under 2 minutes, like scenario 1. With differences in time and solids content, comparisons between the 3 scenarios can be challenging to differentiate.

6.4.4 Dynamics of clogging

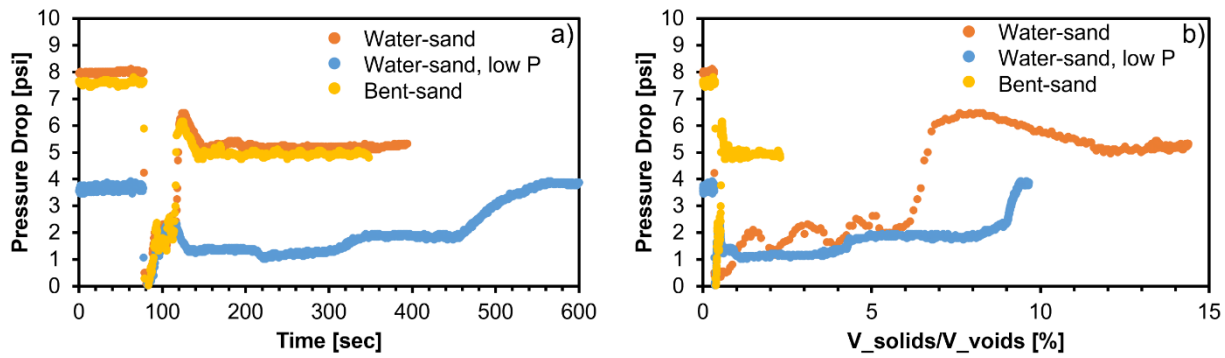

Figure 6.8. Clogging evaluation of the 203 mm (8 inch) cylinder between the 3 scenarios with sand laden fluids; water and sand at 8 psi, water and sand at 4 psi, and bentonite slurry and sand at 8 psi., a) is comparing the temporal clogging dynamics between the 3 scenarios, b) is comparing the 3 scenarios as a function of solids entering the cylinder relative to the total pore volume of the cell.

To better understand and compare the 3 scenarios presented in Figure 6.7, Figure 6.8 directly compares each scenario by time in Figure 6.8a and by solids entering the permeation cell Figure 6.8b. Absolute pressure is used to shed light on clogging between the 3 scenarios. In Figure 6.8a, the absolute pressure change with time between the water-sand and bentonite-sand (scenarios 1 and 3) closely match each other – indicating that clogging is not influenced by the addition of bentonite slurry. This is expected because as seen in Appendix C, Figure C.3, the fluid rheology of 1.5wt% bentonite slurry closely resembles that of water and any differences diminish with increasing shear-rate so any contributions should be negligible. In Figure 6.8b, the same absolute pressure data is plotted against how much solids are filling up the gravel pore spaces in the permeation cell. V_solids/V_voids is calculated using the inlet flow velocity and assuming a homogenous mixture of solids and fluids and using the known volume of sand entering the porous media cylinder divided by the total pore volume of the cylinder based on the

known mass of gravel in the cylinder and the particle density, Equations 6.1 and 6.2. Comparing scenario 1 and 3, less solids are needed to reach clogging when bentonite slurry is present, as indicated by less solids needed to rebuild fluid pressure in the system.

$$V_{solids} = \rho_{sand} \cdot Q_{inlet} \tag{6.1}$$

$$V_{voids} = \frac{m_{gravel}}{\rho_{gravel}} \tag{6.2}$$

The assumption of homogenous solid suspensions fails quickly because as seen during the experiment and collected videos, once clogging starts to occur or a slow flow velocity is imposed, the sand settles in the system, building up a bed that builds or erodes depending on the system flow velocity. The sand particles build up and clog the gravel bed not as a homogenous dispersion but instead as a bed development.

Based on orifice clogging and fluid-driven particulate clogging of orifices, there is a clear connection between pore and particulate diameter and the probability of clogging[80,84]. The fluid flow velocity also plays a role in clogging as well[83]. These two characteristics have been explored empirically and theoretically in literature for single orifice systems, but their application to porous media has not yet been done. The experimental data collected in Figure 6.7, in Figure 6.7, and Figure 6.8 support these two major drivers in clogging. To develop a clogging model, the ratio between particle and pore diameters that have been established for clogging and the extent of settling needs to be further explored. We hypothesize that fluid-driven clogging is a combination of particle to pore size ratio and the Shields parameter, where fluid-driven clogging becomes gravity-driven clogging when Shields parameter is less than 1. Shields parameter is defined in Chapter 4 with Equation 4.7 and states that the shear stress to buoyancy ratio determines whether particles settle or remain dispersed in the fluid. When Shields parameter is less than 1, settling occurs and will lead to an increase in particle density near the pores. Shields parameter will also capture the driving stress moving particles towards the pore to increase frictional contacts that will lead to clogging.

6.5 Conclusions

In this work we have combined fundamental concepts in granular matter for application in underground drilling to provide a means to mitigate fluid circulation loss when porous media is encountered. An experimental setup has been built to explore fluid-driven clogging to recover drilling fluid pressure. The setup is composed of a porous media cylinder filled with gravel while drilling fluid laden with sand is introduced into the cylinder under pressure and the fluid pressure, inlet and outlet flow velocity, and the differential pressure across the cylinder are measured. Experiments supported findings that bentonite slurry alone will be unable to clog gravel or sand, but when sand laden fluid is introduced into a gravel bed, clogging occurs within 200 seconds and fluid pressure can rebuild. Higher fluid pressures were also shown to clog faster. The fluid rheology of bentonite slurries was shown to not impact the dynamics of clogging but could require less sand to induce clogging. These experimental parameters were challenging to control and observe so future work could use Discrete Element Method (DEM) simulations that can handle large particle numbers ($> 10^3$) and be computationally inexpensive to explore the system's major parameters including the force ratio between fluid drag and gravity and the system geometry that affects particle bed formation near the pore. Similar to gravity-driven clogging of orifices, a critical particle density around an opening needs to be reached to clog. This work is an exploratory study of granular clogging because much of the fundamental physics remain unknown and are needed before the additional physics of inertial flow through porous media and particle rheology can be included in the problem. Fluid-driven clogging of porous media with granular particles, like gravity-driven clogging, require a particle density approaching the maximum packing fraction around the pore to clog. But unlike gravity-driven clogging, bed formation becomes a crucial part of the dynamics and clogging can occur with particle sizes smaller than typically seen in gravity-driven clogging.

6.6 Major Findings and Conclusions

Fluid-driven clogging of porous media with granular particles has been shown to have dynamics similar to gravity-driven clogging, but with particle bed formation and can be done with particle sizes smaller than expected compared to gravity-driven clogging. Once a particle bed is formed, the local particle density around the pore allows a particle bridge to form and clog, preventing other particles from flowing through.

CHAPTER 7 FUTURE WORK

Underground drilling covers a wide array of soft matter materials and the unique ways they are processed for this application. Beyond this thesis, the future advancements for each project and for this application overall will be discussed. Since the physics of each project are distinct and minimally overlap with each other, they will be discussed individually. The overall theme of the future work is in characterizing the unique variations soft matter materials experience due to the variability in geological conditions and how that translates to knowing what those changes are and how to operationally prepare for them. This chapter represents the work I have identified as the most interesting from a fundamental or practical perspective using the tools and techniques developed from this work.

7.1 Soil Viscometer

7.1.1 How to include a Herschel-Bulkley constitutive expression instead of a Bingham Plastic expression so that the thin-gap approximation is satisfied?

The effective inner radius approach is the calibration procedure of focus for this manuscript, as determined by the expected flow profiles of the measurement geometry. Our work then uses these developed procedures to apply to soil materials assuming a Herschel-Bulkley constitutive relationship[193].

$$\tau_{r\theta} = \tau_0 + K\dot{\gamma}^n \tag{7.1}$$

$$\tau_{r\theta} = \tau_0 + K\left[\left|r\frac{\partial}{\partial r}\left(\frac{u_\theta}{r}\right)\right|\right]^n$$

$$\frac{\partial\left(\mathrm{r}^2(\tau_{\mathrm{r}\theta})\right)}{\partial \mathrm{r}} = 0 \tag{7.2}$$

$$\frac{u_\theta}{r} = -\frac{1}{2}nr\left[r^{-n-2}\left(\frac{c_1}{K} - \frac{\tau_0}{K}r^2\right)\right]^{\frac{1}{n}}\left(1 - \frac{\frac{\tau_0}{K}r^2}{\frac{c_1}{K}}\right)^{-\frac{1}{n}}[2F_1(a,b,c,r)] \tag{7.3}$$

$$[2F_1(a,b,c,r)] = \sum_{k=0}^{\infty}\frac{(a)_k(b)_k}{(c)_k}\frac{r^k}{k!}$$

$$\Gamma = 2\pi R_i h \cdot R_i \cdot \tau_{r\theta}|_{r=R_i} = 2\pi \mathrm{R_i^2 h} \cdot [\tau_0 + K\dot{\gamma}^n] \tag{7.4}$$

$$\eta(\dot{\gamma}) = \frac{\Gamma}{N}\frac{\left(\frac{R_e}{R_i}\right)^2 - 1}{8\pi^2 L R_e^2} \tag{7.5}$$

$$\dot{\gamma}(N) = \frac{2\pi N}{\ln\left(\frac{R_e}{R_i}\right)} \tag{7.6}$$

The calibration procedure is taking the Herschel-Bulkley constitutive equation, Equation 7.1, and plugging it into the momentum balance using Navier-Stokes in the θ-direction, Equation 7.2. From these two expressions, the velocity profile is solved for using Mathematica, yielding Equation 7.3. The expression for torque is shown with Equation 7.4 and will be used to determine the effective inner radius calibration constant, R_i. Using torque and rotation rate from the mixer to be calibrated and experimental data of the Herschel-Bulkley parameters found on a TA Instruments DHR-3 rheometer, the calibration constant can be solved for. The Herschel-Bulkley model generates a geometric series when the velocity profile is solved for, and Matlab's geometric series function is used to determine the Ri value. Ri will be used as the measurement geometry's calibration constant and be used to solve for the effective shear-rate and viscosity measured in the soil viscometer, using Equations 7.5 and 7.6. The particle size that can be measured by the system is constrained to granular material that does not approach the gap size, <0.1*(Re-Ri) . The calibration fluid of choice was bentonite clay because of its high viscosity and low cost.

7.1.2 How to characterize the viscometry of clay materials that have history?

The calibration of the soil rheometer and the process to calibrate left many unanswered questions and one major open question. The open question is that in clays, at lower water content the material will transition from fluid-like to more plastic-like, characterized qualitatively by the material breaking. At 16.7wt% bentonite the sample in the soil rheometer will still flow but at higher concentrations, like 33.3wt% then the clay breaks apart and reforms by cohesion, history becomes an important characteristic of the material. Seeing Figure 3.6 of 33.3wt% bentonite one could easily imagine a continuous breakdown and build up for clay throughout the soil rheometer chamber, meaning that the geometry mixing the material is affecting the sample in a specific way. Which then begs the question, if history is important and the mixing of the material no longer measures universal viscometric properties then is there any way to characterize the material in a system not in a specific application? Because a main advantage of rheometers is to measure viscometric properties of materials at a representative shear-rate that the same sample would experience in a desired application. But if you can no longer replicate the same kind of deformation with simple shear then what do you do? To begin to explore this, turning the angled

flight geometry into paddles like a vane geometry to achieve more uniform deformation of the sample by making sure more of the material is yielding rather than getting lost in the void space between flights. That could either extend the application of the soil rheometer, or more likely be deforming a plastic-like material in a geometry specific way so that universal viscometric properties cannot be obtained. Then this would fall into the realm of granular media which has made great progress but still face many challenges in producing widely accepted constitutive relationships. But unlike the traditional granular media, sand, the interactions between broken clay is deformations, breakage, and adhesion rather than predominately frictional. Which will result in unique modelling and theoretical challenges not yet addressed by the rheological or granular physics communities. Much fundamental theoretical work is still needed before plastic-like clay rheology can yield universal quantities.

There is precedent in biomass literature for incorporating history effects into viscometric measurements of complex fluids, but these are based on the nature of colloidal versus granular fiber suspensions. Colloidal suspensions do not contribute history effects into a fluid because Brownian motion occurs at a fast enough time-scale to erase shear history. Granular fibers are at a larger length-scale which Brownian motion no longer effects so there is no means of erasing the shear history and how these materials are deformed affects their measured viscometric properties. Clay materials with low water content do not have as clear a distinction with particle size but rather becomes a denser colloidal gel with less water and begins to retain the shear history of the fluid.

Since the water content of clays underground fall into this regime where history will matter, how it is characterized with the soil viscometer needs to be the same between samples so that trends can be obtained. The next challenge for this setup is in modifying the existing geometry to deform any clay material in the same way and not add sample dependent contributions to the shear history. The torque rheometer or a design like it would be a good first look at a design that is sample independent for a wide range of concentrations. Once this has been done then the dynamics of how each type of clay soil (sandy clay, silty clay, clay loam, and heavy clay) will change viscometrically with shear history.

7.1.3 Do granular particles influence viscometry similar to colloids with hard-sphere interaction potentials?

With the calibrated soil viscometer real, dirty material can be characterized viscometrically and their contributions to pure soil materials of only clay. Granular materials are

currently incredibly difficult to measure with lab-scale instruments because particles match or exceed the measurement gap, leading to jamming and producing torque values non-representative of the sample but rather the sample interacting with the instrumentation[194]. To exploit now the ability of measuring samples with granular particles the first tests should be in determining whether Einstein's relationship for the contribution of particles at low volume fraction (particle collisions are negligible) and extending that characterization to higher volume fractions (particle collisions are non-negligible). This would initially be done with smooth spheres, then the influence of anisotropic particles, and then real particles with a wide distribution employing granulometry to characterize the variations. And then compare these results to the scant experimental evidence existing and extend simulation work of whether realistic particles behave the same as model particles[195–198].

7.1.4 What micromechanical modifications are additives making to soil materials to "improve" their viscometric properties?

Beyond particles, there are also many empirical and anecdotal methods of dealing with clays in underground drilling from polymer, oil, suspension additives and many more. But all of those additives have not been explored beyond unreliable field tests and do not use material properties but rather indexing devices that can only quantify differences specific to a device. This viscometer provides material property information that can quantitatively be applied to any system so that a fundamental study can be performed to assess how additives are affecting clay materials and then connect those changes to bulk viscometric properties.

7.2 Flow Loop

7.2.1 How does the formation and dynamics of a particle bed alter the hydrodynamic and viscometric properties of the cuttings returns?

As discussed in Chapter 4, fully dispersed particles were needed to capture the viscometric properties of the drilling fluid slurry with soil cuttings. This was an intentional design of the experiment due to the complexity of particle bed formation and their effects on both fluid rheology and the flow profiles of the fluid. When a particle bed is formed then particles are no longer dispersed in the drilling fluid which reduces hydrodynamic interactions between particles and will alter the viscometric properties of this material. But when a bed is formed the dimensions of the flow loop also change depending on the geometry and dynamics of the particle bed. This can lead to a wide variation in pipe diameter along the flow loop that is also dependent

on time and flow rate. Since the effects of particle content have already been quantified in the work of Chapter 4, the next step is to systematically alter the soil cuttings content in heterogenous flow with particle settling and bed formation, measuring the effective hydrodynamic change while measuring the characteristics of the formed bed to determine how the geometry of the flow loop is changing and the soil cuttings content still dispersed in the drilling fluid.

7.2.2 How do clay cuttings affect drilling fluid rheology over time?

One of the assumptions made in Chapter 4 is that the clay soil cuttings are broken up and become dispersed in the drilling fluid. This assumption was valid because the drill site that was chosen and model soil materials were made for was intentionally chosen because of its high sand and silt content ($\sim 70 wt\%$)but low clay content ($\sim 30 wt\%$). While in practice, the geological breakdown of a location cannot be so easily chosen, and clay is a commonly encountered soil material. The flow loop setup constructed in this work could be used to determine how the drilling fluid with clay cuttings rheology changes with time during breakdown. Because the flow loop circulates the complex fluid through a pump, then clay cuttings will be broken down over time and their corresponding power-law parameters can be measured as a function of clay cuttings breakdown. This approach could be applied to the variations of clay materials that can be expected underground from pure clays of bentonite, kaolinite illite; sandy clay, silty clay, clay loam, and many other variations.

7.3 Series Distributed Pump

7.3.1 Is separation distance important when the rear propeller is operating at a lower rotational speed in contra-rotating propellers?

The literature on contra-rotating propellers functioning as axial pumps is fairly limited, but the work that is there focuses on the rotation rate of each propeller. When operated at the same rotation rate then the rear propeller is overloaded and requires a significant amount of work inputted into it[183]. To address this, the rear propeller is operated at a lower rotation rate, and the rate is …. Because … The work covered in Chapter 6 explored the separation distance between propellers while operating at the same rotation rates. The next steps for this work is to explore those two variables together and determine how both separation distance and an offset in rotation rate will impact their performance as a flow pump. This will determine whether one parameter is

more important than the other, whether it depends on operating conditions, or whether they are equally crucial and provide a significant improvement to performance.

7.3.2 Does propeller design play a larger role in pressure boost when the two propellers are not operating at the same rotational rate?

The other question addressed in Chapter 6 was the effects of singular propeller design on their performance as contra-rotating propellers and was determined to be negligible even though the differences in blade design are quantitatively, qualitatively, and theoretically different. Which then begs the question of whether operating the propellers at different rotation rates will generate flow profiles that are more dependent on propeller design rather than the separation distance between propellers.

7.3.3 How well do any of these empirical design principles hold up with non-Newtonian fluids, like a bentonite slurry?

All of the work covered in Chapter 6 was using water with a rheologically insignificant amount of bentonite present but the application for these axial flow pumps is with drilling fluids of bentonite slurries and with soil cuttings. The general micromechanical model of contra-rotating propeller benefits on performance is dependent on the flow profiles generated by each propeller and their interaction between the two. But from a basic understanding of non-Newtonian fluid flow through pipes tells us that the profiles can be severely different between fluids, transitioned from a fully-developed velocity profile that's quadratic in nature to plug-flow with the bulk of the flow moving as a front while the fluid nearest the pipe walls shear-thins and lubricates the bulk of the flow. Due the complex fluid dynamics of propellers, they already require computational fluid dynamics to evaluate, the addition of non-Newtonian fluids creates a challenging system that will need to be interrogated by an experimental exploration to support the simulation work that is able to be completed for this system.

7.3.4 What would need to be done so that this work could lead to building empirical models?

First there needs to be a normalization for these systems. Current axial pump uses rotor-stator systems, and propeller design is based off of turbine design principles. And propeller design is usually done using CFD to predict the performance. So to encompass all of the variables that go into propeller design, more data needs to be collected with the same types and

configurations of propellers so that statistically significant trends can be determined for the data as a function of the system variables (L/D, RPM, throttle, differences in rotation rate).

7.4 Permeation Cell

The experiments performed in Chapter 6 were informative in learning the fluid-driven clogging can result in drilling fluid pressure recovery, but the understanding of how fluid-driven clogging occurs, and the driving factors are still unclear. Simulations are a tool that can be used to further explore the major forces at play in this system. For granular systems where it is important to characterize discrete particles and their relationship to clogging, Discrete Element Method (DEM) is the standard method[199]. DEM can also be coupled with Computational Fluid Dynamics (CFD), but the addition of CFD makes these systems computationally expensive when hundreds of thousands of particles are present, which are for this system. Leaving DEM as the cost-effective and precise option to further explore this system.

7.4.1 Simulation proposal

DEM simulations are a more accessible and cost-effective tool to explore the interactions between system geometry and forces affecting particles that lead to fluid-driven clogging in porous media. Large-scale Atomic/Molecular Massively Parallel Simulator (LAMMPS) is proposed to model a simple version of the developed experimental system.

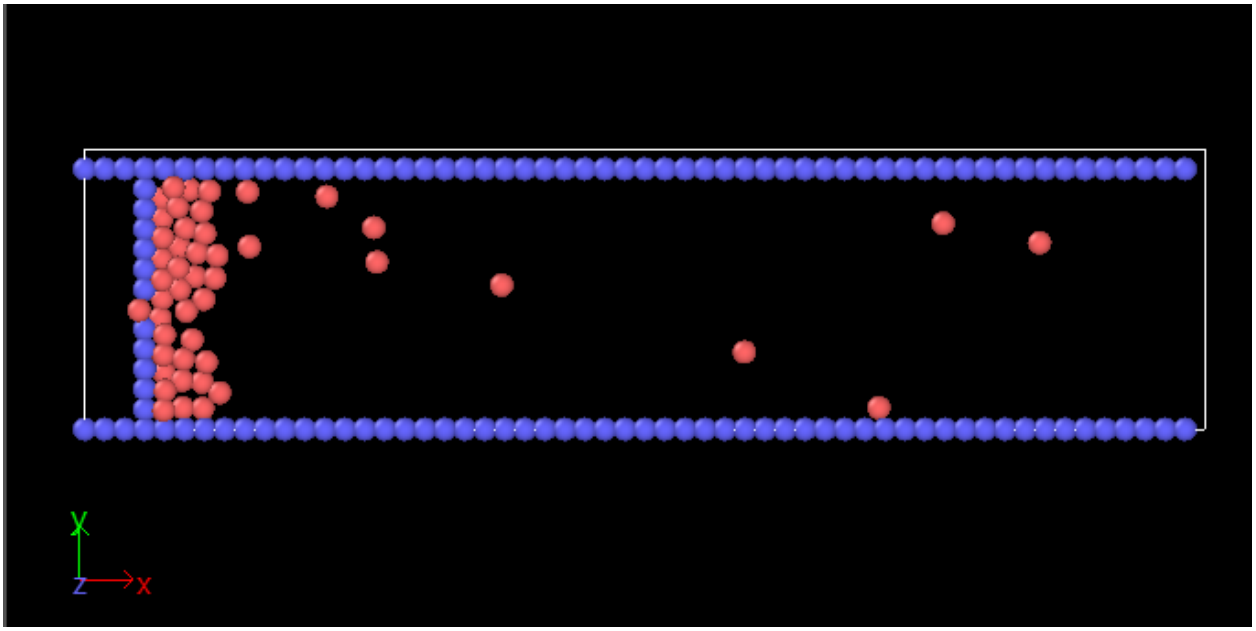

Figure 7.1. LAMMPS system setup

These LAMMPS simulations are composed of stationary blue particles representing gravel that geometrically constrain the system dimensions of the channel and pore. Red particles representing sand that are governed by hard sphere dynamics with the addition of an elastic modulus and frictional interactions captured in the granular package within the LAMMPS software. The system is 2-dimensional and built by setting up the blue-gravel particles to form a boundary capturing the red-sand particles and on the far left there is an open space representing the gravel pore with a boundary that removes any red-sand particles that passes through the pore. Within the system the controlled independent variables are the deposition rate of the red-sand particles, the width of the channel relative to the width of the pore, the width of the pore relative to the particle size, the ratio between horizontal and vertical forces representing gravity and a constant fluid driving force, and seed values to introduce perturbations into the system. The measured parameter is clogging, determined by a particle density calculation once the system reaches a particle density visualized as clogging and the particles can no longer flow out of the system then the system is determined to be clogged. If this density value is not reached, then the particles will be freely flowing and clogging has not occurred. With this system, a parameter sweep is performed with the independent variables to capture expected dimensionless parameters that would be experienced by our experimental system. As discussed in Chapter 6, section 6.4.4, the dominant parameters will be both the particle to pore size ratio and Shields parameter because it is hypothesized that fluid-driven clogging will become gravity-driven clogging once

particle settling occurs and particle density increases to that of gravity-driven systems while maintaining a driving stress to move particles to the pore.

7.4.1.1 Work done to-date

A model system has been developed in LAMMPS that runs at the appropriate time-scales to capture the physics that are occurring within the system and with the interactions representative for granular particles. The model system has also been generalized so that the system parameters can be inputted through the command line or a bash script to quickly submit multiple jobs for each parameter combination rapidly rather than manually. Hydrodynamics are not included in the system for simplicity of the simulations and because of the resource limitations to build and include hydrodynamic interactions.

7.4.1.2 Work to be done

The work left to be done is running the simulations on a supercomputer and writing a python script to post-process the density values of the system so that figures can be made of the data to quantify when clogging occurs and under which geometric and force conditions leads to this phenomenon. The expectation is that the particle bed formation around the pore will be the distinguishing dynamics that will lead to clogging because the geometric and force parameters constrain whether a bed is formed and whether a great enough particle density will be reached that particles can bridge across the pore to stop the flow of particles through the orifice.

The findings of these simulations will provide greater insights into the major driving forces behind clogging and provide guidance in applying that to mitigate fluid circulation loss in underground drilling when porous media is encountered underground. Both fundamental and practical information will be learned in the operation of underground drilling to control particle density and clogging.

7.4.2 How would hydrodynamic contributions affect clogging?

If they do, then how would these contributions vary with particle size of geologically relevant materials, like gravel, cobble, boulders, and distributions in between?

The simulation work performed in Chapter 6 is only granular particle interactions and does include fluid dynamics, yet it is well-known that behind the flow of each particle is a wake that results in flow profiles that will affect the flow of particles around it in a local area[8,9]. Since

the particles explored in Chapter 6 are predominately settled and moving as a bed, the hydrodynamic effects are smaller than that of gravity and is not a major parameter. However, when flow increases and flow regimes beyond settling are reached then hydrodynamics will provide greater contributions to the clogging physics. Hydrodynamics were not addressed in this work because combining particle analysis (DEM) with fluid dynamics (CFD) is a large programming undertaking even using existing software and would be a large Ph.D. project. Currently fluid-driven clogging has been captured by probabilistic models and does not incorporate physics from first-principles. The effects of hydrodynamic contributions remain unclear and need to be further explored to expand our understanding of fluid-driven clogging to more flow regimes and the effects of each flow regime on clogging.

7.4.3 What are the effects of non-Newtonian fluids on flow through porous media at larger pore sizes?

And how does the knowledge from polymer solutions translate to bentonite slurries? Drag reduction can be seen with polymer solutions and suppression of turbulence but it is unclear whether colloidal clay platelets will micromechanically behave the same[200].

Packed beds are a common chemical unit operation with flow through packed beds have been studied for a long period of time and the flow of polymer solutions through packed beds also been studied for a long period of time. But the addition of a non-Newtonian fluid to this system lead to artifacts in the flow rate to pressure drop data that could not be explained until recently with elastic turbulence[201]. This then begs two questions; one, the microstructure of clay platelets will not give the same elastic characteristics that polymer solutions would give so under those same conditions of flow through porous media would bentonite slurries leave similar artifacts in the data; two, how would instabilities translate to larger length-scales with larger pore sizes like those seen in gravel and larger porous media? The pressure drop to flow rate relationship models for non-Newtonian fluid flow through porous media has been researched for a long time but extending that work to flow regimes greater than laminar flow and for materials besides polymer solutions still remains largely unexplored.

7.4.4 Can the particle bed formation that results in clogging be shown with a model experimental system? If so, then can those dynamics be captured in a time-dependent model?

Bed formation of granular particles have been explored experimentally for a while but the theoretical framework behind this phenomenon is still in development. Because of this,

experimental work of a model system of bed formation and its connection to clogging is critical in learning more about the system and understanding its fundamental physics. The work of Chapter 6 presents a model system that could happen in practice and measures clogging, but the visualization and observations of clogging were not able to be made because of the connecting parts. A fully clear system can be constructed to further explore this clogging phenomenon and provide insights that would help build up knowledge that can be used to generate models to capture the physics of the system. Then the step after that would be capturing the dynamics of bed formation and couple that with fluid-driven clogging.

CHAPTER 8 CONCLUSIONS

In underground drilling there are many challenges, and they can be broken up into two areas, material processing and technological. Technological challenges are related to design and building machinery that can breakdown and process soil materials. Material processing challenges are related to understanding how soil materials should be broken down and processed based on the fundamental physics of the material. Technological challenges are more easily accessible to address by a wide audience, but material processing challenges require specialized fundamental knowledge. The aim of this thesis work was in identifying and filling in fundamental knowledge gaps for material processing. Chapters 3-6 have addressed challenges in one of the two processing steps, breaking down soil material experienced by the cutterhead underground, fluidizing those soil cuttings and transporting them out of the tunnel, or potential challenges that could occur in one of these steps.

In the breakdown of in-situ soil materials, Chapter 3 characterizes low water content soils and the effects of granular particles on the viscometry of those soil materials, providing information on the stresses and torques that need to be generated by technology to break down these soil materials. This work also taught us that at low enough water content then the viscometric properties exhibited by clay materials become dependent on how it is broken down. This work also provides a path forward in testing additives that could be used to alter the viscometry of soil materials to make them easier to breakdown. Chapter 7 presents a novel setup to explore characterization of interfacial material with optical microscopy, which can be used with foam conditions that historically have been ineffective with clay materials. The sub-phase exchange cell setup can characterize a breadth of interfacial properties for a range of foam conditioners to distinguish the most important interfacial property if there is one that would stabilize foams in the presence of clay materials. Alternatively, oils have also been used in industry to ease the flow ability and breakdown of clay materials, which can be quantified in the soil viscometer as well as foam conditioners.

The fluidization of soil cuttings were covered in Chapters 4-6, with chapter 4 quantifying the effects of soil cuttings on viscometric properties of drilling fluid returns. The expected viscosity and shear-thinning properties of drilling fluids will increase with greater cuttings content, and the extent of cuttings settling will alter the viscometric properties of the drilling fluid returns. And with the caveat that due to variations in soil cuttings mineralogy and geological makeup, cuttings

from an expected drill site need to be used to obtain accurate viscometric properties. Chapters 5 and 6 address situations where fluidization is interrupted due to frac-out from high drilling fluid pressure, in Chapter 5, or due to fluid circulation loss from encountering porous media, in Chapter 6. To mitigate high drilling fluid pressure, axial flow pumps can be installed in the form of contra-rotating propellers along the drill string to distribute the pressure drop and theoretically extend the length of a borehole and speed of drilling indefinitely. To mitigate encountering porous media, particles can be added to the drilling fluid that will form a bed that will clog the pore space of the porous media, allowing fluid pressure to rebuild and continue fluidizing soil cuttings.

In summary, the findings from this thesis identifies material processing challenges in underground drilling and explores the tools and physics necessary in addressing these challenges. Understanding the fundamental physics of soil materials will guide the design of drilling technology and inform the future capabilities of drill strings. And the devices and methodologies needed to address and explore these physics have been developed.

REFERENCES

(1) Motahhari, H. R.; Hareland, G.; Bond, B. Method of Optimizing Motor and Bit Performance for Maximum ROP. *J. Can. Pet. Technol.* **2009**, *48* (6), 6.

(2) Lang, G.; Pfeff, D. Direct Pipe® as Alternative to HDD in Permeable Soil Conditions. In *Volume 1: Design and Construction; Environment; Pipeline Automation and Measurement*; American Society of Mechanical Engineers: Calgary, Alberta, Canada, 2014; p V001T03A003. https://doi.org/10.1115/IPC2014-33049.

(3) Ansari, A.; Sowaidi, S. A.; Yoshimoto, K. Case Study: Drilling the Longest and Fastest Surface Hole Section in United Arab Emirates U.A.E; SPE: Mumbai, India, 2017; p D031S015R004. https://doi.org/10.2118/185436-MS.

(4) Willoughby, D. A. *Horizontal Directional Drilling: Utility and Pipeline Applications*; McGraw-Hill civil engineering; McGraw-Hill: New York, 2005.

(5) Miles, R.; Gough, A.; Silverthorne, B. The Northampton Mole Project – A Case Study of the Application of Freight Pipelines in an Urban Environment; Arlington, TX; p 10.

(6) Hojjati, A.; Jefferson, I.; Metje, N.; Rogers, C. D. F. Sustainability Assessment for Urban Underground Utility Infrastructure Projects. *Proc. Inst. Civ. Eng. - Eng. Sustain.* **2018**, *171* (2), 68–80. https://doi.org/10.1680/jensu.16.00050.

(7) Santos, H.; Placido, J. C. R.; Oliveira, J. E.; Gamboa, L. Overcoming Hard Rock Drilling Challenges; SPE: New Orleans, LA, 2000; p 6.

(8) Andreotti, B.; Forterre, Y.; Pouliquen, O. *Granular Media: Between Fluid and Solid*; Cambridge University Press: Cambridge, 2013.

(9) Mewis, J.; Wagner, N. *Colloidal Suspension Rheology*; Cambridge Series in Chemical Engineering; Cambridge: Cambridge University Press., 2011.

(10) Allouche; Ariaratnam; Lueke. Horizontal Directional Drilling: Profile of an Emerging Industry. *J. Constr. Eng. Manag.* **2000**, 68–76.

(11) Mohd Norizam, M. S.; Nuzul Azam, H.; Helmi Zulhaidi, S.; Abdul Aziz, A.; Nadzrol Fadzilah, A. Literature Review of the Benefits and Obstacle of Horizontal Directional Drilling. *IOP Conf. Ser. Mater. Sci. Eng.* **2017**, *271*, 012094. https://doi.org/10.1088/1757-899X/271/1/012094.

(12) Allouche, E. N.; Ariaratnam, S. T.; Lueke, J. S. *D. A Survey of Current Horizontal Directional Drilling Practices in Canada and the United States*; Horizontal Directional Drilling: Utility and Pipeline Applications, 1st Edition; 2005.

(13) *How Do You Steer a Drill Below The Earth?*; 2022. https://www.youtube.com/watch?v=JAhdb7dKQpU.

(14) Hair, C. W. *Site Investigation Requirements for Large Diameter HDD Projects*; Seminar; U.S. Fish and Wildlife Service: St. Joseph, Missouri, 1994; p 42.

(15) Schlumberger. *Bottomhole assembly*. Energy Glossary. https://glossary.slb.com/en/terms/b/bottomhole_assembly.

(16) Bogue, D. C.; Metzner, A. B. Velocity Profiles in Turbulent Pipe Flow. Newtonian and Non-Newtonian Fluids. *Ind. Eng. Chem. Fundam.* **1963**, *2* (2), 143–149. https://doi.org/10.1021/i160006a010.

(17) Barbati, A. C.; Desroches, J.; Robisson, A.; McKinley, G. H. Complex Fluids and Hydraulic Fracturing. *Annu. Rev. Chem. Biomol. Eng.* **2016**, *7* (1), 415–453. https://doi.org/10.1146/annurev-chembioeng-080615-033630.

(18) Luckham, P. F.; Rossi, S. The Colloidal and Rheological Properties of Bentonite Suspensions. *Adv. Colloid Interface Sci.* **1999**, *82* (1), 43–92. https://doi.org/10.1016/S0001-8686(99)00005-6.

(19) Das, B. M. *Fundamentals of Geotechnical Engineering*, 5th edition.; Cengage Learning: Mason, OH, 2015.

(20) Guyon, E.; Delenne, J.-Y.; Radjaï, F.; Butler, E.; Kamrin, K. *Built on Sand: The Science of Granular Materials*; The MIT Press: Cambridge, Massachusetts, 2020.

(21) Brown, R. XXVII. A Brief Account of Microscopical Observations Made in the Months of June, July and August 1827, on the Particles Contained in the Pollen of Plants; and on the General Existence of Active Molecules in Organic and Inorganic Bodies. *Philos. Mag.* **1828**, *4* (21), 161.

(22) Tetra Tech EM Inc. *Analysis of Selected Enhancements for Soil Vapor Extraction*; Analysis EPA-542-R-97-887; United States Environmental Protection Agency, 1997.

(23) Marchi, M.; Gottardi, G.; Soga, K. Fracturing Pressure in Clay. *J. Geotech. Geoenvironmental Eng.* **2014**, *140* (2), 04013008. https://doi.org/10.1061/(ASCE)GT.1943-5606.0001019.

(24) Andersen, K. H.; Rawlings, C. G.; Lunne, T. A.; By, T. H. Estimation of Hydraulic Fracture Pressure in Clay. *Can. Geotech. J.* **1994**, *31* (6), 817–828. https://doi.org/10.1139/t94-099.

(25) Krieger, I. M.; Dougherty, T. J. A Mechanism for Non-Newtonian Flow in Suspensions of Rigid Spheres. *Trans. Soc. Rheol.* **1959**, *3* (1), 137–152. https://doi.org/10.1122/1.548848.

(26) Chong, J. S.; Christiansen, E. B.; Baer, A. D. Rheology of Concentrated Suspensions. *J. Appl. Polym. Sci.* **1971**, *15* (8), 2007–2021. https://doi.org/10.1002/app.1971.070150818.

(27) Sweeny, K. H.; Geckler, R. D. The Rheology of Suspensions. *J. Appl. Phys.* **1954**, *25* (9), 1135–1144. https://doi.org/10.1063/1.1721828.

(28) McGeary, R. K. Mechanical Packing of Spherical Particles. *J. Am. Ceram. Soc.* **1961**, *44* (10), 513–522. https://doi.org/10.1111/j.1151-2916.1961.tb13716.x.

(29) Poslinski, A. J.; Ryan, M. E.; Gupta, R. K.; Seshadri, S. G.; Frechette, F. J. Rheological Behavior of Filled Polymeric Systems II. The Effect of a Bimodal Size Distribution of Particulates. *J. Rheol.* **1988**, *32* (8), 751–771. https://doi.org/10.1122/1.549991.

(30) Goto, H.; Kuno, H. Flow of Suspensions Containing Particles of Two Different Sizes through a Capillary Tube. *J. Rheol.* **1982**, *26* (4), 387–398. https://doi.org/10.1122/1.549682.

(31) Kolli, V. G.; Pollauf, E. J.; Gadala-Maria, F. Transient Normal Stress Response in a Concentrated Suspension of Spherical Particles. *J. Rheol.* **2002**, *46* (1), 321–334. https://doi.org/10.1122/1.1428320.

(32) Gadala-Maria, F.; Acrivos, A. Shear-Induced Structure in a Concentrated Suspension of Solid Spheres. *J. Rheol.* **1980**, *24* (6), 799–814. https://doi.org/10.1122/1.549584.

(33) Narumi, T.; See, H.; Honma, Y.; Hasegawa, T.; Takahashi, T.; Phan-Thien, N. Transient Response of Concentrated Suspensions after Shear Reversal. *J. Rheol.* **2002**, *46* (1), 295–305. https://doi.org/10.1122/1.1428321.

(34) Michot, L. J.; Bihannic, I.; Porsch, K.; Maddi, S.; Baravian, C.; Mougel, J.; Levitz, P. Phase Diagrams of Wyoming Na-Montmorillonite Clay. Influence of Particle Anisotropy. *Langmuir* **2004**, *20* (25), 10829–10837. https://doi.org/10.1021/la0489108.

(35) Bonn, D.; Kellay, H.; Tanaka, H.; Wegdam, G.; Meunier, J. Laponite: What Is the Difference between a Gel and a Glass? *Langmuir* **1999**, *15* (22), 7534–7536. https://doi.org/10.1021/la990167+.

(36) Dor, M.; Levi-Kalisman, Y.; Day-Stirrat, R. J.; Mishael, Y.; Emmanuel, S. Assembly of Clay Mineral Platelets, Tactoids, and Aggregates: Effect of Mineral Structure and Solution Salinity. *J. Colloid Interface Sci.* **2020**, *566*, 163–170. https://doi.org/10.1016/j.jcis.2020.01.084.

(37) Johnson, K. L.; Kendall, K.; Roberts, A. D. Surface Energy and the Contact of Elastic Solids. *Proc. R. Soc. Lond. Math. Phys. Sci.* **1971**, *324* (1558), 301–313. https://doi.org/10.1098/rspa.1971.0141.

(38) Hertz, H. On the Contact of Elastic Solids. In *Miscellaneous Papers*; Macmillan: London, 1896; pp 146–183.

(39) Landau, L. D.; Lifšic, E. M.; Landau, L. D.; Landau, L. D. *Theory of Elasticity*, 3. Engl. ed., rev.enlarged, [Nachdr.].; Course of theoretical physics / L. D. Landau and E. M. Lifshitz; Elsevier, Butterworth-Heinemann: Amsterdam Heidelberg, 2009.

(40) Johnson, K. L. *Contact Mechanics*, 1st ed.; Cambridge University Press, 1985. https://doi.org/10.1017/CBO9781139171731.

(41) C Thornton. Interparticle Sliding in the Presence of Adhesion. *J. Phys. Appl. Phys.* **1991**, *24* (11), 1942–1946. https://doi.org/10.1088/0022-3727/24/11/007.

(42) Derjaguin, B. V.; Muller, V. M.; Toporov, Yu. P. Effect of Contact Deformations on the Adhesion of Particles. *J. Colloid Interface Sci.* **1975**, *53* (2), 314–326. https://doi.org/10.1016/0021-9797(75)90018-1.

(43) Yao, H.; Ciavarella, M.; Gao, H. Adhesion Maps of Spheres Corrected for Strength Limit. *J. Colloid Interface Sci.* **2007**, *315* (2), 786–790. https://doi.org/10.1016/j.jcis.2007.07.021.

(44) Greenwood, J. A. Adhesion of Elastic Spheres. *Proc. R. Soc. Lond. Ser. Math. Phys. Eng. Sci.* **1997**, *453* (1961), 1277–1297. https://doi.org/10.1098/rspa.1997.0070.

(45) Johnson, K. L.; Greenwood, J. A. An Adhesion Map for the Contact of Elastic Spheres. *J. Colloid Interface Sci.* **1997**, *192* (2), 326–333. https://doi.org/10.1006/jcis.1997.4984.

(46) Tabor, D. Surface Forces and Surface Interactions. In *Plenary and Invited Lectures*; Elsevier, 1977; pp 3–14. https://doi.org/10.1016/B978-0-12-404501-9.50009-2.

(47) Brilliantov, N. V.; Spahn, F.; Hertzsch, J.-M.; Pöschel, T. Model for Collisions in Granular Gases. *Phys. Rev. E* **1996**, *53* (5), 5382–5392. https://doi.org/10.1103/PhysRevE.53.5382.

(48) Tsuji, Y.; Tanaka, T.; Ishida, T. Lagrangian Numerical Simulation of Plug Flow of Cohesionless Particles in a Horizontal Pipe. *Powder Technol.* **1992**, *71* (3), 239–250. https://doi.org/10.1016/0032-5910(92)88030-L.

(49) Marshall, J. S. Discrete-Element Modeling of Particulate Aerosol Flows. *J. Comput. Phys.* **2009**, *228* (5), 1541–1561. https://doi.org/10.1016/j.jcp.2008.10.035.

(50) Silbert, L. E.; Ertaş, D.; Grest, G. S.; Halsey, T. C.; Levine, D.; Plimpton, S. J. Granular Flow down an Inclined Plane: Bagnold Scaling and Rheology. *Phys. Rev. E* **2001**, *64* (5), 051302. https://doi.org/10.1103/PhysRevE.64.051302.

(51) Coulomb, C. A. *Memoires de Mathematique et Physique Present Esa l'Academie Royale Des Sciences.*; Imprimerie Royale: Paris, 1785.

(52) Bowden, F. P.; Tabor, D. *The Friction and Lubrication of Solids*; Oxford classic texts in the physical sciences; Clarendon Press ; Oxford University Press: Oxford : New York, 2001.

(53) Luding, S. Cohesive, Frictional Powders: Contact Models for Tension. *Granul. Matter* **2008**, *10* (4), 235–246. https://doi.org/10.1007/s10035-008-0099-x.

(54) Mindlin, R. D. Compliance of Elastic Bodies in Contact. *J. Appl. Mech.* **1949**, *16* (3), 259–268. https://doi.org/10.1115/1.4009973.

(55) Mindlin, R. D.; Deresiewicz, H. Elastic Spheres in Contact Under Varying Oblique Forces. *J. Appl. Mech.* **1953**, *20* (3), 327–344. https://doi.org/10.1115/1.4010702.

(56) Thornton, C.; Cummins, S. J.; Cleary, P. W. An Investigation of the Comparative Behaviour of Alternative Contact Force Models during Inelastic Collisions. *Powder Technol.* **2013**, *233*, 30–46. https://doi.org/10.1016/j.powtec.2012.08.012.

(57) Agnolin, I.; Roux, J.-N. Internal States of Model Isotropic Granular Packings. I. Assembling Process, Geometry, and Contact Networks. *Phys. Rev. E* **2007**, *76* (6), 061302. https://doi.org/10.1103/PhysRevE.76.061302.

(58) Reynolds, O. VI. On Rolling-Friction. *Philos. Trans. R. Soc. Lond.* **1876**, *166*, 155–174. https://doi.org/10.1098/rstl.1876.0006.

(59) Eldredge, K. R.; Tabor, D. The Mechanism of Rolling Friction. I. The Plastic Range. *Proc. R. Soc. Lond. Ser. Math. Phys. Sci.* **1955**, *229* (1177), 181–198. https://doi.org/10.1098/rspa.1955.0081.

(60) Tabor, D. The Mechanism of Rolling Friction II. The Elastic Range. *Proc. R. Soc. Lond. Ser. Math. Phys. Sci.* **1955**, *229* (1177), 198–220. https://doi.org/10.1098/rspa.1955.0082.

(61) Tabor, D. A propos du frottement de roulement : Une controverse oubliée. *Rev. Hist. Sci. Leurs Appl.* **1961**, *14* (1), 13–18. https://doi.org/10.3406/rhs.1961.3916.

(62) Estrada, N.; Azéma, E.; Radjai, F.; Taboada, A. Identification of Rolling Resistance as a Shape Parameter in Sheared Granular Media. *Phys. Rev. E* **2011**, *84* (1), 011306. https://doi.org/10.1103/PhysRevE.84.011306.

(63) Wang, Y.; Alonso-Marroquin, F.; Guo, W. W. Rolling and Sliding in 3-D Discrete Element Models. *Particuology* **2015**, *23*, 49–55. https://doi.org/10.1016/j.partic.2015.01.006.

(64) Guyon, E.; Hulin, J.-P.; Petit, L.; Mitescu, C. D. *Physical Hydrodynamics*, Second edition.; Oxford University Press: Oxford, 2015.

(65) Stokes, G. G. On the Effect of the Internal Friction of Fluids on the Motion of Pendulums. In *Mathematical and Physical Papers*; Cambridge University Press, 1850; Vol. 9, p 8. https://doi.org/10.1017/CBO9780511702266.

(66) Guazzelli, E.; Morris, J. F.; Pic, S. *A Physical Introduction to Suspension Dynamics*; Cambridge University Press: Cambridge, 2011. https://doi.org/10.1017/CBO9780511894671.

(67) Kim, S.; Karrila, S. J. *Microhydrodynamics: Principles and Selected Applications*; Dover Publications: Mineola, N.Y, 2005.

(68) Brenner, H. The Slow Motion of a Sphere through a Viscous Fluid towards a Plane Surface. *Chem. Eng. Sci.* **1961**, *16* (3–4), 242–251. https://doi.org/10.1016/0009-2509(61)80035-3.

(69) Gondret, P.; Hallouin, E.; Lance, M.; Petit, L. Experiments on the Motion of a Solid Sphere toward a Wall: From Viscous Dissipation to Elastohydrodynamic Bouncing. *Phys. Fluids* **1999**, *11* (9), 2803–2805. https://doi.org/10.1063/1.870109.

(70) Gondret, P.; Lance, M.; Petit, L. Bouncing Motion of Spherical Particles in Fluids. *Phys. Fluids* **2002**, *14* (2), 643–652. https://doi.org/10.1063/1.1427920.

(71) Merrow, E. *Linking R&D to Problems Experienced in Solids Processing*; The Rand Paper Series; Rand Corporation, 1984.

(72) Darcy, H. *Les fontaines publiques de la ville de Dijon*; libraire des corps imperiaux des ponts et chausees et des mines: Paris, 1856.

(73) Rao, P. T.; Chhabra, R. P. Viscous Non-Newtonian Flow in Packed Beds: Effects of Column Walls and Particle Size Distribution. *Powder Technol.* **1993**, *77* (2), 171–176. https://doi.org/10.1016/0032-5910(93)80054-E.

(74) Rodríguez de Castro, A.; Radilla, G. Non-Darcian Flow of Shear-Thinning Fluids through Packed Beads: Experiments and Predictions Using Forchheimer's Law and Ergun's Equation. *Adv. Water Resour.* **2017**, *100*, 35–47. https://doi.org/10.1016/j.advwatres.2016.12.009.

(75) Chhabra, R. P.; Srinivas, B. K. Non-Newtonian (Purely Viscous) Fluid Flow through Packed Beds: Effect of Particle Shape. *Powder Technol.* **1991**, *67* (1), 15–19. https://doi.org/10.1016/0032-5910(91)80021-A.

(76) Rodríguez de Castro, A.; Radilla, G. Flow of Yield Stress and Carreau Fluids through Rough-Walled Rock Fractures: Prediction and Experiments. *Water Resour. Res.* **2017**, *53* (7), 6197–6217. https://doi.org/10.1002/2017WR020520.

(77) Rodríguez de Castro, A.; Oostrom, M.; Shokri, N. Effects of Shear-Thinning Fluids on Residual Oil Formation in Microfluidic Pore Networks. *J. Colloid Interface Sci.* **2016**, *472*, 34–43. https://doi.org/10.1016/j.jcis.2016.03.027.

(78) Beverloo; Leniger, H. A.; Van de Velde, J. The Flow of Granular Solids through Orifices. *Chem. Eng. Sci.* **1961**, *15*, 260–269.

(79) Zuriguel, I. Invited Review: Clogging of Granular Materials in Bottlenecks. *Pap. Phys.* **2014**, *6* (0), 060014. https://doi.org/10.4279/PIP.060014.

(80) Lafond, P. G.; Gilmer, M. W.; Koh, C. A.; Sloan, E. D.; Wu, D. T.; Sum, A. K. Orifice Jamming of Fluid-Driven Granular Flow. *Phys. Rev. E* **2013**, *87* (4), 042204. https://doi.org/10.1103/PhysRevE.87.042204.

(81) To, K. Jamming Patterns in a Two-Dimensional Hopper. *Pramana* **2005**, *64* (6), 963–969. https://doi.org/10.1007/BF02704158.

(82) To, K.; Lai, P.-Y.; Pak, H. K. Jamming of Granular Flow in a Two-Dimensional Hopper. *Phys. Rev. Lett.* **2001**, *86* (1), 71–74. https://doi.org/10.1103/PhysRevLett.86.71.

(83) Dapena, J. A. On the Kinetic Arrest of Hydrate Slurries, Colorado School of Mines, Golden, CO, 2019.

(84) Lafond, P. G. Particle Jamming During the Discharge of Fluid-Driven Granular Flow, Colorado School of Mines, Golden, CO, 2014.

(85) Shu, B.; Zhang, S. Cuttings Transport in Maxi HDD Boreholes with Front Reaming and One Way Drilling Mud Return Technologies. *Tunn. Undergr. Space Technol.* **2018**, *72*, 1–8. https://doi.org/10.1016/j.tust.2017.11.015.

(86) Kong, L.; Wang, Y.; Wu, B.; Wang, Z. Simulation and Experimental Study on Cuttings-Carrying for Reverse Circulation Horizontal Directional Drilling with Dual Drill Pipes. *Adv. Civ. Eng.* **2019**, *2019*, 1–15. https://doi.org/10.1155/2019/6262308.

(87) Pang, B.; Wang, S.; Lu, C.; Cai, W.; Jiang, X.; Lu, H. Investigation of Cuttings Transport in Directional and Horizontal Drilling Wellbores Injected with Pulsed Drilling Fluid Using CFD Approach. *Tunn. Undergr. Space Technol.* **2019**, *90*, 183–193. https://doi.org/10.1016/j.tust.2019.05.001.

(88) Bradford, S. A.; Leij, F. J. Modeling the Transport and Retention of Polydispersed Colloidal Suspensions in Porous Media. *Chem. Eng. Sci.* **2018**, *192*, 972–980. https://doi.org/10.1016/j.ces.2018.08.037.

(89) Foster, M.; Fell, R. Assessing Embankment Dam Filters That Do Not Satisfy Design Criteria. *J. Geotech. Geoenvironmental Eng.* **2001**, *127* (5), 398–407. https://doi.org/10.1061/(ASCE)1090-0241(2001)127:5(398).

(90) Dincau, B.; Dressaire, E.; Sauret, A. Clogging: The Self-Sabotage of Suspensions. *Phys. Today* **2023**, *76* (2), 24–30. https://doi.org/10.1063/PT.3.5174.

(91) Terzaghi, K.; Peck, R. B.; Mesri, G. *Soil Mechanics in Engineering Practice*, 3rd ed.; Wiley: New York, 1996.

(92) Fannin, J. Karl Terzaghi: From Theory to Practice in Geotechnical Filter Design. *J. Geotech. Geoenvironmental Eng.* **2008**, *134* (3), 267–276. https://doi.org/10.1061/(ASCE)1090-0241(2008)134:3(267).

(93) Yu, J.; Appleby, B. A.; Mooney, M. A.; Samaniuk, J. R. Characterizing the Non-Newtonian Viscosity of High-Solids Drilling Fluid Dispersions by Flow Loop. *Phys. Fluids* **2022**, *34* (5), 053313. https://doi.org/10.1063/5.0083982.

(94) Wilkes, J. O. *Fluid Mechanics for Chemical Engineers: With Microfulidics, Cfd, and Comsol Multiphysics 5*, 3rd edition.; Prentice Hall: Boston, MA, 2017.

(95) Bousmina, M.; Ait-Kadi, A.; Faisant, J. B. Determination of Shear Rate and Viscosity from Batch Mixer Data. *J. Rheol.* **1999**, *43* (2), 415–433. https://doi.org/10.1122/1.551044.

(96) Samaniuk, J. R.; Wang, J.; Root, T. W.; Scott, C. T.; Klingenberg, D. J. Rheology of Concentrated Biomass. *Korea-Aust. Rheol. J.* **2011**, *23* (4), 237–245. https://doi.org/10.1007/s13367-011-0029-z.

(97) Samaniuk, J. R.; Scott, C. T.; Root, T. W.; Klingenberg, D. J. Rheological Modification of Corn Stover Biomass at High Solids Concentrations. *J. Rheol.* **2012**, *56* (3), 649–665. https://doi.org/10.1122/1.3702101.

(98) Scott, C. T.; Samaniuk, J. R.; Klingenberg, D. J. Rheology and Extrusion of High-Solids Biomass. *TAPPI J.* **2011**, *10* (5), 47–53. https://doi.org/10.32964/TJ10.5.47.

(99) Ehrhardt, M. R.; Monz, T. O.; Root, T. W.; Connelly, R. K.; Scott, C. T.; Klingenberg, D. J. Rheology of Dilute Acid Hydrolyzed Corn Stover at High Solids Concentration. *Appl. Biochem. Biotechnol.* **2010**, *160* (4), 1102–1115. https://doi.org/10.1007/s12010-009-8606-z.

(100) Hu, W.; Rostami, J. A New Method to Quantify Rheology of Conditioned Soil for Application in EPB TBM Tunneling. *Tunn. Undergr. Space Technol.* **2020**, *96*, 103192. https://doi.org/10.1016/j.tust.2019.103192.

(101) Hsiau, S.-S.; Shieh, Y.-M. Fluctuations and Self-Diffusion of Sheared Granular Material Flows. *J. Rheol.* **1999**, *43* (5), 1049–1066. https://doi.org/10.1122/1.551027.

(102) Tardos, G. I.; McNamara, S.; Talu, I. Slow and Intermediate Flow of a Frictional Bulk Powder in the Couette Geometry. *Powder Technol.* **2003**, *131* (1), 23–39. https://doi.org/10.1016/S0032-5910(02)00315-7.

(103) Da Cruz, F.; Chevoir, F.; Bonn, D.; Coussot, P. Viscosity Bifurcation in Granular Materials, Foams, and Emulsions. *Phys. Rev. E* **2002**, *66* (5), 051305. https://doi.org/10.1103/PhysRevE.66.051305.

(104) Coussot, P.; Piau, J.-M. The Effects of an Addition of Force-Free Particles on the Rheological Properties of Fine Suspensions. *Can. Geotech. J.* **1995**, *32* (2), 263–270. https://doi.org/10.1139/t95-028.

(105) Biswas, P. K.; Godiwalla, K. M.; Sanyal, D.; Dev, S. C. A Simple Technique for Measurement of Apparent Viscosity of Slurries: Sand–Water System. *Mater. Des.* **2002**, *23* (5), 511–519. https://doi.org/10.1016/S0261-3069(01)00030-9.

(106) Azeredo, G.; Morel, J.-C.; Lamarque, C.-H. Applicability of Rheometers to Characterizing Earth Mortar Behavior. Part I: Experimental Device and Validation. *Mater. Struct.* **2008**, *41* (8), 1465–1472. https://doi.org/10.1617/s11527-007-9343-9.

(107) Scotto di Santolo, A.; Pellegrino, A. M.; Evangelista, A. Experimental Study on the Rheological Behaviour of Debris Flow. *Nat. Hazards Earth Syst. Sci.* **2010**, *10* (12), 2507–2514. https://doi.org/10.5194/nhess-10-2507-2010.

(108) Fiscina, J. E.; Pakpour, M.; Fall, A.; Vandewalle, N.; Wagner, C.; Bonn, D. Dissipation in Quasistatically Sheared Wet and Dry Sand under Confinement. *Phys. Rev. E* **2012**, *86* (2), 020103. https://doi.org/10.1103/PhysRevE.86.020103.

(109) Kang, H. S.; Kim, Y. T. Rheological Properties of Loose Sands Subjected to Upward Flow. *Can. Geotech. J.* **2017**, *54* (5), 664–673. https://doi.org/10.1139/cgj-2016-0171.

(110) Pignon, F.; Magnin, A.; Piau, J. Thixotropic Colloidal Suspensions and Flow Curves with Minimum: Identification of Flow Regimes and Rheometric Consequences. *J. Rheol.* **1996**, *40* (4), 573–587. https://doi.org/10.1122/1.550759.

(111) Pignon, F.; Magnin, A.; Piau, J.-M.; Cabane, B.; Lindner, P.; Diat, O. Yield Stress Thixotropic Clay Suspension: Investigations of Structure by Light, Neutron, and x-Ray Scattering. *Phys. Rev. E* **1997**, *56* (3), 3281–3289. https://doi.org/10.1103/PhysRevE.56.3281.

(112) Ghezzehei, T. A.; Or, D. Rheological Properties of Wet Soils and Clays under Steady and Oscillatory Stresses. *Soil Sci. Soc. Am. J.* **2001**, *65* (3), 624. https://doi.org/10.2136/sssaj2001.653624x.

(113) Bekkour, K.; Leyama, M.; Benchabane, A.; Scrivener, O. Time-Dependent Rheological Behavior of Bentonite Suspensions: An Experimental Study. *J. Rheol.* **2005**, *49* (6), 1329–1345. https://doi.org/10.1122/1.2079267.

(114) Markgraf, W. Microstructural Changes in Soils: Rheological Investigations in Soil Mechanics, Christian-Albrechts-Universität, Kiel, 2006. https://www.researchgate.net/profile/Wibke_Baumgarten/publication/251571886_Microstructural_Changes_in_Soils_Rheological_Investigations_in_Soil_Mechanics/links/54e18a310cf296663792bee4/Microstructural-Changes-in-Soils-Rheological-Investigations-in-Soil-Mechanics.pdf#page=79 (accessed 2020-05-29).

(115) Nguyen, Q. D. The Rheology of Highly Concentrated Red Mud Suspensions, University of Melbourne, Melbourne, 1983.

(116) Meng, Q.; Qu, F.; Li, S. Experimental Investigation on Viscoplastic Parameters of Conditioned Sands in Earth Pressure Balance Shield Tunneling. *J. Mech. Sci. Technol.* **2011**, *25* (9), 2259–2266. https://doi.org/10.1007/s12206-011-0611-9.

(117) Karmakar, S.; Kushwaha, R. L. Development and Laboratory Evaluation of a Rheometer for Soil Visco-Plastic Parameters. *J. Terramechanics* **2007**, *44* (2), 197–204. https://doi.org/10.1016/j.jterra.2006.10.002.

(118) Thewes, M.; Budach, C. Soil conditioning with foam during EPB tunnelling. *Geomech. Tunn.* **2010**, *3* (3), 256–267. https://doi.org/10.1002/geot.201000023.

(119) Galli, M. Rheological Characterisation of Earth-Pressure-Balance (EPB) Support Medium Composed of Non-Cohesive Soils and Foam, Ruhr-Universität Bochum, Bochum, 2016.

(120) Schwarze, R.; Gladkyy, A.; Uhlig, F.; Luding, S. Rheology of Weakly Wetted Granular Materials: A Comparison of Experimental and Numerical Data. *Granul. Matter* **2013**, *15* (4), 455–465. https://doi.org/10.1007/s10035-013-0430-z.

(121) Montgomery, L. F. R.; Schoepp, T.; Fuchs, W.; Bochmann, G. Design, Calibration and Validation of a Large Lab-Scale System for Measuring Viscosity in Fermenting Substrate from Agricultural Anaerobic Digesters. *Biochem. Eng. J.* **2016**, *115*, 72–79. https://doi.org/10.1016/j.bej.2016.08.009.

(122) Stickel, J. J.; Knutsen, J. S.; Liberatore, M. W.; Luu, W.; Bousfield, D. W.; Klingenberg, D. J.; Scott, C. T.; Root, T. W.; Ehrhardt, M. R.; Monz, T. O. Rheology Measurements of a Biomass Slurry: An Inter-Laboratory Study. *Rheol. Acta* **2009**, *48* (9), 1005–1015. https://doi.org/10.1007/s00397-009-0382-8.

(123) Samaniuk, J. R.; Shay, T. W.; Root, T. W.; Klingenberg, D. J.; Scott, C. T. A Novel Rheometer Design for Yield Stress Fluids. *AIChE J.* **2014**, *60* (4), 1523–1528. https://doi.org/10.1002/aic.14329.

(124) Pimenova, N. V.; Hanley, T. R. Measurement of Rheological Properties of Corn Stover Suspensions. *Appl. Biochem. Biotechnol.* **2003**, *105*, 10.

(125) Bertola, V.; Bertrand, F.; Tabuteau, H.; Bonn, D.; Coussot, P. Wall Slip and Yielding in Pasty Materials. *J. Rheol.* **2003**, *47* (5), 1211–1226. https://doi.org/10.1122/1.1595098.

(126) Dasari, R. K.; Berson, R. E. The Effect of Particle Size on Hydrolysis Reaction Rates and Rheological Properties in Cellulosic Slurries. *Appl. Biochem. Biotechnol.* **2007**, *136*.

(127) Damani, R.; Powell, R. L.; Hagen, N. Viscoelastic Characterization of Medium Consistency Pulp Suspensions. *Can. J. Chem. Eng.* **1993**, *71* (5), 676–684. https://doi.org/10.1002/cjce.5450710504.

(128) Viamajala, S.; McMillan, J. D.; Schell, D. J.; Elander, R. T. Rheology of Corn Stover Slurries at High Solids Concentrations – Effects of Saccharification and Particle Size. *Bioresour. Technol.* **2009**, *100* (2), 925–934. https://doi.org/10.1016/j.biortech.2008.06.070.

(129) Bennington, C. P. J.; Kerekes, R. J.; Grace, J. R. The Yield Stress of Fibre Suspensions. *Can. J. Chem. Eng.* **1990**, *68* (5), 748–757. https://doi.org/10.1002/cjce.5450680503.

(130) Bbosa, B.; DelleCase, E.; Volk, M.; Ozbayoglu, E. Development of a Mixer-Viscometer for Studying Rheological Behavior of Settling and Non-Settling Slurries. *J. Pet. Explor. Prod. Technol.* **2017**, *7* (2), 511–520. https://doi.org/10.1007/s13202-016-0270-6.

(131) Blanco, A.; Negro, C.; Fuente, E.; Tijero, J. Rotor Selection for a Searle-Type Device to Study the Rheology of Paper Pulp Suspensions. *Chem. Eng. Process. Process Intensif.* **2007**, *46* (1), 37–44. https://doi.org/10.1016/j.cep.2006.04.003.

(132) Owens, C. E.; Hart, A. J.; McKinley, G. H. Improved Rheometry of Yield Stress Fluids Using Bespoke Fractal 3D Printed Vanes. *J. Rheol.* **2020**, *64* (3), 643–662. https://doi.org/10.1122/1.5132340.

(133) Klingenberg, D. J.; Root, T. W.; Burlawar, S.; Scott, C. T.; Bourne, K. J.; Gleisner, R.; Houtman, C.; Subramaniam, V. Rheometry of Coarse Biomass at High Temperature and Pressure. *Biomass Bioenergy* **2017**, *99*, 69–78. https://doi.org/10.1016/j.biombioe.2017.01.031.

(134) Lu, K.; Brodsky, E. E.; Kavehpour, H. P. Shear-Weakening of the Transitional Regime for Granular Flow. *J. Fluid Mech.* **2007**, *587*, 347–372. https://doi.org/10.1017/S0022112007007331.

(135) Dijksman, J. A.; Wandersman, E.; Slotterback, S.; Berardi, C. R.; Updegraff, W. D.; van Hecke, M.; Losert, W. From Frictional to Viscous Behavior: Three-Dimensional Imaging and Rheology of Gravitational Suspensions. *Phys. Rev. E* **2010**, *82* (6), 060301. https://doi.org/10.1103/PhysRevE.82.060301.

(136) Jeffrey, D. J.; Acrivos, A. The Rheological Properties of Suspensions of Rigid Particles. *AIChE J.* **1976**, *22* (3), 417–432. https://doi.org/10.1002/aic.690220303.

(137) Denn, M. M.; Morris, J. F. Rheology of Non-Brownian Suspensions. *Annu. Rev. Chem. Biomol. Eng.* **2014**, *5* (1), 203–228. https://doi.org/10.1146/annurev-chembioeng-060713-040221.

(138) Christidis, G. Physical and Chemical Properties of Some Bentonite Deposits of Kimolos Island, Greece. *Appl. Clay Sci.* **1998**, *13* (2), 79–98. https://doi.org/10.1016/S0169-1317(98)00023-4.

(139) Zhang, J. R.; Xu, M. D.; Christidis, G. E.; Zhou, C. H. Clay Minerals in Drilling Fluids: Functions and Challenges. *Clay Miner.* **2020**, *55* (1), 1–11. https://doi.org/10.1180/clm.2020.10.

(140) Goodrich; Porter. A Rheological Interpretation of Torque-Rheometer Data. *Polym. Eng. Sci.* **1967**, 45–51.

(141) Bingham, E. C. An Investigation of the Laws of Plastic Flow. *Bull. Bur. Stand.* **1916**, *13* (2), 309. https://doi.org/10.6028/bulletin.304.

(142) El-Emam, N.; Kamel, A. H.; El-Shafei, M.; El-Batrawy, A. New Equation Calculates Friction Factor for Turbulent Flow on Non-Newtonian Fluids. *Oil Gas J.* **2003**, *101* (36), 74.

(143) Gao, P.; Zhang, J. New Assessment of Friction Factor Correlations for Power Law Fluids in Turbulent Pipe Flow: A Statistical Approach. *J. Cent. South Univ. Technol.* **2007**, *14* (S1), 77–81. https://doi.org/10.1007/s11771-007-0219-5.

(144) Szilas, A. P.; Bobok, E.; Navratil, L. Determination of Turbulent Pressure Loss of Non-Newtonian Oil Flow in Rough Pipes. *Rheol. Acta* **1981**, *20* (5), 487–496. https://doi.org/10.1007/BF01503271.

(145) Dodge, D. W.; Metzner, A. B. Turbulent Flow of Non-Newtonian Systems. *AIChE J.* **1959**, *5* (2), 189–204. https://doi.org/10.1002/aic.690050214.

(146) Maglione, R.; Gallino, G.; Robotti, G.; Romagnoli, R.; Rommetveit, R. A Drilling Well as Viscometer: Studying the Effects of Well Pressure and Temperature on the Rheology of the Drilling Fluids; Society of Petroleum Engineers: Milan, Italy, 1996; p 14.

(147) Gul, S.; Erge, O.; van Oort, E. Frictional Pressure Losses of Non-Newtonian Fluids in Helical Pipes: Applications for Automated Rheology Measurements. *J. Nat. Gas Sci. Eng.* **2020**, *73*, 1–16. https://doi.org/10.1016/j.jngse.2019.103042.

(148) Karimi Vajargah, A.; van Oort, E. Determination of Drilling Fluid Rheology under Downhole Conditions by Using Real-Time Distributed Pressure Data. *J. Nat. Gas Sci. Eng.* **2015**, *24*, 400–411. https://doi.org/10.1016/j.jngse.2015.04.004.

(149) Skudarnov, P. V.; Lin, C. X.; Ebadian, M. A. Double-Species Slurry Flow in a Horizontal Pipeline. *J. Fluids Eng.* **2004**, *126* (1), 125–132. https://doi.org/10.1115/1.1637925.

(150) Pilehvari, A. A.; Azar, J. J.; Shirazi, S. A. State-of-the-Art Cuttings Transport in Horizontal Wellbores. *SPE Drill. Complet.* **1999**, *14* (3), 196–200.

(151) Azar, J. J.; Sancez, R. A. Important Issues in Cuttings Transport for Drilling Directional Wells; Society of Petroleum Engineers: Rio de Janeiro, Brazil, 1997; pp 1–4.

(152) Duan, M.; Miska, S.; Yu, M.; Takach, N.; Ahmed, R. Transport of Small Cuttings in Extended Reach Drilling; Society of Petroleum Engineers: Beijing, China, 2006; pp 1–9.

(153) Lan, H. Experimental and Numerical Investigation of Stability of Horizontal Boreholes during Horizontal Directional Drilling, Queen's University, Kingston, Ontario, Canada, 2018.

(154) Rostami, A. Prediction and Evaluation of Annular Pressure in Horizontal Directional Drilling, University of Alberta, Alberta, Canada, 2017.

(155) Kim, Y.-J.; Woo, N.-S.; Hwang, Y.-K.; Kim, J.-H.; Han, S.-M. Transport of Small Cuttings in Solid-Liquid Flow with Inclined Slim Hole Annulus. *J. Mech. Sci. Technol.* **2014**, *28* (1), 115–126. https://doi.org/10.1007/s12206-013-0952-7.

(156) Edwards, M. F.; Smith, R. The Turbulent Flow of Non-Newtonian Fluids in the Absence of Anomalous Wall Effects. *J. Non-Newton. Fluid Mech.* **1980**, *7*, 77–90.

(157) Founargiotakis, K.; Kelessidis, V. C.; Maglione, R. Laminar, Transitional and Turbulent Flow of Herschel-Bulkley Fluids in Concentric Annulus. *Can. J. Chem. Eng.* **2008**, *86* (4), 676–683. https://doi.org/10.1002/cjce.20074.

(158) Andrade, L. C. F.; Petronílio, J. A.; Maneschy, C. E. de A.; Cruz, D. O. de A. The Carreau-Yasuda Fluids: A Skin Friction Equation for Turbulent Flow in Pipes and Kolmogorov Dissipative Scales. *J. Braz. Soc. Mech. Sci. Eng.* **2007**, *29* (2). https://doi.org/10.1590/S1678-58782007000200005.

(159) Heywood, N. I.; Cheng, D. C.-H. Comparison of Methods for Predicting Head Loss in Turbulent Pipe Flow of Non-Newtonian Fluids. *Trans. Inst. Meas. Control* **1984**, *6* (1), 33–45. https://doi.org/10.1177/014233128400600105.

(160) Escudier, M. P.; Presti, F. Pipe Flow of a Thixotropic Liquid. *J. Non-Newton. Fluid Mech.* **1996**, *62* (2), 291–306. https://doi.org/10.1016/0377-0257(96)01417-6.

(161) Trinh, K. T. The Wall Shear Rate in Non-Newtonian Turbulent Pipe Flow. arXiv September 16, 2010. http://arxiv.org/abs/1009.3299 (accessed 2023-09-01).

(162) Werner, B.; Myrseth, V.; Saasen, A. Viscoelastic Properties of Drilling Fluids and Their Influence on Cuttings Transport. *J. Pet. Sci. Eng.* **2017**, *156*, 845–851. https://doi.org/10.1016/j.petrol.2017.06.063.

(163) Ostwald, V. W. Ueber die Geschwindigkeitsfunktion der Viskosität disperser Systeme. I. *Kolloid-Z* **1925**, *36*, 99–117.

(164) Waele, A. d. Viscometry and Plastometry. *J. Oil Colour Chem. Assoc.* **1923**, *6* (33).

(165) Carlsson, C.; Alenius, E.; Fuchs, L. Swirl Switching in Turbulent Flow through 90° Pipe Bends. *Phys. Fluids* **2015**, *27* (8), 085112. https://doi.org/10.1063/1.4928971.

(166) Ono, A.; Kimura, N.; Kamide, H.; Tobita, A. Influence of Elbow Curvature on Flow Structure at Elbow Outlet under High Reynolds Number Condition. *Nucl. Eng. Des.* **2011**, *241* (11), 4409–4419. https://doi.org/10.1016/j.nucengdes.2010.09.026.

(167) Takamura, H.; Ebara, S.; Hashizume, H.; Aizawa, K.; Yamano, H. Flow Visualization and Frequency Characteristics of Velocity Fluctuations of Complex Turbulent Flow in a Short Elbow Piping Under High Reynolds Number Condition. *J. Fluids Eng.* **2012**, *134* (10), 101201. https://doi.org/10.1115/1.4007436.

(168) Wang, S.; Ren, C.; Sun, Y.; Yang, X.; Tu, J. A Study on the Instantaneous Turbulent Flow Field in a 90-Degree Elbow Pipe with Circular Section. *Sci. Technol. Nucl. Install.* **2016**, *2016*, 1–8. https://doi.org/10.1155/2016/5265748.

(169) Homicz, G. *Computational Fluid Dynamic Simulations of Pipe Elbow Flow.*; SAND2004-3467, 919140; 2004; pp SAND2004-3467, 919140. https://doi.org/10.2172/919140.

(170) Holland, F. A.; Bragg, R. Flow of Incompressible Non-Newtonian Fluids in Pipes. In *Fluid Flow for Chemical Engineers*; Elsever, 1995.

(171) Bird, R. B.; Stewart, W. E.; Lightfoot, E. N.; Klingenberg, D. J. *Introductory Transport Phenomena*; 2015.

(172) Ignatenko, Y.; Bocharov, O.; May, R. On a Criterion of Incipient Motion and Entrainment into Suspension of a Particle from Cuttings Bed in Shear Flow of Non-Newtonian Fluid. *J. Phys. Conf. Ser.* **2017**, *894*, 012037. https://doi.org/10.1088/1742-6596/894/1/012037.

(173) Shields, A. Application of Similarity Principles and Turbulence Research to Bed-Load Movement, Prussian Research Institute for Water and Shipbuilding, Berlin, Germany, 1936.

(174) Gul, S.; van Oort, E.; Mullin, C.; Ladendorf, D. Automated Surface Measurements of Drilling Fluid Properties: Field Application in the Permian Basin. *SPE Drill. Complet.* **2020**, *35* (04), 525–534. https://doi.org/10.2118/201094-PA.

(175) Ramadan, A.; Skalle, P.; Johansen, S. T.; Svein, J.; Saasen, A. Mechanistic Model for Cuttings Removal from Solid Bed in Inclined Channels. *J. Pet. Sci. Eng.* **2001**, *30* (3–4), 129–141. https://doi.org/10.1016/S0920-4105(01)00108-5.

(176) Bizhani, M. .; Kuru, E. . Critical Review of Mechanistic and Empirical (Semimechanistic) Models for Particle Removal From Sandbed Deposits in Horizontal Annuli With Water. *SPE J.* **2018**, *23* (02), 237–255. https://doi.org/10.2118/187948-PA.

(177) Pedrosa, C.; Saasen, A.; Ytrehus, J. D. Fundamentals and Physical Principles for Drilled Cuttings Transport—Cuttings Bed Sedimentation and Erosion. *Energies* **2021**, *14* (3), 545. https://doi.org/10.3390/en14030545.

(178) Ytrehus, J. D.; Taghipour, A.; Sayindla, S.; Lund, B.; Werner, B.; Saasen, A. Full Scale Flow Loop Experiments of Hole Cleaning Performances of Drilling Fluids. In *Volume 10: Petroleum Technology*; American Society of Mechanical Engineers: St. John's, Newfoundland, Canada, 2015; p V010T11A041. https://doi.org/10.1115/OMAE2015-41901.

(179) Ozbayoglu, E. M.; Sorgun, M.; University, M. E. T. Frictional Pressure Loss Estimation of Non-Newtonian Fluids in Realistic Annulus With Pipe Rotation. *J. Can. Pet. Technol.* **2010**, *49* (12), 8.

(180) Williams, A. a. Pumps as Turbines for Low Cost Micro Hydro Power; Elsevier: Denver, USA, 1996; Vol. 9, pp 1227–1234.

(181) Samora, I.; Hasmatuchi, V.; Münch-Alligné, C.; Franca, M. J.; Schleiss, A. J.; Ramos, H. M. Experimental Characterization of a Five Blade Tubular Propeller Turbine for Pipe Inline Installation. *Renew. Energy* **2016**, *95*, 356–366. https://doi.org/10.1016/j.renene.2016.04.023.

(182) Shetty, R.; Samaniuk, J.; Mooney, M. Development of Annular Pump to Enhance Drilling Distance and Cuttings Return in Horizontal Directional Drilling. *Tunn. Undergr. Space Technol.* **2023**, *140*, 105324. https://doi.org/10.1016/j.tust.2023.105324.

(183) Furukawa, A.; Shigemitsu, T.; Watanabe, S. Performance Test and Flow Measurement of Contra-Rotating Axial Flow Pump. *J. Therm. Sci.* **2007**, *16* (1), 7–13. https://doi.org/10.1007/s11630-007-0007-4.

(184) Alexander, K. V.; Giddens, E. P.; Fuller, A. M. Axial-Flow Turbines for Low Head Microhydro Systems. *Renew. Energy* **2009**, *34* (1), 35–47. https://doi.org/10.1016/j.renene.2008.03.017.

(185) Shigemitsu, T.; Fukutomi, J.; Okabe, Y. Performance and Flow Condition of Small-Sized Axial Fan and Adoption of Contra-Rotating Rotors. *J. Therm. Sci.* **2010**, *19* (1), 1–6. https://doi.org/10.1007/s11630-010-0001-0.

(186) Cai, G.; Harada, A. B.; Nordstrom, K. Mesoscale Metrics on Approach to the Clogging Point. *Granul. Matter* **2021**.

(187) D18 Committee. *Test Method for Permeability of Granular Soils (Constant Head)*; ASTM International. https://doi.org/10.1520/D2434-19.

(188) Dong, S.; Zeng, C.; Ariaratnam, S. T.; Ma, B.; Yan, X.; Li, Z.; Li, X. Experimental and Performance Analysis of Reverse Circulation Reaming in Horizontal Directional Drilling. *Tunn. Undergr. Space Technol.* **2020**, *95*, 103128. https://doi.org/10.1016/j.tust.2019.103128.

(189) Sun, P.; Mo, D.; Ariaratnam, S. T.; Cao, H.; Zhang, P. Laboratory Study of Fluid Properties Owing to Cutting Intrusions during Horizontal Directional Drilling. *Undergr. Space* **2020**, *5* (1), 20–29. https://doi.org/10.1016/j.undsp.2018.09.004.

(190) Wood, B. D.; He, X.; Apte, S. V. Modeling Turbulent Flows in Porous Media. *Annu. Rev. Fluid Mech.* **2020**, *52* (1), 171–203. https://doi.org/10.1146/annurev-fluid-010719-060317.

(191) Kaviany, M. *Principles of Heat Transfer in Porous Media*, 2nd ed.; Springer, 1995.

(192) Harmens, A. Flow of Granular Material through Horizontal Apertures. *Chem. Eng. Sci.* **1963**, *18*, 297–306.

(193) Herschel, W. H.; Bulkley, R. Measurement of Consistency as Applied to Rubber-Benzene Solutions. *Am. Soc. Test Proced.* **1926**, *26*, 621–623.

(194) Nagy, D. B.; Claudin, P.; Börzsönyi, T.; Somfai, E. Rheology of Dense Granular Flows for Elongated Particles. *Phys. Rev. E* **2017**, *96* (6), 062903. https://doi.org/10.1103/PhysRevE.96.062903.

(195) Firouznia, M.; Metzger, B.; Ovarlez, G.; Hormozi, S. The Interaction of Two Spherical Particles in Simple-Shear Flows of Yield Stress Fluids. *J. Non-Newton. Fluid Mech.* **2018**, *255*, 19–38. https://doi.org/10.1016/j.jnnfm.2018.03.006.

(196) Hormozi, S.; Frigaard, I. A. Dispersion of Solids in Fracturing Flows of Yield Stress Fluids. *J. Fluid Mech. Camb.* **2017**, *830*, 93–137. http://dx.doi.org.mines.idm.oclc.org/10.1017/jfm.2017.465.

(197) Sarabian, M.; Firouznia, M.; Metzger, B.; Hormozi, S. Fully Developed and Transient Concentration Profiles of Particulate Suspensions Sheared in a Cylindrical Couette. *J. Fluid Mech.* **2019**, *862*, 659–671. https://doi.org/10.1017/jfm.2018.982.

(198) Sarabian, M.; Rosti, M. E.; Brandt, L.; Hormozi, S. Numerical Simulations of a Sphere Settling in Simple Shear Flows of Yield Stress Fluids. *J. Fluid Mech.* **2020**, *896*, A17. https://doi.org/10.1017/jfm.2020.316.

(199) Wang, S.; Hu, C.; Luo, K.; Yu, J.; Fan, J. Multi-Scale Numerical Simulation of Fluidized Beds: Model Applicability Assessment. *Particuology* **2023**, *80*, 11–41. https://doi.org/10.1016/j.partic.2022.11.011.

(200) Escudier, M. P.; Presti, F.; Smith, S. Drag Reduction in the Turbulent Pipe Flow of Polymers. *J. Non-Newton. Fluid Mech.* **1999**, *81* (3), 197–213. https://doi.org/10.1016/S0377-0257(98)00098-6.

(201) Browne, C. A.; Datta, S. S. Elastic Turbulence Generates Anomalous Flow Resistance in Porous Media. *Sci. Adv.* **2021**, *7* (45), eabj2619. https://doi.org/10.1126/sciadv.abj2619.

(202) Murdoch, L. C. Mechanical Analysis of Idealized Shallow Hydraulic Fracture. *J. Geotech. Geoenvironmental Eng.* **2002**, *128* (6), 488–495. https://doi.org/10.1061/(ASCE)1090-0241(2002)128:6(488).

(203) Soga, K.; Gafar, K. O.; Ng, M. Y. A.; Au, S. K. A. Macro and Micro Behaviour of Soil Fracturing. In *Geomechanics and Geotechnics of Particulate Media*; Hyodo, M., Murata, H., Nakata, Y., Eds.; CRC Press, 2006; pp 421–427. https://doi.org/10.1201/9781315106656-67.

(204) Bannister, C. E. Evaluation of Cement Fluid-Loss Behavior under Dynamic Condtions; Society of Petroleum Engineers: Houston, Texas, USA, 1985; p 8.

(205) Bezuijen, A.; te Grotenhuis, R.; van Tol, A. F.; Bosch, J. W.; Haasnoot, J. K. Analytical Model for Fracture Grouting in Sand. *J. Geotech. Geoenvironmental Eng.* **2011**, *137* (6), 611–620. https://doi.org/10.1061/(ASCE)GT.1943-5606.0000465.

(206) de Pater, C. J.; Dong, Y. Experimental Study of Hydraulic Fracturing in Sand as a Function of Stress and Fluid Rheology; Society of Petroleum Engineers: College Station, Texas, USA; p 10.

(207) Zhai, Z.; Sharma, M. M. A New Approach to Modeling Hydraulic Fractures in Unconsolidated Sands; Society of Petroleum Engineers: Dallas, TX, USA, 2005; p 14.

(208) Chang, H. Hydraulic Fracturing in Particulate Materials, Georgia Institute of Technology, Atlanta, 2004.

(209) Bezuijen, A.; Tol, F. Compensation Grouting in Sand, Fractures and Compaction. *Proc XIV Eur. Conf. Soil Mech. Geotech. Eng.* **2007**, 1257–1262.

(210) Razakamanantsoa, A. R.; Barast, G.; Djeran-maigre, I. Hydraulic Performance of Activated Calcium Bentonite Treated by Polyionic Charged Polymer. *Appl. Clay Sci.* **2012**, *59–60*, 103–114. https://doi.org/10.1016/j.clay.2012.01.022.

(211) Katsumi, T.; Ishimori, H.; Onikata, M.; Fukagawa, R. Long-Term Barrier Performance of Modified Bentonite Materials against Sodium and Calcium Permeant Solutions. *Geotext. Geomembr.* **2008**, *26* (1), 14–30. https://doi.org/10.1016/j.geotexmem.2007.04.003.

(212) Too, J. L.; Cheng, A.; Khoo, B. C.; Palmer, A.; Linga, P. Hydraulic Fracturing in a Penny-Shaped Crack. Part I: Methodology and Testing of Frozen Sand. *J. Nat. Gas Sci. Eng.* **2018**, *52*, 609–618. https://doi.org/10.1016/j.jngse.2017.12.022.

(213) Khristianovic, S. A.; Zheltov, Y. P. Formations of Vertical Fractures by Means of Highly Viscous Liquid; OnePetro: Rome Italy, 1955.

(214) Center for Environmental Research Information. *Alternative Methods for Fluid Delivery and Recovery*; Manual EPA-625-R-94-003; United States Environmental Protection Agency: Washington, D.C., 1994; p 96.

(215) Alfaro, M. C.; Wong, R. C. Laboratory Studies on Fracturing of Low-Permeability Soils. *Can. Geotech. J.* **2001**, *38* (2), 303–315. https://doi.org/10.1139/t00-096.

(216) Chen, T.; Zhang, L.; Zhang, D. Simulation of Hydraulic Fracture in Unsaturated Soils with High Degree of Saturation. *Adv. Mater. Sci. Eng.* **2014**, *2014*, 1–10. https://doi.org/10.1155/2014/981056.

(217) Zhu, H.; Deng, J.; Jin, X.; Hu, L.; Luo, B. Hydraulic Fracture Initiation and Propagation from Wellbore with Oriented Perforation. *Rock Mech. Rock Eng.* **2015**, *48* (2), 585–601. https://doi.org/10.1007/s00603-014-0608-7.

(218) Wang, S. Y.; Sun, L.; Au, A. S. K.; Yang, T. H.; Tang, C. A. 2D-Numerical Analysis of Hydraulic Fracturing in Heterogeneous Geo-Materials. *Constr. Build. Mater.* **2009**, *23* (6), 2196–2206. https://doi.org/10.1016/j.conbuildmat.2008.12.004.

(219) Wong, R. C.; Alfaro, M. C. Fracturing in Low-Permeability Soils for Remediation of Contaminated Ground. *Can. Geotech. J.* **2001**, *38* (2), 316–327. https://doi.org/10.1139/t00-097.

(220) Wang, J.-J.; Liu, Y.-X. Hydraulic Fracturing in a Cubic Soil Specimen. *Soil Mech. Found. Eng.* **2010**, *47* (4), 136–142. https://doi.org/10.1007/s11204-010-9101-9.

(221) Shu, B.; Ma, B.; Lan, H. Cuttings Transport Mechanism in a Large-Diameter HDD Borehole. *J. Pipeline Syst. Eng. Pract.* **2015**, *6* (4), 04014017. https://doi.org/10.1061/(ASCE)PS.1949-1204.0000190.

(222) Blasius, H. *Das Aehnlichkeitsgesetz Bei Reibungsvorgängen in Flüssigkeiten*; Mitteilungen über Forschungsarbeiten auf dem Gebiete des Ingenieurwesens; VDI-Verlag Berlin, 1913; Vol. 134.

(223) Bird, R. B.; Armstrong, R. C.; Hassager, O. *Dynamics of Polymeric Liquids*, 2nd ed.; John Wiley and Sons Inc., 1987; Vol. 1.

(224) Ferry, J. D. *Viscoelastic Properties of Polymers*; John Wiley & Sons, 1980.

(225) Tschoegl, N. W. *The Phenomenological Theory of Linear Viscoelastic Behavior: An Introduction*; Springer Science & Business Media, 2012.

(226) Dealy, J. M.; Wissbrun, K. F. *Melt Rheology and Its Role in Plastics Processing: Theory and Applications*; Springer Science & Business Media, 2012.

(227) Baravian, C.; Vantelon, D.; Thomas, F. Rheological Determination of Interaction Potential Energy for Aqueous Clay Suspensions. *Langmuir* **2003**, *19* (19), 8109–8114. https://doi.org/10.1021/la034169c.

(228) Cheng, X.; McCoy, J. H.; Israelachvili, J. N.; Cohen, I. Imaging the Microscopic Structure of Shear Thinning and Thickening Colloidal Suspensions. *Science* **2011**, *333* (6047), 1276–1279. https://doi.org/10.1126/science.1207032.

(229) Zimm, B. H. Dynamics of Polymer Molecules in Dilute Solution: Viscoelasticity, Flow Birefringence and Dielectric Loss. *J. Chem. Phys.* **1956**, *24* (2), 269–278. https://doi.org/10.1063/1.1742462.

(230) Rouse, P. E. A Theory of the Linear Viscoelastic Properties of Dilute Solutions of Coiling Polymers. *J. Chem. Phys.* **1953**, *21* (7), 1272–1280. https://doi.org/10.1063/1.1699180.

(231) Chambon, F.; Winter, H. H. Linear Viscoelasticity at the Gel Point of a Crosslinking PDMS with Imbalanced Stoichiometry. *J. Rheol.* **1987**, *31* (8), 683–697. https://doi.org/10.1122/1.549955.

(232) Sollich, P. Rheological Constitutive Equation for a Model of Soft Glassy Materials. *Phys. Rev. E* **1998**, *58* (1), 738–759. https://doi.org/10.1103/PhysRevE.58.738.

(233) Sollich, P.; Lequeux, F.; Hébraud, P.; Cates, M. E. Rheology of Soft Glassy Materials. *Phys. Rev. Lett.* **1997**, *78* (10), 4.

(234) Winter, H. H.; Chambon, F. Analysis of Linear Viscoelasticity of a Crosslinking Polymer at the Gel Point. *J. Rheol.* **1986**, *30* (2), 367–382. https://doi.org/10.1122/1.549853.

(235) Bizmark, N.; Schneider, J.; Priestley, R.; Datta, S. Multiscale Dynamics of Colloidal Deposition and Erosion in Porous Media. *Sci. Adv.* **2020**.

APPENDIX A SOIL VISCOMETER

A.1 Raw torque and rotation rate data from the soil viscometer

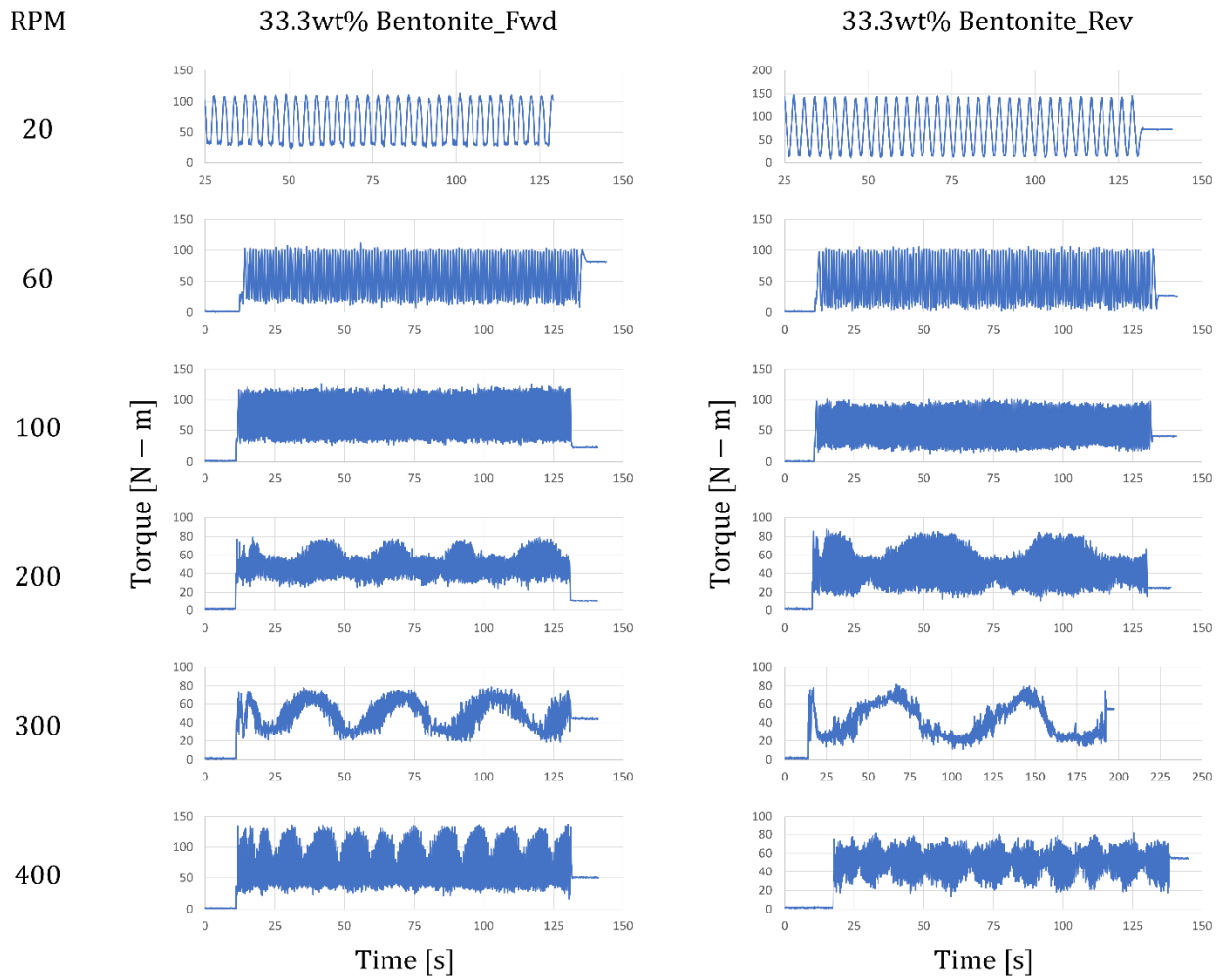

Figure A.1 Raw torque data collected from the soil viscometer across a range of rotation rates over 150 seconds. The torque data points used in Chapter 3 are average values of these data points. This data is for 33.3 wt% bentonite samples.

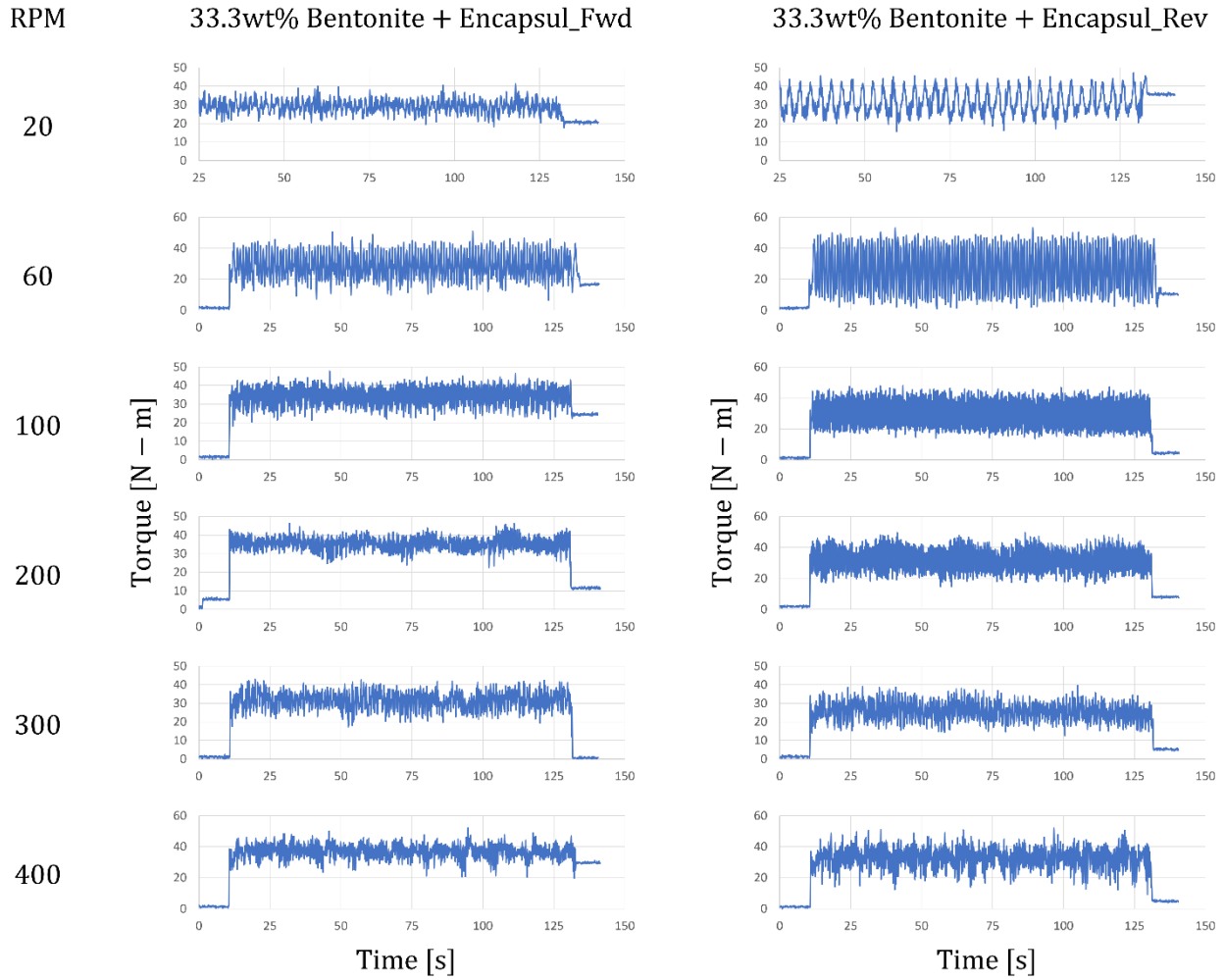

Figure A.2 Raw torque data collected from the soil viscometer across a range of rotation rates over 150 seconds. The torque data points used in Chapter 3 are average values of these data points. This data is for 33.3 wt% bentonite samples + Encapsul.

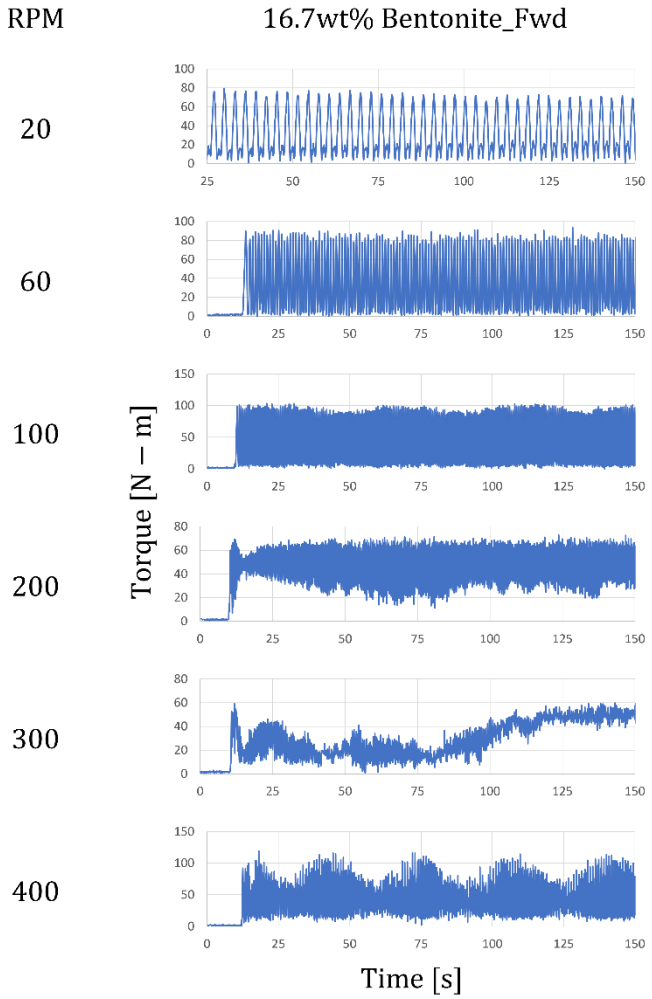

Figure A.3 Raw torque data collected from the soil viscometer across a range of rotation rates over 150 seconds. The torque data points used in Chapter 3 are average values of these data points. This data is for 16.7 wt% bentonite samples.

APPENDIX B FLOW LOOP

B.1 Bentonite dispersion viscosity and yield stress characterization

3wt% Wyoming bentonite (Pondseal-200)

All rheological characterizations are performed in a cup and bob geometry on a TA DHR-3 rheometer.

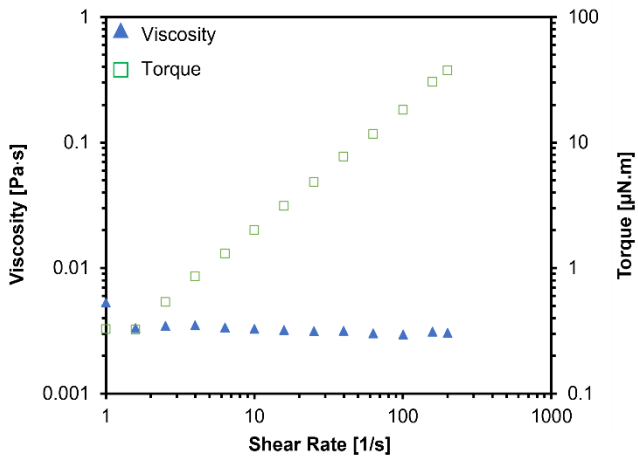

Figure B.1 Flow sweep data of 3wt% bentonite, performed from 1 – 200 1/s, with increasing shear-rate.

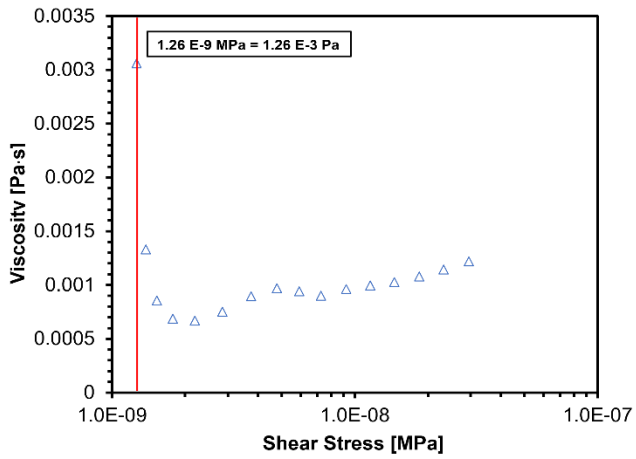

Figure B.2 Flow ramp loop with shear stress as the independent variable, measured from high to low stress. The yield stress was determined by the peak in viscosity to be 0.00126 Pa.

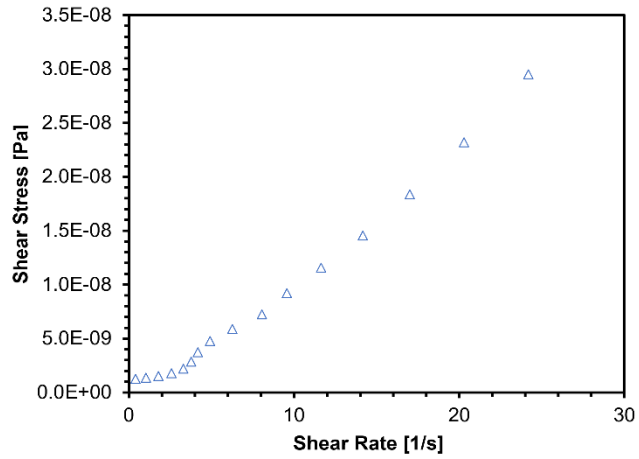

Figure B.3 Flow ramp loop using shear stress as the independent variable but plotting in terms of shear-rate and shear stress.

MaxGel – Wyoming bentonite

3wt% Wyoming bentonite (Michels industry-used Wyoming bentonite)

All rheological characterizations are performed in a cup and bob geometry on a TA DHR-3 rheometer.

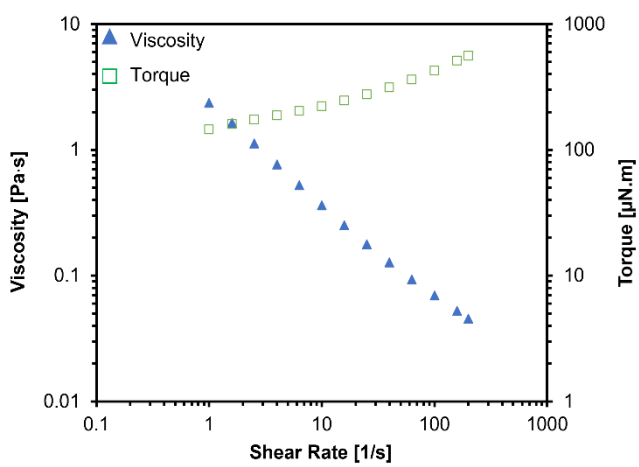

Figure B.4 Flow sweep data of 3wt% Michels bentonite, performed from 1 – 200 1/s, with increasing shear-rate.

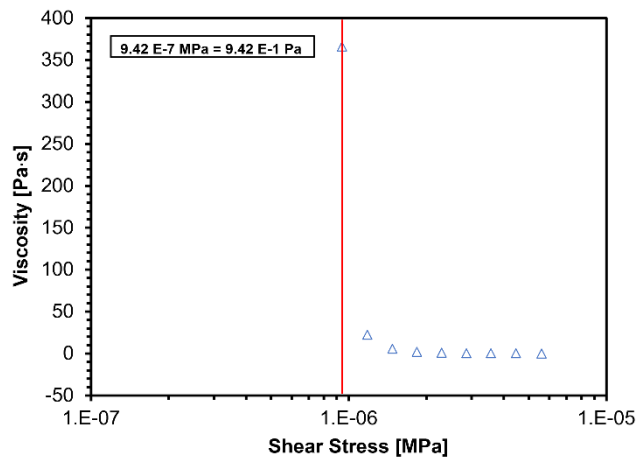

Figure B.5 Flow ramp loop with shear stress as the independent variable, measured from high to low stress. The yield stress was determined by the peak in viscosity to be 0.942 Pa.

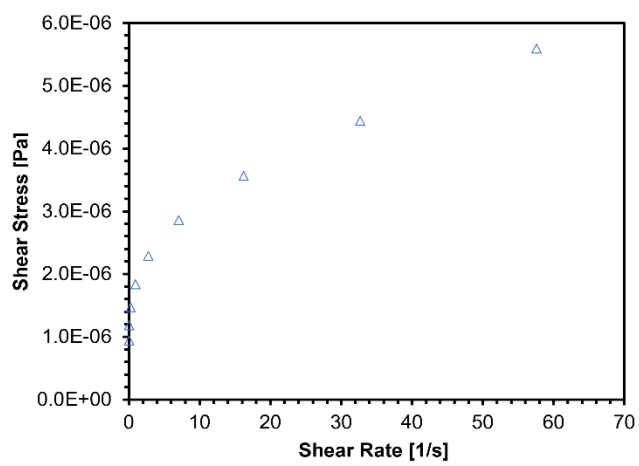

Figure B.6 Flow ramp loop using shear stress as the independent variable but plotting in terms of shear-rate and shear stress.

To determine the greatest effect of yield stress on the pressure drop for the system, a simple force balance of plug-flow between the the pressure drop of the pipe and the fluid yielding is demonstrated.

$$\Delta P \pi R^2 = \tau_0 2\pi R L \tag{B.1}$$

$$\Delta P = \frac{2\tau_0 L}{R}$$

$\tau_0 = 0.94\ Pa$
$L = 1.89\ m$
$R = 0.0508\ m$

$$\Delta P = 70.0\ Pa$$

Even with a notable yield stress of 0.94 Pa, the plastic viscosity term in a bingham model is so great that yield stress negligibly affects the pressure drop and thus the estimated fluid material

properties of the cuttings samples. At the lowest flow rate measured well beyond fluid yielding, the pressure drop of the system is > 900 Pa (Figure 4.3).

B.2 XRD analysis of bentonite samples

Wyoming bentonite (Pondseal-200)

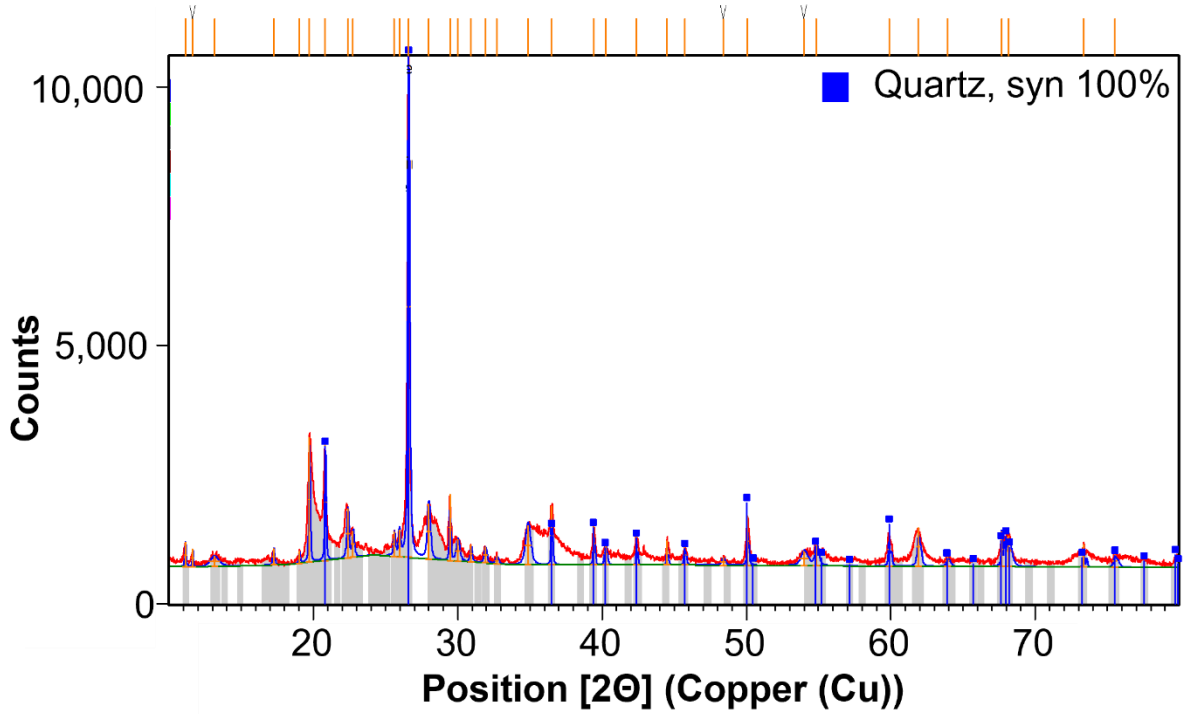

Figure B.7 Powder X-ray diffraction data collected over a 2θ from 10-80 with a step size of 0.02 and 120 seconds per step. The setup was operated with a divergence slit of 1/8", beam attenuator (mask) of 10mm, and anti-scatter slit of 1/2" and set at conditions of 45 kV tension and 40 mA of current. Bragg-Brenato geometry was used for the incident beam optics and Xcelerator optics were used for the diffracted beam optics. Only SiO_2-polymorphs were investigated for the data analysis to focus on the mineralogical differences between the bentonite used in the field-test and model cuttings samples.

MaxGel – Wyoming bentonite supplied by Michels

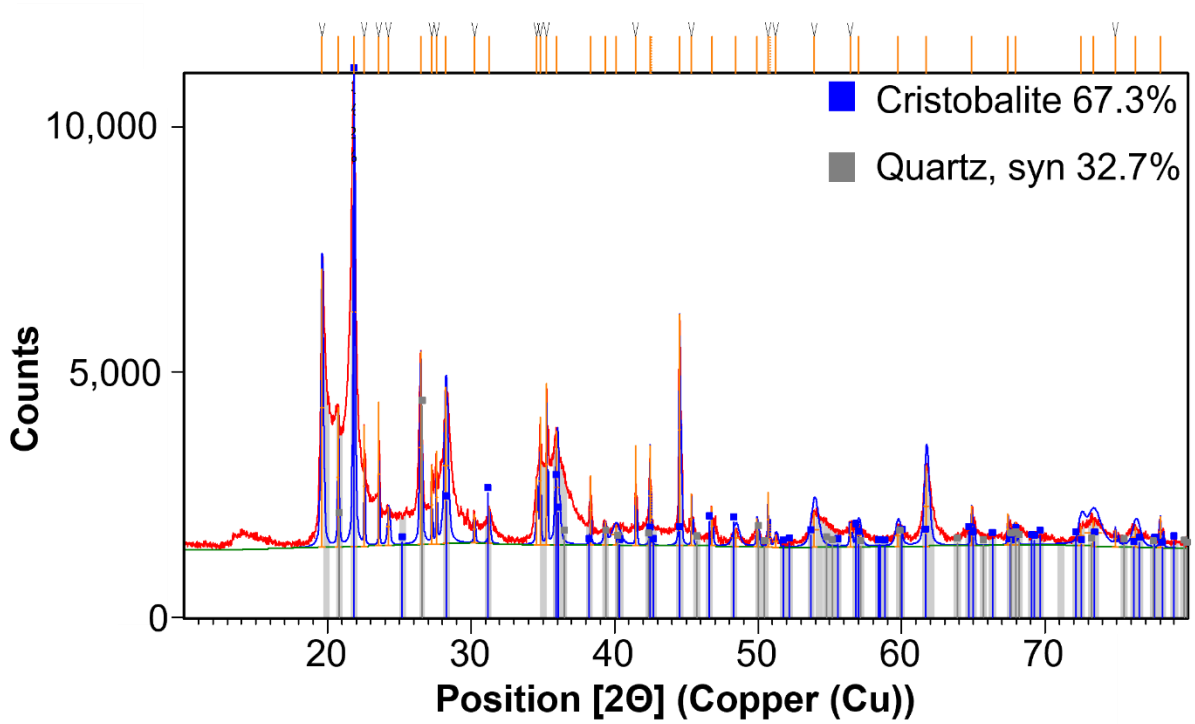

Figure B.8 Powder X-ray diffraction data collected over a 2θ from 10-80 with a step size of 0.02 and 120 seconds per step. The setup was operated with a divergence slit of 1/8", beam attenuator (mask) of 10mm, and anti-scatter slit of 1/2" and set at conditions of 45 kV tension and 40 mA of current. Bragg-Brenato geometry was used for the incident beam optics and Xcelerator optics were used for the diffracted beam optics. Only SiO_2-polymorphs were investigated for the data analysis to focus on the mineralogical differences between the bentonite used in the field-test and model cuttings samples.

The two Wyoming bentonite samples both have high silica oxide contents, but the structure between the two differ as variations in SiO_2-polymorphs. In the Wyoming bentonite sample the SiO_2-polymorphs is quartz while the MaxGel, Wyoming bentonite used by Michels during the interim drill test is Cristobalite. The MaxGel, Wyoming bentonite also has strong signatures of Quartz presence but not as much as the Wyoming bentonite sample.

The mineral phase analysis is performed in HighScore Plus, a software suite developed by Malvern Panalytical. Within the software, the diffraction pattern peaks are identified automatically and manually where needed. The potential elements within the sample are then specified and appropriate compounds are identified from the software database to be compared to

the diffraction pattern peaks to determine the compounds and structures present in each powder bentonite sample.

B.3 Particle size distribution analysis of model and field test formation samples

Model cuttings (Mason Sand)

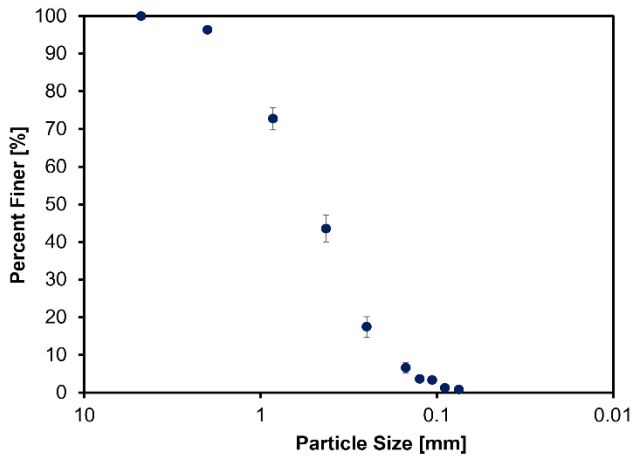

Figure B.9 Sieve test particle size distribution curve for model cuttings sand (Mason sand). The data is from three trials by three separate experimentalists and each data point is an average value with error bars representing the standard deviation between each trial.

Table B.1 Tabulated data collected from the sieve test particle size distribution characterization for Mason sand.

Size of Sieve (mm)	Percent Finer (%)
4.75	4.75
2	2
0.85	0.85
0.425	0.425
0.25	0.25
0.15	0.15
0.125	0.125
0.106	0.106
0.09	0.09
0.075	0.075

Field-test cuttings (Soil core samples)

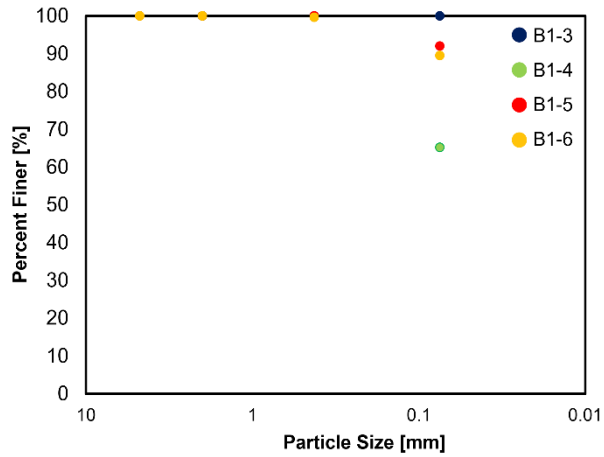

Figure B.10 Sieve test particle size distribution curve for field-test cuttings, represented by core samples collected at representative depths along the drill path. Depths B1-3, B1-4, B1-5, and B1-6 represents 15’-17’, 20’-22’, 25’-27’, 30’-32’, respectively. The first three data points fall on top of one another at the 100% percent finer mark.

Table B.2 Tabulated data collected from the sieve test particle size distribution characterization for field-test cuttings, represented by core samples collected at representative depths along the drill path.

	B1-3	**B1-4**	**B1-5**	**B1-6**
Depth	15'-17'	20'-22'	25'-27'	30'-32'
USCS Classification	Fat clay	Sandy fat clay	Fat clay	Fat clay
Size of Sieves (mm)	Percent Finer (%)			
4.75	100	100	100	100
2	100	100	100	100
0.425	100	99.9	100	99.6
0.075	100	65.2	92	89.5

B.4 Non-linear regression code

MATLAB Code:

```
import numpy as np
import pandas as pd

from scipy.optimize import fsolve, root, minimize
# from sympy import *
from math import pi, log10, sqrt
import matplotlib.pyplot as plt

# static params
diam_m = 0.1016
len_diff_m = 1.8923
rad_m = 0.0508
hzs = [50, 45, 40, 35, 30, 25, 20]

# solve m for given v, p, and n
def solve_m_Szilas(unsolved_value, *data):
    m = unsolved_value[0]
    _n, dP, v, diam_m, density, len_diff_m = data
    ff = (dP*diam_m*0.25)/(0.5*density*v**2*len_diff_m)
    return [
        (4.0/_n)*np.log10((diam_m**_n*v**(2.0-_n)*density)/(m*((3.0*_n+1)/(4.0*_n))**_n \
            *8.0**(_n-1.0))*(4.0*ff)**(1-0.5*_n))+1.51**(1.0/_n)*(4.24+(1.414/_n))-(8.03/_n)-
2.114 - 1/np.sqrt(ff)
    ]

# solve m for given v, p, and n
def solve_m_DodgeNMetzner(unsolved_value, *data):
    m = unsolved_value[0]
    _n, dP, v, diam_m, density, len_diff_m = data
```

```
    ff = (dP*diam_m*0.25)/(0.5*density*v**2*len_diff_m)
    return [
        (4.0/_n**0.75)*np.log10((diam_m**_n*v**(2.0-
_n)*density)/(m*((3.0*_n+1)/(4.0*_n))**_n \
            *8.0**(_n-1.0))*ff**(1-0.5*_n))-0.4/_n**1.2 - 1/np.sqrt(ff)
    ]

## The function to be optimized, which equals to the sum of all right minus left.
def optimize_Szilas(unsolved_value):
    n, m = unsolved_value[0], unsolved_value[1]
    s = 0
    for i in range(len(dP)):
        ff = (dP[i]*diam_m*0.25)/(0.5*density*v[i]**2*len_diff_m)
        s += ((4.0/n)*np.log10((diam_m**n*v[i]**(2.0-n)*density)/(m*((3.0*n+1)/(4.0*n))**n \
            *8.0**(n-1.0))*(4.0*ff)**(1-0.5*n))+1.51**(1.0/n)*(4.24+(1.414/n))-(8.03/n)-2.114 -
1/np.sqrt(ff))**2
    return [s]

## The function to be optimized, which equals to the squared sum of all right minus left.
def optimize_DodgeNMetzner(unsolved_value):
    n, m = unsolved_value[0], unsolved_value[1]
    s = 0
    for i in range(len(dP)):
        ff = (dP[i]*diam_m*0.25)/(0.5*density*v[i]**2*len_diff_m)
        s += ((4.0/n)*np.log10((diam_m**n*v[i]**(2.0-n)*density)/(m*((3.0*n+1)/(4.0*n))**n \
            *8.0**(n-1.0))*ff**(1-0.5*n))-0.4/n**1.2 - 1/np.sqrt(ff))**2
    return [s]

## The function to solve delta P, which equals to right minus left.
def solve_p_Szilas(unsolved_value, *data):
    delta_P = unsolved_value[0]
    n, m, v, diam_m, density, len_diff_m = data
```

```
    return [
        (4.0/n)*np.log10((diam_m**n*v**(2.0-n)*density)/(m*((3.0*n+1)/(4.0*n))**n*8.0**(n-
1.0)) \
                    *(4.0*(delta_P*diam_m*0.25)/(0.5*density*v**2*len_diff_m))**(1-0.5*n))+ \
        1.51**(1.0/n)*(4.24+(1.414/n))-(8.03/n)-2.114 -
1/np.sqrt((delta_P*diam_m*0.25)/(0.5*density*v**2*len_diff_m))
    ]

def solve_p_DodgeNMetzner(unsolved_value, *data):
    delta_P = unsolved_value[0]
    n, m, v, diam_m, density, len_diff_m = data
    return [
        (4.0/n)*np.log10((diam_m**n*v**(2.0-n)*density)/(m*((3.0*n+1)/(4.0*n))**n*8.0**(n-
1.0)) \
                    *((delta_P*diam_m*0.25)/(0.5*density*v**2*len_diff_m))**(1-0.5*n)) \
        -0.4/n**1.2 - 1/np.sqrt((delta_P*diam_m*0.25)/(0.5*density*v**2*len_diff_m))
    ]



# input data
data = pd.read_excel(open('Data for python import.xlsx', 'rb'), sheet_name='Sheet1 (2)')

def plot_by_sample(func, func_name, ns, ne):
    n_dim = 100
    n_cell = np.linspace(ns, ne, num=n_dim)

    cnt_nconv = 0 # count conditions that are not converge
    m_by_n = []
    f_value = []
    for i in range(len(dP)):
    #     print('v-dP set {}c'.format(i))
```

```
        m_tmp, f_tmp = [], []
        for _in, _n in enumerate(n_cell):
            _m = fsolve(func, [1e-5], args=(_n, dP[i], v[i], diam_m, density, len_diff_m))
            m_tmp.append(_m[0])

            _f = func(_m, _n, dP[i], v[i], diam_m, density, len_diff_m)
#           print(_n,_m,_f)

    #       if np.abs(_f) > 1e-7:
    #           cnt_nconv += 1
    #           print(_n, _m, _f)
            f_tmp.append(_f)

        m_by_n.append(m_tmp)
        f_value.append(f_tmp)
    #   print('round {}:'.format(i), f_tmp)
        plt.plot(n_cell, np.log10(m_tmp), label='{} Hz'.format(hzs[i]))
    plt.title(func_name)
    plt.xlabel('n')
    plt.ylabel('log10(m)')
    plt.legend()
    # plt.colormap()
    plt.show()

#   print('not converging rate:', cnt_nconv/(len(dP)*n_dim))

for gid in range(1, 6):
    dP = data[data['GID']==gid]['P'].to_numpy()
    v = data[data['GID']==gid]['Q'].to_numpy()
    density = data[data['GID']==gid]['density'].unique()[0]
    plot_by_sample(solve_m_Szilas, 'Szilas', 0.1, 1.5)
    plot_by_sample(solve_m_DodgeNMetzner, 'D & M', 0.1, 1.5)
```

```
    plot_by_sample(solve_m_Szilas, 'Szilas', 0.4, 0.7)
    plot_by_sample(solve_m_DodgeNMetzner, 'D & M', 0.4, 0.7)
plt.show()

## Find the optimized values of n and m
res_data = [] # parameters with results
bnds = [(0, 1), (0, None)]
init_nm = [(0.6, 0.1), (0.7, 0.02)]

for gid in range(1, 8):
    dP = data[data['GID']==gid]['P'].to_numpy()[-3:]
    v = data[data['GID']==gid]['v'].to_numpy()[-3:]
#     wt = data[data['GID']==gid]['wt'].unique()[0]
    density = data[data['GID']==gid]['density'].unique()[0]

#     print('Group {}: {} wt%, density={}'.format(gid, wt, density))
    for _init in init_nm:
        print('Init n and m:', _init)

        res1 = minimize(optimize_DodgeNMetzner, _init, method='SLSQP', bounds=bnds) #
Method 1 (Dodge and Metzner)
        print(res1.x, 'converge at', res1.fun)

        # Method 2 (Desouky and El-Emam)

        res3 = minimize(optimize_Szilas, _init, method='SLSQP', bounds=bnds) # Method 3
(Szilas)
        print(res3.x, 'converge at', res3.fun)

        res_data.append([gid, density, _init[0], _init[1], res1.x[0], res1.x[1], res1.fun[0],
                    res3.x[0], res3.x[1], res3.fun[0]])
```

```
# results of solved n and m
solved = pd.DataFrame(res_data, columns=['GID', 'density', 'init_n', 'init_m', 'DnM_n', 'DnM_m',
'DnM_SSE', 'Szl_n', 'Szl_m', 'Szl_SSE'])
_solved = solved[['GID', 'density', 'DnM_n', 'DnM_m', 'DnM_SSE', 'Szl_n', 'Szl_m',
'Szl_SSE']].groupby(['GID']).last().reset_index()
_solved.to_csv('solved_m_n_adjusted.csv')

# store delta P with solution to csv
_data = data.copy()
ns, ms = [0.96, 0.74, 0.91, 0.84, 0.84, 0.7, 0.47], [0.0009, 0.016, 0.002, 0.006, 0.011, 0.05, 2.6]
nd, md = [0.96, 0.74, 0.91, 0.84, 0.84, 0.7, 0.44], [0.0009, 0.016, 0.002, 0.005, 0.011, 0.05, 1.6]
delta_P1, delta_P3 = [], []
for _, row in _solved.iterrows():

    dP = data[data['GID']==row['GID']]['P'].to_numpy()
    v = data[data['GID']==row['GID']]['v'].to_numpy()

    for i in range(len(dP)):
        solved = fsolve(solve_p_Szilas, [1e-5], args=(ns[_], ms[_], v[i], diam_m, row['density'],
len_diff_m))
        delta_P1.append(solved[0])

    for i in range(len(dP)):
        solved = fsolve(solve_p_DodgeNMetzner, [1e-5], args=(md[_], md[_], v[i], diam_m,
row['density'], len_diff_m))
        delta_P3.append(solved[0])
print(len(delta_P1), len(delta_P3))
_data['Szl_p'], _data['DnM_p'] = delta_P1, delta_P3

_data.to_csv('solved_p_adjusted.csv')

__solved = _solved[_solved['GID']!=3].reset_index(drop=True)
```

```
# 0.96 0.0009
# 0.74 0.016
# 0.91 0.002
# 0.84 0.006
# 0.84 0.011
# 0.7 0.05
# 0.47 2.6

n, m = [0.96, 0.74, 0.91, 0.84, 0.84, 0.7, 0.47], [0.0009, 0.016, 0.002, 0.006, 0.011, 0.05, 2.6]
f, ax1 = plt.subplots(1, 1, figsize=(10,5))
for _, row in _solved.iterrows():
#     if _<6:
#         continue
    dP = data[data['GID']==row['GID']]['P'].to_numpy()
    v = data[data['GID']==row['GID']]['v'].to_numpy()

    ax1.scatter(v, dP, label='original dP '+str(_))
#     for k in range(len(n)):
    delta_P4 = []
    for i in range(len(dP)):
#         solved = fsolve(solve_p_Szilas, [1e-5], args=(row['Szl_n'], row['Szl_m'], v[i], diam_m,
row['density'], len_diff_m))
        solved = fsolve(solve_p_Szilas, [1e-5], args=(n[_], m[_], v[i], diam_m, row['density'],
len_diff_m))
        delta_P4.append(solved[0])

    # plot different delta P against velocity
    ax1.plot(v, delta_P4, label='recovered dP '+str(_))
    print(delta_P4)
#     break

ax1.set_xlabel('velocity (m/s)')
```

```
ax1.set_ylabel('delta P (Pa)')
ax1.set_title('Use Szilas Model')
ax1.legend()
plt.show()

# 0.96 0.0009
# 0.74 0.016 # not good
# 0.91 0.002
# 0.84 0.006
# 0.84 0.011
# 0.7 0.05
# 0.44 1.6

n, m = [0.96, 0.74, 0.91, 0.84, 0.84, 0.7, 0.44], [0.0009, 0.016, 0.002, 0.005, 0.011, 0.05, 1.6]
f, ax1 = plt.subplots(1, 1, figsize=(10,5))
for _, row in _solved.iterrows():
#     if _<6:
#         continue
    dP = data[data['GID']==row['GID']]['P'].to_numpy()
    v = data[data['GID']==row['GID']]['v'].to_numpy()

    ax1.scatter(v, dP, label='original dP '+str(_))
#     for k in range(len(n)):
    delta_P4 = []
    for i in range(len(dP)):
#         solved = fsolve(solve_p_Szilas, [1e-5], args=(row['Szl_n'], row['Szl_m'], v[i], diam_m,
row['density'], len_diff_m))
        solved = fsolve(solve_p_DodgeNMetzner, [1e-5], args=(n[_], m[_], v[i], diam_m,
row['density'], len_diff_m))
        delta_P4.append(solved[0])

    # plot different delta P against velocity
```

```
    ax1.plot(v, delta_P4, label='recovered dP '+str(_))
    print(delta_P4)
#     break

ax1.set_xlabel('velocity (m/s)')
ax1.set_ylabel('delta P (Pa)')
ax1.set_title('Use DodgeNMetzner Model')
ax1.legend()
plt.show()

## Find the optimized values of n and m, with boundary of m increases with wt
res_data1 = [] # parameters with results
bnds = [(0, 2), (0, None)]
init_nm = (0.8, 1e-2)

for gid in range(5, 0, -1):
    dP = data[data['GID']==gid]['P'].to_numpy()
    v = data[data['GID']==gid]['v'].to_numpy()
    wt = data[data['GID']==gid]['wt'].unique()[0]
    density = data[data['GID']==gid]['density'].unique()[0]

#     print('Group {}: {} wt%, density={}'.format(gid, wt, density))
    res = minimize(optimize_Szilas, init_nm, method='SLSQP', bounds=bnds) # Method 3
(Szilas)
    res_data1.append([gid, wt, density, res.x[0], res.x[1], res.fun[0]])

    bnds[1] = (res.x[1], None)

solved1 = pd.DataFrame(res_data1, columns=['GID', 'wtp', 'density', 'Szl_n', 'Szl_m', 'Szl_SSE'])

# solved delta P with Szilas's solution with boundary of m
f, ax1 = plt.subplots(1, 1, figsize=(10,5))
```

```
for _, row in solved1.iterrows():
    delta_P1 = []

    dP = data[data['GID']==row['GID']]['P'].to_numpy()
    v = data[data['GID']==row['GID']]['v'].to_numpy()
    for i in range(len(dP)):
        solved = fsolve(solve_p_Szilas, [1e-5], args=(row['Szl_n'], row['Szl_m'], v[i], diam_m,
row['density'], len_diff_m))
    #     print(dP[i], '----', solved)
        delta_P1.append(solved)

    # plot different delta P against velocity
    ax1.scatter(v, dP, label='original dP '+str(row['wtp'])+' wt%')
    ax1.plot(v, delta_P1, label='recovered dP '+str(row['wtp'])+' wt%')

ax1.set_xlabel('velocity (m/s)')
ax1.set_ylabel('delta P (Pa)')
ax1.set_title('Use Szilas Data and Szilas Model')
ax1.legend()
plt.show()
```

APPENDIX C PERMEATION CELL

C.1 Hydraulic fracturing in soil mixtures report

Abstract

Hydraulic fracturing in soil is a multi-disciplinary area of research with contributions from a range of research fields, e.g. – environmental remediation, grouting for foundational stability, and directional drilling[22,23,202]. The variety of expertise adding to the field of soil fracture has resulted in numerous experiments, and theory, applying fracture mechanics to soils. The goal of this research is to understand the mechanisms leading to soil fracture and the major contributing factors. A fracture tank (Frac-Tank) has been built to represent a model system of hydraulic soil fracture under confinement pressure to visualize initiation and propagation of fracture formation. Under similar confinement conditions, permeable soil composed of 30% Kaolinite – 70% Sand, fractured at 21 psi, a lower fracture pressure than low-permeability soil composed of 16% Cement – 84% Kaolinite that fractured at 30 psi. The two formulations of soil were chosen because they had similar unconfined compressive strengths of approximately 21 psi and splitting tensile strength around 20 psi. Fluid permeation occurred in the permeable soil before fracture, indicating the potential influence of soil permeation on fluid fracture initiation pressure. Qualitative and anecdotal evidence in the literature have shown low viscosity fluids and greater fluid permeation in soils has resulted in lower fracture initiation pressure[24,203]. Drilling fluid rheology and fluid permeation in natural soil formations have not been well studied in the context of hydraulic fracture in soil, and a more comprehensive investigation of their impact is warranted.

Introduction

Hydraulic fracture in soil commonly occurs when fluid is pressurized past the strength plus minor principle stress limit of the soil[22]. Fractures are terminated if flow is stopped, fluid leak-off meets or exceeds fluid low rate, or the fracture reaches the surface[22]. In tunneling, fractures are undesirable because they result in fluid loss with the potential of causing soil cuttings buildup, borehole collapse, and drill string immobilization resulting in delays and potential loss of equipment[10,204]. Soils are highly variable, spanning gravel, sand, and clays – gravel is highly porous, sand is porous, and clay has low porosity. These differences in porosity lead to different mechanisms and criteria for fracture in soil[23,205]. Clay soils have low permeation, and fracture initiation pressure is linearly dependent on the stress state - soil tensile strength, and

sometimes pore water pressure[23]. Drilling fluid pressure and the stress transfer between the fluid to the formation is the major variable that alters soil conditions leading to fracture[24]. Permeation is the main mechanism of fluid loss in gravel and sandy soils because of drilling fluid can flow through the void spaces and leak-off rather than fracture[206]. The extent of leak-off depends on fluid rheology (shear-thinning and gel strength) and the particle size distribution[205]. High fluid permeation reduces fracture potential due to low fluid pressures. Fracture in sand has been primarily explored in the grouting community, but the mechanism for fracture is unclear and up for debate[205]. The nature of cohesionless material yield alternative fracture criteria and deformation responses to applied stresses. Fracturing in cohesionless soil cannot be dependent on tensile strength like clays because the component structure does not allow a tensile strength to develop as readily[207]. The size and type of sand distribution also yield differences in fracture geometry – finer grading leads to thinner fractures[208]. Low permeability clays encourage fracture formation because pressure can build more readily compared to sands that allow fluid pressure to be leaked off. Fractures can still occur in sands though. If the stress distribution across sand grain networks become anisotropic and zero stress develops in one direction then sand can fracture[209]. Stress distribution in soils are dictated by the principal normal stress, most commonly the confining or overburden pressure from soil and other forces above the soil area of interest, and past stress history.

The material properties of drilling muds can be tuned to soil formations and reduce fluid loss from permeation[210,211]. One function of drilling muds is to be filtered out along the borehole wall, creating a low permeability barrier. This barrier reduces fluid loss from permeation and increases the strength of the borehole, increasing the fluid pressure needed to fracture soil[206]. Drilling fluid – soil interaction is not well studied at a fundamental level regarding the fluid influence on fracture formation. Hydraulic fracturing in soil literature is sparsely studied, we have collected 24 articles spanning 1955 – 2018, and the influence of fluid rheology on soil fracture has not been quantified beyond contributions of increasing viscosity[22–24,203,209,212–217]. The purpose of this paper is to quantitatively and qualitatively explore hydraulic fracture in mixed soil material to provide insight for design and construction of an experimental setup to understand the influence of drilling fluid rheology on hydraulic fracturing in soils.

Soil fracture

Soil fractures were investigated with a preliminary setup, termed Frac-Tank. This setup is seen in Figure C.1. The setup is composed of a plexiglass box without a lid. A soil sample is placed along the front face of the box, while a black wooden insert is applied to the back of the soil sample to confine the soil sample, allowing for ease of visualization and reduces the need for large soil samples. The purpose of the wooden insert is to provide ports that provide access to drill pilot holes providing a point of access for drilling fluid to be introduced into the soil, as seen in Figure C.1a. A standpipe filled with drilling fluid is connected to the back of the wooden insert with a pressure regulator at the top of the standpipe applying air to control fluid pressure. The 2X4 wooden inserts seen in Figure C.1b distribute confining stress as weights are placed on top of them during an experiment. An experiment consists of filling the front of the plexiglass box with desired soil sample – the soil samples were prepared with a 24-hour hydration of the kaolinite mixed with desired weight percent of either sand or cement, with respect to the kaolinite weight. Pilot holes are drilled into the soil sample following the desired port along the wooden insert and the remaining ports are sealed off. Confinement pressure is applied with weights on top of the 2X4 inserts followed by applying drilling fluid into the sample by standpipe. The experiment begins with increasing the fluid pressure in increments of 5 psi while the front face of the plexiglass box is videotaped to record the onset of hydraulic soil fracture. The experiment is terminated once fracture occurs and fluid pressure drastically drops as fluid flows easily through the fracture. A description of the experiments performed are outlined in Table C.1.

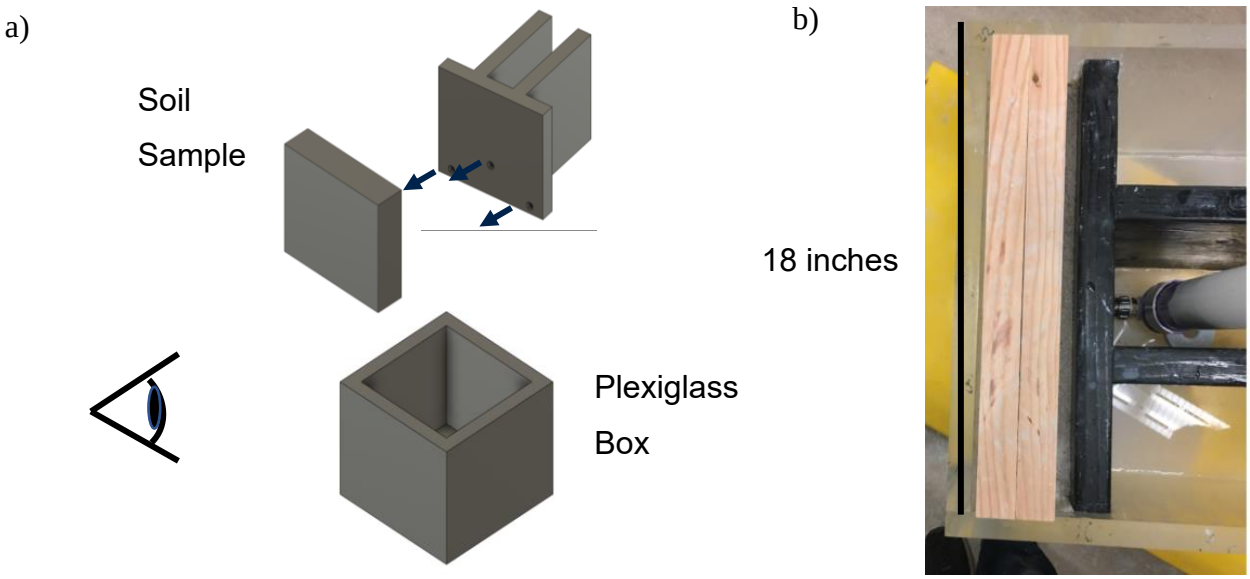

Figure C.1 a) Conceptual design of the fracture tank (Frac-Tank), a plexiglass box houses a wooden insert that confines a soil sample to the front face of the box. Ports in the wooden insert introduce fluid through pilot holes drilled into the soil sample to fracture the soil while observing the front face. b) Top down view of the Frac-Tank, the wooden two-by-fours apply confinement pressure to the soil below them. The black piece is the wooden insert confining the soil sample and introducing fluid into the soil. The white attachment connected to the black insert is a standpipe filled with fluid and air pressure is modulated at the top to measure and control fluid pressure.

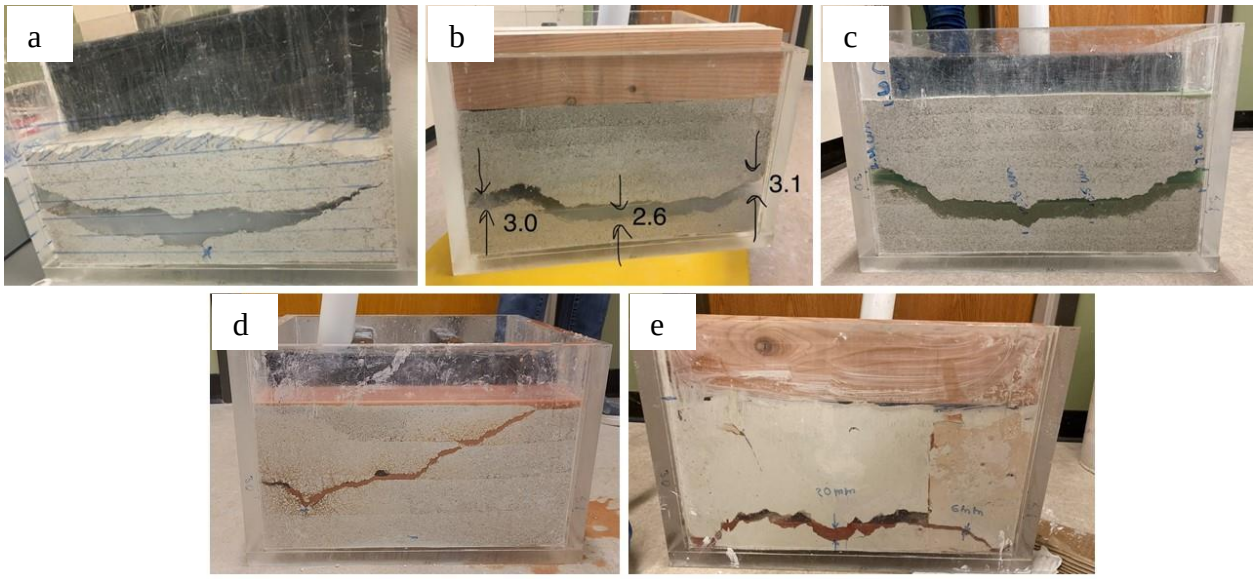

Figure C.2 Post-fracture images of soil fractured in the Frac-Tank. Top row: 30% Kaolinite – 70% Sand central port fluid introduction, a) No confinement pressure, 6, 1 inch tall layers, water, b) 8, 1 inch tall layers, water, 2 psi confinement pressure c) 8, 1 inch tall layers, 2.4wt% Bentonite drilling mud, 2 psi confinement pressure. Bottom row: d) 30% Kaolinite – 70% Sand, 8, 1 inch tall layers, side port 2.4wt% Bentonite fluid introduction, 2 psi confinement pressure, e) 16% Cement – 84% Kaolinite, 8 inch tall, 7 day cure, center port 2.4 wt% Bentonite fluid introduction, 2 psi confinement pressure.

Table C.1. Summary of fracture experiments displayed in Figure C.2

	Soil	Fluid	Port	Sample Height [cm]	Confinement Pressure [psi]	Compaction	Fracture Pressure [psi]	Heave [cm]
a	30% Kaolinite-Sand	Water	Center	15.24	0	6 layers	20	2.54
b	30% Kaolinite-Sand	Water	Center	20.32	2.05	8 layers	20	2
c	30% Kaolinite-Sand	Drilling Mud	Center	20.32	1.99	8 layers	21	2.54
d	30% Kaolinite-Sand	Drilling Mud	Side	20.32	2.34	4 layers	32	1.27
e	16% Cement-Kaolinite	Drilling Mud	Center	19.12	2.26	N/A	30	0.3

Confinement Pressure

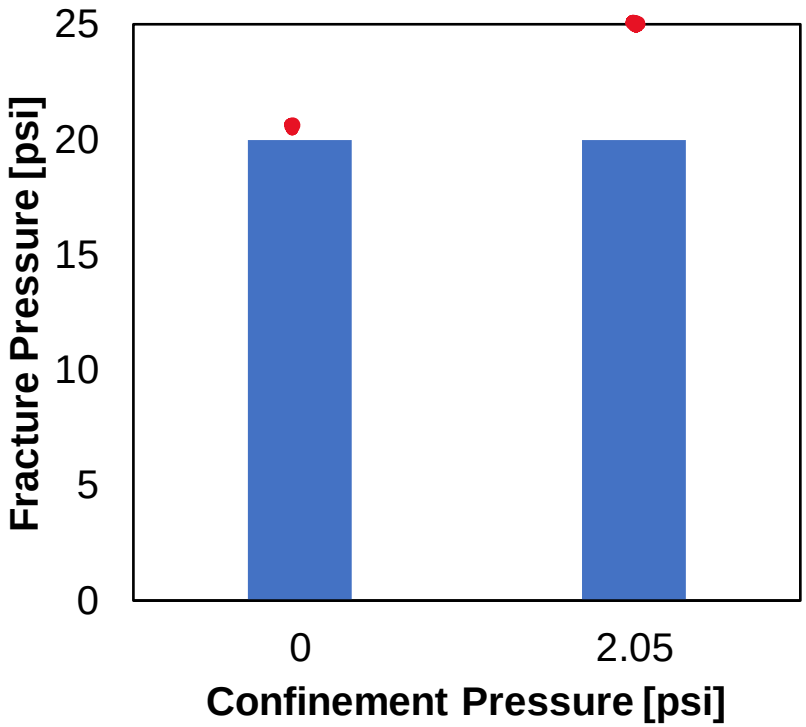

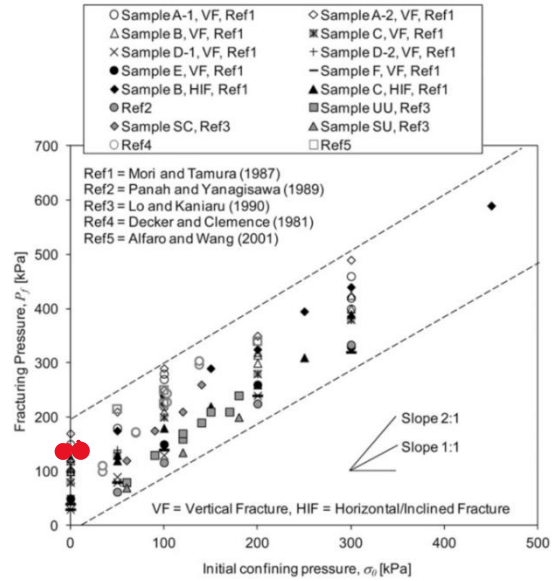

Fig. 2. Fracturing pressure versus initial confining pressure of different soils (modified from Mitchell and Soga 2005)

Figure C.3 (Left) Comparison of fracture pressure of 30% Kaolonite-70% White sand with and without confinement pressure of 2 psi fractured through the center port with water. The data follow experiments in Figure C.2a and C.2b. Most similar to the data of Decker and Clemence (1981) using low plasticity clays at liquidity indices of 0 and 0.5, while the kaolinite used was at 2.23. The red dots are following Elasticity theory outlined in Mitchell and Soga (2005). *Fundamentals of Soil behavior*. (Right) Review of clay fracture data as a response to confining pressure (Marchi *et al*. (2014). Fracturing Pressure in Clay). The red dots represent the data shown in the bar graph (Left). Appendix B shows the liquidity index calculation and comparison to literature.

Confinement pressure was varied for one experiment. The base fracture experiment was an 8 layer, 8-inch-tall 30% Kaolinite-70% White sand (30%K-70%S) sample fractured with water through the central port with a confining pressure of 2 psi (Table C.1). In comparison, a 6 layer, 6-inch-tall 30%K-70%S sample fractured with water through the central port with no confining pressure (Table C.1a, C.1b). Both soil samples fractured at a maximum fluid pressure of 20 psi through the central port (Figure C.3). The fractures can be seen in Figure C.2a and C.2b. The same pressure to achieve fracture of 20 psi indicates that the height of compacted soil layers and the confining pressure insignificantly influence fracture initiation in this system. This is further supported by the large magnitude of friction between the soil sample and the side walls of the Frac-

Tank as seen by both images of the soil after fracture able to maintain their fracture gaps even after fluid pressure and confinement pressure are removed.

Confinement pressure is expected to provide a linear additive pressure to resist hydraulic pressure – a 2 psi confinement pressure should add 2 psi to the fracture initiation pressure[23]. This linear addition is not seen in experiments because wall friction between the soil and plexiglass container is believed to add additional stress to the soil sample. In Figure C.2, the upheaval is the same, but the deformation of the soil is noticeably larger in the no-load vs. loaded soil sample. This further supports the hypothesis that side wall friction is the controlling stress condition related to fracture initiation pressure. In all cases that the fracture reaches both sides of the Frac-Tank, a constant fracture gap is held. The amount of deformation of the soil between the sides varies by confinement pressure, but in all cases the gap extends across the tank and the fracture cannot be closed by manual force. We believe the data collected does not follow fracture theory in clays because the 30%K-70%S sample was compacted, inducing frictional stress that made the confining pressure insignificant (Figure C.3 [Right]).

Drilling Fluid

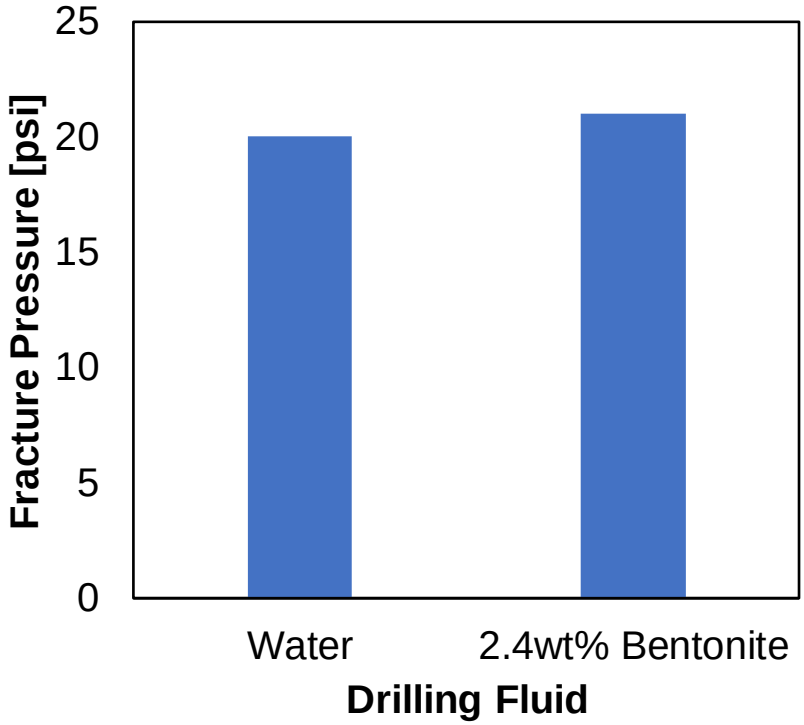

Figure C.4 Comparison of fracture pressure of 30% Kaolinite-70% White Sand fractured through the center port with water and 2.4wt% Bentonite slurry under 2 psi confinement pressure. The data is from experiments in Figure C.2b and C.2c.

The influence of drilling fluid viscosity was evaluated in one experiment series. The base fracture experiment was an 8 layer, 8 inch tall 30%K-70%S sample fractured with water through the central port with a confining pressure of 2 psi (Table C.1b). In comparison, an 8 layer, 8 inch tall 30%K-70%S sample fractured with drilling mud (2.4 wt% bentonite) through the central port with a confining pressure of 2 psi (Table C.1c). The fractures can be seen in Figure C.2b and C.2c. The fracture pressures between the two experiments were approximately the same, 20 psi with water and 21 psi with drilling mud (Figure C.4). The expected outcome was that drilling mud would provide a greater fracture pressure because the mud would be filtered out and add strength to the surrounding soil, similar to filter-cake formation[205].

Drilling fluid permeation before fracture is anecdotally and qualitatively known in the literature to reduce fracture initiation pressure[24,203,218]. The extent of permeation depends on drilling fluid rheology and soil composition. In the experimental comparison between water and drilling fluid, fracture initiation pressure did not vary significantly. This could be because the concentration of bentonite is too low. A bentonite concentration around 2.8-3wt% is the critical concentration that clay platelets reach a critical concentration and begin interacting with one another and assembling into higher ordered structures that yield greater complex rheological properties[34]. Since the drilling fluid concentration was at 2.4wt%, and clay assembly was too weak to noticeably alter the drilling fluid rheology. Alternatively, the pore-spacing in the 30%K-70%S samples could also have been large enough that clay was not being filtered but rather flowing into the interstitial space – not providing strengthening benefits to the soil.

Geometric Confinement

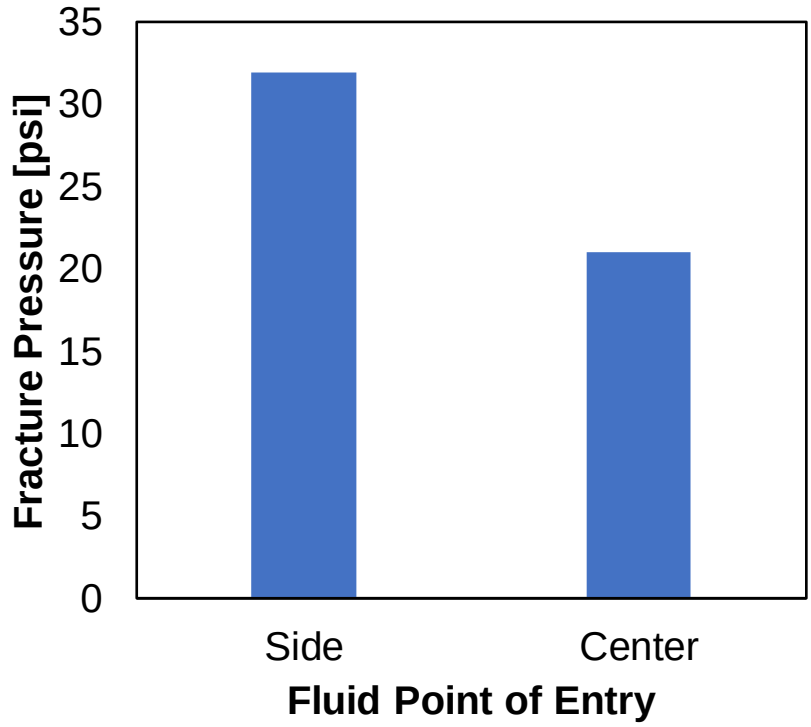

Figure C.5. Comparison of fracture pressure of 30% Kaolinite-70% White Sand fractured through the center port and side port with 2.4wt% Bentonite slurry under 2 psi confinement pressure. The data is from experiments in Figure C.2c and C.2d.

Fluid point of entry was compared in one experiment. The base fracture experiment was an 8 layer, 8 inch tall 30%K-70%S sample fractured with drilling mud (2.4wt% Bentonite) introduced in the central port, with a confining pressure of 2 psi (Table C.1c). In comparison, a 4 layer, 8 inch tall 30%K-70%S sample fractured with drilling mud (2.4 wt% bentonite) introduced through a side port, with a confining pressure of 2 psi (Table C.1d). The fracture pressure for the base experiment was 21 psi, while the side port fracture reached 32 psi. The intention of this experiment was to determine whether fractures could be guided by pressure differences – fluid enters one side port while the opposite side port remains open and the central port remains plugged. The trajectory of fracture instead reached the surface before reaching the opposing side port or side wall, while following the interfaces between compacted layers in a stepwise appearance, Figure C.2d.

Greater fracture initiation pressure was seen when fluid is introduced through the side port. Higher fluid pressures mean greater stress further from the center of the soil sample, supporting the hypothesis that the side walls contribute frictional stresses in close-proximity. With the introduction of fluid into the soil, the soil becomes displaced and moves away from the source of

drilling fluid. However, the additional friction of the side walls results in a greater resistance to soil movement cause by the fluid – yielding greater fluid pressure needed to fracture.

The drilling fluid was also dyed red in this set of experiments, providing support of fluid introduction and permeation into the surrounding soil before fracture occurs (Figure C.2d). Visualization of fluid permeation before fracture bolsters a proposed mechanism that permeation before fracture can weaken and result in smaller fracture initiation pressure.

Soil Permeability

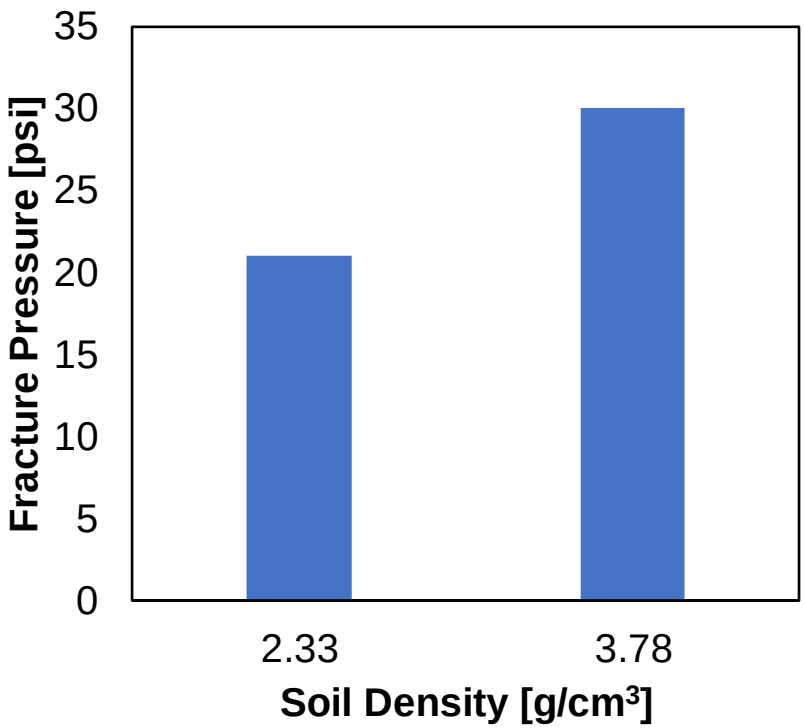

Figure C.6. Comparison of fracture pressure of 30% Kaolinite-70% White Sand and 16% Cement-84% Kaolinite fractured through the center port with 2.4wt% Bentonite slurry under 2 psi confinement pressure. The data is from experiments in Figure C.2c and C.2e.

Soil permeability was compared in one experiment. The base fracture experiment was an 8 layer, 8 inch tall 30%K-70%S (density: 2.33 g/cm^3) sample fractured with drilling mud (2.4wt% Bentonite) introduced in the central port, with a confining pressure of 2 psi (Table C.1c). In comparison, an 8 inch tall 16% Cement-84% Kaolinite (16%C-84%K) (density: 3.78 g/cm^3) sample fractured with drilling mud (2.4 wt% bentonite) introduced in the central port, with a confining pressure of 2 psi (Table C.1e). The fracture for the 30%K-70%S sample was 21 psi, while the 16%C-84%K sample fractured at 30 psi (Figure C.6). 16%C-84%K was selected because

it had a similar compressive strength to 30%K-70%S, but tensile strength should be the true measure of fracture strength because tensile is the main form of failure for low liquidity soils[23].

To further explore permeability, 16%C-84%K was used because clays naturally have low permeability compared to sands and the cement provides additional strength to the soil to match the strength of the 30%K-70%S mixture. No permeation was seen in the 16%C-84%K soil before fracture and fracture occurred at a greater pressure – supporting the hypothesis that clays provide strength against fracture while permeation reduces fracture initiation pressure.

Fracture Analysis

All fractures propagated in predominately horizontal directions. Fracture theory based on fractures in materials with isotropic tensile strength state that fractures propagate in the direction normal to the minor principal stress[24,219,220]. Fracturing in the horizontal direction indicates that the greatest direction of stress in the soil is from the horizontal direction, but the sidewalls do not exert stress onto the soil sample; however, the sidewalls confine the soil sample – allowing the soil to easily displace in the vertical rather than horizontal direction.

All the 30%K-70%S samples were prepared in the Frac-Tank by compaction in layers and had a density of 2.33 g/cm^3. The layering provided interfaces between layers that are weaker, allowing for easier fracture propagation. This can be seen in all 30%K-70%S samples where large lengths of fracture propagation occurred along the interfaces between compacted layers. To mitigate the influence of layers, the experiment where fluid was introduced by the side port (Fig. 2d) had the same total height of soil but half the number of compaction layers. This allowed a larger area for the fluid to interact with the soil before reaching a preferential fracture direction. Halving the number of compaction layers resulted in a sharper vertical fracture peak and angled fracture propagation not seen in the other Kaolinite-Sand samples.

Fracturing in the Cement-Kaolinite sample (density: 3.78 g/cm^3) yielded a downward fracture unseen in the Kaolinite-Sand samples where fractures tended to propagate upwards. This is believed to be due to confinement and the distribution of stress. In the Kaolinite-Sand samples, the stress exerted by the confining pressure is believed to be well distributed along the vertical direction, and because of the confinement of the Frac-Tank bottom, less resisting stress will be experienced as soil displaces upward – encouraging fracture propagation upwards in the lower resistance direction. Conversely, the Cement-Kaolinite sample is predominately clay and when confining pressure is applied not enough time was allowed to pass for consolidation to occur and the distribution of stress did not have enough time to distribute to the bottom of the soil sample –

resulting in a stress gradient with larger confining stresses at the top of the sample than the bottom. Since fractures propagate along the path of least resistance, the fracture moved downwards where confining stress had not yet been allowed to propagate. A valuable point of discussion that may refute this inference is that the downwards propagation seem to happen at the two points where hairline fractures already existed in the soil sample. In Figure C.2e, a hairline fracture on the left and right exist and were present in the sample before fracture. These hairlines may have deviated the trajectory of fracture favoring the downwards direction. Wang *et al*. (2009) found that depending on stress conditions, the orientation of fracture could be affected – at low stress contrasts the vertical to horizontal stress ratio, K0, controls fracture geometry, while at high stress contrasts flow rate controls fracture geometry[218].

Table C.2 Comparing the influence of soil compressive and tensile strength with fracture initiation pressure of 30%Kaolinite-Sand and 16%Cement-Kaolinite fractured through the center port with drilling mud (2.4wt% Bentonite) under 2 psi of vertical confining pressure.

	Unconfined Compressive Strength [psi]	Splitting Tensile Strength [psi]	Fracture Initiation Pressure [psi]
30%K-S	22.18	20.95	21
16%C-K	17.40	20.44	30

$$P_f = a \cdot \sigma_0 + b \cdot \sigma_t' - c \cdot u_0 \tag{C.1}$$

Equation C.1 is the general form of fracture pressure in clays following tensile failure summarized in Marchi *et al.* (2014)[23]. Fracture pressure (P_f) is an additive linear function of confinement pressure (σ_o), tensile strength (σ_t'), and pore water pressure (u_0). The coefficients "a", "b", and "c" generalize this equation derived from different theory and approaches.

Fracture initiation pressure of 16%C-K was 30 psi and 30%K-S was 21 psi, a stark difference in fracture pressure (Table C.2). Under the same simulated stress conditions, around 2 psi of confinement pressure, and fractured through the central port with drilling fluid indicates a fracture mechanism not captured by theory (Table C.1). Equation C.1, is a generic form of fracture pressure in clays summarized by Marchi *et al.* – its major parameters are confinement stress, soil tensile strength, and pore water pressure[23]. Both samples have approximately the same confinement pressure and tensile strength and pore water pressure is assumed to be negligible yet

an influence uncaptured by theory resulted in a 10 psi increase in fracture pressure for the 16%C-K sample compared to 30%K-S (Table C.2). Two potential influences are drilling fluid permeation and wall friction. Drilling fluid permeation is expected to reduce fracture initiation pressure bases on qualitative and anecdotal evidence in the literature[24,203]. Permeation can be seen in the K-S sample but not in the C-K samples supporting this. However, since fracture occurred above the tensile strength of both soil samples, the dominating influence is an additive stress. Depending on whether permeation is influencing the system or not, an additive stress is either on the order of magnitude as the confinement stress or larger. Wall friction or internal friction is believed to be the controlling stress affecting fracture initiation. The K-S sample had no lubrication applied to the walls, but after fracture the soil material appears to be in a jammed state where the fracture cannot be closed by external loading, whereas the C-K sample walls were lubricated with silicone oil to reduce adhesion of the cement to the plexiglass but still maintains the fracture gap after fracture indicating wall friction (Figure C.2). Both samples have roughly the same density around 1.7 g/cm^3. The K-S sample is believed to fracture at a pressure greater than the tensile strength because of the internal friction between the sand particles as they jam due to fluid displacement into the soil sample, increasing the strength of soil against fracture. The C-K sample is believed to fracture at a pressure greater than the tensile strength because the wall-friction lends additional strength against hydraulic fracture.

The side port fracture in Kaolinite-Sand soil was the only sample that fracture naturally propagated to the surface. Another explanation for upwards or downwards direction of propagation could be fluid pressure. This experiment experiences the greatest fluid fracture initiation pressure and sustained pressure following, yielding the greatest fracture propagation upwards reaching the surface rather than terminating at a side wall like the other fractures. In contrast, the Cement-Kaolinite sample also experienced large fracture initiation pressure but followed by the greatest reduction in pressure when drilling fluid reached the existing hairline fracture and bled off to the surface. The reduction in pressure can also be seen by the reduction in fracture thickness significantly decreasing from origination of fracture to the regions after the hairline fractures.

Soil heave appears to reduce with fracture initiation pressure. The upward displacement of soil after fracture in experiments 1-3, as seen in Figure C.2a-c, all experienced fracture around 20 psi and a heave of 1 inch, while the remaining experiments, 4 and 5, experienced greater fracture initiation pressure but less than half the amount of heave. This could be due to contrasts in stress – Alfaro & Wong (2001) saw that smaller contrasts between vertical and horizontal stress resulted in multiple, deviated fractures, whereas larger stress contrasts were resulted in distinct fractures[215]. The potential for different stress contrasts is evident in similar confinement pressure and geometry conditions yet variations in fracture initiation pressure depending on soil composition and location of fluid introduction.

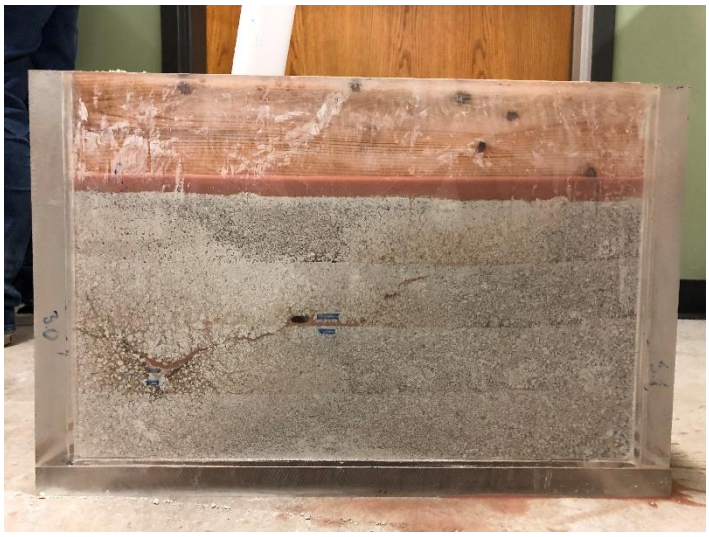

Figure C.7. After fracture of the side port experiment in Figure C.2d, the fracture was manually closed, and fluid pressure was applied to fracture again.

Predominately, the focus of this paper has been on the initiation of fracture and the geometry of fractures, but in the case that fracture cannot be prevented, fluid loss through fracture will be discussed. Two of the experiments touched on fluid loss from fracture, side port fracture of Kaolinite-White Sand and fracture of Cement-Kaolinite. Kaolinite-White Sand fracture was performed but following fracture, due to a smaller number of compaction layers, the soil was able to be pressed down and the fracture closed. The experiment was run again by introducing drilling mud through the side port - pressure built up to 8 psi, flowed preferentially along the fracture, and began eroding the fracture resulting in greater flow and a reduction of pressure. Cement-Kaolinite was not a repeated experiment, but because of the pre-existing hairline fractures showed the occurrence of fluid leak-off with fracture propagation and be the main means of fracture termination in natural soil formations[214]. Both cases show that once a fracture exists, flow

predominately flow along the fracture at high flow rates and low pressures. For drilling muds, this is difficult to stop because the assembly of clay platelets are broken up at high flowrates and rheological properties will more closely resemble the Newtonian behavior of water.

Conclusion

From this study we came to the following conclusions:

1. The geometry of the Frac-Tank alters the fracture strength and behavior of fracture propagation. Side wall friction adds an additional stress, resulting in greater fracture initiation pressure than expected. Confinement of the sidewalls are also believed to result in horizontal fracture since the soil cannot be moved horizontally, vertical soil heave is the only direction to relieve fluid pressure. Confinement pressure was of low influence in fracture initiation pressure compared to wall friction in the permeable 30%K-70%S samples.

2. Drilling fluid permeation is noted to occur in permeable soils before fracture. This phenomenon does not prove fluid permeation alters soil fracture pressure but lends support that permeation could influence fracture pressure since the event occurs before fracture takes place.

3. Compressive and tensile soil strength was insignificant in predicting soil fracture initiation pressure between permeable and low-permeability soil. 30%K-70%S had the same compressive strength as 16%C-84%K at around 20 psi, yet fracture occurred at 21 psi for the permeable soil and 30 psi for the low-permeability soil.

4. Drilling fluid rheology did not significantly affect fracture initiation pressure. Fracture of 30%K-70%S occurred at 20 psi for water and 21 psi for 2.4wt% Bentonite drilling mud.

5. Once fracture occurs, fluid will flow quickly and readily through these preferential channels. Once drilling fluid reaches a fracture, as seen in the refracture experiment of 30%K-70%S and the fracture of 16%C-84%K, the fluid pressure drops dramatically, and fluid readily flows preferentially along the fractures.

<u>Areas of concern are:</u>

1. Frictional contribution of sidewalls for low permeability soils.
2. At small-scale experiments, wall effects will dominate soil fracture and fluid rheology influence will be smeared out

<u>Proposed plan moving forward:</u>

1. Friction contributions will have to be addressed for low-permeability, high adhesion materials. Lubrication alternatives will be explored to mitigate this problem.
2. The Kaolinite-Sand samples represent soils that will be encountered in the interim testing, fracture pressure of those soils was near the tensile strength of the soils indicating that frictional contributions were either negligible or similar magnitude as the confinement pressure. This indicates that the small 4-inch thickness of the Frac-Tank is not an issue for central port fractures. Also, the confinement pressure can be increased to limit the influence of frictional contributions.
3. Increasing confinement will also allow greater fluid pressures to be reached. This may result in greater fluid rheology influence, where greater time and or driving force is provided for the fluid to interact with the soil before fracture.
4. Confinement poses additional frictional contributions as seen in the side wall versus the center port experiments. A more pancake-like Fracture-Chamber geometry is proposed to help mitigate this contribution – greater length and width compared to height of chamber.

Hypothesis: With a pancake-shaped fracture chamber that mitigates geometric confinement, increased confinement pressure applied to the soil sample will allow the drilling fluid rheology to be a significant contribution to lowering fracture pressure of permeable soil materials.

C.2 Flow regimes

Flow regimes are distinctions in the flow behavior of a system, distinguished by Reynolds number (Figure C.8). For flow through porous media, a pore Reynolds number is defined (Equation C.2). The pore Reynolds number is a nondimensional number signifying the ratio between inertial to viscous stresses under a flow condition. The inertial term is composed of fluid density, ρ, fluid superficial velocity, U, and pore size, d_p, commonly assumed to match particle size. The viscous term is the fluid viscosity. The flow regimes in order of increasing pore Reynolds numbers are Darcy/viscous, inertial, unsteady-laminar, turbulent, and asymptotic flow regimes[190].

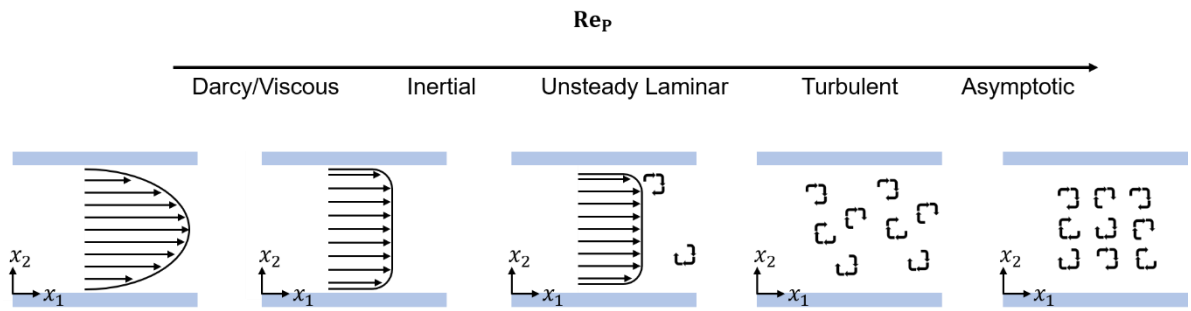

Figure C.8 Schematic of flow regimes dependent on values of pore Reynolds numbers, Re_P.

$$Re_P = \frac{\rho||U||d_p}{\mu} \tag{C.2}$$

Each flow regime is represented by a phenomenon description, but each description is also sensitive to fluid rheology. The Darcy/viscous regime is represented by flows so slow that the viscous nature of the fluid dominates the flow behavior. Inertial flow marks the transition where the fluid momentum overtakes viscous behavior, and the driving force of the fluid dictates the flow phenomenon. Unsteady-laminar flow is a continuation of inertial flow with the addition of eddy formations that act as a mechanism to dissipate momentum within flow. Turbulent flow is described as non-unidirectional laminar flow, where the previous flow regimes exist as an assembly in all directions and increased eddy formation occurs. Asymptotic flow is turbulent flow at such a high Reynolds number that the turbulence becomes isotropic throughout the system[190]. For non-Newtonian fluids, such as drilling muds, the viscosity term in the pore Reynolds number will be dependent on the flow condition, including the flow rate and geometry of the pore bed. This dependence of the viscosity on flow condition can shift flow regimes from their typical pore Reynolds number values and can alter the flow phenomenon.

Fluid loss to highly porous formations cover a wide range of flow regimes. At low flow regimes, the rheological properties of fluids will dominate flow behavior, while at large flow regimes, the strain on the fluid will be so great that additives in the fluid will no longer be interacting, significantly decreasing the influence of fluid rheology. In a fluid loss event, this is represented by first encountering coarse soils—fluid will rapidly flow into the formation, representing high flow regimes. As the fluid travels further and the fluid becomes less energized by a pressure driving force, lower flow regimes will be experienced. The designed system will be able to replicate high and low flow regimes representative of a fluid loss event. Low flow regimes will be the focus

because at these regimes the fluid rheology will play a dominant role in controlling fluid loss to formation.

Figure C.9 is a representation of the expected flow to occur in the designed system as governed by flow regimes. At low Re_P, the viscous nature of bentonite will dominate but at greater flow rates in inertial flow, plug-flow is expected to develop[221]. Plug-flow occurs when a shear-thinning fluid is flowing down a pipe. The shear rates along the radii of the pipe will be greatest at the wall and smallest at the pipe center. This means that the drilling mud will be greatly sheared along the outer radii resulting in low viscosities that act as a lubricant for the central region of fluid to create a plug, hence plug-flow. Then with greater Re_P, more eddies will develop, dissipating momentum, as represented by increasing pressure drop across the permeation cell.

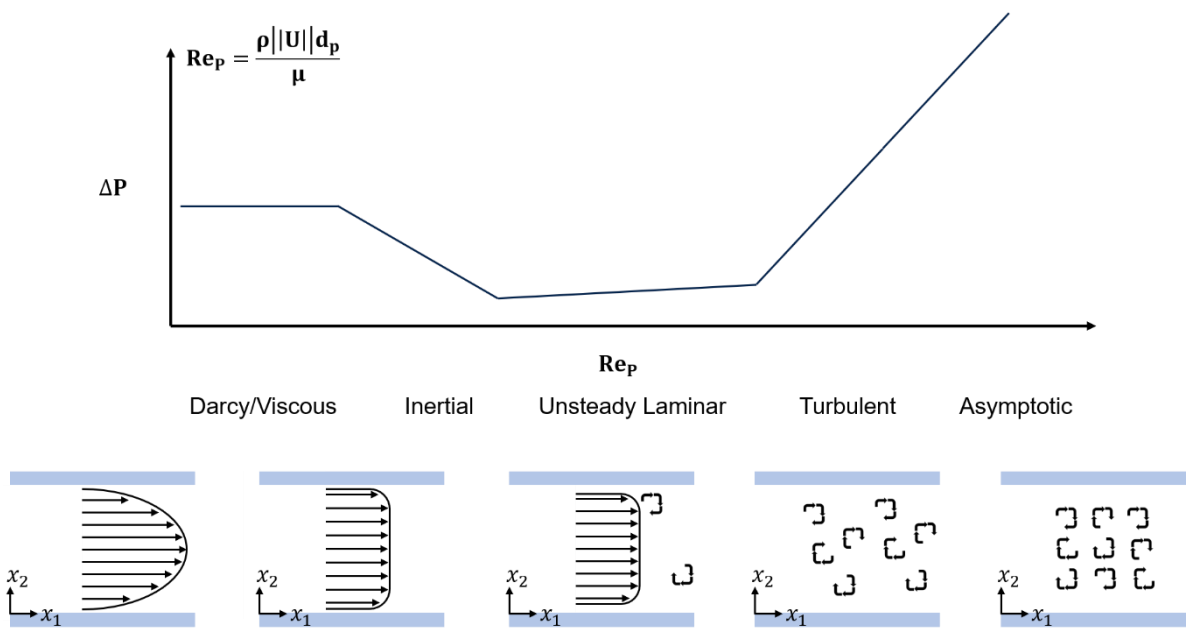

Figure C.9 Predicted pressure drop behavior across the permeation cell dependent on the flow regime experienced as defined by pore Reynolds number.

The equations to be used follow the work of Rodríguez de Castro & Radilla (2017) for low Re_P up to inertial flow of shear-thinning fluids, Equations 2.16 & 2.17[74]. At higher Re_P, the expected shear rates will be so large that the fluid rheology will not be an influencing variable in the flow rate–pressure drop relationship, and turbulent pipe flow of water will be used to predict the flow rate–pressure drop relationship. Equation C.3 represents the pressure drop–flow rate relationship of turbulent Newtonian pipe flow through a smooth walled pipe[222].

$$\frac{dp_f}{dL} \propto q^{1.75} \tag{C.3}$$

Equations 2.16 & 2.17 and Equation C.3 encompass the current state of the literature and are limited to steady-state flow, without suspensions in the fluid. In the event of fluid loss, flow will be transient from high pressure at the cutter head to low pressure into the surrounding porous formation. The drilling fluid surrounding the cutterhead will also be laden with solids content from soil cuttings. To represent this dynamic event, a new model will be developed to represent fluids transitioning from high to low flow and solids content accumulating and clogging flow propagation.

C.3 Flow sweep of drilling fluid

Viscosity is a quantity measuring resistance to flow and shear rate is the speed the fluid is flowing, normalized by a geometric distance of the container the fluid flows through. These curves are useful to quantify fluid flowability because they are generalized to any system because any system can be characterized by a shear-rate. A common method of quantifying the viscosity curves is to fit the shear-thinning regime to a power-law constitutive equation, Equation C.4.

$$\eta = M \cdot \dot{\gamma}^{n-1} \tag{C.4}$$

The power-law equation is unrealistic at low and high shear-rates because it is unable to account for the viscosity plateaus seen in Figure C.10, but it is useful to quantify the differences in viscosity between fluids, M parameter, and the extent of shear-thinning, n parameter. Viscosity is η and shear-rate is $\dot{\gamma}$, Table C.3.

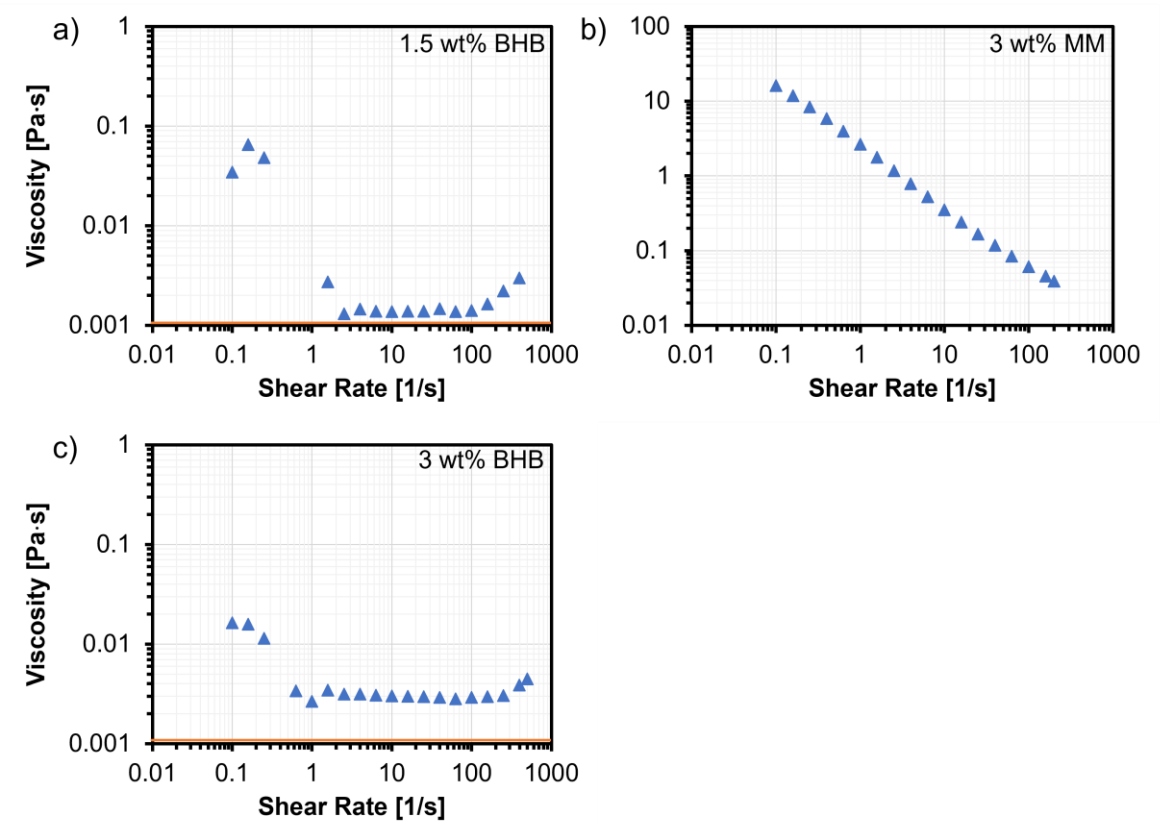

Figure C.10 Viscosity curves of a) 1.5wt% Black Hills Bond Bentonite slurry (BHB), b) 3wt% Michels Maxgel bentonite slurry, and c) 3wt% BHB. The blue triangles are the viscosity curves of the bentonite slurries and the orange line at the bottom of a) and c) are the viscosity curves of water to reference the viscosity of water and its Newtonian behavior, independent of shear-rate.

In Figure C.10a and C.10c are viscosity curves of Wyoming bentonite slurry from Black Hills Bond LLC (BHB) and panel "b" is Maxgel a Wyoming bentonite fluid from Michels (MM). As seen in Figure 10a and 10c, the bentonite slurries exhibit a higher viscosity at a low shear-rate, representing slow fluid velocities, and as the fluid velocity increases the viscosity decreases. At low shear-rates the Brownian dynamics of the bentonite clay platelets dominate their orientation into random movement resulting in the greatest resistance to flow indicated by a higher viscosity. With increasing flow the bentonite clay platelets align in the direction of flow, reducing the resistance to flow[36]. A viscosity plateau is reached once the time-scale of flow dominates the time-scale of Brownian platelet dynamics and the resistance to flow reaches a minimum state. The plateau viscosity of the 3wt% BHB is higher than that of 1.5wt% BHB because with greater solids content in the water more energy is needed to move the clay platelets resulting in a higher resistance to flow. The difference in power-law parameters between Figure 10a and 10c is small compared to 3wt% MM. MM has orders of magnitude larger viscosity and no plateau behavior across the

same experimental shear-rate range. The mechanism for shear-thinning behavior of MM is the same as BHB, but the chemical composition of MM yields different electrostatic interactions that dictate how the clay platelets assemble and disassemble during flow. Across a broader range of shear-rate values the MM is expected to exhibit the same trend as BHB. Mining location and selection of Wyoming bentonite can have drastic differences in rheological properties based on the mineral content and composition.

C.4 Small Angle Oscillatory Shear (SAOS) rheology of drilling fluid

To incorporate non-Newtonian rheology into our models, each fluid will be characterized under oscillatory-shear and steady-shear experiments with a rheometer. Rheometers are instruments that sensitively measure the stress-strain relationship of fluid samples to probe material properties representative of low Reynolds number regimes where fluid properties will have the greatest influence.

Small angle oscillatory shear (SAOS) is a non-destructive technique to quantify the strength and unique electrostatic interactions between structures in fluids, including clay platelet aggregates[223–226]. Interactions between platelets will be sensitive to concentration, additives, pH, contaminants, and any other factor influencing the strength and timescale of their assembly. The rheometer can measure the elastic moduli, a critical material property encompassing the interactions between platelets. Additional information on these measurements is included in Appendix C.

In preparation for this task, drilling mud rheology has been collected on industrially used drilling muds which include bentonite with and without mixed-metal hydroxide (MMH) additives at appropriate concentrations. Figure C.11 provides a summary graph of SAOS measurements made on a range of bentonite concentrations and a sample of bentonite with MMH added. The x-axis is frequency, the rate at which a small strain is applied to the sample, and longer time-scale phenomena are probed at larger frequency values. The y-axis is storage moduli, synonymous with elastic moduli. The trend in data is that with increasing bentonite concentration, the elastic moduli increases. This is because the clay platelet concentration has surpassed a critical value so that clay platelets are interacting, aggregating, and forming into larger structures; with more bentonite content, those structures are continuing to build in density as represented by higher elastic moduli values[34]. With the increasing bentonite content, a plateau in elastic moduli will eventually be

reached, indicating the maximum packing fraction of the platelets[227]. The deviations for the fluids away from constant elastic moduli with frequency above 10 rad/s is indicative of gel breakdown due to frequencies that align with the timescale of electrostatic and Brownian dynamics that lead to clay platelet assembly.

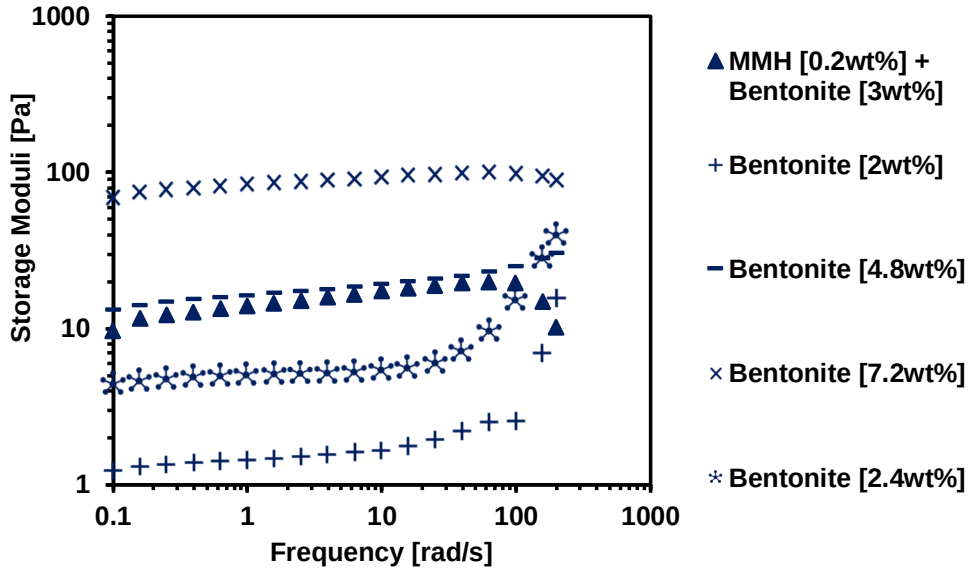

Figure C.11 Elastic moduli data collected for drilling fluids to date. Data obtained from using SAOS to quantify electrostatic interactions between clay platelets of drilling fluids.

Gel strength of bentonite slurries is a commonly characterized property but in terms of material properties, both yield stress and elastic moduli are measured in conjunction for this characterization. The elastic modulus is the strength of interactions between clay platelets while yield stress is the stress threshold capturing the transition from stationary to flowing fluid. Typical gel strength experiments obfuscate both by measuring both at the same time. SAOS experiments and steady-shear experiments can separately characterize the two material properties.

C.5 Shear-thinning characterization

Steady-shear experiments will measure shear-thinning behavior that evaluates the structural changes of complex fluid under laminar flow with increasing strain, performed on a rheometer. Steady-shear experiments are done to evaluate bulk properties, viscosity, shear stress, normal stress, etc., as a sample is deformed at constant rates that increase in a stepwise fashion. The purpose of steady-shear experiments is to mimic real-life flow phenomena because the rate of deformation in any process can be simplified to the rate at which a fluid is deformed, the shear rate. Most fluids under steady shear will be shear-thinning with increasing shear rate, as shown in

Figure C.12. The characteristic of shear-thinning is evident in paint, polymers, and mud slurries, but the mechanisms behind the behavior are different. In clay and suspensions, the mechanism behind shear-thinning will be dependent on structural breakdown if there are electrostatic interactions between suspended particles, alignment of structures or particles if the particles are anisotropic, and entropic state if there are Brownian suspensions that aggregate[9,228]. A means to quantify shear-thinning behavior is to use the power-law constitutive equation for fluids, as stated in Equation C.4. Power-law rheology has been around for a long time and originated from describing the shear-thinning behavior of polymer solutions, but has grown to describe many systems including gels and glasses[229–234]. This model will be used as a simple expression to quantify the shear-thinning behavior of the clay suspensions.

From Equation C.4, the pre-factor, K, and the exponent, n-1, will be compared amongst clay suspension concentrations and, with the addition of to-be-determined additives, will be used to evaluate interaction effects on structure breakdown and shear-thinning behavior, as shown in Table C.3.

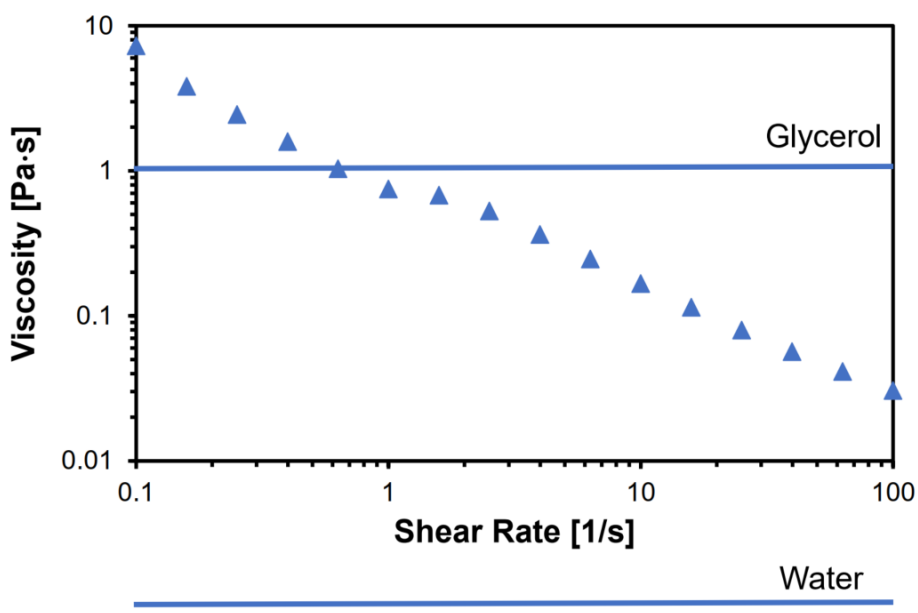

Figure C.12 Steady-shear measurement of 2.8wt% bentonite in a DHR-3 rheometer.

Table C.3 Pre-factor and exponent to quantify shear-thinning behavior of drilling muds using the power-law model as a convenient exponential expression, $\eta = K \cdot \dot{\gamma}^{n-1}$.

Fluid	Pre-Factor (K)	Exponent (n-1)
MMH [0.2wt%] + Bentonite [3wt%]	3.356	-0.738
Bentonite [2wt%]	0.393	-0.716
Bentonite [2.4wt%]	0.930	-0.744
Bentonite [4.8wt%]	5.598	-0.842
Bentonite [7.2wt%]	14.083	-0.877

Within the range of Wyoming bentonite concentrations from 2 wt% to 7.2 wt%, the exponent magnitude increases and remains negative, indicating greater exponential decay characteristic of shear-thinning. As the concentration of Wyoming bentonite increases, resulting in greater packing, the destruction of the assemblies will have a greater magnitude, which expresses the transition from ordered structure to disordered platelets.

Each drilling fluid tested in the permeation cell will be characterized with steady-shear and oscillatory-shear experiments to determine the dynamic and static material properties of the fluid. This will then be used in determining the relationship between pressure drop and flow rate in addition to developing a time-dependent model.

C.6 Dynamic clogging model – Relating pressure and flow rate

Figure C.13 Schematic representation of the permeation cell filled with gravel. Drilling fluid is flowing through the system (left), followed by the introduction of solids to the drilling fluid leading to plugging of pores in the cell (right).

A transient model of fluid clogging in highly porous soil will need to be developed to represent fluid loss followed by flow reduction and stoppage. The conceptual model of a solids-laden fluid clogging highly porous media is depicted in Figure C.13. The bottom of the figure shows the progression of the clogging from left to right: 1) initial porous soil condition, 2) large pore sizes before drilling mud is lost to formation, 3) drilling mud flooding the system and coating the gravel, 4) solids cuttings included in the drilling mud filling the voids and reducing porosity, and 5) sand accumulating in the system and drilling mud bridging the solid material until flow ceases. During the time-lapse of this event the void spaces are shrinking over time. The pressure drop and flow rate of the system, shown in the top part of Figure C.13, assume constant pressure drop conditions, and as the pore sizes decrease the flow rate is expected to exponentially decrease to maintain constant pressure drop.

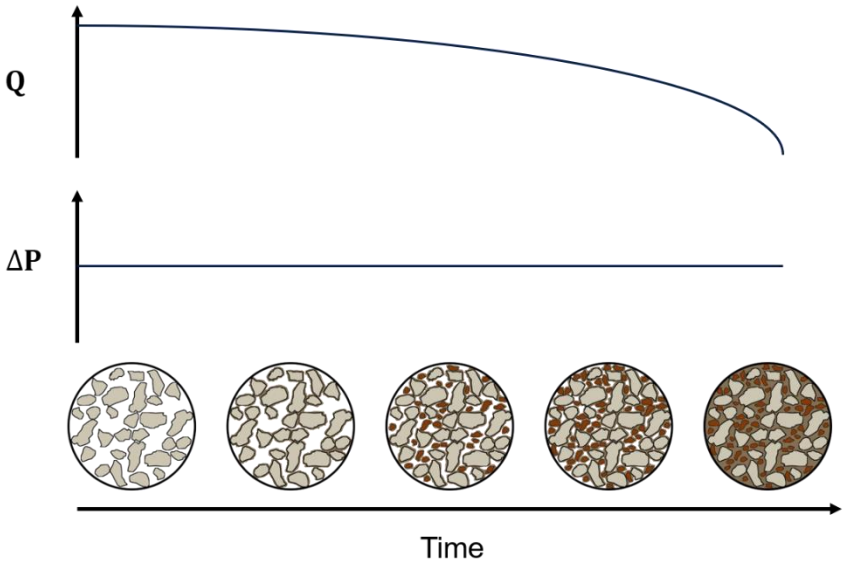

Figure C.14 Expected flow rate and pressure drop behavior of the permeation cell with respect to the evolution of plugging.

A simple time-dependent model will capture the major independent variables of the system controlling the clogging of pore spaces. Bizmark *et al.* recently published work in this area, exploring laminar flows of colloidal suspensions depositing in microscopic porous media modeled as a change in permeability of the medium with time (Equations C.6 and C.7)[235]. In Equation C.6, the first term represents colloids deposited into the porous media, while the second term is pristine and without colloidal deposits.

$$\Delta P = \frac{\mu Q(t) L_d(t)}{A k_d(t)} + \frac{\mu Q(t)[L - L_d(t)]}{A k_0} \tag{C.6}$$

In Equation C.7, the pressure drop equation can be solved at the initial pristine condition and initial system permeability with the time dependent permeability results in this expression, making it a model of permeability change with time as colloidal aggregates are deposited in the porous medium.

$$\tilde{k}(t) \equiv \frac{k(t)}{k_0} = \tilde{Q}(t) \equiv \frac{Q(t)}{Q_0} = \frac{1}{1 + \tilde{L}(t)\left[\frac{1}{\tilde{k}_d(t)} - 1\right]} \tag{C.7}$$

$$\tilde{L}_d(t) \equiv \frac{L_d(t)}{L}$$

$$\tilde{k}_d(t) \equiv \frac{k_d(t)}{k_0}$$

The model expressed by Equations C.6 and C.7 is limited to viscous dominated laminar flows with pore Reynolds numbers on the order of 10^{-4}[235]. Our proposed design will be exploring larger void spaces on the inch-length scale and at higher flow rates resulting in a wide range of Reynolds numbers. It is expected that a model like this could be used but will need to incorporate the pore Reynolds number because flow regime will dictate the influence of fluid rheology, and as seen in Bizmark *et al*.'s work, flow rate within a single flow regime will control the deposition and ultimately the plugging of flow in porous media[235].

APPENDIX D USE OF COPYRIGHTED MATERIAL AGREEMENTS

The following pages contain pictures of the appropriate copyright agreements.

Chapter 4: Flow loop paper, no permission from the publisher required and permission from a co-author attached below: https://publishing.aip.org/resources/researchers/rights-and-permissions/permissions/

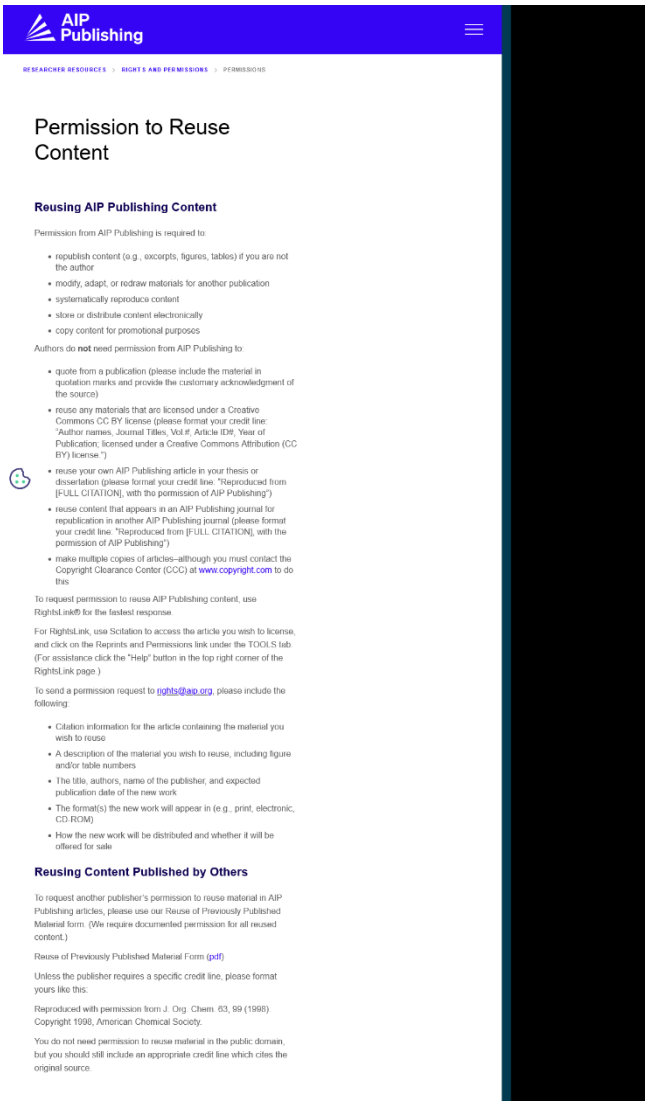

AIP Publishing

RESEARCHER RESOURCES > RIGHTS AND PERMISSIONS > PERMISSIONS

Permission to Reuse Content

Reusing AIP Publishing Content

Permission from AIP Publishing is required to:

- republish content (e.g., excerpts, figures, tables) if you are not the author
- modify, adapt, or redraw materials for another publication
- systematically reproduce content
- store or distribute content electronically
- copy content for promotional purposes

Authors do **not** need permission from AIP Publishing to:

- quote from a publication (please include the material in quotation marks and provide the customary acknowledgment of the source)
- reuse any materials that are licensed under a Creative Commons CC BY license (please format your credit line: "Author names, Journal Titles, Vol #, Article ID#, Year of Publication; licensed under a Creative Commons Attribution (CC BY) license.")
- reuse your own AIP Publishing article in your thesis or dissertation (please format your credit line: "Reproduced from [FULL CITATION], with the permission of AIP Publishing")
- reuse content that appears in an AIP Publishing journal for republication in another AIP Publishing journal (please format your credit line: "Reproduced from [FULL CITATION], with the permission of AIP Publishing")
- make multiple copies of articles–although you must contact the Copyright Clearance Center (CCC) at www.copyright.com to do this

To request permission to reuse AIP Publishing content, use RightsLink® for the fastest response.

For RightsLink, use Scitation to access the article you wish to license, and click on the Reprints and Permissions link under the TOOLS tab. (For assistance click the "Help" button in the top right corner of the RightsLink page.)

To send a permission request to rights@aip.org, please include the following:

- Citation information for the article containing the material you wish to reuse
- A description of the material you wish to reuse, including figure and/or table numbers
- The title, authors, name of the publisher, and expected publication date of the new work
- The format(s) the new work will appear in (e.g., print, electronic, CD-ROM)
- How the new work will be distributed and whether it will be offered for sale

Reusing Content Published by Others

To request another publisher's permission to reuse material in AIP Publishing articles, please use our Reuse of Previously Published Material form. (We require documented permission for all reused content.)

Reuse of Previously Published Material Form (pdf)

Unless the publisher requires a specific credit line, please format yours like this:

Reproduced with permission from J. Org. Chem. 63, 99 (1998). Copyright 1998, American Chemical Society.

You do not need permission to reuse material in the public domain, but you should still include an appropriate credit line which cites the original source.

Figure D.1 Copyright permission for re-use of paper published in Physics of Fluids in Chapter 4. Characterizing the Non-Newtonian Viscosity of High-Solids Drilling Fluid Dispersions by Flow Loop, *Physics of Fluids* 34, no. 5 (May 2022): 053313. Copyright 2022 American Institute of Physics.

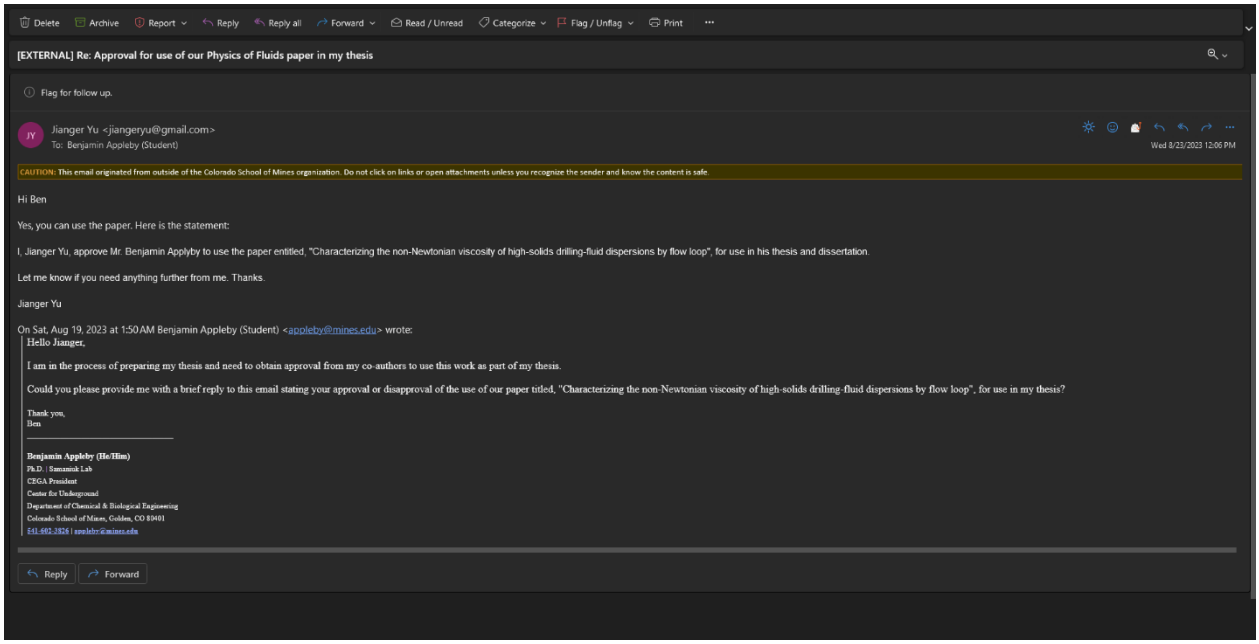

Delete Archive Report Reply Reply all Forward Read / Unread Categorize Flag / Unflag Print ...

[EXTERNAL] Re: Approval for use of our Physics of Fluids paper in my thesis

Flag for follow up.

JY Jianger Yu <jiangeryu@gmail.com>
To: Benjamin Appleby (Student)
Wed 8/23/2023 12:06 PM

CAUTION: This email originated from outside of the Colorado School of Mines organization. Do not click on links or open attachments unless you recognize the sender and know the content is safe.

Hi Ben

Yes, you can use the paper. Here is the statement:

I, Jianger Yu, approve Mr. Benjamin Applyby to use the paper entitled, "Characterizing the non-Newtonian viscosity of high-solids drilling-fluid dispersions by flow loop", for use in his thesis and dissertation.

Let me know if you need anything further from me. Thanks.

Jianger Yu

On Sat, Aug 19, 2023 at 1:50 AM Benjamin Appleby (Student) <appleby@mines.edu> wrote:

Hello Jianger,

I am in the process of preparing my thesis and need to obtain approval from my co-authors to use this work as part of my thesis.

Could you please provide me with a brief reply to this email stating your approval or disapproval of the use of our paper titled, "Characterizing the non-Newtonian viscosity of high-solids drilling-fluid dispersions by flow loop", for use in my thesis?

Thank you,
Ben

Benjamin Appleby (He/Him)
Ph.D. | Samanuk Lab
CEGA President
Center for Underground
Department of Chemical & Biological Engineering
Colorado School of Mines, Golden, CO 80401
541-602-3826 | appleby@mines.edu

Reply Forward

Figure D.2 Co-author permission for re-use of paper published in Physics of Fluids in Chapter 4. Characterizing the Non-Newtonian Viscosity of High-Solids Drilling Fluid Dispersions by Flow Loop, *Physics of Fluids* 34, no. 5 (May 2022): 053313. Copyright 2022 American Institute of Physics.